2017

Fiber Optic Guided Wave Sensors For Structural Health Monitoring

Erik Frankforter
University of South Carolina - Columbia

FIBER OPTIC GUIDED WAVE SENSORS FOR STRUCTURAL HEALTH MONITORING

by

Erik Frankforter

Bachelor of Science
University of South Carolina, 2012

Master of Engineering
University of South Carolina, 2015

Submitted in Partial Fulfillment of the Requirements

For the Degree of Doctor of Philosophy in

Mechanical Engineering

College of Engineering and Computing

University of South Carolina

2017

Accepted by:

Victor Giurgiutiu, Major Professor

Sourav Banerjee, Committee Member

Bin Lin, Committee Member

Lingyu Yu, Committee Member

Paul Ziehl, Committee Member

Cheryl L. Addy, Vice Provost and Dean of the Graduate School

ACKNOWLEDGEMENTS

This work would have not been possible without the many members of the USC community who helped foster and support my development as a researcher.

I would like to thank my PhD advisor, Dr. Victor Giurgiutiu (Dr. G) for his support, guidance, and encouragement over these past five years. Dr. G: you have fostered this incredible LAMSS research group and community, and I'm proud to be a part of it. Years ago, when I first joined the lab, you said you planted apple trees, not wheat. In truth, you have grown a forest; my roots wouldn't be as deep without you.

I would also like to thank Dr. Sourav Banerjee, Dr. Bin Lin, Dr. Lingyu Yu, and Dr. Paul Ziehl. To each of you, thank you for being on my committee and providing guidance over the years. And thank you for agreeing to read a 300+ page dissertation in your spare time!

Next, I would like to thank the postdoctoral researchers I learned from, Jingjing (Jack) Bao and Bin, Lin. Thank you both for serving as teacher and mentor. Dr. Bao: you taught me how to think like a programmer and a scientist. Dr. Lin: you went to great lengths to train me in the lab; first you showed me which buttons to push and why, and then how to make my own buttons.

Thank you to Dr. Guiren Wang. Dr. Wang, you provided several engineering consultations at critical points, helping to strengthen my experimental work. Beyond the engineering, thank you for your geniality and kindness over the years.

I would be remiss without acknowledging my fellow graduate students in the lab, past and present. Special mention goes Dr. Catalin Roman to whom my work follows. I'd also like to thank Dr, Banibrata Poddar, Dr. Yanfeng Shen, Dr. Ayman Kamal, and Dr. Tuncay Kamas for welcoming me to the lab and helping me grow into it. And I'd like the thank all my fellow LAMSS members and graduate students who have helped bring life (both academically and through friendship) during my tenure here, including William, Saad, Asaad, YB, Hanfei, Robin, Stephen, and Darun.

I would like to thank my mother and father Kristine and Steven Frankforter for the constant love and support. And thank you to my brother Keith for your camaraderie, good humor, and editing help. Of course, special thanks go to my wife. Zoë: thank you for your patience and support. I would not have made it so far without you.

This material is based on work supported by Office of Naval Research grant numbers N000141110271 and N000141512102, Dr. Ignacio Perez technical representative. Any opinions, findings, and conclusions or recommendations expressed in this material are those of the authors and do not necessarily reflect the views of the Office of Naval Research.

This work was partially supported by the 2015-2016 SPARC Graduate Grant from the Office of the Vice President for Research at the University of South Carolina.

.

ABSTRACT

Risks and costs associated with aging infrastructure have been mounting, presenting a clear need for innovative damage monitoring solutions. One of the more powerful damage monitoring approaches involves using ultrasonic guided waves which propagate through a structure and carry damage-related information to permanently bonded sensors. Ultrasonic fiber-optic sensors are one of the most promising technologies for this application: they are immune to electromagnetic interference, present no ignition hazard, and transmit their data over tens of kilometers. However, before they can be widely employed, several limitations need to be overcome: poor sensitivity, unidirectional sensing, and loss of ultrasonic functionality due to static loading.

In this dissertation, these limitations were addressed using a mechanical design approach, combining a mechanical resonator with a fiber-optic sensing element. Based on this principle, two fiber-optic sensors were developed: a ring sensor and a wave-absorbing acoustic black hole sensor. Sensitivity improvements up to 28 dB were achieved through mechanical resonance. Prototypes were shown to be insensitive to static loads and detected waves omnidirectionally. The sensors were also miniaturized and designed to be sensitive to different types of wave motion; the ring sensor was sensitive to out-of-plane motion only, and the acoustic black hole sensor was sensitive to both in-plane and out-of-plane motion. The sensor development process is presented from concept sketch to modeling, design, verification, optimization, and calibration.

TABLE OF CONTENTS

LIST OF TABLES

LIST OF FIGURES

CHAPTER 1

INTRODUCTION

1.1 MOTIVATION

Risks and costs have been mounting with the prolonged use of aging infrastructure, presenting a clear need for innovative damage monitoring technologies. These same technologies present opportunities within the aerospace industry to monitor aging fleets and to support the usage of composite materials in the next generation of aircraft. To name a few prominent cases:

- Almost one quarter of US bridges are classified as structurally deficient or functionally obsolete, with an estimated $31.6 trillion needed for remediation (U.S. Federal Highway Administration, 2014). Technology which ensures structural reliability with prolonged use can increase safety and reduce remediation costs
- Postponement of the United States national nuclear waste repository has necessitated extensions of on-site nuclear storage. Monitoring of nuclear dry cask storage canisters will be necessary to mitigate failure risk since their use has been extended past their intended design lifespans (Hamilton et al. 2012; Sun 2015)
- There is a trend towards increased usage of composite materials in aerospace vehicles, such as the Boeing 787 which is comprised of 50%

composites by weight. However, inspection costs of aerospace composites are very high, representing approximately a full third of their lifecycle costs (Diamanti and Soutis 2010).

The emerging field of structural health monitoring (SHM) seeks to address such concerns by supplementing manual scheduled inspection with continuous *in situ* monitoring (Giurgiutiu 2014). Many technologies have the potential for use in SHM applications, many of them transitioned from the well-established field of nondestructive evaluation (NDE). The distinction between the two fields relates to the development and use of damage detection technology for continuous monitoring in SHM, or for periodic inspection in NDE.

SHM is incredibly demanding in its scientific and technological challenges. However, there is a strong case for its development and application. In some cases, conventional inspection approaches are difficult or impossible (e.g. in extreme temperatures, explosive environments, and space applications). Continuous monitoring presents the potential to increase assurances of reliability, reducing structural downtime and high costs by decreasing the requisite number of manual inspections. SHM also has the potential to catch unexpected damage in-service with potential savings in money, structures, and lives. From a long-term outlook, SHM can enable advanced design paradigms such as the digital twin, where damage information is used to update a high-fidelity model of an aerospace vehicle. This would allow digital testing of operations and maneuvers prior to execution during flight (Glaessgen and Stargel 2012).

One of the most prominent SHM techniques involves the use of ultrasonic guided waves. These are waves that propagate through a solid medium along free surfaces or

material interfaces, traveling long distances to interact with damage and carry damage-related information. In some cases, guided waves can be initiated by damage events itself such as impacts and acoustic emissions from crack growth. These waveforms are detected by an ultrasonic sensor and can be subsequently interpreted to obtain information about the damage state.

Over the past several decades, there has been a great deal of interest in advancing fiber-optic sensors for ultrasonic sensing as an alternative to conventional piezoelectric sensors. This is because fiber-optic sensors possess many inherent advantages that piezoelectric sensors do not. Fiber-optic sensors are immune to electromagnetic interference and ideal for monitoring in explosive environments. They are corrosion resistant, lightweight, and possess an exceptional form factor. They also possess the advantages inherent in fiber-optic telecommunication technologies such as multiplexing and remote interrogation.

Despite their advantages, fiber-optic technology is not yet mature enough to be in widespread use for ultrasonic guided wave applications. Currently, there are several technical limitations associated with fiber-optic sensors. Some of the most pressing limitations are:

1. Ultrasonic fiber-optic sensors have lower sensitivity and higher noise than their piezoelectric counterparts. This inhibits their ability to detect waveforms associated with small flaws before they begin to cause problems with structural reliability
2. For ultrasonic strain or displacement sensing, fiber-optic sensors tend to only detect the component of motion unidirectionally along the fiber's axis. This is a hindrance

in guided wave applications where waveforms can arrive from any number of incident angles

3. Some of the most promising fiber-optic sensing configurations cease to operate in the presence of static strain. For common implementations such as surface-bonded fiber-optic sensor, this precludes their use for monitoring a structure in-service.

Developments in fiber-optic sensing technology which mitigate these limitations help shift the cost-benefit analysis towards feasibility in SHM applications.

1.2 Research Scope and Objectives

1.2.1 Research Scope

The scope of the research presented in this dissertation is to address fundamental limitations of ultrasonic fiber-optic sensors through a mechanical design approach, where a fiber-optic sensing element is combined with a mechanical resonator. This includes the steps necessary to design, model, verify, characterize, and optimize these mechanically amplified fiber-optic sensors. The emphasis is on guided wave sensing due to its potential for SHM applications.

1.2.2 Research Objectives

In terms of the sensors themselves, one objective of the work presented in this dissertation is to work towards the development a mechanical fiber-optic sensor which would perform reliably in a variety of guided wave applications. This work should move towards allowing an end-user to just “bond the sensor to their structure” to obtain reliable results, decreasing the current level of cross-domain expertise required for fiber-optic sensing. In terms of specific performance characteristics, the following performance characteristics are sought:

- Mechanical resonance amplification to increase sensitivity as compared to a surface-bonded fiber-optic sensor
- Omnidirectional sensing, i.e. ability to sense waves from any incident angle
- Insensitivity to quasi-static strain
- Sensitivity to in-plane motion, out-plane motion, or both by design
- Small sensor size

Since this dissertation started with a sensor candidate in-hand, the first goal was to develop a proof of concept for a resonant mechanical fiber-optic sensor. This involved calibration of a fiber-optic sensing system as well as experiments on both the free sensor and Lamb wave sensor response experiments. The next objective was to characterize the sensor experimentally, guided by theories of guided wave propagation.

A finite element modeling (FEM) framework was a key feature of this project, both for understanding a sensor's mechanism of action and improving the sensor performance. A FEM-based design exploration and optimization framework was performed for each sensor developed, with the goal of maximizing sensitivity through mechanical amplification.

Towards the end of the development process for the first fiber-optic sensor, the second sensor was developed from the point of view that the best approach was not just to use an arbitrarily chosen resonant geometry. Rather, the approach taken was to exploit novel applications of physics and provide high amplitude and desired sensing features. A wave trapping geometry was identified and worked into several sensor configurations to try to provide both high amplification and sensitivity to the desired type of wave motion.

Finally, one of the biggest gaps identified in a review of fiber-optic mechanical sensors (Chapter 6) was the lack of measured or transferrable performance standards with respect to sensitivity. To this end, one objective of this work was to calibrate the sensors in this work, developing quantitate metrics of sensor performance that both allow for internal comparisons and refer sensor motion back to surface motion of its host structure.

It should be noted that intent of the work presented in this dissertation is to develop mechanical fiber-optic sensors which are generally suited for the detection of ultrasonic guided waves. Some of the research framework presented herein may be skewed more towards AE applications. However, that is because its long history and development provide powerful tools for sensor characterization which are broadly applicable to ultrasonic guided wave sensing.

1.3 Organization of this Dissertation

Chapter 2 of this dissertation presents a review on structural health monitoring and ultrasonic guided waves. Chapter 3 provides a review of acoustic emissions.

Chapter 4 presents a review of ultrasonic NDE and SHM sensors, with an emphasis on piezoelectric wafer active sensors (PWAS), conventional ultrasonic transducers, and acoustic emission sensors.

Chapters 5 and 6 present information in fiber-optic sensors. Chapter 5 presents general principles of fiber optics and fiber-optic sensors to help provide a reader with a background on the topic as applied to ultrasonic sensing. Chapter 6 presents a survey on fiber-optic guided wave sensing with an emphasis on mechanical fiber-optic attachment.

Chapters 7-11 present the experimental work performed in this dissertation. In Chapter 7, a proof-of-concept for a ring sensor is developed, where a ring resonator is

combined with a fiber Bragg grating (FBG) sensor and PWAS. Chapter 7 also includes optical system characterization and calibration.

Chapter 8 presents the use of FEM simulations for free sensors and Lamb wave to investigate the ring sensor mechanisms of action. FBG placement, and PWAS placement and type were studied.

In Chapter 9, a design optimization was performed for both miniaturization and sensitivity enhancement of the ring sensor. The miniature ring sensor prototype is verified experimentally.

In Chapter 10, a wave trapping acoustic black hole (ABH) concept is adapted for sensing applications. A concept of a point-contact bonded optical fiber waveguide is combined with the ABH local vibration. Preliminary experimental investigations were performed.

In Chapter 11, a review on AE sensor calibration methodology is performed, followed by calibration experiments for the sensors developed in this dissertation to put the work performed herein on a better absolute quantitative and transferrable footing.

Chapter 12 presents summary, conclusions, and recommendations for future work.

CHAPTER 2

STRUCTURAL HEALTH MONITORING AND GUIDED WAVE REVIEW

2.1 ULTRASONIC STRUCTURAL HEALTH MONITORING

The developments of this dissertation fall within the scope of ultrasonic SHM, one of the most prominent and promising approaches for damage monitoring. In ultrasonic SHM, permanent structurally embedded transducers transmit and receive ultrasonic guided waves. These waves have the potential to propagate over large areas to interact with damage. Waves that have interacted with damage propagate to a sensor; the detected waveform can be analyzed to determine damage location, type, severity, and even geometry. In some cases, the energy that constitutes the waves can originate from the damage itself, such as from impact and acoustic emission (AE) events.

Interpreting waveforms to characterize damage is fundamentally an inverse problem. This has motivated a growing body of research to develop high fidelity models which represent the forward problem of wave propagation and wave-damage interaction (Poddar and Giurgiutiu 2016). This is further supplemented by data-driven waveform analysis approaches trying to bypass the physics of the problem by using machine learning, parametric correlation, and baseline signal comparison.

A conceptual framework for an SHM system can be understood by analogy to a human nervous system. A human nociceptor ("pain receptor") detects internal damage. Neurons transmit the signals to the brain where signals are interpreted and associated with

damage. Analogously for the SHM system, elastic waves are detected by a structurally embedded sensor, and optical or electrical connectors transmit the information to a computer which interprets the signals as damage-related through data processing algorithms. For the SHM system to be successfully, the embedded sensor must be sufficiently sensitive to damage-induced waves, and the algorithms must be able to judiciously segregate damage-related from non-damage-related events.

2.1.1 Active and Passive SHM Approaches

SHM methods can be divided into two broad categories: passive SHM and active SHM. In passive SHM, no energy from a transducer is input into the structure; rather sensors just "listen" to the structure and are used to infer structural health. In active SHM, an embedded transducer inputs energy into the structure. This excites a wave which interacts with damage, and is subsequently detected by the same or another transducer. A conceptual sketch of several common active and passive ultrasonic guided wave SHM methods is shown in Figure 2.1 (Giurgiutiu 2016). In this figure, the emphasis is on a prominent SHM sensor called a piezoelectric wafer active sensor (PWAS) which is described in more detail in Chapter 4.

2.1.2 Active SHM – Pitch-Catch, Pulse-Echo, and Phased Array

Active SHM methods are categorized through the transmitter and receiver setup. These include pitch-catch, pulse-echo, and phased array. Each method uses guided waves for far-field damage monitoring. The distinction is in the transmitter and receiver configuration. In a pitch-catch configuration, one transmitter generates a waveform which interacts with damage, and a separate receiver senses the waveform. In a pulse-echo setup, a single transducer acts as transmitter and receiver; upon interaction with damage, the back-

scattered portion of the wave is sensed by the same transducer. In a phased array setup, a group of transducers are placed in distinct spatial locations, and multiple transducers are excited to act as spatial filters using beamforming algorithms. This allows for the scanning of regions across space.

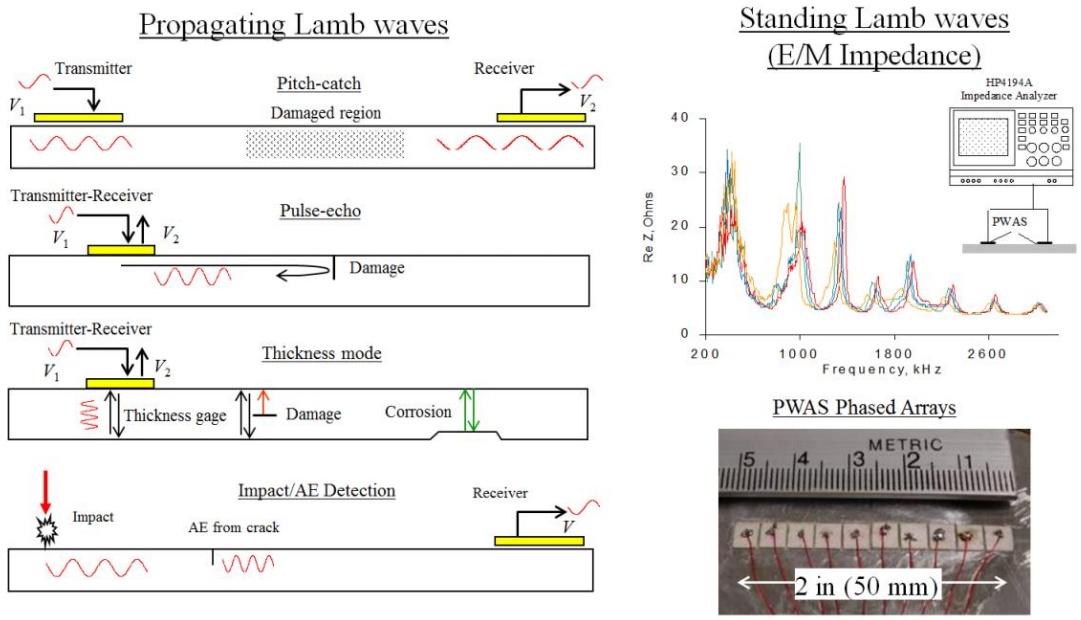

Figure 2.1: Methods of PWAS damage monitoring (Giurgiutiu 2010)

2.1.3 Passive SHM – Impact and Acoustic Emission Methods

Impact and acoustic emission (AE) damage detection methods differ in that the energy input comes from the damage source. Impact is of concern in composite structures since they are prone to low-velocity impact damage, e.g. from dropping a hand tool onto a thin composite part. In composites, the damage often occurs within the lamina, e.g. delamination, and results in barely visible damage. Impact detection can include detecting the waveform associated with the impact itself; this waveform does not necessarily indicate damage, but simply indicates that an impact occurred. When a damage event occurs, waveforms released from the damage propagate, typically at different frequencies and

wave speeds. In composites, the frequency components can correlate to characteristic types of damage. Although this could be considered impact detection (detecting damage associated with impact), it can also be considered a form of AE sensing as the damage-induced waveform itself is an AE.

AEs are elastic waves generated when a material incurs changes in its internal structure, often associated with damage. They can be associated with cracks, plastic deformation, delamination, fretting, etc. AE is considered a field in its own right, with its own equipment, terminology, analysis methods, and commercial applications. AE sensing is challenging in understanding and interpretation. Application of AE techniques often has components of statistical parametric analysis, clustering algorithms, and damage localization; the question of the exact dynamics of wave propagation is often not assessed. Although recently, there have been trends to characterize source mechanics and wave dynamics in AE for better understanding and predictive power. Improving the forward modeling process is a critical step in advancing the use of AE for SHM sensing, as it allows for a quantitative assessment of the AE-damage relationship, particularly for use in advanced materials such as composites. The theory and application of AE is central to this work and is presented in detail in Chapter 3.

2.2 Review of Elastic Wave Propagation

2.2.1 Axial and Flexural Waves in Bars and Beams

Axial and flexural wave capture many fundamental aspects of wave propagation phenomenon, and their resulting equations repeat in more complex cases (see Chapter 10 for a similar analytical workup for flexural waves in variable thickness structures). The frequency dependence of flexural waves in beams serves as a good starting point for

discussion of dispersion phenomenon. An important note is that axial and flexural wave formulations are approximations to the more accurate elastic wave formulations.

Axial waves: For an axial wave in a bar, assume a uniform, elastic, isotropic bar undergoes motion $u(x,t)$ along the bar's axial direction. The motion in the bar is prescribed by the wave equation

$$c^2 u'' = \ddot{u} \tag{2.1}$$

where the wave speed in the bar c is given by $c^2 = \frac{EA}{m}$ or $c^2 = \frac{E}{\rho}$ for a uniform bar, E being the elastic modulus, m being the mass per unit length, and ρ being the mass density of the bar.

A method of solving (2.1) is given by the d'Alembert solution where the displacement is equal to the superposition of a forward and backward propagating wave, i.e.

$$u(x,t) = g(x+ct) + f(x-ct) \tag{2.2}$$

The initial value problem consists of finding the solution to (2.1) subject to initial conditions

$$\begin{aligned} u(x,0) &= u_0(x) \\ \dot{u}(x,0) &= v_0(x) \end{aligned} \tag{2.3}$$

where applying the d'Alembert solution results in

$$u(x,t) = \frac{1}{2}\left[u_0(x-ct) + u_0(x+ct)\right] + \frac{1}{2c}\int_{x-ct}^{x+ct} v_0(z^*)dz^* \tag{2.4}$$

Flexural waves: For a flexural wave in a beam, assume a uniform, elastic, isotropic beam undergoes vertical displacement $w(x,t)$. The equation of motion for flexural wave in a beam is given by

$$a^4 w''''(x,t) + \ddot{w} = 0 \tag{2.5}$$

where the constant a is given by $a^4 = \frac{EI}{m}$, E being the elastic modulus, I being the area moment of inertia, and m being the mass per unit length.

Assuming harmonic motion $w(x,t) = \hat{w}(x)e^{i\omega t}$, a separation of variables solution yields the general solution

$$w(x,t) = Ae^{i(\gamma x + \omega t)} + Be^{-i(\gamma x - \omega t)} + Ce^{\gamma x}e^{i\omega t} + De^{-\gamma x}e^{i\omega t} \tag{2.6}$$

where the wavenumber γ is given by $\gamma^4 = \frac{\omega^2}{a^4}$. Following the relation between wave speed and wavenumber

$$\gamma = \frac{\omega}{c} \tag{2.7}$$

the flexural wave speed c_F is given be

$$c_F(\omega) = \frac{\omega}{\gamma} = a\sqrt{\omega} \tag{2.8}$$

2.2.2 Dispersion Phenomenon and Group Velocity

When the speed of a wave is a function of frequency, that wave is considered dispersive. Consider that a typical propagating wave does not consist of a single frequency, but can be broadband, or at least have a spread about a single carrier frequency (e.g. a tone burst). Different frequency components of this wave will travel at different speeds. Because of this, a dispersive wave will tend to "spread out" (i.e. disperse) as it travels further away from the source. Waves with velocities that are not a function of frequency are considered nondispersive; they travel as a coherent package without spreading out.

In practice, waves have the tendency to travel in discrete "packets" of localized waves traveling as a unit. If the wave is dispersive, then the wave packets travel at a velocity called the group velocity c_g which is defined by

$$c_g = \frac{d\omega}{d\gamma} \tag{2.9}$$

Note that the group velocity differs from the wave speed c. Solving equation (2.8) for ω and differentiating as in equation (2.9), the group velocity for a flexural wave in a beam is given by $c_{gF}(\omega) = 2c_F(\omega)$, such that the flexural group velocity is twice as fast as the flexural wave speed.

The concepts of dispersion, wave packets, and group velocity are of particular importance for guided waves, as dispersive guided waves (e.g. Lamb waves) naturally break down into a number of separate packets each with their own distinct characteristics.

2.2.3 Straight-Crested Axial and Flexural Waves in Plates

Axial and flexural waves in plates are approximations to elastic plate waves which are useful for their simplicity. The tradeoff is that the conditions of the assumptions must be valid, so their scope is limited in applicability. Straight-crested axial and flexural waves serve as approximations to straight-crested S_0 and A_0 Lamb wave modes at low frequency-thickness products. Their formulations are presented here in further detail as they serve as a foundation for modeling the wave propagation in variable thickness plates presented in Chapter 10.

To formulate the equations for straight-crested axial and flexural wave, start with the 3D elasticity equations using engineering constants E, ν, and G in a compliance formulation:

$$\begin{aligned}
\varepsilon_{xx} &= \frac{1}{E}\sigma_{xx} - \frac{\nu}{E}\sigma_{yy} - \frac{\nu}{E}\sigma_{zz} \qquad \varepsilon_{xy} = \frac{1}{2G}\sigma_{xy} \\
\varepsilon_{xy} &= \frac{-\nu}{E}\sigma_{xx} + \frac{1}{E}\sigma_{yy} - \frac{\nu}{E}\sigma_{zz} \quad , \quad \varepsilon_{yz} = \frac{1}{2G}\sigma_{yz} \\
\varepsilon_{zz} &= \frac{-\nu}{E}\sigma_{xx} - \frac{\nu}{E}\sigma_{yy} + \frac{1}{E}\sigma_{zz} \qquad \varepsilon_{zx} = \frac{1}{2G}\sigma_{zx}
\end{aligned} \tag{2.10}$$

where

$$G = \frac{1}{2(1+\nu)}E \tag{2.11}$$

Plate waves are formulated under plane stress assumptions ($\sigma_{zz} = 0$), such that the 3D elasticity equations reduce to

$$\begin{aligned}
\varepsilon_{xx} &= \frac{1}{E}\sigma_{xx} - \frac{\nu}{E}\sigma_{yy} \qquad \varepsilon_{xy} = \frac{1}{2G}\sigma_{xy} \\
\varepsilon_{xy} &= \frac{-\nu}{E}\sigma_{xx} + \frac{1}{E}\sigma_{yy} \quad , \quad \varepsilon_{yz} = \frac{1}{2G}\sigma_{yz} \\
\varepsilon_{zz} &= \frac{-\nu}{E}\sigma_{xx} - \frac{\nu}{E}\sigma_{yy} \qquad \varepsilon_{zx} = \frac{1}{2G}\sigma_{zx}
\end{aligned} \tag{2.12}$$

Solving equations (2.12) for σ_{xx}, σ_{yy}, and σ_{xy} we obtain

$$\begin{aligned}
\sigma_{xx} &= \frac{E}{1-\nu^2}(\varepsilon_{xx} + \nu\varepsilon_{yy}) \\
\sigma_{yy} &= \frac{E}{1-\nu^2}(\nu\varepsilon_{xx} + \nu\varepsilon_{yy}) \\
\sigma_{xy} &= 2G\varepsilon_{xy}
\end{aligned} \tag{2.13}$$

Under small strain approximations, the strain-displacement relations relating to equation (2.13) are

$$\varepsilon_{xx} = \frac{\partial u}{\partial x} \qquad \varepsilon_{yy} = \frac{\partial v}{\partial y} \qquad \varepsilon_{xy} = \frac{1}{2}\left(\frac{\partial u}{\partial y} + \frac{\partial v}{\partial x}\right) \tag{2.14}$$

Taking an infinitesimal element of a plate with force resultants (force per unit width) N_x, N_y, N_{xy}, the force resultants can be obtained by integrating the stresses across the thickness and using equations (2.13) and (2.14)

$$\begin{aligned} N_x &= \int_{-h/2}^{h/2} \sigma_{xx} dz = \frac{Eh}{1-\nu^2}\left(\frac{\partial u}{\partial x} + \nu \frac{\partial v}{\partial y}\right) \\ N_y &= \int_{-h/2}^{h/2} \sigma_{yy} dz = \frac{Eh}{1-\nu^2}\left(\nu \frac{\partial u}{\partial x} + \frac{\partial v}{\partial y}\right) \\ N_{xy} &= \int_{-h/2}^{h/2} \sigma_{xy} dz = Gh\left(\frac{\partial u}{\partial y} + \frac{\partial v}{\partial x}\right) \end{aligned} \tag{2.15}$$

And, applying Newton's second law to the infinitesimal element results in

$$\begin{aligned} \frac{\partial N_x}{\partial x} + \frac{\partial N_{xy}}{\partial y} &= \rho h \frac{\partial^2 u}{\partial t^2} \\ \frac{\partial N_y}{\partial y} + \frac{\partial N_{xy}}{\partial x} &= \rho h \frac{\partial^2 v}{\partial t^2} \end{aligned} \tag{2.16}$$

Under the conditions of a straight-crested wave, the motion is constant across a single wave front (taken here as the y direction) such that

$$\begin{aligned} u(x, y, t) &= u(x, t) \\ v(x, y, t) &= 0 \end{aligned} \tag{2.17}$$

where u is the displacement in the x-direction perpendicular to the wave front and v is the displacement in the y-direction along the wave front. Thus, equations (2.15) reduce to

$$\begin{aligned} N_x &= \frac{Eh}{1-\nu^2}\frac{\partial u}{\partial x} \\ N_y &= \frac{Eh}{1-\nu^2}\nu \frac{\partial u}{\partial x} \\ N_{xy} &= N_{yx} = 0 \end{aligned} \tag{2.18}$$

The second of equations (2.16) is satisfied, and the first of equations (2.16) becomes

$$\frac{\partial N_x}{\partial x}+\frac{\partial N_{xy}}{\partial y}=\frac{Eh}{1-\nu^2}\frac{\partial^2 u}{\partial x^2}=\rho h\frac{\partial^2 u}{\partial t^2} \tag{2.19}$$

This can be rearranged to obtain the wave equation

$$c_L\frac{\partial^2 u}{\partial x^2}=\frac{\partial^2 u}{\partial t^2} \tag{2.20}$$

where c_L is the longitudinal wave speed in a plate given by

$$c_L^2=\frac{1}{1-\nu^2}\frac{E}{\rho} \tag{2.21}$$

Thus, the analysis of a straight-crested axial wave of a plate follows the analysis of a straight-crested axial wave in a bar, only with a different wave speed c_L.

For flexural waves in a plate, the assumptions of Kirchoff-Love plate theory are followed; the plate thickness does not change; straight lines normal to the mid-plane of the plate remain straight and normal after deformation. Under these kinematic assumptions, displacements at any location z along the plate thickness are given by

$$\begin{aligned} u&=-z\frac{\partial w}{\partial x}\\ v&=-z\frac{\partial w}{\partial y}\\ w&=w \end{aligned} \tag{2.22}$$

where w is the displacement along the z-direction along the mid-surface of the plate. Applying equations (2.22) to (2.14), the relevant strains are

$$\begin{aligned} \varepsilon_{xx}&=-z\frac{\partial^2 w}{\partial x^2}\\ \varepsilon_{yy}&=-z\frac{\partial^2 w}{\partial y^2}\\ \varepsilon_{xy}&=-z\frac{\partial^2 w}{\partial x\partial y} \end{aligned} \tag{2.23}$$

Substituting (2.23) into (2.13) yields

$$\begin{aligned}\sigma_{xx} &= -z\frac{E}{1-\nu^2}\left(\frac{\partial^2 w}{\partial x^2}+\nu\frac{\partial^2 w}{\partial y^2}\right)\\ \sigma_{yy} &= -z\frac{E}{1-\nu^2}\left(\nu\frac{\partial^2 w}{\partial x^2}+\frac{\partial^2 w}{\partial y^2}\right)\\ \sigma_{xy} &= -2zG\frac{\partial^2 w}{\partial x\partial y}\end{aligned} \tag{2.24}$$

The moment resultants (moment per unit width) can be obtained by through integration across the plate thickness h:

$$\begin{aligned}M_x &= \int_{-h/2}^{h/2}\sigma_{xx}z dz = -D\left(\frac{\partial^2 w}{\partial x^2}+\nu\frac{\partial^2 w}{\partial y^2}\right)\\ M_y &= \int_{-h/2}^{h/2}\sigma_{yy}z dz = -D\left(\nu\frac{\partial^2 w}{\partial x^2}+\frac{\partial^2 w}{\partial y^2}\right)\\ M_{xy} &= \int_{-h/2}^{h/2}-\sigma_{xy}z dz = (1-\nu)D\frac{\partial^2 w}{\partial x\partial y}\end{aligned} \tag{2.25}$$

where D is the plate flexural stiffness, i.e.

$$D = \frac{Eh^3}{12(1-\nu^2)} \tag{2.26}$$

Taking an infinitesimal plate element subject to moments and vertical forces, Newton's second law can be applied to obtain

$$\begin{aligned}\frac{\partial Q_x}{\partial x}+\frac{\partial Q_y}{\partial y} &= \rho h\frac{\partial^2 w}{\partial t^2}\\ \frac{\partial M_x}{\partial x}+\frac{\partial M_{xy}}{\partial y}-Q_x &= 0\\ \frac{\partial M_y}{\partial y}+\frac{\partial M_{xy}}{\partial x}-Q_y &= 0\end{aligned} \tag{2.27}$$

where Q_x, Q_y are the transverse shear force resultants on the lateral faces of the differential element. Upon simplification (2.27) becomes

$$\frac{\partial^2 M_x}{\partial x^2} - \frac{\partial M_{xy}}{\partial x \partial y} + \frac{\partial^2 M_{xy}}{\partial x \partial y} + \frac{\partial^2 M_y}{\partial y^2} = \rho h \frac{\partial^2 w}{\partial t^2} \tag{2.28}$$

Substituting (2.25) into (2.28):

$$D\left(\frac{\partial^2 w}{\partial x^4} + 2\frac{\partial^4 w}{\partial x^2 \partial y^2} + \frac{\partial^4 w}{\partial y^4}\right) + \rho h \frac{\partial^2 w}{\partial t^2} = 0 \tag{2.29}$$

which can be further simplified using the biharmonic under z-invariant conditions

$$\nabla^4 = \frac{\partial^4}{\partial x^4} + 2\frac{\partial^2}{\partial x^2 \partial y^2} + \frac{\partial^4}{\partial y^4} \tag{2.30}$$

resulting in

$$D\nabla^4 w + \rho h \frac{\partial^2 w}{\partial t^2} = 0 \tag{2.31}$$

This is the general equation of motion for a flexural wave propagating in a plate. Note that, although Cartesian coordinates were used in the formulation, in general equation (2.31) is not limited to the use of Cartesian coordinates.

When the conditions of straight crested waves are imposed, i.e.

$$w(x, y, t) = w(x, t) \tag{2.32}$$

equation (2.31) simplifies to

$$Dw'''' + \rho h \ddot{w} = 0 \tag{2.33}$$

This is analogous to the flexural vibration of a beam, admitting the solution

$$w(x,t) = Ae^{i(\gamma_F x + \omega t)} + Be^{-i(\gamma_F x - \omega t)} + Ce^{\gamma_F x}e^{i\omega t} + De^{-\gamma_F x}e^{i\omega t} \tag{2.34}$$

where the flexural wave speed in a plate is given by

$$c_F = \left(\frac{D}{\rho h}\right)^{1/4} \tag{2.35}$$

and the flexural wavenumber in a plate is given by

$$\gamma_F = \omega / c_F \tag{2.36}$$

2.2.4 Bulk waves

In an unbounded medium, waves propagate in all directions. This can be modeled using 3D elasticity theory, where a plane wave propagating along a direction $\vec{n} = n_1\vec{e}_1 + n_2\vec{e}_2 + n_3\vec{e}_3$ can be represented by a displacement

$$\vec{u} = \vec{A} f(\vec{n} \cdot \vec{r} - ct) \tag{2.37}$$

where the amplitude vector $\vec{A}$ is given by $\vec{A} = A_1\vec{e}_1 + A_2\vec{e}_2 + A_3\vec{e}_3$. Using the 3D linear elastic equations of motion in an isotropic medium, i.e. the Navier-Lamé equations:

$$(\lambda + \mu)\vec{\nabla}(\vec{\nabla} \cdot \vec{u}) + \mu\nabla^2\vec{u} = \rho\ddot{\vec{u}} \tag{2.38}$$

Substitution of (2.37) into (2.38) and subsequent manipulation yields an eigenvalue problem

$$\left[(\lambda + 2\mu) - \rho c^2\right]\left(\mu - \rho c^2\right)^2 = 0 \tag{2.39}$$

The solution to which is three eigenvalues, two being identical

$$\begin{aligned} c_1 &= c_P = \sqrt{\frac{\lambda + 2\mu}{\rho}} \\ c_2 &= c_3 = c_S = \sqrt{\frac{\mu}{\rho}} \end{aligned} \tag{2.40}$$

The first eigenvalue has motion parallel to the direction of propagation, i.e. a pressure wave. The second and third eigenvalue have motion perpendicular to the direction of propagation, i.e. shear waves. The two shear waves are mutually orthogonal.

2.2.5 Wave Potentials

Using Helmholtz decomposition, or Helmholtz's theorem, a sufficiently smooth vector field can be expressed in terms of a scalar potential Φ and a vector potential $\vec{H}$ such that

$$\vec{u} = \vec{\nabla}\Phi + \vec{\nabla} \times \vec{H} \tag{2.41}$$

This is accompanied by the uniqueness condition

$$\vec{\nabla} \cdot \vec{H} = 0 \tag{2.42}$$

Application of Helmholtz decomposition is a useful tool in the derivation of many fundamental wave propagation methods, in particular those for guided waves. For bulk waves, equations (2.41) can be substituted into the Navier-Lamé equations (2.38) to express wave propagation in unbound media in terms of wave potentials, i.e.

$$\begin{aligned} c_P \nabla^2 \Phi &= \vec{\nabla}\ddot{\Phi} \\ c_S \nabla^2 \vec{H} &= \ddot{\vec{H}} \end{aligned} \tag{2.43}$$

In this sense, it can be considered that both the scalar and vector wave potentials follow the wave equation, propagating at the pressure speed and shear speed of the medium, respectively.

2.2.6 Rayleigh Waves

Guided waves are waves which propagate along interfaces in a structure. A guided wave which propagates along a traction free surface in a half-space is called a Rayleigh wave. Rayleigh waves travel at the Rayleigh wave speed, which is the sole real root of the solution

$$\left(\frac{c^2}{c_S^2}\right)^3 - 8\left(\frac{c^2}{c_S^2}\right)^2 + \left(24 - 16k^{-2}\right)\left(\frac{c^2}{c_S^2}\right) - 16\left(1 - k^{-2}\right) = 0 \tag{2.44}$$

where c_S is the shear wave speed and k is the ratio of wave speeds in the medium, i.e.

$$k^2 = \frac{c_P^2}{c_S^2} = \frac{2(1-\nu)}{1-2\nu} \tag{2.45}$$

A common approximation to the Rayleigh wave speed is given by

$$c_R(\nu) = c_S\left(\frac{0.87+1.12\nu}{1+\nu}\right) \tag{2.46}$$

Modeling Rayleigh waves under z-invariant conditions, the particle motion is given by

$$\begin{aligned} u_x(x,y,t) &= \hat{u}_x(y)e^{i(\xi x-\omega t)} \\ u_y(x,y,t) &= \hat{u}_y(y)e^{i(\xi x-\omega t)} \end{aligned} \tag{2.47}$$

where x is the propagation direction, and y is along the thickness of the half space. The component $e^{i(\xi x-\omega t)}$ represents the forward propagating component of the wave. The mode shapes are given by

$$\begin{aligned} \hat{u}_x(y) &= Ai\left(\xi e^{-\alpha y} - \frac{\beta^2+\xi^2}{2\xi}e^{-\beta y}\right) \\ \hat{u}_y(y) &= A\left(e^{-\alpha y} + i\frac{\beta^2+\xi^2}{2\beta}e^{-\beta y}\right) \end{aligned} \tag{2.48}$$

with the parameters

$$\begin{aligned} \alpha^2 &= \xi^2\left(1-\frac{c^2}{c_P^2}\right) \\ \beta &= \xi^2\left(1-\frac{c^2}{c_S^2}\right) \end{aligned} \tag{2.49}$$

and c is the real root of equation (2.44).

From analysis of the equation (2.48), the amplitude of the particle velocity decays exponentially away from the surface, which is why the wave is considered to be guided along the surface. This condition can also be approximated by high frequency-thickness

products in finite thickness plates. Secondly, the polarization of the particle motion is elliptical in nature; that is, the direction of displacement caused by both u_x and u_y rotates in a retrograde fashion (counterclockwise for a wave traveling to the right). An interesting characteristic of Rayleigh waves is that at the surface, the ratio between in $\hat{u}_x$ and $\hat{u}_y$ is constant for a given material (although below the surface, the ratio is frequency-dependent). This constant ratio between in-plane and out-of-plane displacements becomes important for calibration in Chapter 11.

2.2.7 Shear Horizontal Waves

Shear horizontal waves are the simplest elastic plate waves to model, as they do not couple with the pressure or shear vertical waves. SH waves are modeled with propagation along the x-axis, straight-crested with z-invariance, and the thickness along the y-axis. The plate surfaces are traction free at the plate top and bottom surfaces $y = \pm d$. The particle motion only has the u_z component, and is given by

$$u_z(x, y, t) = h(y)e^{i(\xi x - \omega t)} \tag{2.50}$$

where $h(y)$ is a standing wave across the plate thickness, and $e^{i(\xi x - \omega t)}$ represents the forward propagating component. The characteristic equation for SH waves is

$$\sin \eta d \cos \eta d = 0 \tag{2.51}$$

where $\eta = \frac{\omega^2}{c_S^2} - \xi^2$. Equation (2.51) admits solutions which are both symmetric and antisymmetric about the plate midline. The solutions are symmetric under the condition

$$\sin \eta d = 0 \tag{2.52}$$

which has eigenvalues

$$\eta^S d = 0, \pi, 2\pi, ..., (2n)\frac{\pi}{2} \ , \ n = 0,1,... \tag{2.53}$$

Each eigenvalue admits a value of η, each representing a separate mode in the general solution, which for symmetric modes becomes

$$u_z^S(x, y, t) = C_2 \cos(\eta y) e^{i(\xi x - \omega t)} \tag{2.54}$$

The solutions are antisymmetric under the condition

$$\cos \eta d = 0 \tag{2.55}$$

which has eigenvalues

$$\eta^A d = \frac{\pi}{2}, 3\frac{\pi}{2}, 5\frac{\pi}{2}, ..., (2n+1)\frac{\pi}{2} \ , \ n = 0,1,... \tag{2.56}$$

Each eigenvalue admits a value of η, each representing a separate individual propagating mode in the general solution, which for antisymmetric modes becomes

$$u_z^A(x, y, t) = C_1 \sin(\eta y) e^{i(\xi x - \omega t)} \tag{2.57}$$

It should be noted that because $\eta = \eta(\omega)$, shear horizontal modes are dispersive (except for the first symmetric shear horizontal S_0 mode, which has an eigenvalue of 0). At high frequency-thickness products, the phase velocity and group velocity of both the symmetric and antisymmetric modes asymptotically approach that of the S_0 mode.

Not all shear horizontal modes propagate in a plate at a given frequency-thickness product. For low-frequency-thickness products, some wave modes have wave speeds which become imaginary and indicate non-propagation. The lowest frequency-thickness product at which a mode propagates is called the cut-off frequency, and is given by

$$\omega_{cr} = \frac{c_S}{d}(\eta d) \tag{2.58}$$

Imaginary modes do not propagate, but exist in a non-propagating form called evanescent modes. These modes form around local discontinuities and serve to meet local boundary conditions, but do not transmit energy or information. For elastic waves, a complete solution must involve purely real modes which propagate, purely imaginary modes which do not propagate, and complex modes which propagate with decaying amplitude.

2.2.8 Lamb Waves

Lamb waves are elastic waves which propagate in finite thickness plates. Unlike axial and flexural plate waves, Lamb waves do not require a low frequency-thickness approximation; rather, they are a direct result of applying linear elastic theory to an isotropic plate with the top and bottom surfaces traction free at $y = \pm d$. This review of Lamb waves in this section assume straight crested propagation along the x-axis with z-invariance, although solutions are readily available for circular crested waves. Lamb waves are more complex in their formulation than shear horizontal waves, as they are formed by coupled pressure and shear vertical waves. Lamb wave are comprised of symmetric and antisymmetric wave modes, analogous to axial and flexural waves, respectively. Symmetric wave modes are symmetric about the plate midline (u_y is equal and opposite), and antisymmetric wave modes are antisymmetric about the plate midline (u_x is equal and opposite). For the symmetric modes, the displacements are given by

$$\begin{aligned} u_x^S &= -iC^S\left[2\xi^2\eta_S\cos\eta_s d\cos\eta_P y - \eta_S\left(\xi^2-\eta_S^2\right)\cos\eta_P d\cos\eta_S y\right]e^{i(\xi x-\omega t)} \\ u_y^S &= C^S\xi\left[2\eta_p\eta_S\cos\eta_s d\sin\eta_P y + \left(\xi^2-\eta_S^2\right)\cos\eta_P d\sin\eta_S y\right]e^{i(\xi x-\omega t)} \end{aligned} \tag{2.59}$$

where C^S is an arbitrary constant, η_P, η_S are given by

$$\eta_P{}^2 = \frac{\omega^2}{c_P^2} - \xi^2$$
$$\eta_S{}^2 = \frac{\omega^2}{c_S^2} - \xi^2 \tag{2.60}$$

The wavenumbers ξ of each symmetric mode are eigenvalues from the symmetric Rayleigh-Lamb equation

$$\frac{\tan \eta_P d}{\tan \eta_S d} = -\frac{(\xi^2 - \eta_S{}^2)^2}{4\xi^2 \eta_P \eta_S} \tag{2.61}$$

where the phase velocity of each mode is given in general by $c = \frac{\omega}{\xi}$. Similarly, the displacements for the antisymmetric modes are given by

$$u_x^A = -iC^A \eta_S \left[2\xi^2 \sin \eta_s d \sin \eta_P y - \left(\xi^2 - \eta_S^2 \right) \sin \eta_P d \sin \eta_S y \right] e^{i(\xi x - \omega t)}$$
$$u_y^A = C^A \xi \left[2\eta_p \eta_S \sin \eta_s d \cos \eta_P y + \left(\xi^2 - \eta_S^2 \right) \sin \eta_P d \cos \eta_S y \right] e^{i(\xi x - \omega t)} \tag{2.62}$$

The wavenumbers ξ_A of each antisymmetric mode are eigenvalues given by the antisymmetric Rayleigh-Lamb equation

$$\frac{\tan \eta_P d}{\tan \eta_S d} = -\frac{4\xi^2 \eta_P \eta_S}{(\xi^2 - \eta_S{}^2)^2} \tag{2.63}$$

A dispersion curve for a Lamb wave is shown in Figure 2.2. Like shear horizontal waves, Lamb waves have cutoff frequencies, frequency-thickness products below which wave modes become imaginary and do not propagate. All symmetric and antisymmetric Lamb wave modes are dispersive, each approaching the Rayleigh wave speed at high frequency-thickness products. The first symmetric mode (S_0) and first antisymmetric mode (A_0) at low frequency-thickness products can be approximated by axial and flexural waves, respectively. Just as with shear horizontal modes, a complete solution requires must

involve all complex modes. This involves the superposition of symmetric and antisymmetric real (propagating), imaginary (evanescent), and complex (propagating with decaying amplitude) modes.

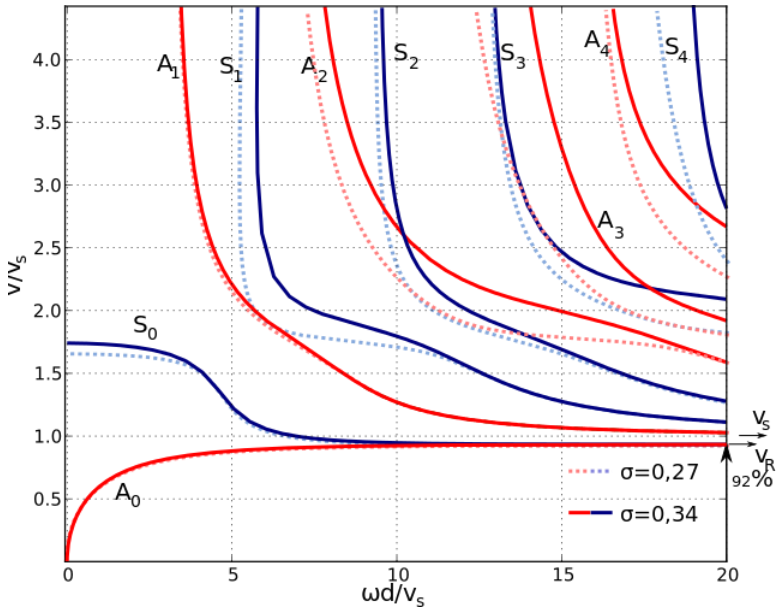

Figure 2.2: Lamb wave symmetric and antisymmetric dispersion curves ("Lamb Waves," n.d.); used under CC license https://creativecommons.org/licenses/by/3.0/

2.2.9 Longitudinal Elastic Waves in Cylindrical Rods

Contrasting with the approximate axial wave solutions for bars and beams, there is a closed form solution for elastic waves in circular rods (Graff 1975) which are better applicable to some wave propagation cases such as wave propagating along an optical fiber waveguide.

The formulation is via the Navier-Lamé equations in cylindrical coordinate r, θ, z with waves propagating in the longitudinal z axis of the rod. Boundary conditions are traction free, with $\sigma_{rr} = \sigma_{r\theta} = \sigma_{rz} = 0$ at $r = a$ for a rod with radius a. Just as in the Lamb wave formulation, there is a separate characteristic equation for multiple modes of motion; in this case the modes are longitudinal, flexural, and torsional. Relevant to the sensor

development work in this dissertation, the interest is in wave modes which produce a longitudinal motion u_z at the center of an optical fiber modeled by an elastic rod. The torsional mode has only a u_θ component and the flexural mode has a zero u_z component at the center of the rod where $r = 0$. Because of this, the torsional and flexural elastic wave formulations are omitted. A detailed analytical workup can be found in the work of Graff (1975).

The radial and longitudinal displacements for the longitudinal modes are given by

$$\begin{aligned} u_r &= B_2 \left\{ -\frac{A}{B_2} \eta_P J_1(\eta_P r) + i\xi J_1(\eta_S r) \right\} e^{i(\xi x - \omega t)} \\ u_z &= B_2 \left\{ \frac{A}{B_2} i\xi J_0(\eta_P r) - \eta_S \xi J_0(\eta_S r) \right\} e^{i(\xi x - \omega t)} \end{aligned} \tag{2.64}$$

where

$$\frac{A}{B_2} = -\left(\frac{\eta_S}{\eta_P} \right)^2 \frac{\eta_S^2 - \xi^2}{2\xi^2} \frac{J_1(\eta_S a)}{J_1(\eta_P a)} \tag{2.65}$$

and η_P, η_S are the same as for Lamb waves from equation (2.60). The characteristic equation for the longitudinal modes is given by

$$\begin{aligned} \frac{2\eta_P}{a}\left(\eta_S^2 + \xi^2\right) J_1(\eta_P a) J_1(\eta_S a) - \left(\eta_S^2 - \xi^2\right)^2 J_0(\eta_P a) J_1(\eta_S a) \\ -4\xi^2 \eta_P \eta_S J_1(\eta_P a) J_0(\eta_S a) = 0 \end{aligned} \tag{2.66}$$

which is known as the Pochhammer frequency equation for longitudinal modes, developed by Pochhammer in 1876. J_0, J_1 represent the Bessel equation of the first kind for 0^{th} and 1^{st} order, respectively. The wavenumber is given by ξ, and η_P, η_S are the same as those of the Rayleigh-Lamb equation from (2.60). Noting that J_0 is a maximum at $J_0(0)$ and

J_1 is zero at $J_1(0)$, analysis of (2.64) indicates that $u_r|_{r=0} = 0$ and only the u_z component is present at the center of the rod. In the context of an optical fiber, the $u_z|_{r=0}$ component of the longitudinal modes provide strain to the optical waveguide portion at the very center of an optical fiber, which is what is detectable by in-fiber strain sensors such as the fiber Bragg grating sensor presented in Chapter 5.

CHAPTER 3

REVIEW OF ACOUSTIC EMISSIONS

3.1 INTRODUCTION

Acoustic emissions (AE) are elastic waves which emanate from a source which has undergone irreversible material changes. Examples of such irreversible changes include crack initiation, crack growth, and plastic deformation in metals; in composites, examples include delamination, matrix cracking, debonding, fiber cracking, and fiber pullouts (Unnþórsson 2013).

Just as in the theory of fracture mechanics, the wave energy originates from the loading of the structure itself to cause an irreversible material change (e.g. crack growth). Contrasting from fracture mechanics, in the theory of AE, the process is treated as transient. In a transient context, the material change effects a rapid change in boundary conditions and stress field (i.e. a stress drop in a given volume); these changes inherently provide the source of an elastic wave. From there, the waves then radiate outwards according to the wave mechanics of the underlying media, such as Lamb waves, Rayleigh waves, bulk waves, etc. as discussed in Chapter 2. Since AE waveforms are integrally connected with the origin of a damage event, they can be judiciously post processed to obtain information such as the source location, damage type, and damage characteristics. Methods of analyzing AE waveforms are discussed further in Section 3.2.

The history of AE is closely tied with the advent of modern computational resources. The first observations of acoustic emissions were in the 1950s, attributed to Kaiser (Kaiser 1950). In the 1970s, storage and processing of waveform parameters became feasible with advancements in microprocessor technology (Hardy 2005); around the same time, the first AE sensors were being developed (see Chapter 4 for details). In the 1980s to 1990s, the use of computer-based data acquisition systems allowed for mass storage of waveforms and better processing capabilities (Drouillard 1996). To better make use of the ability to capture and store AE waveforms, there have been continual advancements in the theory of AE from the 1980s continuing through present day, discussed further in Section 3.3.

There have been extensive studies to assess AE mechanics and support AE as a damage assessment tool in various engineering materials and associated structures. In metals, AE characteristics due to fatigue cracks and plastic deformation has been studied extensively (Scruby, 2009). Crack-initiated AE events in metals tend to produce burst-type AE events with energy highly localized in the time domain on the order of tens to hundreds of microseconds. Plastic deformation in metals tends to produce continuous-type AE events with consistent amplitude over a relatively longer timeframe (Ono 2005). In carbon fiber reinforced composites, different failure mechanisms such as fiber cracking fiber pullout, matrix cracking, and delamination have been shown to produce characteristic AE frequency spectra which can be used for identification (de Groot, Wijnen, and Janssen 1995; Giordano et al. 1998). Acoustic emission has been studied extensively in concrete and reinforced concrete, with applications such as microcrack characterization (Ouyang,

Landis, and Shah 1991), correlation of AE parameters with concrete damage (Sagar and Prasad 2012).

AE has been widely proposed and used in commercial SHM and NDE applications. A few examples include aircraft monitoring (Holford et al. 2009), bridge monitoring (Nair and Cai 2010; Abdelrahman, ElBatanouny, and Ziehl 2014; ElBatanouny et al. 2014), leak detection (ASTM E1211), manufacturing process monitoring (Inasaki 1998), bucket truck testing (ASTM F914), and pressure vessel testing (ASTM E1419).

3.2 Acoustic Emissions Analysis Methods

In practice, the theory of AE is complex in nature, and it takes a strong base of theoretical knowledge of AE, fracture mechanics, and wave propagation to associate an AE waveform with its source. This is confounded by signal analysis complexities; receiving tens of thousands to hundreds of thousands of waveforms over the course of a few hours is typical when monitoring a damage process. Because of this, a natural bifurcation in analysis methods is present in the field of AE: parametric AE analysis and waveform-based AE analysis.

In parametric AE analysis, parameters are extracted from the waveform and used to correlate with damage. The waveform itself is not stored, reducing data storage and analysis complexity. Examples of parameters extracted include maximum amplitude, rise time, duration time, energy, and cyclic counts. The number of hits, i.e. the number of individual waveforms is also used as a parameter (Figure 3.1). The work of Sagar (Sagar and Prasad 2012) reviews numerous approaches to using parametric AE for identifying damage in concrete and reinforced concrete. Plots of AE hits and hit rate can be used to assess fatigue crack initiation, growth, and stage (Huang et al. 1998; Roberts and

Talebzadeh 2003). Parametric AE can also be used for preliminary sorting of AE waveforms prior further analysis, and machine learning and pattern recognition techniques have been applied to this end (Anastassopoulos and Philippidis 1995; Crivelli et al. 2014).

The advent of modern computational resources allows for storage and analysis of each of the received waveforms, permitting analysis using the waveforms themselves. These approaches are sometimes termed modal AE analysis methods, but the term waveform-based AE analysis is used herein to underscore the use of wave propagation rather than vibrational modes. In waveform-based AE analysis, wave propagation mechanics can be used to infer information about the AE event. These methods draw on the large body of work since the 1980s on AE source mechanics and propagation, described in Section 3.3. Waveform-based AE has been applied to source identification in fatigue cracks in metals through moment tensor models (Roberts and Talebzadeh 2003; Bhuiyan and Giurgiutiu 2017), separation of AE from non-AE waveforms (Hamstad and McColskey 1997), and identification of carbon fiber reinforced composite damage modes (2012, Sause).

Damage localization plays an essential role in both parametric and waveform-based AE analysis methods. It is the most common application of AE, as any SHM or NDE method that identifies damage must be able to locate it for external validation and repair. AE source localization has been performed in isotropic plates using Lamb waves (Maji, Satpathi, and Kratochvil 1997). In carbon fiber overwrapped pressure vessels, AE source localization has been performed using classical time of flight localization methods and neural network localization techniques (Kalafat and Sause 2015). A single-sensor AE source localization has also been performed in finite isotropic plates using arrival time of

various reflections (Ernstet, Zwimpfer, and Dual 2016). In general, source localization algorithms applicable in the broader field of ultrasonics and guided waves apply to AE, as the wave propagation mechanics are an integral component of the medium.

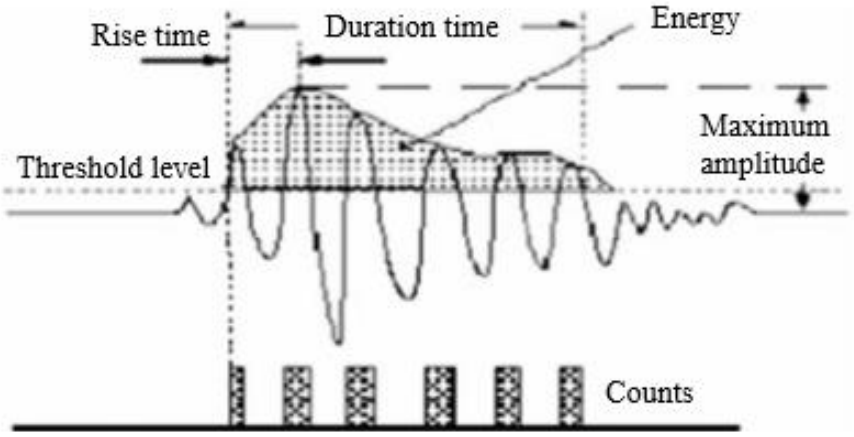

Figure 3.1: Conceptual sketch of an acoustic emission waveform and various signal parameters (Sagar and Prasad 2012)

3.3 Theory of Acoustic Emission

3.3.1 Transfer Function Approach to AE Signal Analysis

The signal recorded by an AE event depends on many factors: AE source, wave propagation, sensor response, and electrical response. The voltage sensed by the data acquisition can be obtained as a convolution of a source function $S(t)$, Green's function for the media $G(t)$, sensor function $T(t)$, and electrical transfer function $E(t)$ (J. Michaels, T. Michaels, and Sachse 1981):

$$V(t) = S(t) * G(t) * T(t) * E(t) \tag{3.1}$$

Convolution in the time-domain is equivalent to multiplication in the frequency domain, which is enabled using the FFT. In practice, deconvolution, i.e. dividing by the transfer function response at each frequency, can be used to obtain absolute measurements

of surface motion or source functions if the relevant transfer functions are known. This transfer function approach is used extensively in Chapter 11, as appropriate application of convolutions and deconvolutions are necessary to calculate a sensor calibration curve.

3.3.2 Analytical Modeling of Acoustic Emission Sources

It has been shown that the moment tensor formulation adapted from seismology can model type I, II, and III crack growth. In what has been called a moment tensor inversion scheme, the moment tensor source (and its associated damage type) is recovered by deconvolution between the sensor and structural transfer function (Rice 1980; Ohtsu 1995; Grosse and Finck 2006). Ono (Ono and Ohtsu 1984) presented a framework for modeling AE events and their wavefields based on a Green's function solution in a half space. Lysak (Lysak 1996) developed an analytical model for an AE in an unbounded medium by directly solving the Navier-Lamé equations subject to a localized step in a stress response. He was able to use this to create some simple relationships between the AE waveform bandwidth and crack length. Andreykiv (Andreykiv et al. 2001) used a model of a penny shaped crack to model AE waves associated with crack nucleation and growth, studying the relative influence that free surfaces and waveguides have on AE waves.

3.3.3 Finite Element Modeling with Fracture-Driven Acoustic Emission Source Models

Gary, Hamstad and O'Gallagher (Gary and Hamstad 1994; Hamstad, Gary, and O'Gallagher 1996) developed an FEM approach to modeling AE events propagating as Lamb and Rayleigh waves in thin and thick plates. Numerical calculations of waveforms that propagate in response to an explicitly prescribed source force function were comparable to experimental measurements. Factors such as element size, source diameter,

and source rise time factored into the veracity of the FEM. Hamstad (1999) found that a pair of force dipoles with a prescribed rise time could represent the motion of both faces of a crack and model crack growth-excited AE waveforms. Source localization and characterization can be based on an inverse approach using dipole methods; it has been shown that both rise time and dipole depth are associated with frequency spectrum and different ratios of symmetric and antisymmetric Lamb wave modes (Hamstad 2010).

Sause and Horn (2010) performed FEM of AE in composite materials. The use of a cross-shaped pseudo-crack allowed for directly imposing a crack face displacement in any of three directions. With appropriate variations in source rise time, crack depth, and direction, AE waveforms agreed with experimental AE waveforms associated with matrix cracking, fiber breakage, and matrix-fiber interface failure. Vibration of crack faces was observed as a natural phenomenon of the elastic properties and crack geometry.

3.3.4 Fracture Model Initiation of Computational AE Waveforms

Recently, the direct coupling of fracture models with AE events has been demonstrated. In this approach, rather than an explicitly defined source function, a fracture model is solved dynamically using FEM, or otherwise used to initiate a dynamic FEM where the propagation of the AE wave is modeled. Sause and Richler (2015) demonstrated that a cohesive zone crack extension model could predict AE waveforms time-frequency response and even amplitude very closely with actual AE events obtained by matrix cracking and fiber breakage. Cuadra (Cuadra et al. 2015) used a data-driven approach of using digital image correlation to construct cohesive zone and finite element fracture models in aluminum. These models were coupled directly into a dynamic solver to calculate the wavefield of the AE event. These approaches show significant promise in

extending theoretical knowledge of AE. Rather than considering AE as separate from fracture, it can be understood as a natural extension of modeling fracture as a dynamic phenomenon.

CHAPTER 4

ULTRASONIC SHM AND NDE SENSORS

4.1 INTRODUCTION

To provide a broader context for our sensor development in this work, this chapter is dedicated to the discussion of SHM and NDE sensors which rely on ultrasonic principles. Although the emphasis is on SHM, both SHM and NDE are presented as there is some merging of the enabling sensor technologies between the two fields. The development of ultrasonic sensors and AE sensors historically falls into the category of NDE. PWAS and fiber-optic sensors are typically used in SHM applications. This is not a hard and fast rule; there is a trend towards permanently embedding AE sensors for SHM applications, and some configurations of fiber-optic AE sensors are best-suited for NDE.

Both SHM and NDE sensors generally convert electromagnetic, mechanical, or thermal energy into an electrical signal which can be conveyed to data acquisition equipment for storage and further analysis. For ultrasonic sensors, factors such as wave focusing, guiding, and attenuation of the energy affect their applications. The sensors discussed in this chapter are PWAS, ultrasonic NDE transducers, AE sensors, and LDV. There are several types of fiber-optic ultrasonic sensors, most prominently the fiber Bragg grating sensor and the Fabry-Pérot interferometer. Since fiber optics are the key sensing technology used in this dissertation, they are treated separately in Chapters 5 and 6.

The list of sensors and associated damage detection methods in this chapter is not exhaustive, and many methods have been omitted such as the categories of electromagnetic and radiographic NDE. Other prominent NDE inspection approaches not discussed here include visual inspection, mechanical impedance, liquid dye penetrant, terahertz imaging, microwave imaging, and X-Ray computational tomography (Bøving 2014).

4.2 Piezoelectric Wafer Active Sensors

Piezoelectric wafer active sensors (PWAS) are broadband transducers which enable the generation and detection of ultrasonic guided waves. A representative photo of PWAS used in this research is shown in Figure 4.1. They consist of a piezoelectric disc polarized in the thickness direction and sandwiched between a pair of electrodes. PWAS are small, inexpensive, lightweight, and simple to bond, making them ideal for SHM. They have proven extremely useful as broadband strain exciters and receivers, transmitting and receiving guided waves which can propagate over large distances. PWAS material properties are well-characterized, and the wafer-type geometry is very simple in its form. This makes their analytical and FEM modeling quite tractable, contrasting with commercially available ultrasonic and AE sensors which can be black box and more difficult to accurately model.

Piezoelectric transducers couple electrical and mechanical energy through the piezoelectric effect. This effect can be related through the linear piezoelectric equations:

$$\begin{aligned} S_{ij} &= s^{E}_{ijkl} T_{kl} + d_{kij} E_k \\ D_j &= d_{jkl} T_{kl} + \varepsilon^{T}_{jk} E_k \end{aligned} \tag{4.1}$$

S_{ij} is the mechanical strain, T_{kl} is the mechanical stress, E_k is the electrical field, and D_j is the electrical displacement. The tensor s^{E}_{ijkl} is the mechanical compliance measured at

zero electric field, ε_{jk}^{T} is the dielectric permittivity measured at zero mechanical stress, and d_{kij} represents the piezoelectric coupling effect. The generation of electric charge by application of a mechanical force is termed the direct piezoelectric effect. The generation of mechanical force by application of an electric charge is termed the converse piezoelectric effect.

(a) 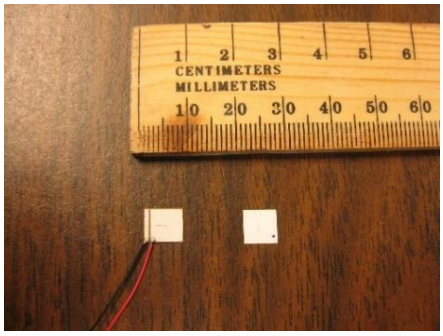

(b) 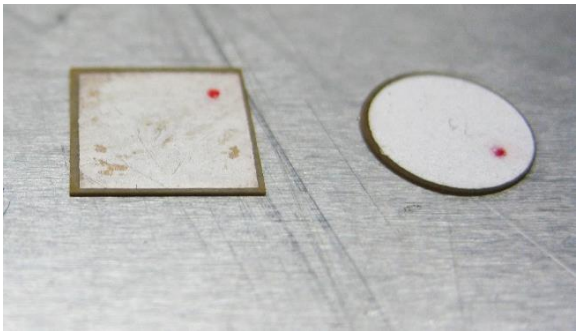

Figure 4.1: Photographs of piezoelectric wafer active sensors

There is also an active area of research into guided wave interaction with damage (Shen, 2016), and the determination of optimal PWAS distributions to best detect a given damage type (Bhuiyan, Shen, and Giurgiutiu 2017). There is still consideration regarding whether PWAS are ideal for AE applications (Yu, 2011), although that does not preclude their usefulness in research. Presently, the limitation for AE application is electrical noise, and there is a potential that further development such as a miniature Faraday shield and careful attention to its electrical response may mitigate this effect. For research involving modeling waveforms, PWAS have advantages over black box ultrasonic and AE sensors since their geometry and properties are well-known. They also sense both the in-plane and out-of-plane surface responses (Giurgiutiu 2014; Bhuiyan and Giurgiutiu 2017), whereas detection of solely the out-of-plane response is more typical with conventional AE transducers. This section provides a brief overview of PWAS. Further reading on PWAS,

their theoretical foundation, and their SHM applications can be found in the work of Giurgiutiu (Giurgiutiu 2014).

4.2.1 Electromechanical Impedance Spectroscopy

The attachment of a PWAS to a structure permits a local vibrational method for near-field interrogation, called electromechanical impedance spectroscopy (EMIS). When a PWAS is bonded to a structure, the mechanical response of the structure is directly coupled to the electromechanical response of the PWAS. Because of this, the impedance of the PWAS as measured by an impedance analyzer can be used to assess the damage state. Nearfield damage changes the local vibrational characteristics which are represented by changes in impedance and admittance peaks. Tracking these peaks allows for damage assessment.

EMIS of a free 1-D PWAS is the simplest of the closed-form analytical solutions, capturing some of the fundamental aspects of EMIS. Theoretical consideration of a 1-D PWAS under electrical excitation yields its impedance and admittance as a function of frequency, i.e.

$$Y = i\omega C\left[1-k_{31}^2\left(1-\frac{1}{\frac{1}{2}\gamma l\cdot\cot\frac{1}{2}\gamma l}\right)\right] \tag{4.2}$$

and

$$Z = \frac{1}{i\omega C}\left[1-k_{31}^2\left(1-\frac{\tan\frac{1}{2}\gamma l}{\frac{1}{2}\gamma l}\right)\right]^{-1} \tag{4.3}$$

where C is the capacitance, k_{31} is an electromechanical coupling coefficient, γ is the wavenumber, and l is the length. The impedance Z and admittance Y are related to the complex voltage V and current I such that

$$Z = \frac{V}{I} = Y^{-1} \tag{4.4}$$

An interesting feature of a PWAS resonator is that their electromechanical resonance frequencies depend only on the material properties and geometry, and not on the electrical or piezoelectric properties. The electromechanical resonance frequencies can be given by

$$f_n^{EM} = (2n-1)\frac{c}{2l} \tag{4.5}$$

The PWAS electromechanical resonances are the same as the PWAS antisymmetric mechanical resonances. This can be understood by examining the mechanical and electrical coupling. For an antisymmetric resonance, displacement is antisymmetric, but its derivative (strain) is symmetric. The electric field is uniform across a PWAS, which is also a symmetric pattern. When both the strain and electric field are symmetric, the coupling between them is a maximum and resonance occurs.

4.2.2 Tuning Phenomenon for Lamb Wave Excitation

The tuning phenomenon is one of the fundamental interaction between a PWAS and the structure to which it is bonded. Because of the finite geometry of PWAS, there are frequency-dependent variations in response amplitude. The amplitude is a maximum when the PWAS length is an odd multiple of the guided wave half-wavelength. For a PWAS ideally bonded to a plate, a Lamb wave solution for propagating strain and displacement is given by

$$\varepsilon_x(x,t) = -\frac{a\tau_0}{\mu}\sum_{\xi^S}\left(\sin\xi^S a\right)\frac{N_S(\xi^S)}{D_S'(\xi^S)}e^{i\left(\xi^S x-\omega t\right)} - \frac{a\tau_0}{\mu}\sum_{\xi^A}\left(\sin\xi^A a\right)\frac{N_A(\xi^A)}{D_A'(\xi^A)}e^{i\left(\xi^A x-\omega t\right)}$$
$$u_x(x,t) = -\frac{a^2\tau_0}{\mu}\sum_{\xi^S}\frac{\sin\xi^S a}{\xi^S a}\frac{N_S(\xi^S)}{D_S'(\xi^S)}e^{i\left(\xi^S x-\omega t\right)} - \frac{a^2\tau_0}{\mu}\sum_{\xi^A}\frac{\sin\xi^A a}{\xi^A a}\frac{N_A(\xi^A)}{D_A'(\xi^A)}e^{i\left(\xi^A x-\omega t\right)} \quad (4.6)$$

where $2a$ is the PWAS length, τ_0 is the amplitude of harmonic shear stress boundary excitation, and μ is the shear modulus, and

$$\begin{aligned} N_S &= \xi\eta_S(\xi^2+\eta_S{}^2)\cos\eta_P h\cos\eta_S h \\ N_A &= \xi\eta_S(\xi^2+\eta_S{}^2)\sin\eta_P h\sin\eta_S h \\ D_S &= (\xi^2-\eta_S{}^2)^2\cos\eta_P h\sin\eta_S h + 4\xi^2\eta_P\eta_S\sin\eta_P h\cos\eta_S h \\ D_A &= (\xi^2-\eta_S{}^2)^2\sin\eta_P h\cos\eta_S h + 4\xi^2\eta_P\eta_S\cos\eta_P h\sin\eta_S h \end{aligned} \quad (4.7)$$

Just as for Lamb waves in Chapter 2, we have

$$\begin{aligned} \eta_P &= \frac{\omega^2}{c_P^2} - \xi^2 \\ \eta_S &= \frac{\omega^2}{c_S^2} - \xi^2 \end{aligned} \quad (4.8)$$

The response of individual Lamb wave modes can be separated using equation (4.6) to obtain relations for Lamb wave mode tuning curves. Due to the dispersive phenomenon of Lamb wave modes, some modes can be "tuned out" to a low response while other modes retain a high degree of coupling with the structure (Figure 4.2). A similar sort of behavior is also seen in AE sensors. For AE sensors and ultrasonic transducers this phenomenon is termed the "aperture effect". It is common to reduce the contact area of the transducer to ensure that the operating frequency range is below the first node, i.e. the first zero value in the frequency response.

4.3 Ultrasonic Transducers

Ultrasonic transducers use one or more piezoelectric transduction elements, packaged with electrical and mechanical components which improve the generation and

detection of ultrasonic waves. Although ultrasonic transducers are not directly implemented in this work, AE sensors are a main focus, and conventional AE sensors are built from the foundational principles of ultrasonic transducers.

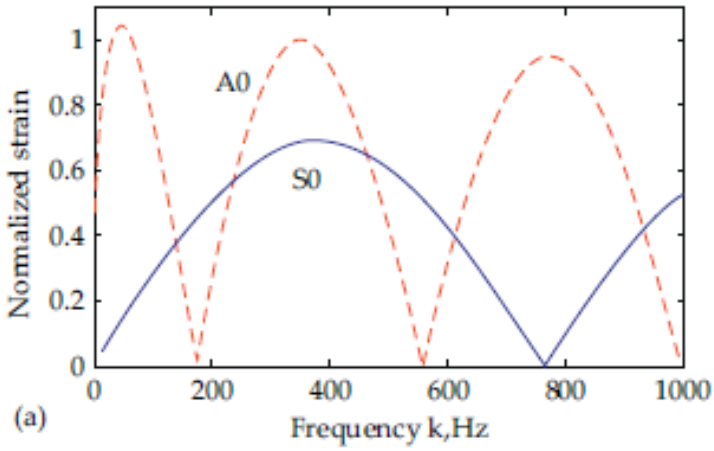

Figure 4.2: Strain variation with frequency (tuning curves) for straight created S_0 and A_0 Lamb wave modes interacting with a perfectly bonded PWAS (Giurgiutiu 2014)

Ultrasonic NDE transducers have significantly higher sensitivity and lower noise levels than PWAS; they also present the potential for bulk wave inspections. Their downside is that they are limited to NDE applications due to their size and weight. Ultrasonic transducers are commonly used in the 1 – 20 MHz frequency range, although ranges as low as 100 kHz and up into the hundreds of MHz have also been used depending on the application.

4.3.1 Acoustic Impedance Matching

The acoustic impedance of transducer materials dictates the proportion of ultrasonic wave energy which passes between the transducer and the medium. The ideal case is for 100% transmission, which is the case for a wave propagating between two materials with matched acoustic impedance. Since acoustic impedance is not typically matched between

multiple materials used in a transducer, a matching layer can be used. An ideal configuration of this matching layer can maintain 100% transmission for normal wave incidence at a given frequency. The acoustic impedance of a material is given by the product between wave speed and density, i.e.

$$Z = \rho c \tag{4.9}$$

where Z is the acoustic impedance, ρ is the mass density, and c is the wave speed in the medium. Acoustic impedance is measured in Rayl, which is $1\ \frac{kg}{m \cdot s^2}$ and commonly in the Mrayl which is 10^6 Rayl. The acoustic impedance of lead zirconate titanate (PZT) piezoelectric material is relatively high, around 30 MRayl depending on the PZT type. For reference, the acoustic impedances of aluminum 2024 T4, stainless steel 302, and naval brass are 17.6, 45.5, and 37.3, respectively.

The effect of acoustic impedance can be observed by its effect on transmission and reflection coefficients. These coefficients represent the proportion of wave energy that is transmitted or reflected when a wave encounters a boundary between two media. The transmission and reflection coefficient between two materials A and B is (Temkin, 1981)

$$T = \frac{2Z_A}{Z_A + Z_B} \quad , \quad R = \frac{Z_B - Z_A}{Z_B + Z_A} \tag{4.10}$$

From (4.10), total transmission in a two-material interaction can only be obtained when the acoustic impedances of the two materials are matched ($Z_A = Z_B$). Otherwise, losses in ultrasonic transducer efficiency are present via reflection of a portion of the wave.

To eliminate or mitigate these losses, a matching layer is used. The ideal impedance matching characteristics can be found by assessing the transmission coefficient at normal incidence for two media with a matching layer in between (Nakamura 2012):

$$T = \frac{4Z_A Z_B}{\left(Z_A + Z_B\right)^2 \cos^2\theta + \left(Z_M + Z_A Z_B / Z_M\right)^2 \sin^2\theta} \tag{4.11}$$

The terms Z_A and Z_B refer to the acoustic impedances of materials A and B where the term Z_M refers to the acoustic impedance of the matching layer. For example, this could be used for the case of a wave propagating through a piezoelectric layer, matching layer, and host structure.

The parameter θ is given by

$$\theta = \frac{2\pi L}{\lambda_M} \tag{4.12}$$

where L is the thickness of the matching layer and λ_L is the wavelength in the matching layer. As pointed out by Nakamura (Nakamura 2012), in the case of $L = \lambda_L / 4$, equation (4.11) becomes

$$T = \frac{4Z_A Z_B}{\left(Z_M + Z_A Z_B / Z_M\right)^2} \tag{4.13}$$

To get a perfect transmission of $T = 1$, the matching layer must have acoustic impedance

$$Z_M = \sqrt{Z_A Z_B} \tag{4.14}$$

This is a commonly used equation which represents the acoustic impedance of the ideal matching layer, demonstrating that it can provide perfect transmission of wave energy under these assumptions. This effect is bidirectional, improving both transmission and reception in the context of an ultrasonic transducer.

In practice, perfect transmission is not achieved in all cases due to two limitations. First, when the wave does not interact with the interface at normal incidence, the path length in the matching layer is larger than the matching layer thickness L, such that an

ideal matching layer is only prescribed for one incident angle. Second, the wavelength λ_L is a function of frequency, which means that the condition $L = \lambda_L / 4$ is only met at a single frequency. The transmission coefficient will decrease when moving away from this frequency. Even though perfect transmission is only obtained for an optimal case, overall performance can still be improved when using a matching layer at sub-optimal frequencies and incident angles. In practice, the implementation of a matching layer can be incredibly difficult. For example, in the literature on AE sensor development, entire sensor components such as the wear plate have been removed since the implementation of a matching layer was insufficient to provide a repeatable, high fidelity response.

4.3.2 Ultrasonic Transducer Components

Figure 4.3 (Nakamura 2012) shows a conceptual sketch of an ultrasonic transducer. It is comprised of the following series of primary components which directly influence the received waveform: wear plate, piezoelectric material, damping material, and matching layers. It is also comprised of ancillary components for protection and conveyance of the electrical output: casing, wiring and electrical connectors.

The piezoelectric element is the key component of an ultrasonic transducer. Piezoceramics such as PZT and barium titanate are commonly employed, whereas polymer materials such as poly(vinylidene fluoride) (PVDF) are softer and sometimes used in specific applications where sensing alone is sufficient. The mechanics of the energy transduction through the piezoelectric element is governed by the same linear piezoelectric equations as previously described for PWAS, equations (4.1).

Impedance matching layers are used to improve wave transmission for excitation and sensing as shown in section 4.4.1. Sometimes more than one matching layer is used to

fine-tune the transducer response, e.g. improving performance across the frequency spectrum.

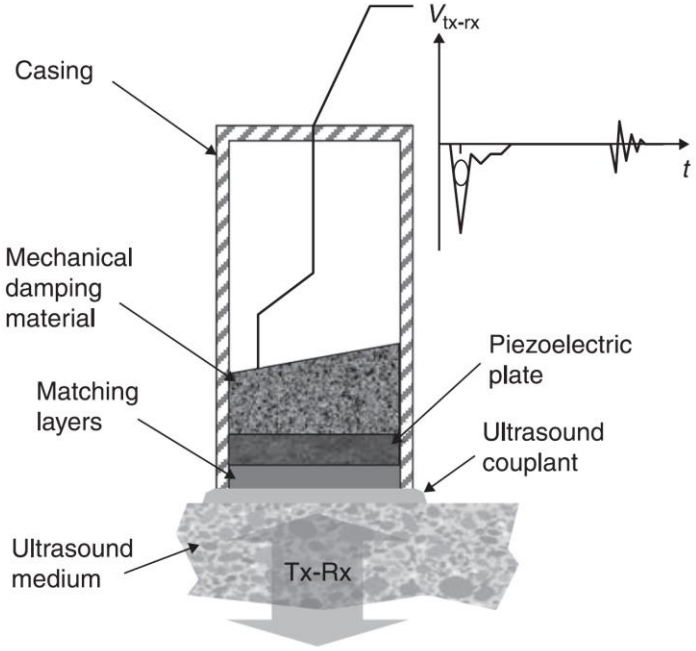

Figure 4.3 Concpetual sketch highlighting components of an ultrasonic transducer (Nakamura 2012)

The wear plate is the bottom surface of the transducer which is coupled to the external media. The wear plate plays roles in impedance matching and protecting of the piezoelectric element. If damage is suffered by the active sensing element, particularly if it fractures a brittle piezoceramic, it could severely diminish sensor performance or render the sensor inoperable. The wear plate prolongs the life of the transducer, allowing for a degree of normal wear such as continual re-bonding of the sensors if they are handled with care.

The sensor casing serves to mechanically protect sensor components. Together, the metal casing and wear plate also act as a Faraday shield, electrically isolating the active elements of the transducer to reduce electrical noise. To take the electrical isolation a step

further, a preamplifier can be built within the metal case of the transducer itself. This amplifies small currents provided by the piezoelectric element before they are exposed to electromagnetic interference, reducing the impact of external noise. This is performed when high sensitivity and low noise is necessary at the cost of increased transducer size.

The damping material (sometimes called the backing material) comprises a large portion of the ultrasonic transducer's mass. The damping of the sensor reduces resonance effects, shortening the time-duration of the signal by reducing the number of cyclic counts until the signal returns to zero at a given frequency. This is beneficial, as it helps the transducer transmit shorter time-duration bursts which more accurately represent the time-domain waveform of received signals. The downside of overly increasing damping is that any energy that is damped out is not converted into electrical energy by the piezoelectric transducer. Note that in the conceptual sketch of Figure 4.3, the damping layer is angled. This is to reduce the effect of back-reflections.

4.4 Acoustic Emission Sensors

An AE sensor is a type of ultrasonic sensor custom-designed to detect damage-associated AE waveforms. Its functional components are the same as an ultrasonic transducer. There have been many refinements and alternative approaches to AE sensor designs over the past four decades as discussed in Section 4.4.4. However, most commercially available AE sensors can be conceptually represented similarly to an ultrasonic transducer just as in Figure 4.3.

AE sensors operate on the lower end of the frequency range compared to ultrasonic transducers; nominally AE sensors detect signals between 50 – 1000 kHz. Some AE measurements consider a larger nominal frequency range, often up to 2000 kHz. When the

frequency range is increased, calibration tends to be less accurate due to mechanical effects on the low end of the range and due to electrical effects on the high end of the range.

Typically, an AE sensor is configured to work as a part of an AE data acquisition system which contains additional hardware and software suited to preliminary signal analysis. Two of the most prominent suppliers of such hardware and software are Vallen Systeme and MISTRAS. On the hardware side, a preamplifier is required to increase voltages to detectable levels; analogous to ultrasonic transducers, the use of an internal preamplifier provides a higher fidelity signal at the cost of increased sensor size. On the software side, parametric AE methods are used to preprocess, store, and sort, AE waveforms. Such a software system is used to reduce the quantity of data captured, as AE commonly produce tens of thousands to hundreds of thousands of waveforms during an experiment. Thus, efficient algorithms to precondition, sort, and store AE data is critical to effective implementation.

AE sensors tend not to be optimized for excitation the way ultrasonic transducers are (Blodgett et al. 2009; Nakamura 2012). However, most still exhibit the potential for excitation since there is a piezoelectric element (in some cases, an internal preamplifier without bypass circuitry precludes use of an AE sensor for wave excitation). In most cases, AE sensor excitation is used to assess bond quality and for self-diagnostics.

4.4.1 Broadband and Resonant AE Sensors

In the design of piezoelectric AE sensors, one must also consider the electromechanical resonance of the sensor system due to the piezoelectric element response coupled with the mechanical components of the sensor system. To provide sufficient levels of sensitivity (voltage output per unit input), it is typical to localize a large number of

resonance modes within a desired frequency range. If high sensitivity is desired from the AE sensor, the damping is kept low. This is called a **resonant AE sensor**. In a resonant AE sensor configuration, clear peaks and valleys are present in the frequency response, and a longer time-domain response is observed. The benefit is that the high sensitivity can be used to detect smaller signals, and fewer sensors are required for sensor arrays.

For many applications, the sensitivity of resonant AE sensors is already more than sufficient, with thresholds of detection on the order of hundreds of femtometers (Scala, 1983; Scruby, 1985). Thus, unless significantly improved sensitivity levels are required, the damping is increased through the addition of damping material. The result is termed a **broadband AE sensor**. The threshold of detection reduces by approximately an order of magnitude to the order of picometers (Ranganayakulu et al. 2016). Multiple resonance peaks flatten and merge, thus providing a frequency response without as many peaks and valleys, and sometimes even a flat response.

In the time-domain, a waveform detected by broadband AE sensors tends to decay more rapidly than a resonant AE sensor. This is an important feature for AE testing since multiple AE events can occur nearly simultaneously. In this case, a reduced decay time allows for better time-domain resolution between multiple AE waveforms, decreasing the chance that multiple waveforms will be overlapped and sensed as a single event.

In Chapters 7-10, fiber-optic AE sensors are designed as resonant AE sensors. This is because for fiber-optics sensors, as later discussed in Chapter 6, sensitivity is low relative to noise levels for ultrasonic sensing applications. For piezoelectric AE sensors, unless the increased sensitivity is required, broadband AE sensors are generally preferred due to their reduced signal decay time and flatter frequency response.

The use of a sensor with a flat frequency response is beneficial; without it, a deconvolution in the frequency domain is necessary to obtain the frequency response of the underlying wave motion. In practice, this requires increased skill of the operator. Additionally, the need to use the calibration curve of an AE sensor for deconvolution may be a problem. There are very well-characterized methods and standards for AE sensor calibration, as discussed in Chapter 11. However, there are systematic errors in current calibration practices of many commercial AE manufacturers. These include misrepresentation of proper use of the correct calibration standards and representation of calibration curves in terms of surface stress, which is not physically admissible due to traction free conditions (Ono 2016). From one perspective, if calibration standards were better controlled for commercially available AE sensors, the only practical drawback of using resonant sensors would be the increased data processing requirements and antiresonances in their frequency spectrum. However, since at present calibration standards are not precisely applied, the use of a poorly calibrated resonant AE sensor can distort waveforms and preclude accurate quantitative analysis.

4.4.2 Early AE Sensor Development and Development of the NIST Reference Sensor

In 1975, Breckenridge (Breckenridge, Tschiegg, and Greenspan 1975) used a piezoelectric transducer to sense AE, calibrating the transducer and identifying that the subsequent AE events propagate as Lamb waves in a plate structure. Shortly following, Scruby and Wadley (1978) and Breckenridge (Breckenridge and Greenspan 1981) provided a solid foundation for AE sensor calibration by developing capacitive AE sensors. These detected how the out-of-plane component of an AE-generated wave changed the length of an air gap. Since the voltage-air gap calibration curve could be independently

measured, these provided a strong theoretical and empirical foundation for calibration of future AE sensors.

Proctor (Proctor 1982) developed an AE sensor with a conical element; shown in Figure 4.4, this became a reference standard AE sensor known as the NBS conical transducer (it later became known as the NIST conical transducer when the NBS changed its name into NIST). The wear plate and casing were removed to improve the consistency of the sensor frequency response; in AE sensor designs of that time, the use of a case and a thick wear plate provided high variations in response associated with impedance mismatches and geometric tolerances. A conical piezoelectric element was made to directly contact the test surface, with a 1.5 mm diameter providing approximately a point response. This sensor was calibrated against a capacitive AE sensor (Breckenridge and Greenspan 1981), yielding higher average sensitivity than resonant AE sensors commercially available at the time while providing the flat frequency response of a broadband sensor.

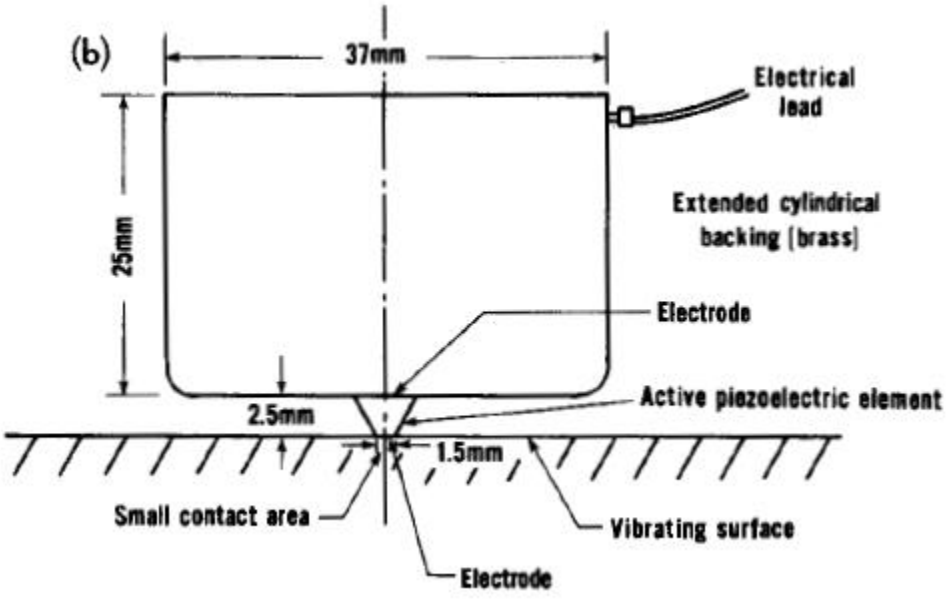

Figure 4.4 NBS conical AE sensor (Proctor 1982)

Proctor (Proctor 1986) developed several improvements to the NIST conical transducer. The size was reduced, silver electrodes were replaced with nickel for better wear characteristics, and iridium solder provided more consistent bonding characteristics while being below the PZT curie temperature. Greenspan (Greenspan 1987) performed analytical modeling of the NIST transducer, helping to build a case for its use as a standard reference transducer. The NIST conical transducer eventually became widely used as a standard reference transducer for calibration of other sensors. More recently, Sause (2012) have performed finite element modeling of the NIST conical transducer in response to Lamb wave propagation. This study was quite powerful, as experimental verification has indicated the potential to determine the absolute transfer function via FEM for varies sensor configurations in arbitrary propagation media and geometries.

Scruby (1985) developed a modified conical point-contact transducer, most significantly adding a casing to the design which allowed for its successful testing, including fatigue-generated AE source localization experiments. Koberna (Koberna 1993) optimized and extended the NIST conical transducer design, adding both a brass casing and a 20 μm thick wear plate to protect the piezoelectric element without diminishing its response.

4.4.3 Electrical, Material, and Mechanical Advancements in Piezoelectric AE Sensing

Since the substantial development of the standard NIST conical transducer, there have been significant advancements in AE sensor materials, electrical components, and mechanical sensor design. Hamstad (Hamstad and Fortunko 1995) incorporated a field effect transistor an AE sensor casing. This reduced noise from electromagnetic interference by providing a degree of preamplification prior to the low signal voltage exiting the

Faraday shield created by the sensor casing. This was an early predecessor of current commercially available AE sensor designs which include the use of a fully miniaturized preamplifier within the sensor casing. Yan (2004) developed an approach for self-calibrating a conical sensor which is used to actively transmit a waveform. By incorporating a second PZT sensor bonded to the far side of the backing material, the response of this sensor provided a measure of the signal strength that was transmitted into the medium, with applications in sensor calibration.

There has been an interest in developing sensors which detect the in-plane component of AE waveforms. In some cases, the in-plane component of the waveform provides a higher signal strength, or senses wave modes which are better suited for damage identification. Complementing the NIST conical transducer, an in-plane transducer was developed with a 0.5 mm contact size pyramidal PZT element with brass-tin backing (Proctor 1988). Yalcinkaya and Ozevin (2013) developed an in-plane transducer based on a cut cylindrical sensor with PZT poling along the in-plane direction. The in-plane sensor was found to be more sensitive to the less dispersive L(0,2) mode in a cylinder, making it better suited for pipeline leak detection than a conventional PZT AE sensor.

On the materials side, Or (Or, Chan, and Choy 2000) fabricated AE sensors with polyvinylidene fluoride / trifluoroethylene (P(VDF-TrFE) copolymer films. Compared to a similar AE sensor with a PZT-7A piezoceramic sensing element, the compliant copolymer films exhibited fewer resonance peaks with only an approximate 6 dB drop in peak sensitivity. Marin-Franch (Marin-Franch et al. 2002) showed that piezoceramic/polymer composites made of calcium modified lead titanate (PTCa) ceramic and polyetherketoneketone (PEKK) could combine the benefit of high piezoelectric

coefficients of piezoceramics with the mechanical sensing benefits of the more flexible polymers.

4.5 Non-Contact Ultrasonics via Laser Doppler Vibrometry

An LDV is a non-contact ultrasonic sensor which measures ultrasonic velocity or displacement using the Doppler effect. A surface is excited by a coherent light source and a portion of this light is reflected to a detector. Using an interferometer (see Chapter 5 for further detail), frequency shifts can be measured related back to surface velocity using the Doppler effect given by

$$f = \frac{2v}{\lambda} \tag{4.15}$$

where f is the frequency, v is the objects velocity along the direction of the light source, and λ is the wavelength of the electromagnetic wave. With proper configuration, detection thresholds LDV are on the order of 10 nm/s/$\sqrt{\text{Hz}}$ and displacements in the sub-picometer /$\sqrt{\text{Hz}}$ (Tabatabai, 2013). Due to the high costs of LDV systems, it is best used as an NDE tool in application, or as a research tool when noncontact measurement of ultrasonic waves is indicated. Some modern LDV systems support not only a single-point measurement, but allow for scanning and 3-axis sensing.

CHAPTER 5

PRINCIPLES OF ULTRASONIC FIBER-OPTIC SENSING

5.1 FIBER-OPTIC SENSORS: TRENDS, ADVANTAGES, AND ROOM FOR GROWTH

The fundamental principle behind fiber-optic sensors is that external conditions can be tracked by measuring their influence on light propagating through an optical fiber. These conditions can be environmental, such as temperature or humidity, or mechanical, such as pressure or dynamic strain (Peters 2009b).

In the 1980s and early 1990s, fiber-optic sensing was done primarily in a research environment due to the expensive and relative immaturity of the technology. Since then, fiber-optic sensors have piggybacked onto the growth of fiber-optic telecommunication and optoelectronics industries. This has driven reduction in costs, enabling broad scientific exploration and continuous product development. Fiber optics have now grown to the point that it dominates various commercial sensor markets; current trends indicate a great deal of continued growth (Udd, 1995).

This growth is driven in a large sense by the many advantages fiber-optic sensors have over conventional electrical sensors. Fiber-optic sensors present no ignition hazard and are immune to electromagnetic interference. They are extremely lightweight with an exceptional form factor, which provides advantages in industries where weight and size is at a premium, such as in aerospace applications. Their shape, small size, and properties make them ideal candidates for embedment into composite materials. Optical fibers are

easily made corrosion resistant for naval applications. For sensing, fiber optics also have the same advantages as in fiber-optic telecommunication. Remote interrogation can be performed with one inlet and outlet port. Dozens of sensors can be multiplexed with a single interrogation system. Signal attenuation is extremely low, at approximately 0.25 dB/km in the 1550 nm transmission window, allowing interrogation of sensors tens of kilometers away (Udd, 1995; Peters 2009b).

Despite the many advantages of fiber optics, they still are not broadly used in SHM or NDE. There are two primary reasons for this:

First, the technology is not mature. Although there are many methods for high speed acousto-ultrasonic fiber-optic sensing, none have yet been produced in commercial-off-the-shelf systems (Lin and Giurgiutiu 2014a). This means that implementation of an embedded fiber system is prohibitive unless one is willing to suffer the cost, expertise, and risk of custom system development and implementation.

Second, fiber-optic sensors have lower signal to noise ratios (SNRs) than their piezoelectric counterparts, particularly for ultrasonic applications. This limits their potential to detect damage-related signals before the damage becomes substantial. Much of the current research in fiber-optic sensing is focused on developing high sensitivity, low noise systems as this provides a ceiling on their practical applicability.

This chapter describes the background and principles of fiber-optic sensors necessary to provide a reader with a background on the topic of fiber-optic ultrasonic strain sensing. This includes the enabling aspects of fiber-optic sensors, fiber Bragg grating sensors (FBG), Fabry-Pérot interferometers (FPI), and strain resolutions for sensing

systems. The application of these methods for guided wave sensing will be discussed in Chapter 6.

5.2 Overview of Optical Fibers Sensing Applications

5.2.1 Optical Fiber Configuration and Light Wave Propagation

Optical fibers consist of three components: core, cladding, and coating (Figure 5.1). The purpose of the core and cladding is to guide the wave along the fiber. A relative small (< 1%) difference in refractive index between the core and the cladding guide one or more linearly polarized light modes along the fiber. The purpose of the coating is to increase mechanical durability, protect from moisture, and assist in strain transfer. The term "single mode fibers" refers to fibers which permit the propagation of only one light wave mode. These are preferred for long distance communication due to lower attenuation (Peters 2009b).

5.2.2 Other Configurations of Optical Fibers

Polymeric optical fibers (POFs) provide alternative mechanical properties compared conventional optical fibers. They were first used with FBG sensor by Xiong, Peng, Wu, and Chu (1999). POFs have the advantages of a high elastic strain limit, high bending flexibility, and low Young's modulus. POFs are primarily available as multimode fibers, although single mode POFs have been developed. In particular, POFs have been designed with the purpose of embedment into host structures. They are also particularly useful for monitoring compliant structures, where the stiffness of a conventional optical fiber would diminish the mechanical response (Peters 2010).

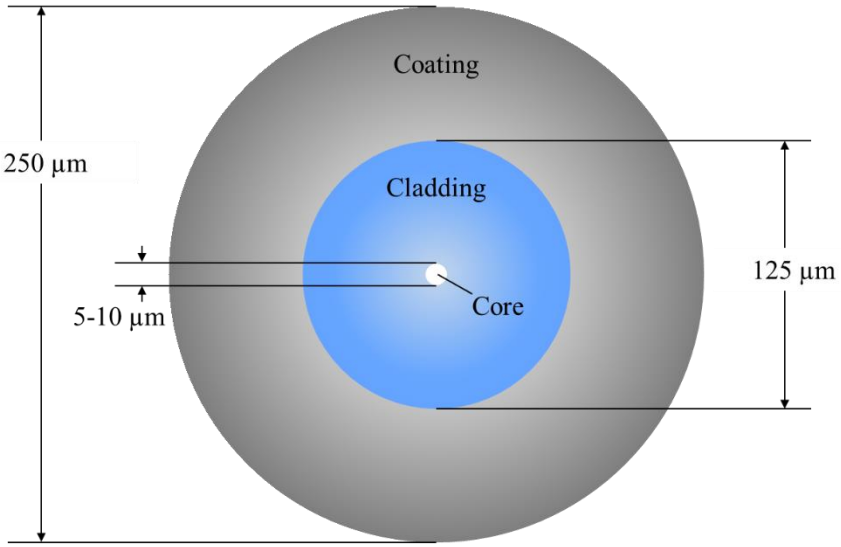

Figure 5.1: Dimensions and composition of a single mode optical fiber

Reduced diameter optical fibers have also been developed, with applications in embedment into a host structure (Takedaet, 2002; Takeda, 2005). By reducing the diameter of the fiber, adverse effects of embedding an optical fiber into a host structure can be minimized. Typically, reduced diameter optical fibers and POFs are investigated for embedment in composite structures. They reduce the detrimental effect of embedment, counterbalancing against the positive benefits of *in situ* sensing.

5.2.3 Mechanical Properties of Optical Fibers

For dynamic strain sensing applications, it is often sufficient to assume that an optical fiber is more compliant than a host structure, where the mechanics of the optical fiber do not overly affect the response. In cases where the optical fiber is stiffer than the host structure, or otherwise diminishes structural strength such as during embedment, the mechanics of the fiber must be considered.

For wave propagation purposes, the mechanical properties of the coating can be ignored; fused silica fibers can then be treated as linear elastic, isotropic, and homogeneous

with elastic modulus $E = 66$ GPa, Poisson's ratio $\nu = 0.15$, mass density $\rho = 2170$ kg/m^3 (Wee, 2017).

5.3 Fiber Bragg Grating Sensors

Fiber Bragg grating (FBG) sensors are passive strain and temperature sensors originally developed in 1978 (Hill et al. 1978). They are of great interest because they are incorporated directly into an optical fiber and thus retain the multitude of advantages of fiber-optic sensing. FBG sensors are capable of high-sensitivity, high-bandwidth sensing of strain and temperature. They are most desirable for their strain sensing capabilities, and are a potential alternative to conventional piezoelectric sensors for ultrasonic sensing.

5.3.1 Principle of FBG Sensing

An FBG, shown in Figure 5.2, is a region within the core an optical fiber where a periodic variation in refractive index has been created via alternating bands ("gratings"). These gratings are most often created by transverse writing, developed in 1989 (Meltz, Morey, and Glenn 1989), where ultraviolet light is transmitted through a phase mask to illuminate the fiber core through the side of the cladding.

These periodic refractive index variations cause that region of an optical fiber to serve as a wavelength-dependent notch filter, reflecting light within a small wavelength band. The point of maximum reflectivity, i.e. the Bragg wavelength λ_B, is calculated by (Peters 2009a)

$$\lambda_B = 2\eta_{eff}\Lambda \tag{5.1}$$

where Λ is the grating period and η_{eff} is the effective refractive index, which falls between the refractive indices of the high-index and low-index gratings $\eta_1 < \eta_{eff} < \eta_2$.

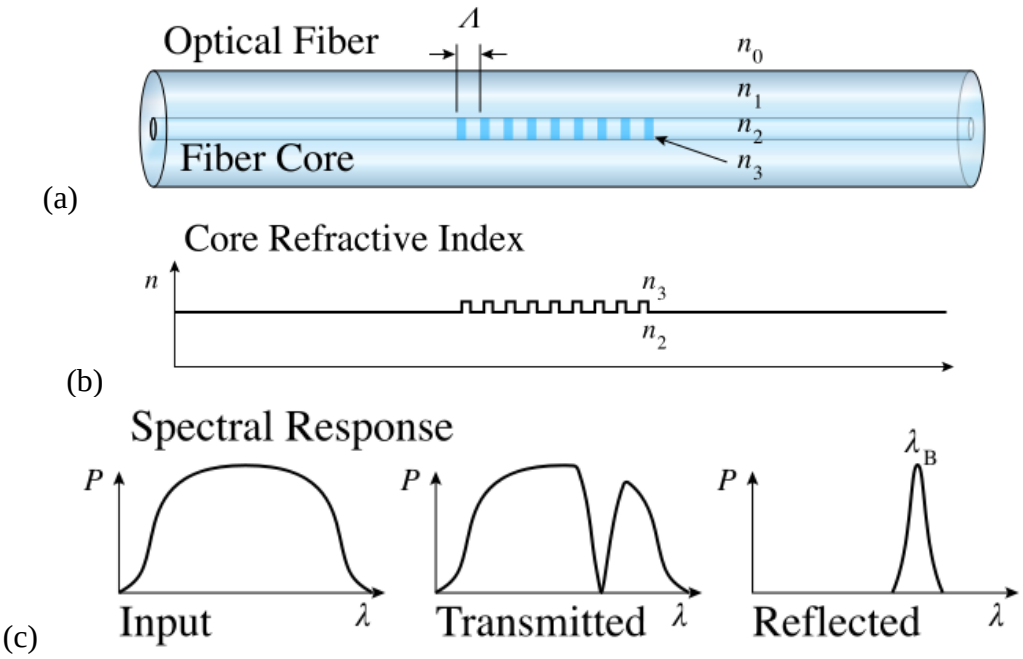

Figure 5.2 (a) Illustration of an FBG within an optical fiber, (b) variation in refractive index within fiber core, (c) spectral response of an FBG ("Fiber Bragg Grating," n.d.); used under CC license https://creativecommons.org/licenses/by/3.0/

As a strain ε_{axial} along the axial direction of the fiber is applied, the grating period Λ is changed, and the Bragg wavelength λ_B is shifted. A variety of FBG configurations are available, such as chirped or apodized FBGs which invalidate the assumption of a constant grating period. In these approaches, the reflectivity-wavelength spectrum of an FBG can be calculated through the transfer matrix method. The principle of equation (5.1) still holds.

Note that the FBG is insensitive to its transverse strain component $\varepsilon_{transverse}$, such that FBG sensing of off-axis signals only depends upon the projection of the strain component in the axial direction.

The relationship between axial strain and Bragg wavelength shift is given by (Peters 2009a; Norman and Davis 2011)

$$\frac{\Delta\lambda_B}{\lambda_B} = (1-\rho_{eff})\varepsilon_{axial} \tag{5.2}$$

where ρ_{eff} is the effective photoelastic constant for axial strain, with a typical value of 0.22 for silica optical fibers.

The relationship between temperature shift ΔT and Bragg wavelength shift is given by (Peters 2009a)

$$\frac{\Delta\lambda_B}{\lambda_B} = (\alpha+\zeta)\Delta\mathrm{T} \tag{5.3}$$

where α is the coefficient of thermal expansion and ζ is the thermal-optical coefficient. A typical value of $\alpha+\zeta$ for silica optical fibers is $0.66\times10^{-6}/°C$ (Peters 2009a). For discriminating between strain and environmental temperature, one method is to use two FBGs, one of which is subjected to the environmental temperature only for calibration. For guided wave sensing applications, temperature changes can be ignored by intermittently measuring the Bragg wavelength, effectively calibrating a single FBG.

5.3.2 Intensity Demodulation Approach for FBG Interrogation

To measure strain, direct tracking of the FBG spectrum or the Bragg wavelength λ_B is not necessarily. Through an FBG intensity demodulation approach (Figure 5.3), a narrow linewidth tunable laser source can be used to relate spectrum shifts directly to intensity shifts through the following steps (Lissak, Arie, and Tur 1998; Betz et al. 2003; Norman and Davis 2011):

1. Sweeping across the wavelength spectrum of an FBG
2. Fixing the laser on a linear portion of an FBG spectrum, most commonly the half-maximum point

3. Measuring change in power using a photodetector

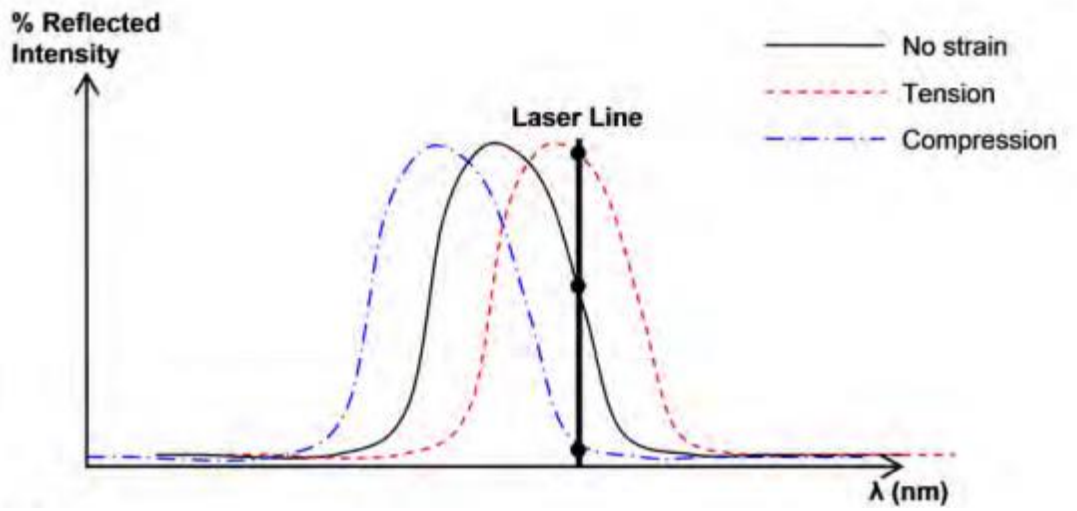

Figure 5.3: Intensity demodulation approach for FBG dynamic strain sensing (Norman and Davis 2011)

When the strain is approximately constant across the length of an FBG, spectrum shifts rigidly. That is, the peak wavelength shift $\Delta\lambda_B$ is equal to any wavelength shift $\Delta\lambda$. In the linear portion of the reflectivity spectrum, the wavelength shift is related to the power of the reflected light P through the slope m at the lasing wavelength

$$\varepsilon_{axial} \propto \Delta\lambda_B = \Delta\lambda = \Delta P / m \tag{5.4}$$

In this manner, reflected power can be measured through a photodetector and directly related to axial strain of the FBG. As the slope m increases, smaller strains can be detected. The downside of this method is that it requires the use of a tunable laser source, adding additional expense. Additionally, the dynamic strain range is limited to the linear portion of the FBG. The upside of this method is that it is highly sensitive and robust. This is the method used for the FBG experimental work in later chapters of this dissertation.

5.3.3 Pi phase-shifted Fiber Bragg Grating Sensors

Agrawal (Agrawal and Radic 1994) showed that phase pi shifts introduced into an FBG (pi-FBGs) can be used to create narrowband transmission windows in the wavelength spectrum. A sample reflection spectrum of a pi-FBG is shown in Figure 5.4. These transmission and reflection windows have an extremely high slope which is useful for sensing applications. Cranch (2008) used pi-FBGs as the reflector for a DFB laser high bandwidth high sensitivity strain sensing system. Rosenthal (Rosenthal, Razansky, and Ntziachristos 2011) developed a fiber-optic hydrophone based on a pi-FBG. Wu and Okabe (2012) used a pi-FBG with a balanced photodetector which rejected the DC component and rejected the noise from the tunable laser source.

The high slope of pi-FBGs has the potential to offer extremely sensitive strain readings. This is apparent when used with an intensity demodulation method. In the work of Wu (2012) the slope, and thus the pi-FBG sensitivity, was 180 times higher than its conventional FBG counterpart with a gentler slope. The downsides of pi-FBGs are that they have a very narrow wavelength range, making it easy to exceed their dynamic range. Thus, some sort of wavelength calibration method, or else a mechanical isolation from quasi-static strain is required for practical use. Additionally, if the noise comes from laser intensity or frequency noise, which is a significant component of the noise of an optical system (Norman and Davis 2011), then the noise is amplified along with the signal sensitivity, leading to no practical improvement in signal-to-noise ratio.

5.4 Fabry-Pérot Interferometers

Besides the FBG, Fabry-Pérot Interferometer (FPI) sensors have received a great deal of attention for high frequency acousto-ultrasonic sensing. FPIs are made of two

opposite facing reflective surfaces, at least one of which is partially reflective. Laser light shined through one of these surfaces, enters the gap between them, and creates an interference pattern through multiple reflections in the optical resonance cavity. The reflection and transmission coefficients depend on the wavelength of the light and the length of the gap between the two reflective surfaces. As the gap length changes, this can be sensed through changes in the reflected intensity. Contrasting the FPI sensor with the FBG sensor, an FPI detects displacement whereas an FBG detects strain.

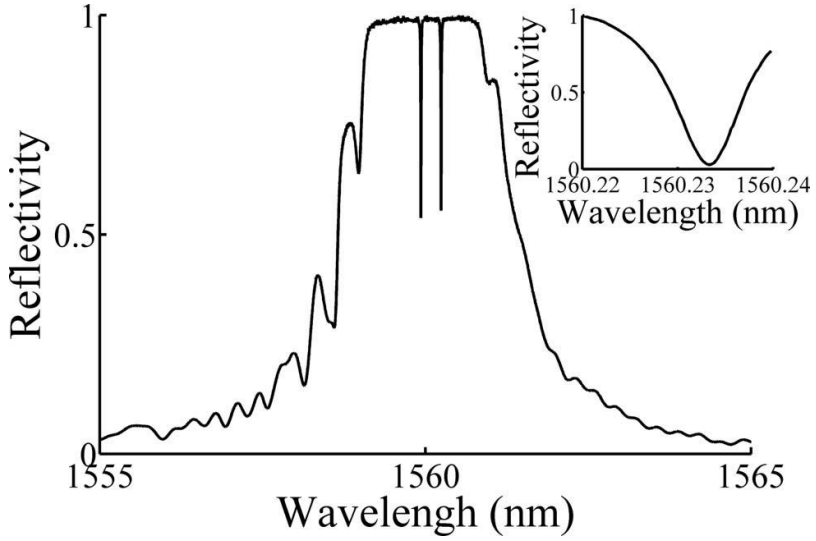

Figure 5.4: Spectrum of a pi-phase shifted FBG (Rosenthal, Razansky, and Ntziachristos 2011)

A common fiber optic implementation of an FPI sensor is called an extrinsic Fabry-Pérot interferometer (EFPI), shown in Figure 5.5. In this configuration, one fiber serves as both transmitter and receiver of the laser light. A second fiber acts as a reflector only. The gap between the two fibers is precisely positioned, for example using a piezo motor fiber positioner.

Several methods of aligning the fibers have been proposed. Empty fiber-optic jackets, glass capillaries, steel tubes, etc. have been used to hold both fibers in place for

alignment. Two single mode fibers can be aligned, although this requires high-precision alignment. More often, a multimode fiber is used as the reflector since it has a larger fiber core and offers more tolerance in the alignment. However, in principle, any reflector could be used. It is important that the two sides are not mechanically coupled, e.g. by bonding both to the alignment housing. Typically, one side is bonded to the alignment housing, whereas the other side is bonded to a separate fixture to keep it held in place. This allows for relative displacement between the two fibers which can be detected through interferometric methods.

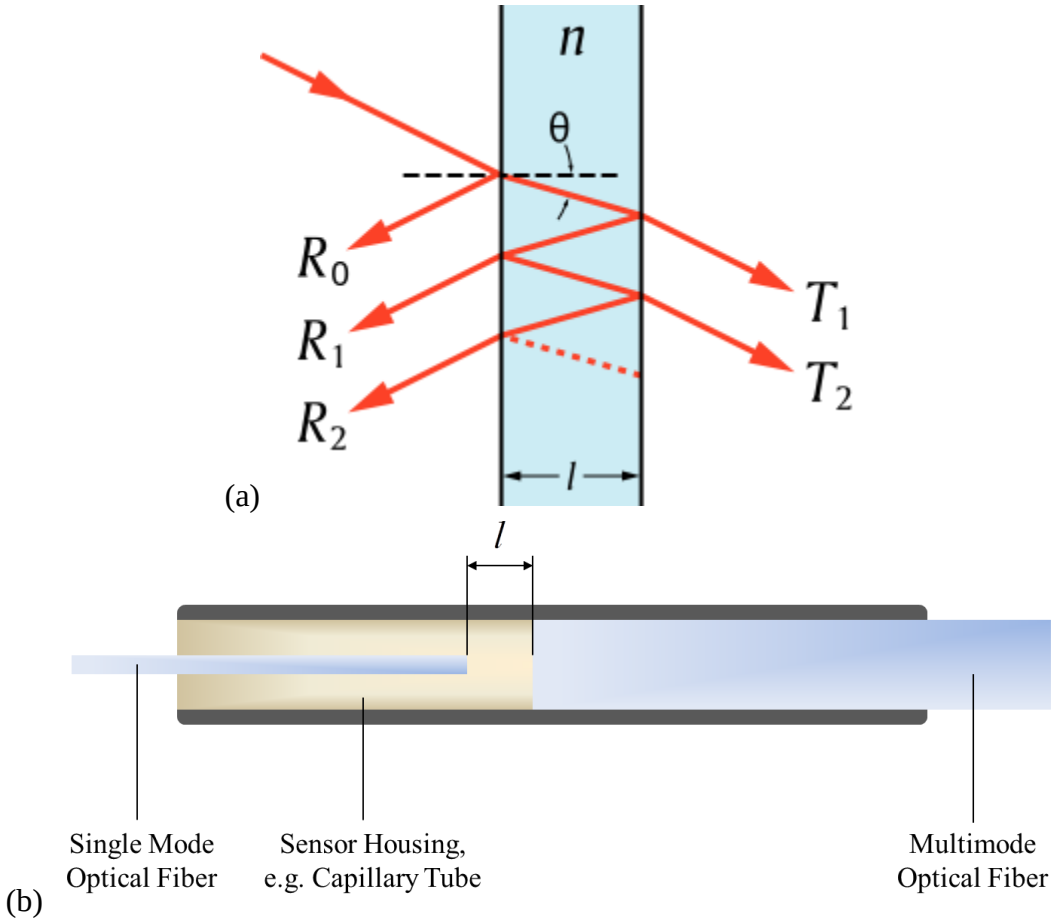

Figure 5.5: Fabry-Pérot interferometer (a) optical resonance cavity formed between two partially reflective surfaces ("Fabry-Pérot Interferometer," n.d.), (b) external Fabry-Pérot interferometer; used under CC license https://creativecommons.org/licenses/by/3.0/

One of the difficulties in implementing EFPI sensors is that when the displacement exceeds the wavelength of the light, a fringe is passed over where the reflected intensity is not monotonic, but passes over a peak value and repeats. To obtain absolute displacement values of any significant magnitude, it is necessary to track the number of fringes passed over by using a digital setup in post processing, or preferable in real-time. Complicating matters, if the displacement reverses direction at a peak or valley of a fringe, this goes unnoticed.

Several methods are available for treating this issue; Murphy (Murphy et al. 1991) developed an EFPI with two single mode fibers reflecting off a single multimode fiber reflector. The gap size between each fiber was different, separated by the length needed to produce a quadrature phase shift. Thus, when one fiber is at a fringe and unable to detect changes in direction, the other is always at the most sensitive part of the FPI spectrum. Schmidt and Fürstenau (1999) used a less cumbersome single EFPI, with instead three excitation wavelengths for phase demodulation. A broadband superluminescent diode was used as the optical source, and three optical band pass filters used to transmit each of three separately wavelengths of light to the EFPI. Since each wavelength had a different displacement-reflection spectrum, the number of zero crossings could be monitored. Read (Read, Foote, and Murray 2001) used this method with two wavelengths instead of three, with good success, using FBGs as the wavelength filters.

5.5 Strain Resolution of Various Fiber-Optic Systems

One of the chief motivators influencing research in acousto-ultrasonic applications of fiber-optic sensors is increasing the strain resolution, i.e. the smallest strain that the sensor can resolve. Part of what motivates this is the potential for using fiber-optic sensors

in the AE industry; AE events are extremely low in amplitude and occur as single events which preclude averaging to increase their SNR.

Strain resolutions are often expressed as a spectral density with strain normalized by $\sqrt{\text{Hz}}$. This considers that not all measurements necessarily happen over the same bandwidth, and factors such as digital sampling rate and filtering can reduce the overall noise. In fact, it is a common tactic to add a filter into the data acquisition chain to reduce the noise level for a smaller resolvable strain reading.

For EFPI sensors, Murphy (Murphy et al. 1991) reported a strain sensitivity of. Naturally, the laser power and noise sources would factor into any eventual strain resolution measurements. Perhaps more immediately accessible, Chow (Chow et al. 2005) reported a strain resolution less than 1 $p\varepsilon/\sqrt{Hz}$, although this requires one stabilized laser per sensing cavity, precluding multiplexing. Cranch (Cranch, Flockhart, and Kirkendall 2006) reported strain resolutions of $2\ n\varepsilon/\sqrt{Hz}$ and $30\ n\varepsilon/\sqrt{Hz}$ for EFPI and FBG sensors, respectively. Cranch's DFB laser system in 2008 (Cranch, Flockhart, and Kirkendall 2008) achieved an FBG strain resolution of $118\ \text{f}\varepsilon/\sqrt{Hz}$. This system is the best FBG strain resolution we have found in the literature. Betz (Betz et al. 2003) has reported a better resolution at $40\ \text{f}\varepsilon/\sqrt{Hz}$, although this figure is artificially depressed as the signal was averaged 128 times. Norman (Norman and Davis 2011) reported sub-microstrain resolution, although the bandwidth is left unspecified. Wu and Okabe (2012) used a balanced photodetector and pi-FBG, reporting a strain resolution of $9\ n\varepsilon/\sqrt{Hz}$.

The resolution depends largely not only upon the sensor, but on the equipment and method used. The work of Cranch (Cranch, Flockhart, and Kirkendall 2008) has the best

strain resolution among the sources I have seen yet, by at least one or two orders of magnitude, although replication requires a great deal of expertise.

The intensity modulation approach used in this work is simple to implement, although more sophisticated sensing approaches in the literature have superior strain resolutions. The upside of this is that the sensor development components of this work are based on the mechanical component of fiber-optic sensors; this means that the advancements to the mechanical response of a sensor are transferrable to other sensing systems. This is analogous to an engineer amplifying the response of a piezoelectric ultrasonic sensor through mechanical design, which is separable from advancements in piezoelectric materials science which can occur independently.

CHAPTER 6

STATE OF THE ART IN FIBER-OPTIC GUIDED WAVE SENSING

6.1 FIBER-OPTIC SENSOR GUIDED WAVE APPLICATIONS

A few examples of fiber-optic sensor applications are medical ultrasound (Webb, 1996), ship hull monitoring (Wang, 2001), and embedded monitoring of reinforced concrete (Maalej et al. 2004). Fiber-optic sensors have also been applied to bridge monitoring (Chan et al. 2006) and embedded composite material monitoring (Kuang et al. 2001; Takeda 2002; Takeda, 2005; de Oliveira et al. 2008; Park, Peters, and Zikry 2010).

There has been a large body of research in fiber-optic sensors for acousto-ultrasonic guided wave monitoring (Tsuda, 2006; Betz et al., 2007; Davis et al. 2014), and acoustic emission monitoring (Perez, Cui, and Udd 2001; Chen et al. 2004; Kageyama et al. 2005; de Oliveira et al. 2008; Tsuda, 2009). This chapter covers pertinent research on active and passive SHM using fiber optics for guided wave sensing. It is organized into the following sections

- Section 6.1 covers research on applications in fiber-optic guided waves and acoustic emission sensing
- Section 6.2 covers the topic of mechanical attachment. This section is of particular note, as it discusses mechanical systems that have been used to modify and enhance an FBG response

AE sensing and mechanical fiber-optic sensors are emphasized, as they are core to this dissertation. There is naturally some overlap between sections 6.1 and 6.2, as novel methods of optical fiber mechanical attachment used active SHM and AE sensing for proof-of-concept. The choice to include material in Section 6.2 rather than Chapter 5 depended on whether mechanical attachment was novel or a critical feature of the article.

6.1.1 Fiber-Optic Sensing of Guided Waves

The development of high frequency dynamic sensing capabilities in fiber-optic sensing has largely been motivated by guided wave sensing. The requisite sensing frequencies are high, ranging from tens of kHz to several MHz. Strain resolutions are also low, in the low microstrain range, and even smaller for AE signals. A single sensor is not needed for each type of damage detection method, e.g. impact, AE, pitch-catch, etc. Rather, a sensor must have a suitable size and strain sensitivity; it must be able to detect the motion that propagates in the structure. This can be expressed in terms of in-plane and out-of-plane motion; it can also be expressed in terms of responsivity to guided wave modes (e.g. Lamb wave modes S0, A0, S1, A1, etc.) which can be resolved into the in-plane and out-of-plane components of their motion.

It should be noted that in plates with traction free surfaces, waves propagate as Lamb waves regardless of the source (e.g. pitch-catch, impact, or AE). This is of particular note in AE literature, where recent trends have moved away from using axial and flexural waves towards Lamb wave formulations, to greater predictive and descriptive success. In practice, practical considerations such as amplitude, wave modes, frequency range, etc. are still related to the source.

Betz (Betz et al. 2003) demonstrated FBG intensity modulation acousto-ultrasonic sensing in a pitch-catch configuration across a Perspex plate. A PZT actuator was used as a transmitter, and both FBG and PZT used as receivers. Both symmetric and antisymmetric Lamb wave modes were sensed, with a minimum detectable strain of 16 nanostrain for the optical system; however, this research took advantage of a feature of pitch-catch SHM, in that it allows averaging to reduce noise, and the results are from the averaging of 128 consecutive signals.

Tsuda (2006) demonstrated FBG sensing of Lamb waves in a cross-ply CFRP using a broadband source and a narrowband tunable laser sources for FBG sensing. Only S_0 waves were transmitted using a conventional ultrasonic transducer, as the S_0 wave has a larger in-plane component which could be sensed by the FBG; both propagation through pristine and impact-damaged regions was assessed, with damage-related features observed. Using the average of 512 waveforms, SNRs of over 40 and 70 dB were observed for the broadband laser and the narrowband tunable laser, respectively.

Betz (Betz et al. 2007) used a narrowband source intensity modulation approach for FBG Lamb wave sensing on a thin aluminum plate for damage localization. Three FBGs were placed in a rosette configuration, where the directional properties of FBG allowed for the direction of the incident wave to be calculated. Using two FBG rosettes and PWAS actuators, the localization of a flaw was demonstrated.

Davis (Davis et al. 2014) established that a ratio of wavelength to FBG length must be at least 8.8 to resolve the response of a dynamic strain field with less than 2% loss from the true strain value. A ratio of 4.8 could be used to resolve a dynamic strain field with less than 5% loss from the true strain value. Experimentally, these values were obtained by

calculating the wavelength of a Lamb wave in a 0.8 mm aluminum plate, and varying the excitation frequency in a pitch-catch configuration in a range where only the fundamental S_0 and A_0 modes would propagate. The ratios held true across a range of FBG lengths from 0.2 mm to 5 mm. This research provides well-verified rule-of-thumb metrics for designing experiments with FBGs, although the results may not necessarily be valid for higher order Lamb wave modes.

This work shows that in a general sense, FBG sensors are well suited for active SHM using both PWAS and ultrasonic transducer actuators. The signals obtained were clear, with high SNRs, and could generally be used to distinguish damage-related features and localize damage, so long as practical considerations like FBG length were appropriately used. One of the main advantages of pitch-catch active SHM is the use of horizontal acquisition – averaging many signals together to obtain high SNRs. Thus, these positive results are not necessarily transferrable to passive SHM, where horizontal acquisition is infeasible or inappropriate. Thus, suitability for passive SHM, including AE sensing must be shown separately.

6.1.2 Fiber-Optic Acoustic Emission Sensing

AE sensing is an area of great interest for fiber-optic sensors. There is a large market for AE sensors, and conventional AE sensors use piezoelectric sensing elements. The advantages of fiber optics, specifically its multiplexing capabilities have a lot to offer for AE sensors; traditional AE sensors cost hundreds of dollars, and implementation over large structures can be bulky and costly. This is of particular importance true for the aerospace industry and for industries where sensors must be intrinsically safe to not ignite a flammable environment. Despite these advantages and great interest, fiber-optic sensing

has not yet broken into the AE market, largely due to their noise and lower sensitivity than their piezoelectric counterparts. Much of the research into fiber-optic sensing of AE has been aimed at proof of concept demonstrations, and incrementally mitigating the noise issues.

In fiber-optic AE sensing research, there is often a misconception of the definition of an AE event. Generally, claims of AE sensing in the literature fall into three categories:

1. Crack-related, or other damage-induced "true" AE events. A test using a true AE event, or a proven AE calibration method is the best indicator of the functionality of an AE sensor
2. Simulated AE events, such as pencil-lead-break (PLB), glass rod fracture, or even impact. PLB-simulated AE events is most commonly seen. But for various reasons, it is distinctly different than crack-related AE events: lower frequency range (hundreds of kHz), higher amplitude, and a monopole versus dipole source
3. Pitch-catch configurations which are called AE events due to a desire to continue research in AE. Although pitch-catch configurations are a good starting point for developing and testing AE sensors and systems, ultimately the results are not necessarily directly comparable as the waveforms are often higher in magnitude by orders of magnitude

Fiber-optic AE sensing has been an active area of research at least since the early 2000s. For FBG sensing, Perez (Perez, Cui, and Udd 2001) demonstrated the capability for FBG sensing of ultrasonic waves transmitted by piezoceramic active transduction, as well as PLB-AE. This work served as a proof of concept for FBG sensing of AE-type signals.

Read (Read, Foote, and Murray 2001) was able to detect AE during a fatigue test of a large composite specimen made to resemble an aerospace panel. This was done using a surface-bonded EFPI sensor, with a fatigue test performed with intermittent impacts of increasing amplitude. This can be considered highly favorable conditions for AE detection due to the large extent of damage and the composite specimen with higher amplitude AE events. Upon searching, this seems be the first demonstration of true damage-related AE capture by fiber-optic sensors.

Chen (Chen et al. 2004) developed a fiber-optic sensor based on a fused-tapered fiber two-input, two-output (2 x 2) coupler. The principle of operation is that an elastic strain field changes the coupling coefficient through elasto-optic effects, and can be used to track the applied strain. Mechanical strain amplification was used to increase sensor sensitivity; for this sensor, a V-groove was used for strain concentration, and the fiber coupler was bonded via two-points across the groove. Additionally, the tapered region at the center of the 2 x 2 coupler acted as a strain concentrator. The AE sensing was done by PLB only, with the fused-tapered fiber-optic sensor showing a lower signal-to-noise ratio than a conventional piezoelectric AE sensor.

Kageyama (Kageyama et al. 2005) used a principle of a Doppler effect in a curved light waveguide for fiber-optic sensing. Light frequency shifts were tracked in an optical fiber, these shifts being related to motion in the fiber. A full-scale model of a reinforced concrete railway girder was loaded to failure, and the load history tracked by piezoelectric AE sensors and this new fiber-optic sensor. The author reports that the fiber-optic sensor has sensitivity equal or greater than conventional AE sensors. In principle, it is difficult to

compare this work to the rest of the literature since AE events associated with a test to failure of such a large-scale specimen can be very high in amplitude.

de Oliveira (de Oliveira et al. 2008) assessed the response of embedded FBG and EFPI sensors to PLB and impact excitation. The EFPI was more sensitive, but still had limitations with a low SNR. Fu (Fu et al. 2009) used a fused-tapered 2 x 2 coupler sensor inside a silica capillary tube for embedment into CFRP specimens. During a three-point bending test of a composite specimen, AE events could be detected, but not until a piezoelectric AE sensor detected large increases in AE event amplitude, nearing catastrophic failure of the specimen. Tsuda (2009) used an intensity modulation approach with a cantilevered FBG to sense AE events during a pressure test of a curved filament-wound CFRP tank. The AE hits started and ended around the same time during the test for both conventional piezoelectric AE sensors and the FBG sensor, indicating that the FBG performed well compared to the conventional AE sensor. This work underscored the potential for an FBG to serve as mechanical waveguide which has become a new area of research in the last few years. Yu (2016) detected AE events during quasi-static tension of CFRP specimens using an intensity demodulation approach with a pi-FBG and a balanced photodetector.

6.2 Mechanical Attachment of Fiber Bragg Grating Sensors

The mechanical attachment of fiber-optic sensors plays a large role in its eventual efficacy. The simplest and most common approach to the use of fiber-optic sensors is by bonding it to the surface of the host structure. However, other attachment methods are possible, each with distinct advantages and disadvantages. The most common attachment methods are:

- Surface bonding of the entire sensing region of an optical fiber. This is typically an attempt to cause the fiber to exactly reflect the surface strain of a stiffer substrate. Limitations of this method are the direction dependence of the fiber and the sensing of quasi-static strain which can cause methods such as FBG intensity demodulation to cease functioning
- Two-point bonding of an optical fiber. Typically, the fiber is bonded across an air gap. This is to cause the fiber to stretch as the size of the gap increases. Limitations of this method are directional dependence and concerns about fiber buckling or suboptimal behavior in compression
- Single-point bonding of an optical fiber. In this case, the optical fiber itself serves as either a flexural beam or a waveguide. There are indications that this can provide a higher response amplitude for a sensor along the unbonded region of the fiber, but necessitates an exposed region of fiber which may be prone to damage. Factors such as the optical fiber mechanical properties and length of the exposed region also begin to play a larger role in this configuration
- Bonding an optical fiber to an external mechanical sensor (e.g. a mechanically tuned resonant component). This configuration provides a large degree of flexibility, customization, and potential improvement of the sensor response. The problem is the difficulty in design. It also changes the form factor of the sensor, precluding embedment in most cases, and making it less attractive to bond to a surface.

6.2.1 Embedment of Optical Fibers in Composite Structures

The shape of an optical fiber allows it to be embedded directly into polymer based composite materials (e.g. CFRP, GFRP). This has been one of the key areas of research in fiber-optic acousto-ultrasonic sensing, as direct embedment provides logistical advantages, and the ability to better detect flaws buried within a laminate. There are also drawbacks in terms of diminishing the sensing capability, compromising the performance of the composite material.

Kuang (Kuang et al. 2001) investigated the embedment of FBG into CFRP, GFRP, and fiber metal laminates. He found that FBGs could be used to measure residual stresses generated during the manufacturing process due to distortion of the FBG spectrum. It was found that the laminate stacking sequence had a large effect on the applicability of FBG sensors. Depending on the stacking sequence, the FBG spectrum could show deviations anywhere from a small broadening of its spectrum to the splitting of the reflectivity spectrum into multiple distinct peaks.

Takeda (2002) investigated the embedment of small diameter (52 μm) FBG sensors into CFRP laminates. The FBG maintained a strong single-peak spectrum upon embedment, and the FBG was able to reflect spectral changes caused by delamination-induced changes to the strain field. Takeda (2005) further investigated embedded small diameter FBG sensors for Lamb wave detection in CFRP. Characteristic features of wave delamination interaction were measured by the embedded FBG and corresponded well with FEM simulations. De Oliveira (de Oliveira et al. 2008) investigated the embedment of FBG and EFPI sensors in CFRP for strain and wave propagation measurements. The FBG was capable of sensing the quasi-static strain, and the EFPI successfully detected PLB-AE

events, albeit at a low signal-to-noise ratio. Park (Park, Peters, and Zikry 2010) investigated the effect of optical fiber density (number of fibers per unit length) on CFRP mechanical properties. Total energy dissipated and contact force from impact experiments were used as a measure of the laminate lifetime and stiffness, respectively. At low optical fiber densities, both lifetime and stiffness dropped sharply with increasing optical fiber density. At higher densities, both parameters increased constant thresholds as the failure began to be dominated by the mechanics of the optical fibers.

The advantages of embedment of fiber optics are clear – it allows direct measurement within a structure at critical regions; the sensor is also intrinsically protected from the outside environment, albeit at the cost of diminishing material performance. The sensing limitations are primarily due to the limitations of mechanical attachment. Embedment of an optical fiber prevents optimization of bonding. For example, a strain concentration can be used for mechanical amplification. However, this would not be appropriate embedded in a region of a structure so critical that it requires monitoring for damage.

6.2.2 Two-Point Contact Bonding

Two-point bonding of an FBG is an innovative way of bonding to a host structure. It allows the relative motion of two points to excite a sensor bonded across an air gap. This also bypasses some of the issues with bonding the sensor itself to a substrate, for example FBG length/wavelength conditions that are modified by use of the optical fiber itself for the final mechanical transduction.

The biggest drawback of a two-point bonding regime is the behavior in compression. There are concerns that a fiber may behave sub-optimally in compression,

maybe even buckling and not transmitting a waveform (Cranch, Flockhart, and Kirkendall 2008). Factors such as the distance between the two bonded points and type of optical fiber affect this. For example, an EFPI has a mechanical separation between two separate optical fibers, so a two-point mechanical attachment may be ideal for this sensor configuration. A pretension may also help prevent buckling. The two-point bonding may also be useful in the creation of custom mechanical host structures. An example is a fork-shaped FBG accelerometer (Stefani, 2012), where a pre-tensioned polymeric optical fiber spanned the gap. Out-of-plane acceleration created a relative antisymmetric motion of each side of the fork, tensioning and compressing the FBG bonded across the span.

6.2.3 Single-Point Contact Bonding with Optical Fiber Waveguide

Single-point bonding of an optical fiber has a great potential, notably for FBG sensing. In this configuration, a single point on the optical fiber distal to the sensing region is bonded to the host structure. The length and mechanical properties highly influence the response. For a short length, the fiber can be considered an axially vibrating bar (this has also been called a cantilever beam, although in principle flexural modes will not excite the center of the optical fiber, and only longitudinal modes are sensed). One such application is the work of Tsuda (2009) where a 45 mm cantilever was created by adhesively bonding a fiber to the side of a cylindrical CFRP pressure vessel. In this configuration, the FBG was insensitive to quasi-static strain. Additionally, during pressure loading, initial AE events started at the same time for piezoelectric and FBG AE sensors, indicating high sensitivity. The downside is a that observed waveforms continue ringing on the order of seconds, indicating an incredibly low damping and continued vibration not generally acceptable for practical AE sensing.

Lee (J. Lee, S. Lee, and Yoon 2008) used multiple FBGs connected via light intensity dividers for multipoint sensing via an intensity modulation approach. The FBGs were attached via single-point bonding, where the optical fiber was bonded with a Teflon insert, and the insert removed after bonding was complete to create a fiber-optic waveguide on a plate structure. SNRs on the order of 50 dB were obtained using a frequency domain calculation method on height from the noise floor to a signal peak.

Wee (2016) investigated Lamb wave sensing on a metallic plate via a point-bonded optical fiber with distal FBG. Rather than a cantilever beam, due to its length the optical fiber served as a waveguide. After accounting for geometric spreading, bonding the optical fiber away from the FBG accounted for a 5.1 times mechanical amplification compared to directly bonding the region of the optical fiber with the FBG. For wave transduction, both A_0 and S_0 Lamb wave modes coupled into a longitudinal L_{01} and F_{11} longitudinal and flexural modes of the fiber, with only L_{01} exciting the FBG. It was found that reducing the bond length compared to the Lamb wavelength increased the signal response.

6.2.4 Mechanical Sensors with Fiber-Optic Sensing Elements

A mechanical host structure offers a number of distinct advantages for fiber-optic sensors. It provides a large degree of flexibility, customization, and potential for improvement of the sensor response. Mechanical amplification can be incorporated through resonance or strain concentrations. The frequency response is tunable through the localization of one or more resonance peaks at desired locations of the spectrum. A unidirectional FBG or FPI sensor can become omnidirectional if it is attached to a host structure which responds omnidirectionally. Similarly, the host structure can respond different to wave modes, sensing out-of-plane rather than in-plane, and combining in-plane

and out-of-plane motion (or otherwise responding differently to Lamb wave modes than directly bonded fiber-optic sensors). The downside of mechanical host structures is in its size, weight, and form factor. In some sense, this mitigates a few of the advantages of fiber-optic sensors. However, in consideration that they provide a means of sensing that is otherwise unavailable, the noted faults must be tolerated. And particularly with mechanical amplification, the use of mechanical host structures may be one method of advancing fiber-optic sensor feasibility for AE applications.

Initial fiber-optic mechanical host structures focused on developing FBG accelerometers. Since FBGs sense in-plane strain, a tuned mechanical host structure is necessary to be able to detect out-of-plane acceleration. Gerges developed an FPI accelerometer based on a weighted diaphragm with a mirror serving as one side of an FPI (Gerges et al. 1989). Todd developed an FBG accelerometer consisted of an FBG bonded to an assembly of two flexural beams and a proof mass (Todd 1998). Mita (Mita and Yokoi 2000) developed an FBG accelerometer based on a cantilever beam and proof mass and spring system, held inside a metallic case. The fork shape accelerometer (Stefani, 2012) presented in Section 6.7.3 similarly converts out-of-plane acceleration to in-plane FBG strain.

Lee (J. Lee and Tsuda 2005) developed a mobile FBG sensor head for AE sensing consisting of an FBG bonded to an acrylate plate. The acrylate plate could be bonded to flat surface by a suitable couplant, making the structure ideal for NDE applications. Evaluation was done by tensile testing of a composite specimen until failure. AE signals obtained by piezoelectric AE sensors and the FBG sensor head were obtained by quasi-static tensile testing of a composite specimen until failure by matrix cracking. The author

reports a 10 dB higher SNR from the FBG sensor head compared to the piezoelectric AE sensor; although, this is difficult to justify as the noise floor appears to be DAQ equipment and digitization noise. That is, a sufficiently high amplitude AE signal was generated, but only a lower bound on the SNR can be obtained from such a signal. In a later study, the SNR of this setup was compared to a plate-bonded FBG, and found that it reduced the SNR by 6 dB (Tsuda, 2010). However, the SNR reduction was considered tolerable as it allowed for convenient NDE application and omnidirectional guided wave sensing.

Takuma (2014) investigated an FBG glued to a cylindrical mechanical host structure and investigated the frequency response, directional dependence, and AE sensing. The sensor was wideband in the 0-1000 kHz range, sensed omnidirectionally, and sensed AE events during a three-point bending test of a CFRP specimen. The cylindrically-bonded FBG sensor sensed AE events during the three-point bending test, albeit at a lower SNR than the conventional piezoelectric AE sensor. It is difficult to get an understanding to what degree from the data presented, as the piezoelectric AE sensor noise floor appeared to be due to DAQ equipment.

A number of advantages have been found using mechanical host structures for FBGs: changing the mode of sensing, omnidirectionality, tuning the frequency response, and potentially mechanical amplification. However, further characterization is needed, particularly to support claims of mechanical amplification. In some manner, it is intuitive that a resonant structure might increase amplitude; AE sensors with tuned mechanical components respond with higher sensitivity than PWAS bonded directly to a plate.

Other sensor configurations show potential for AE sensing, but do not quantify their effectiveness. This is taken as a lesson for research in later chapters. At the very least, a

comparison to plate-bonded FBG using the same sensing system should be done. Better yet would be calibration or obtaining metrics of sensitivity or SNR.

6.3 Research Trends in Fiber-Optic Acoustic Emission Sensing

From this review, it is very clear that pursuing fiber-optic AE sensing is highly desirable in view of the breadth of research over the last two decades, even despite a lack of commercially available products. Throughout the literature, custom incremental modifications were made on the optical systems and sensors themselves; this can be attributed to an attempt to make improvements to systems which still do not perform as well as conventional piezoelectric AE sensors. Much of the research where PLB and impact experiments were performed made claims of sensor efficacy for AE sensing. This makes studying this topic difficult, as the same language is used for sensing true damage-induced AE events. However, damage-induced AE events are much lower in amplitude and more difficult to sense, making such comparisons not entirely appropriate.

From a thorough literature search, no research has been found with successful fiber-optic sensing of damage-induced AE in metallic structures. This is despite sensing in metals being one of the most common uses of commercial piezo AE sensors. However, fiber-optic sensing of actual damage induce AE signals was reported for CFRP and reinforced concrete structures, often loaded up to failure which produces higher amplitude AE events. To this end, research with damage-induced AE events was done under only the most highly favorable conditions. Proof-of-concept demonstrations are lacking for critical applications which present less favorable conditions for damage detection. For example, if a sensor cannot sense a fatigue-induced AE event in metal, this precludes its use for most aerospace applications. However, these are conditions where conventional piezoelectric

transducers are still highly effective. These conclusions hold true even when fiber-optic sensing is further enhanced with attention to mechanical amplification by sensor housings and resonators.

Fiber-optic sensing is incrementally approaching feasibility for damage-induced AE sensing. Because of this, there is much room for growth in the field. In a general sense, fiber-optic sensors and systems must be developed to detect damage-induced AE signals under more moderate conditions, prior to failure. At present, bench-scale proof-of-concept demonstrations do not replicate this more difficult metric. Because of this, claims that have been made of comparability or even superiority of fiber-optic sensors to convention AE sensors cannot be justified. The upside of the large body of research in fiber-optic AE sensing is that there is a large base of concepts to build from for incremental improvement. However, one must be careful to clearly assess the limitations of a sensing system under consideration, and calibration methods or quantifiable performance characteristics must be employed for research to be of broad benefit.

CHAPTER 7

PROOF OF CONCEPT FOR A PIEZO-OPTICAL RING SENSOR

7.1 OVERVIEW AND BACKGROUND FOR THE RING SENSOR CONCEPT

7.1.1 Initial Ring Sensor Concept

This chapter outlines the development of an ultrasonic sensor based on the concept of a ring resonator (Figure 7.1). Its principle of operation is based on the localization of a fundamental resonance mode at a frequency which is tunable by design. This resonance mode is preferentially excited by out-of-plane motion. The ring deformation is sensed by an FBG and PWAS which are bonded to the ring. This concept has been termed a piezo-optical ring sensor (Giurgiutiu 2014) due to its ability to use a piezoelectric or fiber-optic sensing element, and is called a ring sensor in this work for conciseness. Contributions to the ring sensor development including design, evaluation, modeling, and refinement have been published in two conference proceedings (Frankforter, Lin, and Giurgiutiu 2014; Frankforter et al. 2015) and two journal articles (Giurgiutiu et al. 2014; Frankforter, Lin, and Giurgiutiu 2016).

The initial concept of the ring sensor was presented in a 2013 dissertation by Roman (2013); a patent was awarded (Giurgiutiu et al. 2013). The objective was to develop a resonator which could use an FBG sensor to detect out-of-plane motion associated with AE events in a manner similar to conventional AE sensors. This dissertation entered development of the ring sensor at a point when the initial design and prototypes had already

been developed. Although the ring sensor was designed for fiber-optic sensing, its capability to excite an FBG had not yet been demonstrated. Similarly, its capabilities to serve as an ultrasonic wave sensor had also not been established. In this chapter, the proof of concept for the ring sensor to detect guided waves using an FBG sensing element is demonstrated.

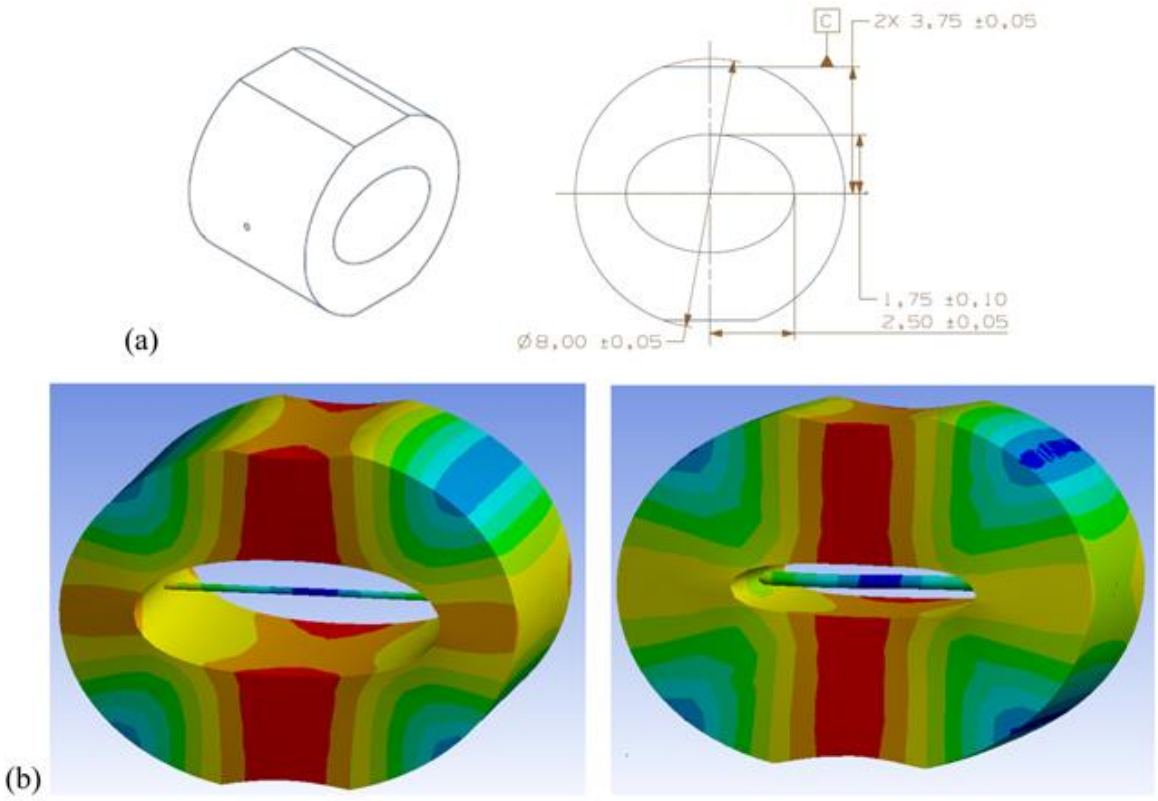

Figure 7.1 (a) 100 kHz ring sensor geometry and (b) fundamental resonance mode shape (Roman, 2013)

7.1.2 Initial Refinement of the Ring Sensor

Development of the ring sensor geometry by Roman (2013) occurred in multiple stages. Initially, a ring-shaped geometry was used (a circular outer profile and circular inner hole). This allowed the resonance frequency f_i to be approximated using a formula from the work of Blevins (Blevins 1980; Roman 2013):

$$f_i = \frac{i(i^2-1)}{\sqrt{2\pi R^2(i^2+1)}}\sqrt{\frac{EI}{m}} \tag{7.1}$$

where i is the mode number, R is the radius of the midline of the ring, E is the Young's Modulus, I is the moment of inertia, and m is the mass per unit length.

Roman (2013) then refined the ring geometry in an attempt to maximize the response and provide better bonding characteristics (Figure 7.1a). Instead of a circular hole for the ring, an elliptical hole was tested with the idea of forcing the maximal displacement preferentially along the major axis of the ellipse on which the FBG was placed. The bottom surface was flattened to provide better bonding characteristics, with the top surface flattened as well for symmetry; the top surface also permitted the bonding of a PWAS as a second sensing element. A small hole was incorporated along the major axis of the ellipse to bond an FBG sensing element. These changes gave the ring sensor a fundamental "breathing"-type vibrational mode (Figure 7.1b) analogous to the motion of a breathing crack. The two lateral sides of the ring sensor move 180° out of phase from each other, tensioning and compressing an FBG stretching across the hole and exciting a PWAS on the top surface.

Roman (2013) used the commercially available FEM software ANSYS Workbench to perform 3D modal analysis and created designs with resonance frequencies targeted at 100 kHz, 200 kHz, and 300 kHz. For reference, the 100-kHz ring sensor was 8.00 mm in diameter and the 300-kHz ring sensor was 4.35 in diameter. These are roughly the size of the smallest commercially available AE sensors (for reference, the MISTRAS Pico sensor is 4.78 mm in diameter and 3.94 mm in height). The 100 kHz and 300 kHz ring sensors were prototyped and outfitted with PWAS for testing under free conditions. The resonance

frequencies were experimentally validated using the EMIS method and chirp excitation, yielding resonance frequencies at 113 kHz for the nominally 100 kHz ring sensor, and 270 kHz for the nominally 300 kHz ring sensor respectively.

7.1.3 Ring Sensor Proof of Concept – Scope and Approach

From a review of AE, fiber-optic, and ultrasonic sensor design literature, it was found that the scope needed to be expanded for the development of a sensor which could be practical for SHM application. The initial concept was to develop a sensor which detected out-of-plane motion from AE events using resonance amplification principles (Roman, 2013). Two additional goals were added which could be readily tested:

- Create a sensor whose FBG detects a higher strain than a plate-bonded FBG. Previously, it was assumed that sensing about a resonance frequency would be sufficient for amplification; however, there are losses that need to be minimized in the transfer of energy to the optical fiber.
- Create a sensor which imparts omnidirectional sensing capabilities to an FBG. Plate-bonded FBGs have the major limitation that they only sense along the optical fiber's longitudinal axis.

A third goal: "create a sensor that isolates its FBG from quasi-static strain" required the use of additional facilities, and was thus tested later (Chapter 9): This third goal ensured that the FBG would not cease operation when modest structural loads provided produced strains which exceeded the FBG strain range allotted for dynamic sensing.

To develop a proof-of-concept for the use of the ring sensor as an *in situ* FBG ultrasonic wave sensor, the following experimental work was performed:

- Implementation and testing of an FBG interrogation system

- Testing an FBG sensing element on a free (unbonded) ring sensor
- Experimental validation of a plate-bonded ring sensor's capability to detect guided waves
- Characterizing the sensor's mechanical performance, including bonding effects, strain amplification, and directional response

The rest of this chapter focuses on this proof of concept and characterization of the initial ring sensor prototype. The focus was on the 100 kHz prototype as this was larger and easier to handle. It also served as a good basis for miniaturization and sensitivity improvements as discussed later in Chapter 9.

7.2 Characterization of the FBG Interrogation System

At the time of writing this dissertation, there are still no commercially available turn-key FBG interrogation systems for ultrasonic guided wave detection. Therefore, such a system was developed and tested in-house. This section outlines the equipment setup, calibration, and noise assessment for an FBG interrogation system. Credit for the optical equipment setup goes to the work of Lin (Lin and Giurgiutiu 2014a). The calibration allowed for direct conversion between voltage and FBG strain. Noise assessment was done to characterize the limits of the system and identify if incremental performance improvements could be obtained by modifying the optical equipment.

7.2.1 Data Acquisition and Optical Equipment – Setup

The data acquisition equipment and FBG interrogation setup used in this section is used throughout the rest of Chapters 7-11. EMIS experiments were performed using an HP 4194A impedance analyzer. Signal excitations were performed using a HP 33120A function generator. For chirp excitation experiments, self-triggering of the HP 33120A

function generator was necessary to start each chirp signal in phase for signal averaging. An HSA4014 power amplifier was used when pulse excitation or excitations higher than 20 V were needed. Signals were collected using a Tektronix TDS5034B digital oscilloscope. With the use of a preamplifier, fiber-optic signals could also be directly obtained by a MISTRAS Micro II AE data acquisition system.

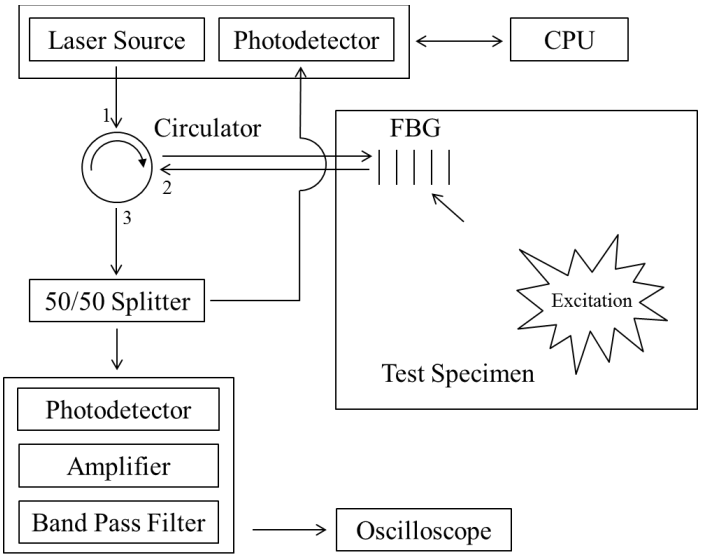

Figure 7.2: Instrumentation schematic for the FBG optical interrogation system and data acquisition equipment

The instrumentation for FBG sensing is shown in Figure 7.2. It consists of a LUNA Phoenix 1400 tunable laser source, an optical circulator (AFW Technologies Pty, #CIR-3-15-L-1-2), a 50/50 optical splitter (AFW Technologies Pty, #FOSC-1-15-50-C-1-S-2), and a Thorlabs photodetector (PDA10CF). A New Focus 2053 photodetector with was used for some of the experimental work in Chapters 8 and 9. The FBGs used were 10 mm long with more than 90% reflectivity, supplied by AtGrating Technologies. Some of the FBGs used were 3 mm long – it is stated explicitly when these are used. The FBG were made from acrylate fiber (SMF-28e) with acrylate recoating. The FBG is located 1 meter from an

FC/APC connector, with another 1 meter as a pigtail. The gratings are apodized with a center wavelength of 1530 nm or 1550 nm, both excitable by the tunable laser source.

7.2.2 Data Acquisition and Optical Equipment – Calibration

All of the ultrasonic FBG strain detection in this work used the intensity demodulation approach described in Chapter 5. In this method, a narrow linewidth laser is fixed on the half-maximum point of the FBG falling slope. One advantage of this approach is that absolute strain measurements can be obtained with proper system calibration. Recall the FBG strain-wavelength equation

$$\frac{\Delta\lambda_B}{\lambda_B} = (1-\rho_{eff})\varepsilon_{axial} \tag{7.2}$$

where $\Delta\lambda_B$ is the peak wavelength shift, λ_B is the peak wavelength, ρ_{eff} is the photoelastic constant for axial strain, and ε_{axial} is the axial strain. We can assume the FBG spectrum shifts rigidly if the wavelength of the elastic wave is significantly longer than the FBG length. Therefore, the shift in the peak wavelength can be tracked by the shift of any wavelength in the FBG spectrum, i.e.

$$\Delta\lambda_B = \Delta\lambda \tag{7.3}$$

The reflected power and the wavelength shift is related through the falling m slope of the FBG:

$$m = \frac{\Delta P}{\Delta\lambda} \quad \rightarrow \quad \Delta\lambda = \frac{\Delta P}{m} \tag{7.4}$$

The photodetector converts the change in power to a change in the current I_{PD} via the photodetector responsivity R_{PD}:

$$R_{PD} = \frac{\Delta P}{\Delta I_{PD}} \tag{7.5}$$

The change in current is converted to a change in voltage via a transimpedance amplifier with gain G:

$$\Delta V = G\Delta I_{PD} \tag{7.6}$$

where R is the input impedance of the photodetector. This was used at the low impedance setting of $50\ \Omega$. By combining equations (7.2) through (7.6), we obtain the strain-voltage transfer function for the FBG, optical, and data parts of the acquisition equipment:

$$\varepsilon_{axial} = \frac{R_{PD}V}{Gm\lambda_B\left(1-\rho_{eff}\right)} \tag{7.7}$$

The change in voltage ΔV was converted to a direct voltage reading V through the AC coupling of the oscilloscope. Note that R_{PD} and G depend on the choice of photodetector. Also, m varies between FBG. In experimental measurements, these values were appropriately changed when different FBG and photodetectors were used.

The veracity of strain calculations from equation (7.7) was tested in a quasi-static cantilever beam strain calibration (Figure 7.3) which shows a cantilever beam held at a downward displacement by a micrometer screw acting at a fixed location on the beam. Lin did the bulk of the experimental component of the calibration (Frankforter, Lin, and Giurgiutiu 2014); I replicated the calibration experiments and performed analytical modeling to verify them. The strain readings from FBG and the strain gauge were measured experimentally at $34.0\ \mu\varepsilon$ and $33\ \mu\varepsilon$, respectively (the strain gauge had a minimum reading of $1\ \mu\varepsilon$). The experimentally obtained values of beam dimensions, input displacement, and input displacement position were used to calculate the theoretical strain

via Euler-Bernoulli beam theory and a finite element beam model. The analytical and finite element models predicted $33.8\ \mu\varepsilon$ and $33.5\ \mu\varepsilon$. This puts the error of the quasi-static strain at 3% at the worst (comparison with the strain gauge) or 0.6% at the best (comparison with the finite element model). This was sufficient to demonstrate the accuracy of FBG strain calculations and support the veracity of future FBG strain measurements (Frankforter, Lin, and Giurgiutiu 2014).

Ultrasonic calibration was performed using the same cantilever beam specimen in the work of Lin (Lin and Giurgiutiu 2014b). A 300 kHz 3-count Hanning windowed tone burst was transmitted across the cantilever beam, excited by a PWAS transducer. The FBG was used to calibrate the PWAS with the assumption that the PWAS solely sensed in-plane strain via the g_{31} piezoelectric coefficient. The theoretical voltage to strain ratio based on PWAS material properties was $0.16\ \text{V}/\mu\varepsilon$ and the FBG-calibrated ratio was $0.21\ \text{V}/\mu\varepsilon$.

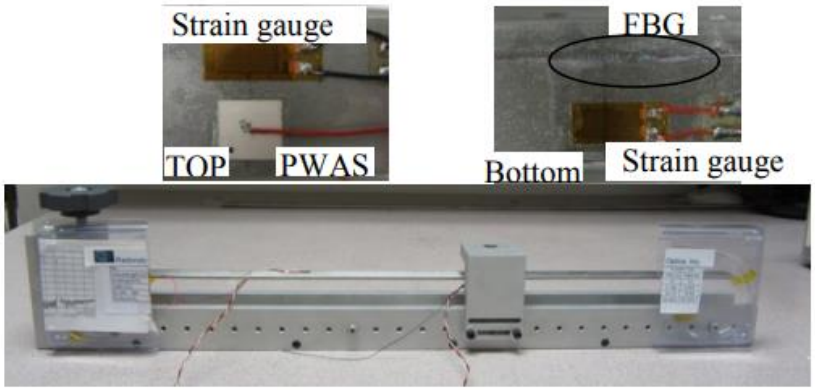

Figure 7.3: Cantilever beam specimen for static strain testing
(Frankforter, Lin, and Giurgiutiu 2014)

Given the simplicity of the in-plane sensing assumption (PWAS also sense out-of-plane motion), this is sufficient for this application to show transferability of strain calibration results to ultrasonic measurements. If a more precise verification of calibration

is needed, the theoretical model for the PWAS should be used to determine if any correction factors are needed.

7.2.3 Data Acquisition and Optical Equipment – Noise Assessment

Measurements were taken from the optical system under no external excitation to obtain noise signals and establish the system's strain resolution. The laser was turned on with the FBG in place and all components were configured just as in a wave propagation experiment. A milliseconds-long signal was obtained with a 5 MHz sampling frequency (the total sampling time was increased until the root-mean-square (RMS) noise levels leveled out). To obtain a single value for noise, the RMS noise was calculated as 0.0724 mV. The following optical system parameters Table 7.1 allowed for conversion of the RMS noise floor directly to a strain floor:

Table 7.1: FBG optical system strain calibration parameters

ρ_{eff}	λ_B	m	G	R_{PD}
0.22	1550.096 nm	31.921 mW/nm	1 x 10^4 V/A	1.04 A/W

Note that the Bragg wavelength λ_B and FBG slope m depend on the individual FBG. Converting the RMS voltage to strain using (7.7), the RMS strain is calculated at $6.23\,\mathrm{n}\varepsilon$, which can serve as a metric for the strain floor. As a first approximation, this can be normalized by the square root of a nominal $2.5\,\mathrm{MHz}$ bandwidth described by the Nyquist cutoff frequency; a strain resolution of $3.94\,\mathrm{p}\varepsilon/\sqrt{Hz}$ is estimated by this approach. However, this is approximation is non-conservative as there would naturally be some diminishment in noise amplitude close to the Nyquist frequency.

Comparing to the work of Cranch, a more sophisticated demodulation approaches can obtain $118\ \mathrm{f}\varepsilon/\sqrt{Hz}$ (Cranch, Flockhart, and Kirkendall 2006). Using an intensity demodulation approach in 2014, Wu obtained a strain resolution of $9000\ \mathrm{p}\varepsilon/\sqrt{Hz}$ using an intensity demodulation approach (Wu & Okabe, 2012). Since this method predicted a better strain sensitivity by orders of magnitude compared to a similar approach by Wu (2012), further analysis may be warranted. If further assessment of the strain floor is necessary, the next step would be to calculate the power spectral density as a method of obtaining the noise floor rather than normalizing by a nominal bandwidth.

Next, a characterization of the optical system noise was performed. Noise levels were observed higher than the thermal noise of the oscilloscope. Two potential primary-noise sources were identified: the photodetector and the tunable laser source. First, the Thorlabs PDA10CF photodetector was swapped for a DET08CFC photodetector. After using an external preamplifier with the DET08CFC photodetector, no changes in noise levels were observed. Second, the relationship between noise and output power of the Luna Phoenix 1400 was assessed (Figure 7.4). Although only 3 points were collected, there is a trend of noise increasing with increasing output power; there may be a linear trend, as each of the three measurements fall close to a linear trend line.

A linear trend passing above the origin is consistent with the sources of noise in a tunable laser source and how they interact with the effective gain of the FBG slope. In a tunable laser source, there are fluctuations in both output power (intensity noise) and laser frequency (frequency noise). The noise ΔP_{Noise} from a tunable laser source conveyed to a photodetector can be considered a summation of the intensity noise ΔP_I and frequency noise ΔP_f :

$$\Delta P_{Noise} = \Delta P_I + \Delta P_f \tag{7.8}$$

where the noise may be considered as the change in power from P_0, the DC component of the FBG half-maximum power value, i.e. $\Delta P_{Noise} = P_{Noise} - P_0$. (Fluctuations in laser frequency are inherently associated with wavelength λ_f fluctuations through the frequency-wavelength relation $\lambda = c / f$.) Through equation (7.4), wavelength is related to power through the FBG slope m:

$$\Delta P_f = m\Delta\lambda_f \tag{7.9}$$

Since the FBG reflects a portion of the laser power to the photodetector, the FBG slope m is directly proportional to the laser output power P_{Out}:

$$m = m_0 P_{Out} \tag{7.10}$$

where m_0 is a constant that reflects the bandwidth of the specific FBG and the power losses in the circulator and optical fibers. Substituting (7.9) and (7.10) into (7.8) yields

$$\Delta P_{Noise} = P_{Out} m_0 \Delta\lambda_f + \Delta P_I \tag{7.11}$$

where and $\Delta\lambda_f$, and ΔP_I are optical system parameters. From equation (7.11), the noise in units of power conveyed to the photodetector is related to the power output via a straight line passing above the origin.

Since equations (7.5) and (7.6) state that optical power is proportional to voltage, the noise in units of voltage conveyed to the oscilloscope takes form of a line $y = mx + b$ as supported experimentally by Figure 7.4.

The linearity of noise with power output supports two observations. First, it indicates that increasing the FBG slope (such as using a pi-FBG) will not provide

significant enhancements in signal to noise ratio. Benefits of increasing FBG slope only occur until the frequency noise becomes large when compared to the intensity noise. After that, the FBG slope will amplify the noise by the same factor it amplifies the signal, to no benefit. The use of a balanced photodetector to compensate for frequency noise may mitigate this problem (Wu & Okabe, 2012), but has not been conclusively shown.

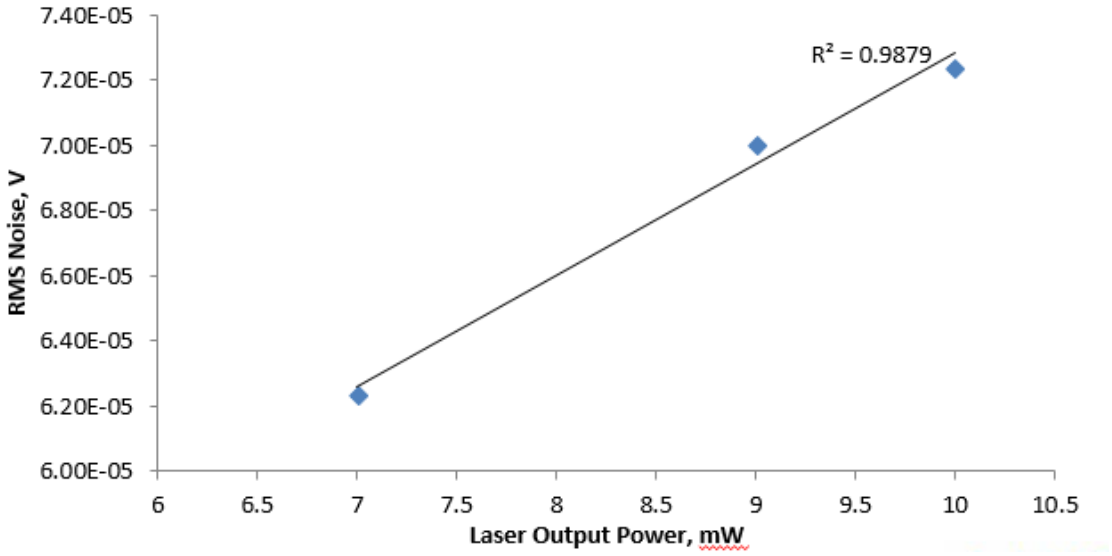

Figure 7.4: Relationship between laser output power and RMS noise

Second, the linearity of noise with power output is an indicator that the noise predominantly comes from the tunable laser source. Since the tunable laser source is essentially a black box system, performance increases cannot be obtained by refinement of the optical system without switching FBG interrogation methods. Norman (Norman and Davis 2011) also noted that the tunable laser source was likely the primary contributor to noise in an intensity demodulation approach.

The supposition that the tunable laser source was the primary contributor to noise was independently validated by testing the performance of a second tunable laser source (Keysight N7714A) available in our lab. A single FBG was used under equivalent

mechanical excitation. The signal-to-noise ratio was calculated using the Luna 1400 and Keysight N7714A laser sources in an otherwise equivalent equipment setup (Figure 7.5). (The details of the FBG excitation are not relevant and omitted for clarity, since it involves a mechanical sensor configuration developed in Chapter 10.)

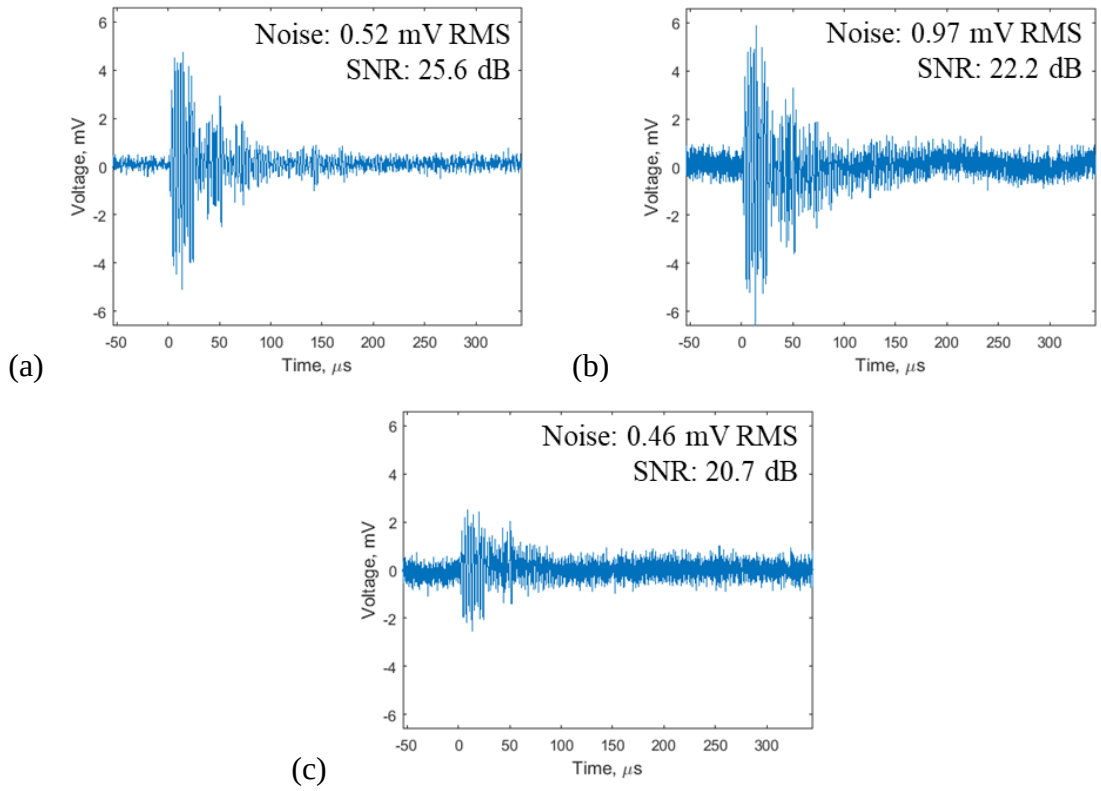

Figure 7.5: (a) FBG response via Luna Phoenix 1400 laser with 10 mW output power, and (b,c) FBG response via Keysight N7714A laser with 10 mW and 4 mW output power, respectively

The Luna Phoenix 1400 output power was set to 10 mW; the Keysight N7744A output power was set to 10 mW and 4 mW for two separate measurements. The SNR was determined using the equation

$$SNR = 20\log_{10}\frac{V_{Signal}}{V_{Noise}} \tag{7.12}$$

where V_{Signal} is the peak-to-peak signal voltage and V_{Noise} is the RMS noise from the pre-trigger region of the signal. A 3.4 dB drop in SNR can be seen from the Keysight N7714A response. Since a change in SNR was obtained by swapping out components, it can be concluded that the tunable laser source is the primary contributor to noise. Lowering Keysight laser output power decreased noise levels, but not proportionally, just as for the Luna laser. However, the signal decreased proportionally. This can be observed as a drop in SNR between the 10 mW and 4 mW excitation as seen in Figure 7.5b and Figure 7.5c.

7.3 Experimental Assessment of the Ring Sensor – Free Conditions

7.3.1 Motivation of Free Ring Sensor Testing

Before assessing the ring sensor response to Lamb waves, the 100 kHz ring sensor was first characterized under free boundary conditions (unbonded). This had the advantage that it limited the number of confounding factors which may come from plate bonding such as bonding effects, changing boundary conditions, and directional dependence. It also allowed for a direct comparison with the simple harmonic models of the free ring

sensor. There were several goals of the free ring sensor analysis which are explored in this section:

- Detecting the ring sensor motion via a bonded FBG
- Evaluating the ring sensor frequency response via PWAS and FBG
- Investigation into resonance effects of the ring sensor

7.3.2 Experimental Investigation of the Frequency Response

To assess the response of a ring sensor under free conditions, as well as its ability to excite bonded sensing elements, a 100 kHz aluminum ring sensor was instrumented with PWAS and FBG. The PWAS were bonded flush with its top and bottom flat surfaces. A

"wrap-around" electrode type PWAS was used, where the negative electrode wraps from the bottom to the top of the PWAS for soldering of both electrical connections to the same PWAS face.

(a)

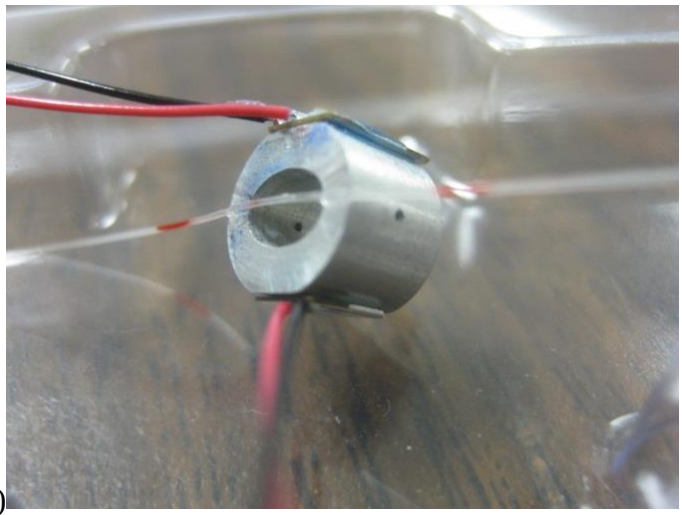

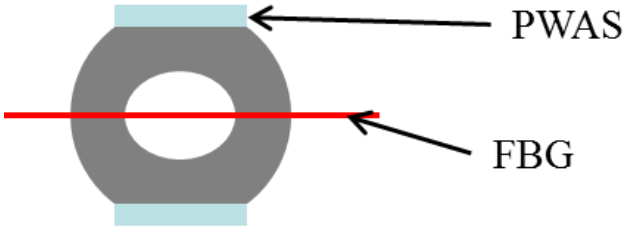

(b)

Figure 7.6: 100 kHz ring sensor outfitted with PWAS on top and bottom and a side-bonded FBG

To forego the difficulty in bonding technique by threading the FBG through the central hole, a 10 mm FBG was bonded to the side of the ring parallel to the 250 μm hole (Figure 7.6). The FBG was 2 mm longer than the ring sensor, although this did not appear to negatively affects its performance, possibly due to the apodized ends of the grating (no distortions of the FBG spectrum were observed, as would be associated with a non-uniform strain). An M-Bond 200 cyanoacrylate general purpose strain gauge adhesive from Vishay

Precision Group (www.vpgsensors.com) was used for bonding; this had shown good bonding characteristics, longevity, and durability in previous studies (Giurgiutiu 2014).

Two types of experiments were performed: EMIS and linear chirp. Using the EMIS method, the electromechanical impedance of a PWAS bonded to the ring was used to detect the structural resonances. This was done for each of the two PWAS, as seen in Figure 7.7.

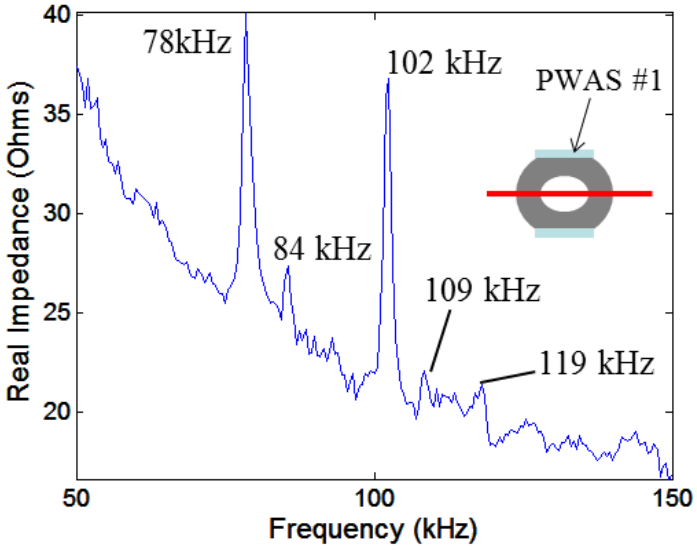

(a)

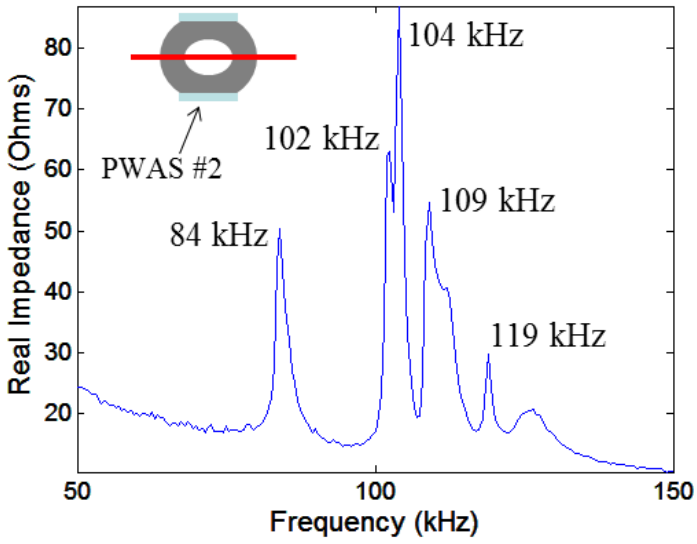

(b)

Figure 7.7: (a) EMIS response of PWAS #1 showing dominant resonances about 100 kHz, and (b) EMIS response of PWAS #2 showing a clearer signal with similar peaks compared to PWAS #1

Both PWAS #1 and #2 had peaks in the EMIS spectrum at 84, 102, 109, and 119 kHz. PWAS #1 had an additional peak at 78 kHz, and registered much more noise compared to the smooth response of PWAS #2. The additional peak may be due to geometric asymmetry. The noise is likely due to bond quality, as in practice it was difficult to bond the PWAS to the small flat surface of the ring sensor.

The chirp experiments were performed by exciting PWAS #2 with a linear chirp function and sensing the response with the FBG. The linear chirp function is given by

$$x(t) = A\cos(2\pi f(t)t)$$
$$f(t) = \frac{f_1 - f_0}{2T}t + f_0 \tag{7.13}$$

where A represents the voltage, T represents the time duration of the chirp signal, f_0 is the initial frequency, and f_1 is the final frequency. For this experiment, a 100 ms, 50-150 kHz linear chirp was excited.

The response of the FBG and its FFT is shown is Figure 7.8. The same 102, 109, and 119 kHz resonances are present just as in the EMIS results. However, several resonance modes determined in the EMIS are not seen in the chirp results. This is interpreted as the FBG not being excited by those modes. Nonetheless, as several resonances were distinctly sensed by the FBG, this shows the ring sensor was sufficient to excite the fiber. The multi-modal result is somewhat interesting, in that there was only one breathing-type mode predicted in this frequency range. This indicates that other types of motion were exciting the FBG too; thus, the ring sensor concept is not necessarily limited to the single breathing-type mode, but other modes may be exploited as well. There is a drawback that separate modes may respond differently to distinct guided wave modes; this

must be counterbalanced by the benefit of a larger sensor frequency range obtained by localization of a large number of modes in a given frequency range.

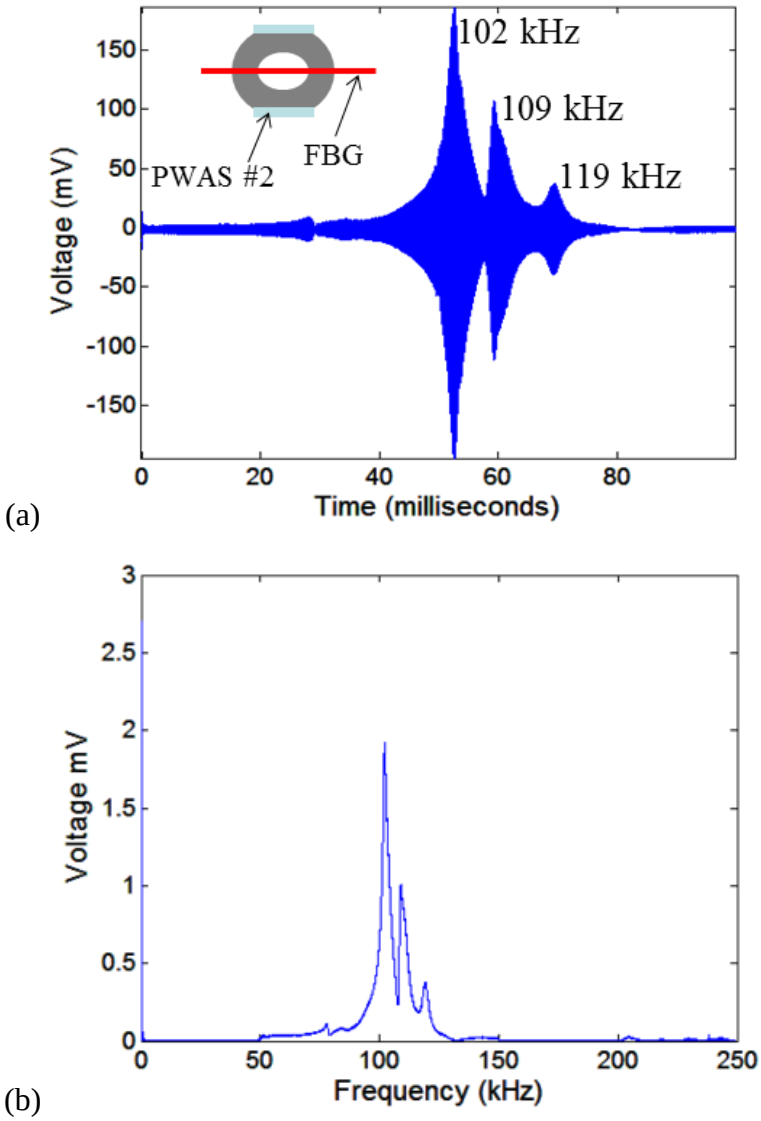

Figure 7.8: Chirp response of the ring sensor in (a) time domain and (b) frequency domain

7.3.3 Experimental Investigation of Ring Sensor Resonance

A pitch-catch experiment was performed across the free ring sensor. PWAS #2 was excited by a Hanning windowed tone burst, given by the equation

$$F(t) = \frac{1}{2}(1 - \cos(2\pi ft / N_b)) * \sin(2\pi ft) \tag{7.14}$$

where f is the center frequency and N_b is the number of counts. The response was sensed by the side-bonded FBG.

To assess resonance effects of the sensor, a scheme was developed where the number of counts was varied exponentially from 1, 2, 4, etc. to 248 counts (with a few additional data points added in the low-count range). As the number of counts increases for a Hanning windowed tone burst, the time duration of the signal increases, and the spread of its frequency contents about its center frequency narrows (Figure 7.9). (The center frequency shown in the plots was not used in this experiment. It is there to demonstrate the principle behind the experiment). In this manner, the increasing number of counts gradually approached the nature of a continuous harmonic wave. Since a higher number of counts leads to a narrowband excitation, the experiment was highly sensitive to the excitation frequency. The optimal excitation frequency was identified by sweeping with a sinusoidal excitation until a maximal amplitude response was found to within 0.1 kHz. This gave a 102.1 kHz excitation frequency, used with a 20 V_{pp} amplitude.

The results of this experiment can be seen in Figure 7.10. There is a linear range where increasing count number increases the response. Later, the growth flattens out so the signal reaches a constant value near the response to of a pure sinusoidal excitation. A time-domain interpretation of this result is that as the sensor stores more energy, more energy is attenuated through internal damping. With short duration signals, the rate of attenuation is negligible compared to the rate of input energy, giving the linear region. With longer duration signals, the rate of attenuation eventually approaches equilibrium with the rate of input energy, providing the asymptotic behavior.

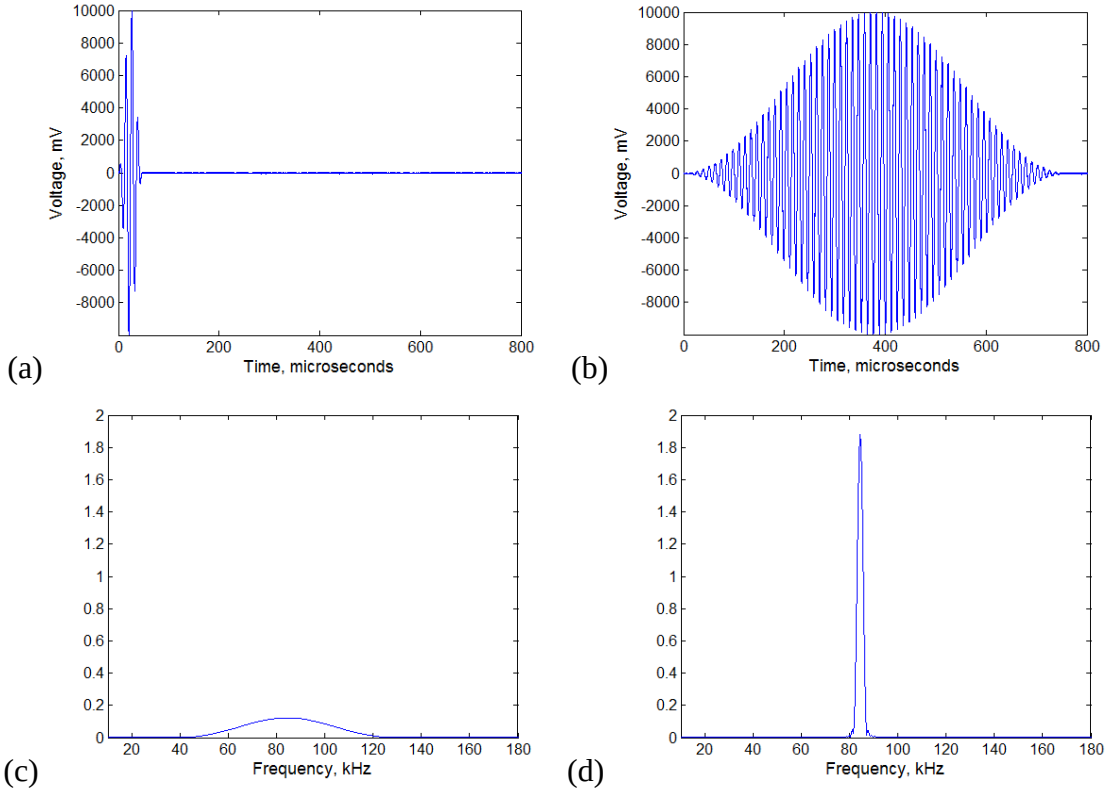

Figure 7.9: (a, c) Time and frequency domain for a three count tone burst, and (b, d) time and frequency domain for a 64-count tone burst

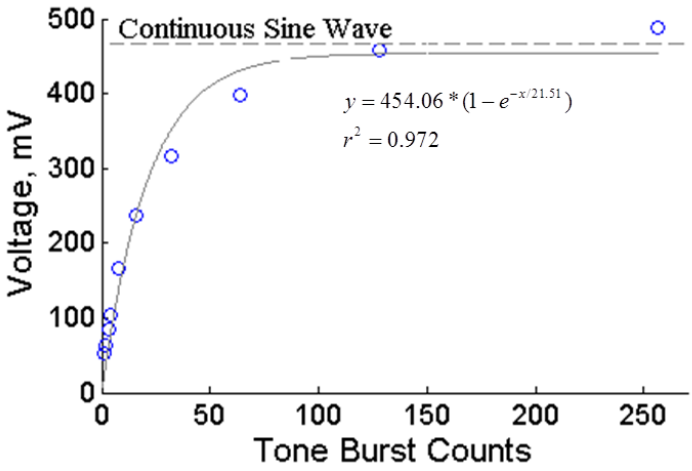

Figure 7.10: Effect of number of tone burst counts on sensor response amplitude

A second frequency-domain interpretation of this result is that the frequency content of the signal needed to fall sufficiently close to the ring sensor's resonance

frequency. As the number of counts increased and the excitation frequency narrowed to the ring sensor's frequency, a higher amplitude was excited due to resonance amplification effects. Likely, both interpretations should be used in tandem to explain the phenomena.

7.4 Experimental Validation of Lamb Wave Detection

7.4.1 Motivation and Overview

The free ring sensor experiments showed the viability of FBG sensing via the ring sensor. This was sufficient for proof of concept of the ring sensor as a resonator. The next stage was to bond the ring sensor to a host surface for a proof of concept as a wave sensor. Several groups of plate-bonded ring sensor experiments were performed to address the following:

- Investigating the bonding effect on sensor resonance
- Sensing PWAS-generated Lamb waves in a pitch-catch configuration
- Sensing waveforms generated by pencil-lead-break (PLB) AE events

7.4.2 Experimental Setup

The ring sensor was tested on a 1200 mm x 900 mm x 1.2 mm aluminum 2024-T3 plate. The aluminum plate was instrumented with the following sensors and receivers (see Figure 7.11 for a photo of the plate):

- A stainless steel 100 kHz ring sensor was bonded approximately at the plate center. This was the same ring sensor used in the free experiments, with PWAS #1 removed and PWAS #2 retained as it had the cleaner response
    - One PWAS with a wrap-around electrode was bonded to the top of the ring
    - One FBG was bonded to the side of the ring at its thickest region, parallel to the major diameter of the ellipse

- One PWAS receiver was bonded to the plate in the immediate proximity of the ring
- One FBG optical receiver was bonded to the plate in the immediate proximity of the ring. The FBG sensor's longitudinal direction was parallel to the axis of the FBG bonded to the ring sensor
- Two PWAS transmitters were placed 150 mm away from the cluster of receivers
    - One PWAS generated guided waves traveling longitudinal to the FBG axis
    - One PWAS generated guided waves traveling transverse to the FBG axis

For the AE experiments, the output signals from the optical equipment were sent to a 40 dB preamplifier, connected to a Micro-II Digital AE System (www.physicalacoustics.com) for data acquisition.

7.4.3 Bonding Effect on Sensor Resonance

To assess the plate-bonding effect on the frequency response of the ring sensor, EMIS and chirp experiments were performed with a plate-bonded ring sensor. The EMIS response, shown in Figure 7.12, was measured using the PWAS bonded to the top of the ring sensor. There are three resonances, at 83, 99, and 119 kHz. Compared to the EMIS of the free ring sensor, the resonances are closer together. But, only three resonances rather than the four seen in the free response. The relative amplitudes had also changed. The chirp experiments, shown in Figure 7.13, used the ring sensor PWAS for excitation. The experiment was performed with the ring sensor bonded to the plate; the chirp excitation was 100 ms in duration, 50 V_{pp}, and 0-200 kHz. The FBG was used as a receiver. The resonances frequencies shifted from 102, 109 and 119 kHz in the free response to 82, 99, and 125 kHz. The relative amplitudes had also changed.

To explain the resonance frequency shift, consider heuristically that for the same structure, a fixed boundary condition will lower resonance frequencies compared to a free boundary condition.

(a)

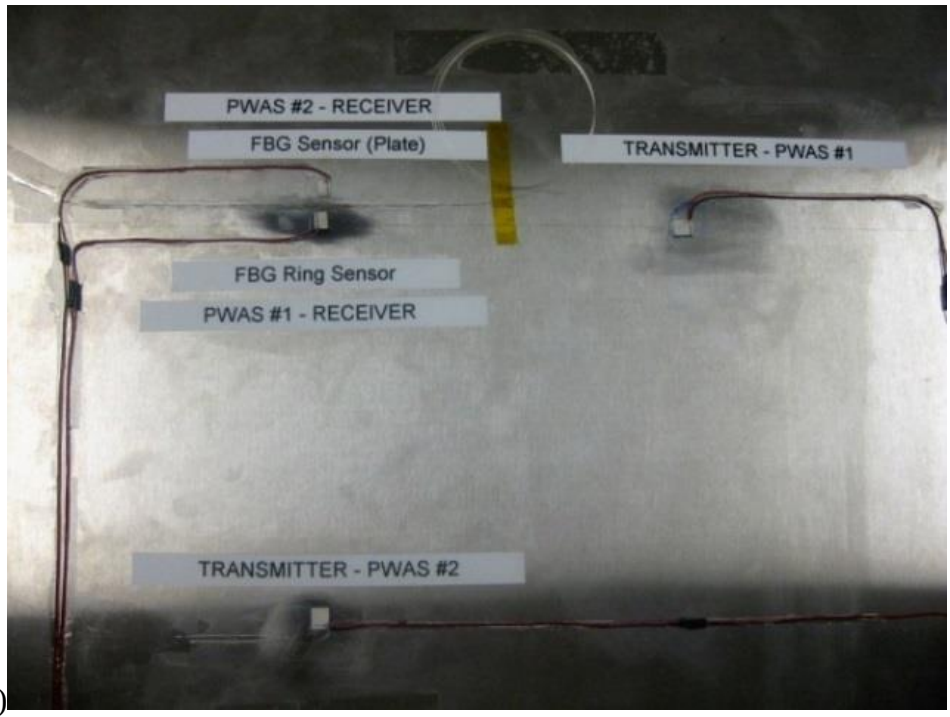

(b)

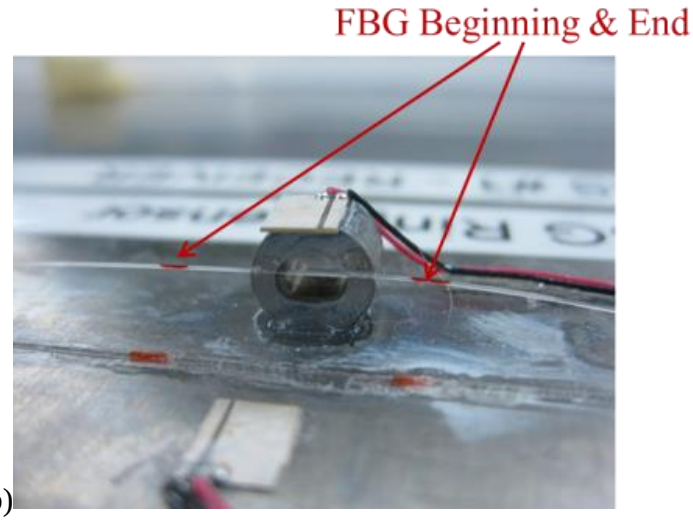

Figure 7.11: Experimental setup for plate-bonded ring sensor testing with longitudinal and transverse PWAS 150 mm away, and a cluster of sensors for testing

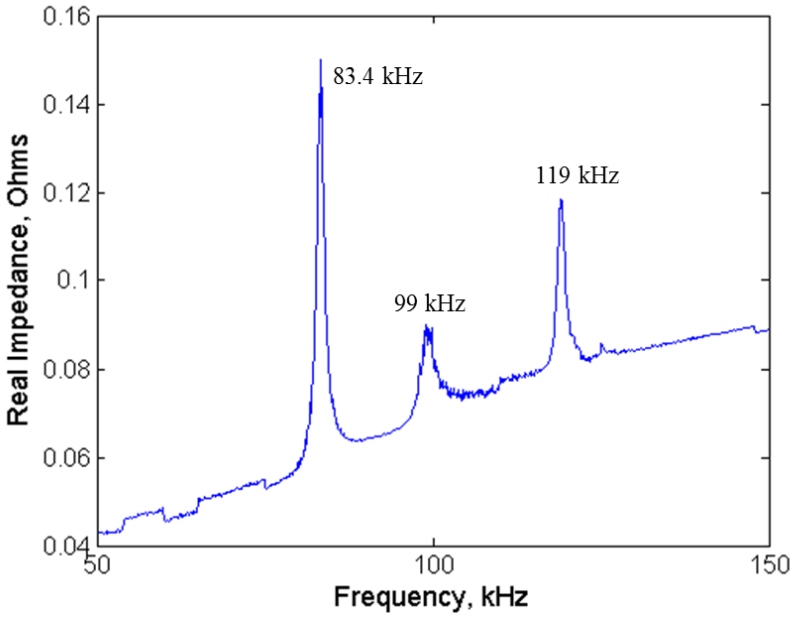

Figure 7.12: EMIS of the stainless steel 100 kHz ring sensor bonded to a 1.2 mm aluminum plate

Plate-bonding adds an elastic boundary condition, which lowers resonance frequencies to a range between the free and fixed boundary conditions. In practice, the resonance frequencies of the plate-bonded boundary condition depend on the properties of both the sensor and the plate (e.g. density, stiffness, thickness) and are difficult to determine a priori.

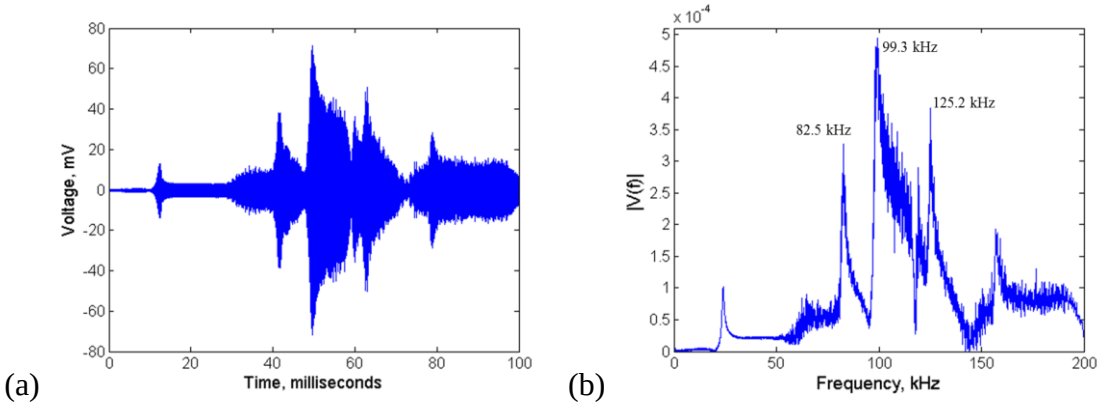

Figure 7.13: Chirp response in (a) time domain, and (b) frequency domain for the plate-bonded stainless steel ring sensor FBG, excited by the ring sensor PWAS

In practice, AE sensors are designed with thick structures in mind which greatly simplifies many such factors, but the results are not directly transferrable to thin plates. Since this research focuses on application to thin plates, sensors are designed herein for free conditions, allowing that mechanics will ultimately depend on the host structure.

Thus, the drop from 102 to 82 kHz and 109 to 99 kHz may be attributed to plate-bonding. However, the increase from 119 to 125 kHz in the plate-bonded response indicates that new modes may be present in the plate-bonded response which were not seen in the free response.

In practice, it is difficult to determine exactly which modes of ring sensor motion are excited. It would be more appropriate to visualize modes LDV (laser Doppler vibrometry). However, the ring sensor proved too small for the LDV0. Instead, an FEM-driven method of assessing individual modes and resonance frequencies was chosen. Given a multi-modal sensor response, plate-bonding introduced complicated changes which may be different from one host structure to the next. Exploring and mitigating this effect is explored further in Chapter 8.

7.4.4 Pitch-Catch Experiments on the Plate

Pitch-catch experiments were performed using, in turn, the longitudinal PWAS and transverse PWAS, both 150 mm away from the collocated sensors. Waveforms were sensed by (a) the PWAS on the plate, (b) the PWAS on the ring sensor, (c) the FBG on the plate, and (d) the FBG on the ring sensor. The S0 and A0 Lamb wave modes were identified using group velocity dispersion curves obtained from the DISPERSE software, matching with the experimentally observed time of flight (Pavlakovic and Lowe 2003).

7.4.5 Tuning Curves

Tuning curves were generated by measuring the amplitude of the received A0 wave packet for various excitation frequencies (see Chapter 4 for further detail on PWAS tuning principles). Here, the tuning principle was extended to assess the response of the FBG on the plate and ring sensor as well. A sweep over a 30-150 kHz frequency range was performed in 3 kHz increments with 20 V_{pp} three-count Hanning windowed tone bursts.

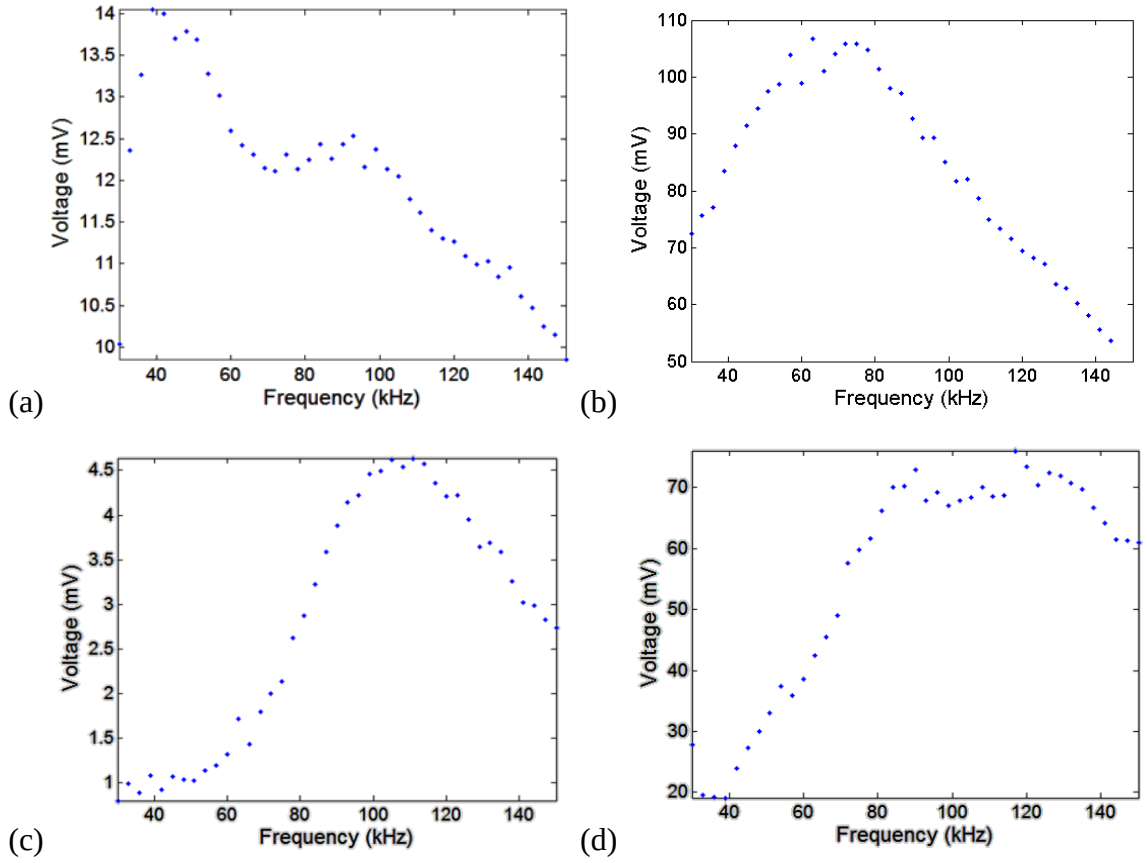

Figure 7.14: A0 Lamb wave mode tuning curve for (a) plate-bonded PWAS, (b) plate-bonded FBG, (c) ring sensor PWAS, and (d) ring sensor FBG

Figure 7.14 shows the tuning curves under longitudinal excitation with the PWAS placed at 150 mm. with the 150 mm longitudinal PWAS. The PWAS bonded to the plate (Figure 7.14a) experienced a maximum tuning at low frequencies (~40 and ~90 kHz) and subsequently decays. This behavior was similar for the FBG bonded to the plate (Figure

7.14b), which experienced a maximum at ~70 kHz and subsequently decays. The behavior of the PWAS and FBG bonded to the ring sensor (Figure 7.14c) showed peaks around the ring sensor's resonance frequencies (roughly in the ~85 – 125 kHz range). The PWAS on the ring sensor had a sharper, clearly defined peak, whereas the FBG signal has a flatter peak spread over a wider frequency range (Figure 7.14d). The explanation is that the FBG is sensing multiple modes, seen by rises and dips in the "flat" range, where the PWAS is responding to only one mode, or otherwise multiple modes collocated in their frequency.

7.4.6 Mode Selectivity of the Ring Sensor

Figure 7.15 shows the response of the co-located FBG sensors, one bonded to the plate (Figure 7.15a) and one bonded to the ring sensor (Figure 7.15b). Both signals showed the A0 Lamb wave packet, but the signal from the plate-bonded FBG also had a strong S0 Lamb wave packet which is almost missing from signal of the ring sensor FBG.

The explanation for this difference is that the FBG bonded to the plate detects the in-plane strain of the plate, whereas the ring sensor detects the out-of-plane motion of the plate. Both the A0 and S0 Lamb wave modes have significant in-plane strain components in the frequency range assessed; hence, both A0 and S0 packets are seen for the FBG bonded to the plate. But, only the A0 mode (which resembles a flexural wave) has

significant out-of-plane motion whereas the S0 mode (which resembles an axial wave) has little out-of-plane motion. To put this on more quantitative footing, in-plane and out-of-plane displacement magnitude for S0 and A0 Lamb wave modes were calculated using the Lamb wave relations from Chapter 1 (Figure 7.16). In the 100 kHz range, For the S0 Lamb wave mode at 100 kHz, the ratio is approximately 35, indicating predominant in-

plane motion. For the A0 Lamb wave mode at 100 kHz, the ratio is approximately 3.2, indicating the presence of both in-plane and out-of-plane motion.

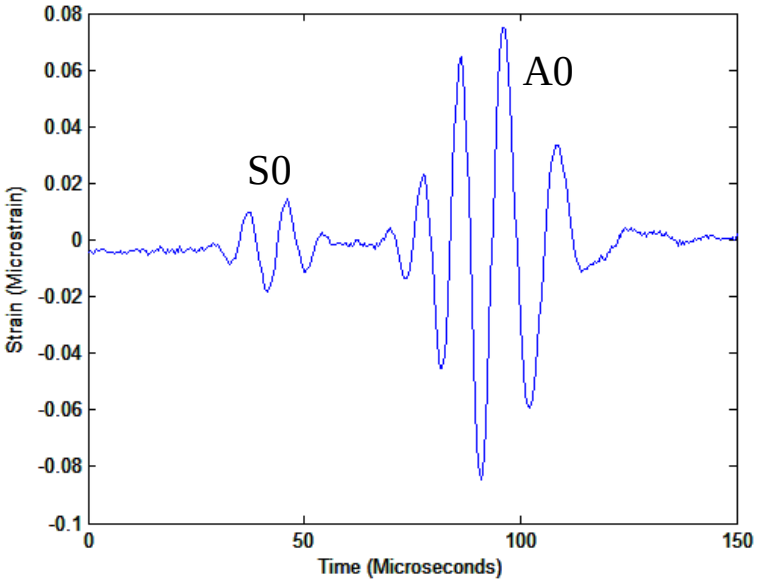

(a)

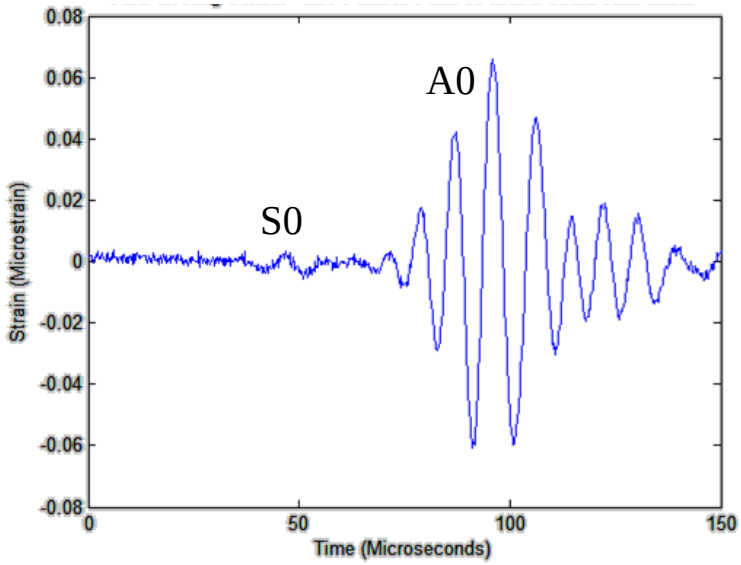

(b)

Figure 7.15: (a) Plate-bonded FBG sensing both S0 and A0 Lamb wave modes, and (b) ring sensor FBG sensing predominantly the A0 Lamb wave mode

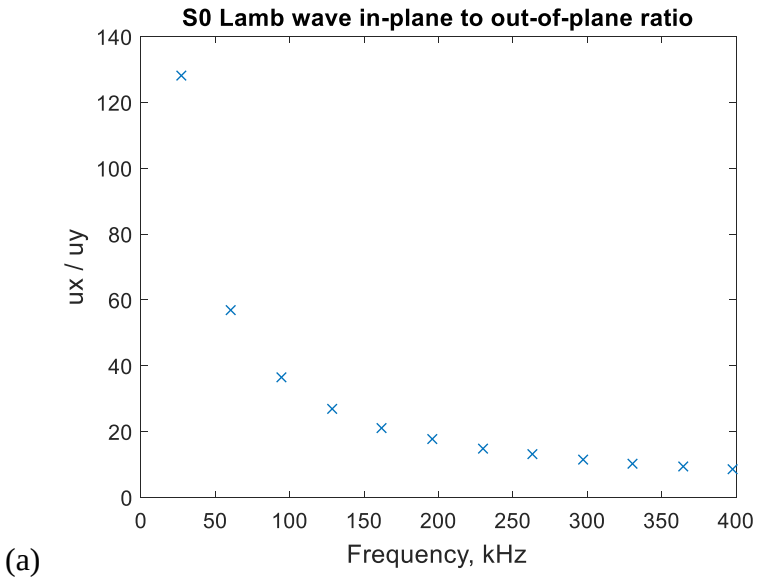

(a)

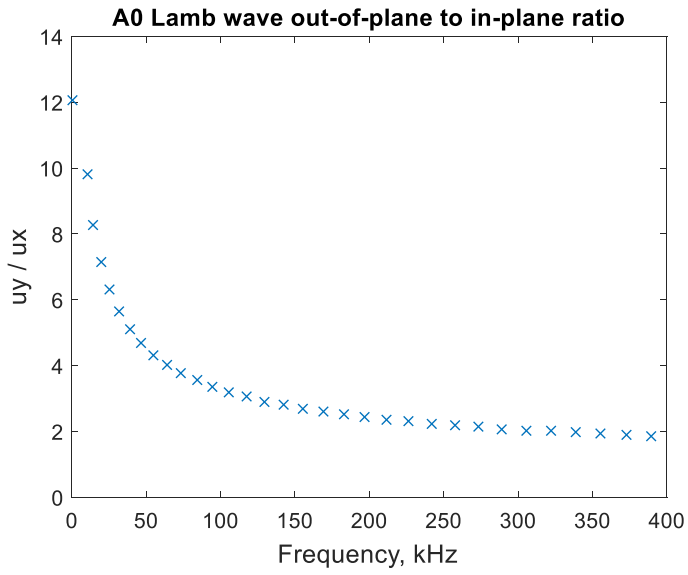

(b)

Figure 7.16: Ratios between in-plane (u_x) and out-of-plane motion (u_y) for S0 and A0 straight-crested Lamb wave modes in a 1 mm aluminum plate

7.4.7 Omnidirectional Sensitivity of the Ring Sensor

Recall that an FBG written into an optical fiber is nominally sensitivity only to the strain along the longitudinal axis of the fiber. If waves travel along a plate at an angle to the fiber, the FBG readings are affected by a trigonometric projection along the axis of the

fiber. FBG readings from a wave traveling transverse to the fiber only occur due to a Poisson effect.

This behavior was tested by measuring the response to 99kHz 20 V_{pp} 3-count Hanning windowed tone bursts excited from two PWAS 150 mm away, one PWAS was longitudinal and one PWAS was transverse to the axes of the FBGs. Figure 7.17 shows the effect of waveform directionality on the sensitivity of the plate-bonded FBG and the ring sensor-bonded FBG.

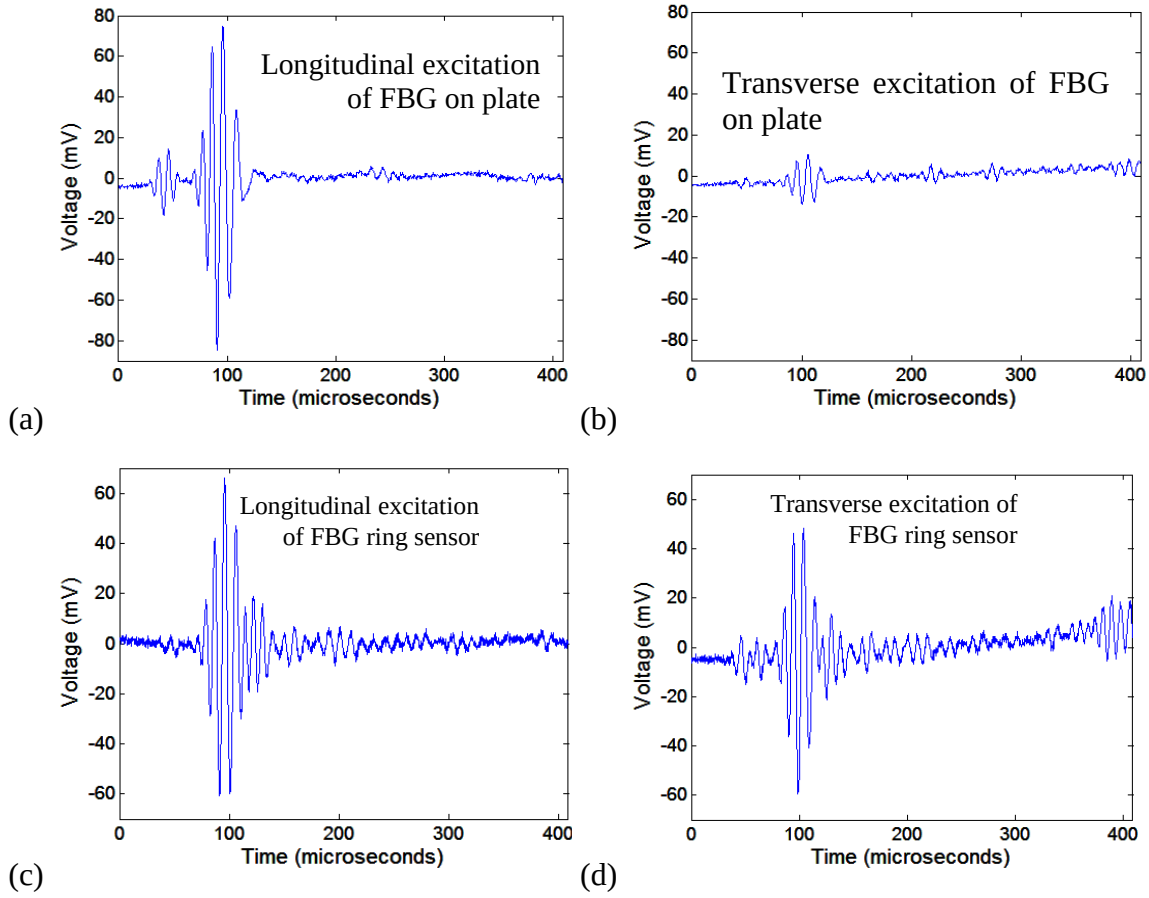

Figure 7.17: Longitudinal and transverse PWAS Hanning window tone burst 99 kHz excitations, sensed by (a,b) plate-bonded FBG, and (c,d) ring sensor FBG

For the plate-bonded FBG, the waveform captured from longitudinal excitation showed a much higher amplitude than the waveform from the transverse excitation. This

is expected, as the FBG sensed only the strain component along its longitudinal axis. In contrast to the plate-bonded FBG, the ring sensor signals in the two perpendicular directions were only slightly different in magnitude. The amplitude decreased slightly in the transverse direction.

7.5 Ring Sensor Response to Pencil Lead Break Excitation

A series of simulated AE tests were performed on the aluminum plate. The AE events were simulated with a 2H-hardness 0.3 mm PLB. The PLBs were applied 100 mm away with a longitudinal transmission path with respect to the axes of the FBGs. The AE waveforms received by the PWAS bonded to the plate and the PWAS on the ring sensor are shown in Figure 7.18.

A clear, high-amplitude signal was received by both the PWAS on the plate and the ring sensor. However, the waveforms were clearly distinct between the two figures. The PWAS bonded to the ring sensor detected a much tighter AE "burst" than the PWAS bonded to the plate. This is advantageous in processing the AE waveform. These differences are clarified by the examination of the frequency domain spectra, where the PWAS on the plate shows a much larger bandwidth and more low-frequency amplitude than the PWAS on the ring sensor. In addition, high-frequency peaks were present for the PWAS on the ring sensor which were not present for the PWAS on the plate. The explanation for this lies in the resonant characteristics of the ring sensor which filtered out the low-frequency part of the excitation.

If the ring sensor can be designed to detect AE events, it could potentially offer advantages in terms of isolation from other noise sources and isolation of the FBG from

quasi-static strain. However, further comparisons are needed, particularly in terms of sensor sensitivity.

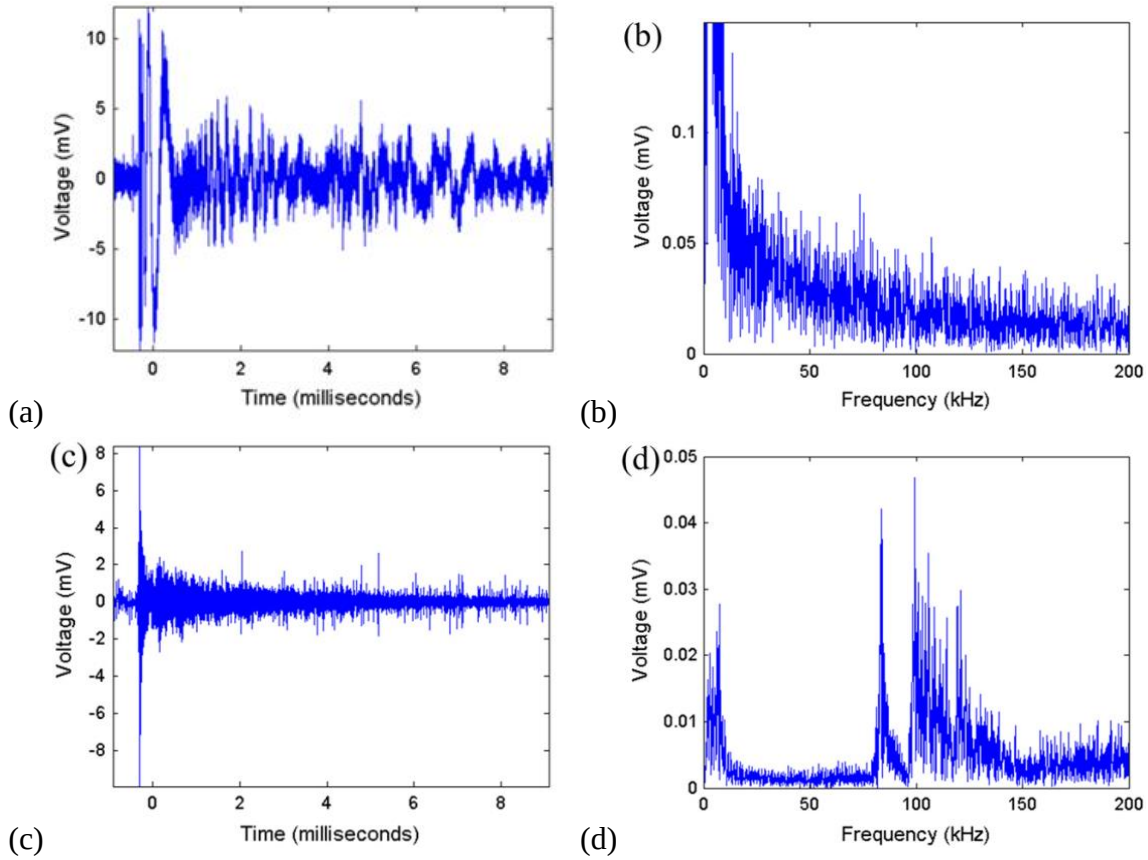

Figure 7.18: 100 mm longitudinal PLB sensed detected by (a,b) PWAS in the time and frequency domain, and (c,d) ring sensor PWAS in the time and frequency domain

7.6 Summary and Conclusions

This chapter has demonstrated that a ring sensor can be used to detect the out of plane motion of a Lamb wave with preference for a frequency as specified by design. An FBG interrogation optical system was calibrated for absolute strain. The largest source of optical system noise was identified as a combination of both frequency noise and intensity noise from the tunable laser source. Both free and plate-bonded testing of the ring sensor was performed. In the free ring sensor experiments, several resonance frequencies were

identified around 100 the kHz design resonance through both chirp and EMIS experiments. Chirp experiments performed with an FBG receiver demonstrated the capability of the ring sensor to operate as a fiber-optic sensor. In plate-bonded sensor experiments, a proof of concept was shown for the ring sensor's use as an ultrasonic sensor, as the ring sensor could detect Lamb waves using both its piezoelectric and fiber-optic sensing elements.

Plate-bonding of the ring sensor demonstrated a complicated change in the resonance frequencies, with new resonance modes appearing and a drop in resonance frequencies. Lamb wave pitch-catch testing of the plate-bonded sensor showed the ring sensor had the following enhancements over that of a plate-bonded FBG:

- Mode selectivity: the S0 Lamb wave mode was rejected and the A0 Lamb wave mode was sensed. This is due to the ring sensor sensitivity to out-of-plane motion much like a typical AE sensor, in contrast to a plate-bonded FBG which is sensitive to in-plane strain.
- Omnidirectionality: the ring sensor was sensitive to motion both longitudinal and transverse to the axis of its FBG. This is highly significant, as typical FBG applications require multiple sensors for omnidirectional sensing. The cause of the ring sensor omnidirectionality is hypothesized as the sensitivity to out-of-plane motion, which is converted to stretching of the FBG through ring sensor resonant "breathing". Regardless of orientation angle, the waves from any direction still imparts an out-of-plane component to the base of ring sensor which is then sensed by the FBG bonded to the ring.
- Frequency Tunability: By designing for a vibrational resonance of 100 kHz, the ring sensor has a maximal amplitude in the 100 kHz range, although it is still able to

sense motion outside this range. In practice, it is not necessary to exclude any frequencies in the ultrasonic range by tuning them out mechanically, as an electrical or digital filter can be used downstream in data acquisition system. Rather, the resonance nature of this sensor provides indications that mechanical amplification effects may be possible with redesign.

PLB-AE testing of the ring sensor showed a tighter burst in the time-domain which can be advantageous for AE data acquisition. In the frequency domain, much of the low-frequency contents of the PLB-AE were filtered out, and a resonant-type response is visible in to the 100 kHz vicinity.

In this chapter, the ring sensor was experimentally characterized. However, due to the small sensor size, it is currently intractable to experimentally measure the sensor vibrational modes. This leaves room for further FEM characterization. Additionally, the sensor has a multi-modal response which has some drawbacks because each mode responds differently upon plate-bonding. These drawbacks must be counterbalanced against the positive sensing characteristics of providing more resonances modes in a frequency range of interest. These modes may reflect the effect of sensor mechanics and placement of the PWAS and FBG on the ring sensor. This is studied further in Chapter 8. It is also apparent from the plate-bonded ring sensor experiments that the ring sensor did not amplify the waves to provide advantages in terms of sensitivity. This will require a redesign, which will be the focus of Chapter 9. Finally, the rejection of low-frequency components in the frequency response is a preliminary indication that the ring sensor may be insensitive to quasi-static strain, which is a key factor for practical implementation. This needs to be

followed up by wave propagation testing on a loaded specimen, which is also performed in Chapter 9.

CHAPTER 8

MODEL-BASED REFINEMENT OF THE RING SENSOR

8.1 MOTIVATION FOR REFINEMENT OF THE RING SENSOR

In Chapter 7, a proof of concept was demonstrated for a ring sensor which could use FBG or PWAS sensing elements. In Lamb wave response experiments, three sensing enhancements were demonstrated over that of a plate-bonded FBG:

- Omnidirectionality: the capability for the ring sensor FBG to sense waves from multiple directions, compared to surface-bonded FBG which sense the wave component only along one axis
- Mode selectivity: the capability to reject in-plane motion and accept out-of-plane motion. This translates into rejecting wave modes that do not have out-of-plane motion and accepting only wave modes with substantial out-of-plane motion
- Frequency tunability: the capability to respond to a selected frequency as specified by design

Although the sensing characteristics of the ring sensor were a positive indicator, there were many obstacles that needed be overcome for practical application:

- The above sensing mechanisms were identified, but not well characterized, hindering optimization and redesign.
- The frequency response was multi-modal, each mode not changing uniformly in amplitude and frequency upon plate-bonding. It was beneficial to be able to

understand, and possibly control factors which contribute to the sensor frequency response.

- The frequency tunability was focused on a single-resonance approach. However, one approach to sensor design is to localize numerous resonance modes in a desired frequency range. The sensor modeling and characterization needed to be expanded to a broader frequency range to complete characterization, as artificial limitation to sensing near 100 kHz did not take full advantage of the sensor's capabilities.
- Mechanical strain amplification via the ring sensor to its FBG sensing element had not been demonstrated. It was helpful to identify the potential for strain amplification at this stage to assess the potential for sensitivity optimization in a redesign.

In this chapter, these shortcomings were addressed by modeling the ring sensor dynamic response and enhancing FBG and PWAS placement. To this end, the three sensing characteristics of frequency tunability, omnidirectionality, and mode selectivity were investigated in FEM. A ring sensor with improved placement of PWAS and FBG was designed and experimentally investigated in both free sensor experiments and plate-bonded experiments. These served as a preliminary step for the ring sensor optimization in Chapter 9. Many of the developments of this chapter have been published in a peer-reviewed journal article (Frankforter, Lin, and Giurgiutiu 2016).

8.2 FEM Modeling for Sensor Characterization

8.2.1 Combined Vibration-Wave Propagation Framework for Sensor Development

A combined vibration-wave propagation modeling approach provided both simplicity in understanding, and precision in predictive power. The wave propagation

modeling demonstrated the nature of the wave-sensor interaction; the vibrational modeling helped explore and understand why the interaction occurred. A few of the advantages of using a vibrational approach to sensor modeling and design were:

- The resonance modes provided a basis for understanding sensor mechanisms.
- Undesired frequency content could be eliminated and desired frequency content could be enhanced by exploiting mode shapes.
- The influence that each ring sensor resonance mode exerts on its sensing elements could be analyzed separately due to mode superposition, simplifying the design process.

The basis for a vibrational approach was derived from modal expansion, where the response of a linearly elastic system is represented as a linear combination of its resonance modes (Giurgiutiu 2014). For a resonant sensor with a single-mode response, eliminating modes under a vibrational model could be simplified to the exploitation of the nodal points and symmetry in the mode shapes. Understanding sensor mechanisms for a single-resonance response simplified to understanding the action of a single resonance mode. However, a vibrational model was not sufficient to capture transient phenomenon such as interaction with a propagating Lamb wave. For the understanding of this latter phenomenon, wave propagation models needed to be added.

8.2.2 Framework for FEM Models

3D FEM modeling was performed using ANSYS Workbench 15.0. All the models considered in this dissertation used 3D elasticity, linear piezoelectricity when applicable, and nonreflective boundaries (NRB) on any lateral edges of a plate. Two types of analyses

were used for vibration (modal analysis and harmonic analysis) and one type of analysis was used for wave propagation (transient analysis). Convergence studies were performed separately for the ring sensor and the plate. For the ring sensor, a sufficient number of quadratic tetrahedral elements were used such that the highest mode shape of interest was accurately represented. For the plate, at least ten quadratic hexahedral elements per wavelength and six elements across the thickness were used.

The generic aluminum alloy material properties from ANSYS Workbench was used for modeling plates and ring sensors, unless otherwise stated. The difference between density and elastic properties in common aluminum grades were minor enough to use the general alloy properties; this allowed the exact grade to be decided in consultation with the university machinists to aid the prototype manufacturing process.

PWAS were represented by coupled-field elements which incorporated the linear piezoelectric equations of Chapter 4. The PWAS polarization axis was specified as the thickness-direction. The bottom face of the PWAS was specified as an electrical ground, with a voltage applied at the top face of the PWAS. The PWAS material properties were modeled as APC-850 (Gresil et al. 2012).

The bonding between the ring sensor and the plate, as well as PWAS on the plate and ring sensor was done by contact/target element pairs. This closely approximated a perfectly bonded condition. The FEM implementation of bonding characteristics is nonlinear and difficult in practice to characterize, and justifies its own investigation well outside the scope of sensor development. Rather, it should be taken as a limitation that viscoelastic effects of the damping layer are intentionally ignored.

Modal analysis represents the system as an eigenvalue problem under the assumption of free harmonic motion. It was used to determine the natural frequencies and mode shapes of a structure. This tool was used for exploration and heuristic design, such as exploiting points of maxima and nodes of the mode shape for sensing element localization.

Harmonic analysis assumes a harmonic forcing function and determines the steady-state response of a structure. Harmonic analysis provided responses for a frequency sweep which allowed for analysis over a frequency band, including points of maximal amplitude.

The transient analysis assumed only linear elasticity (and coupled field piezoelectricity, when appropriate). Thus, the transient analysis directly solved the 3D elasticity equations of motion of a solid medium presented in Chapter 2. These equations under stress free conditions devolve into the Rayleigh-Lamb equations and will numerically solve for Lamb waves if a plate with stress free conditions is set up in the FEM formulation. A numerical solution is necessary to assess the sensor mechanics, although in practice one can use an analytical approach for the wave propagation in the plate, such as in research by Gawronski on transducer design (Gawronski et al. 2017).

8.2.3 Nonreflective Boundaries for Wave Propagation Modeling

The presence of reflections off of free boundaries is a natural component of wave propagation phenomenon. However, there was an impetus to reduce FEM size, as increasing size required increased computational resources. Typically, there is a tradeoff between increasing FEM computational time and accepting the presence of edge reflections which cause complications in post processing and analysis of FEM wave propagation models. One way of eliminating the edge reflections from the signal of interest is to

increase the size of the domain such that no reflections occur within the time window under investigation. However, the computational time of doing so makes this approach expensive or even prohibitive. Another way to avoid edge reflections is to use nonreflective boundaries (NRB) which absorbs edge reflections, allowing a region of a finite domain to be modeled as infinite.

The elimination of edge reflections was done using a modified Lysmer-Kuhlemeyer NRB method developed for Lamb waves; this method absorbs the Lamb waves at plate free edges (Shen and Giurgiutiu 2015). Viscous damping boundaries are placed around lateral boundaries of the plate, top, bottom, and edge-wise with damping coefficients starting small at a distance from the edge and gradually increasing to a desired value at the edge. These viscous boundaries were provided by one-dimensional damping elements (implemented in ANSYS as a 1D spring-damper element with a zero spring stiffness prescribed). The damping elements were attached to a rigid ground for each node within a NRB region. A damping element was provided for each of three principal directions for each node at the border between two elements.

To prevent reflections due to the discontinuity provided by the NRB itself, the NRB must be smoothly increased. To this end, a half Hanning window function was used as described by Shen (Shen and Giurgiutiu 2015). This prescribes the profile of the viscous damping factor as

$$f(x) = \frac{\delta}{2}\left[1 - \cos\left(\frac{\pi x}{n\lambda}\right)\right] \quad , \quad x \in (0, n\lambda) \tag{8.1}$$

The x direction here is a local coordinate, normal to the plate edge. The parameter λ is the longest wavelength under consideration. For the choice of the damping parameter δ, it was

found by Shen and Giurgiutiu (2015) that a value between 0.15 to 0.30 provided acceptable results. At the lateral edges of the plate, $f(x)=1$ was used as suggested by Lymser (1969).

To account for finite element discretization, the damping also depends on element size. Material properties are also considered through density ρ , pressure wave speed c_P , and shear speed wave c_S

$$\begin{aligned} C_N &= \frac{f(x)}{4}(A_1+A_2+A_3+A_4)\rho c_P \\ C_P &= \frac{f(x)}{4}(A_1+A_2+A_3+A_4)\rho c_S \end{aligned} \tag{8.2}$$

The parameters A_i, $i=1,2,3,4$ are the neighboring element facet areas surrounding the boundary node.

It was shown that this NRB method could be used for both transient and harmonic analysis. Each provides an extremely powerful analysis tool. Using an NRB method with a harmonic analysis, a harmonic wave in an infinite domain can be simulated in FEM and a frequency sweep can be performed. This can give a frequency response for a given phenomenon; from a sensor design perspective, a response in a pitch-catch configuration can be modeled across a frequency spectrum. It can also be used to find natural frequencies and determine calibration curves for a plate-bonded sensor, which in practice is otherwise difficult, because without the NRB, a modal or harmonic analysis does not decouple the sensor from the vibrational mode shapes of the plate.

This method was validated in every model in which it was used. Each time this NRB approach was used, the results were only accepted if the maximum displacement at any point at the edge of the plate was less than 1% of the maximum displacement at the

beginning of the NRB region. This precluded taking the assumptions of the NRB approach at face value, and rather required that the application was successful for each model.

8.2.4 FEM Evaluation of Vibrational Modes for Guiding Sensing Element Placement

In a modal analysis of the ring sensor under free boundary conditions, multiple breathing-type resonance modes were present – the first harmonic at 107 kHz, for which the ring was designed, and a second harmonic at 268 kHz (Figure 8.1). Many other modes were identified with distinctly different shapes. There was a "shear"-type and a "torsional"-type mode present near the 107 kHz resonance (Figure 8.2). These mode shapes had nodes along certain lines of symmetry, e.g. at the central hole for the optical fiber and at the top of the ring. This indicated that PWAS and FBG bonded along these lines of symmetry would not detect these resonance mode's contributions to the ring sensor dynamic response.

A harmonic analysis was used to assess the steady-state vibrational response of the ring sensor. Two 1 N harmonic line forces were oriented at either side of one of the flat faces of the ring sensor, out of phase and directed parallel to the longitudinal FBG axis. This was analogous to a pin force model, which approximates the excitation of a PWAS bonded to the top flat surface (Giurgiutiu 2014).

To obtain a metric for frequency response of the FBG longitudinal strain, it was assumed that (a) the FBG responded with uniform strain, and (b) it was compliant enough to not significantly

contribute to the ring sensor's dynamic response. Under these assumptions, the displacements were calculated at each of the ring sensor's holes, and then subtracted as complex numbers to preserve relative phase information. The amplitude of this differential

displacement was normalized by the 8 mm ring diameter to obtain a measure of strain (Figure 8.3a).

(a) 

(b) 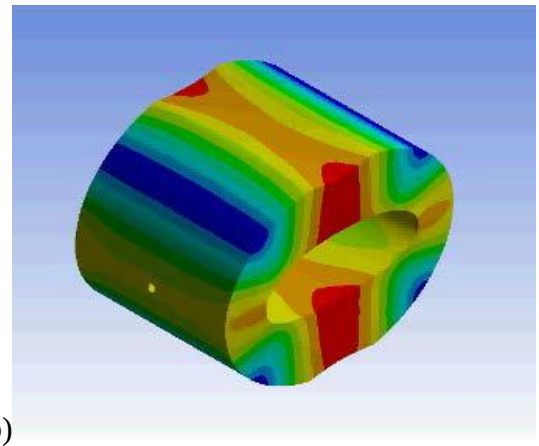

(c) 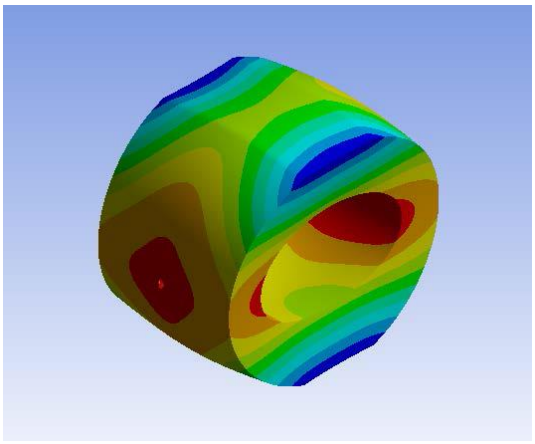

Figure 8.1: (a) 100 kHz ring sensor, (b) fundamental breathing-type resonance nominally at 100 kHz modeled at 107 kHz, and (c) second breathing-type harmonic modeled at 268 kHz

As an approximation, the Von Mises strain was averaged along the top where the PWAS was to be bonded (Figure 8.3b). Both responses, the FBG bonding location (Figure 8.3a) and the PWAS bonding location (Figure 8.3b) show a first peak at 107 kHz and a second peak at 268 kHz. A third peak is observed on the ring sensor top face just above the 268 kHz resonance (Figure 8.3b).

No additional modes were detected proximal to the 100 kHz resonance, compared to the multiple additional modes observed in the proof of concept experiments in Chapter 7.

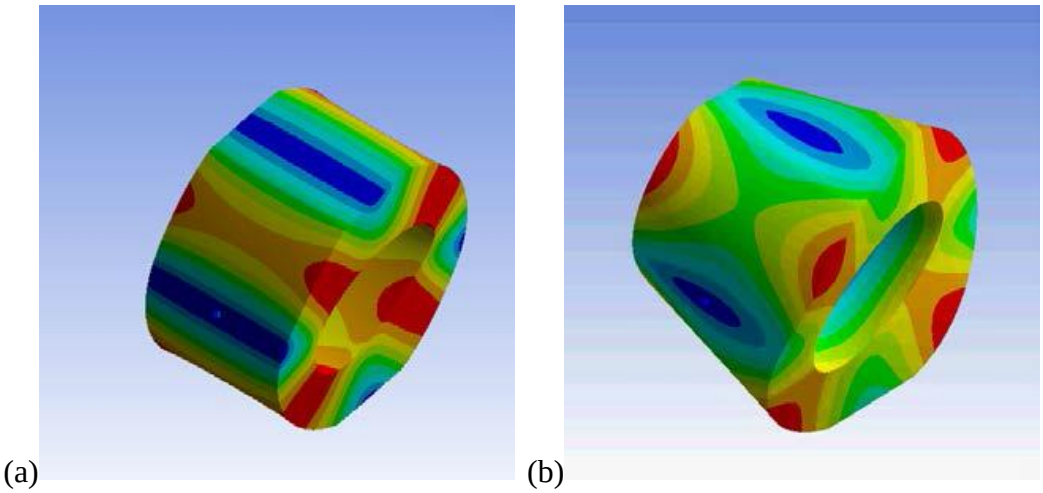

(a) (b)

Figure 8.2: Additional (a) shear-like and (b) torsional-like ring sensor modes near 100 kHz

From this result, it was concluded that bonding of sensors along lines of symmetry could suppress these resonances. This had a potential benefit in terms of consistency of the frequency spectrum, as that the relative amplitude of these modes changed in the proof of concept experiments. By eliminating some of these modes, it was hoped that a more consistent response may be obtained between rebonding and between specimens. The downside of eliminating them is that these modes would otherwise positively contribute to the ring sensor's amplitude. However, from Figure 8.1c, the higher amplitude second harmonic of the fundamental breathing-type mode is a maximum at the FBG hole, counteracting this effect.

To provide a more consistent frequency response, it was decided that the lines of symmetry should be exploited for the bonding of the PWAS and FBG. In the 0-300 kHz

frequency range assessed here, the presence or lack of the modes eliminated by exploitation of symmetry would not change the frequency response in a qualitative way.

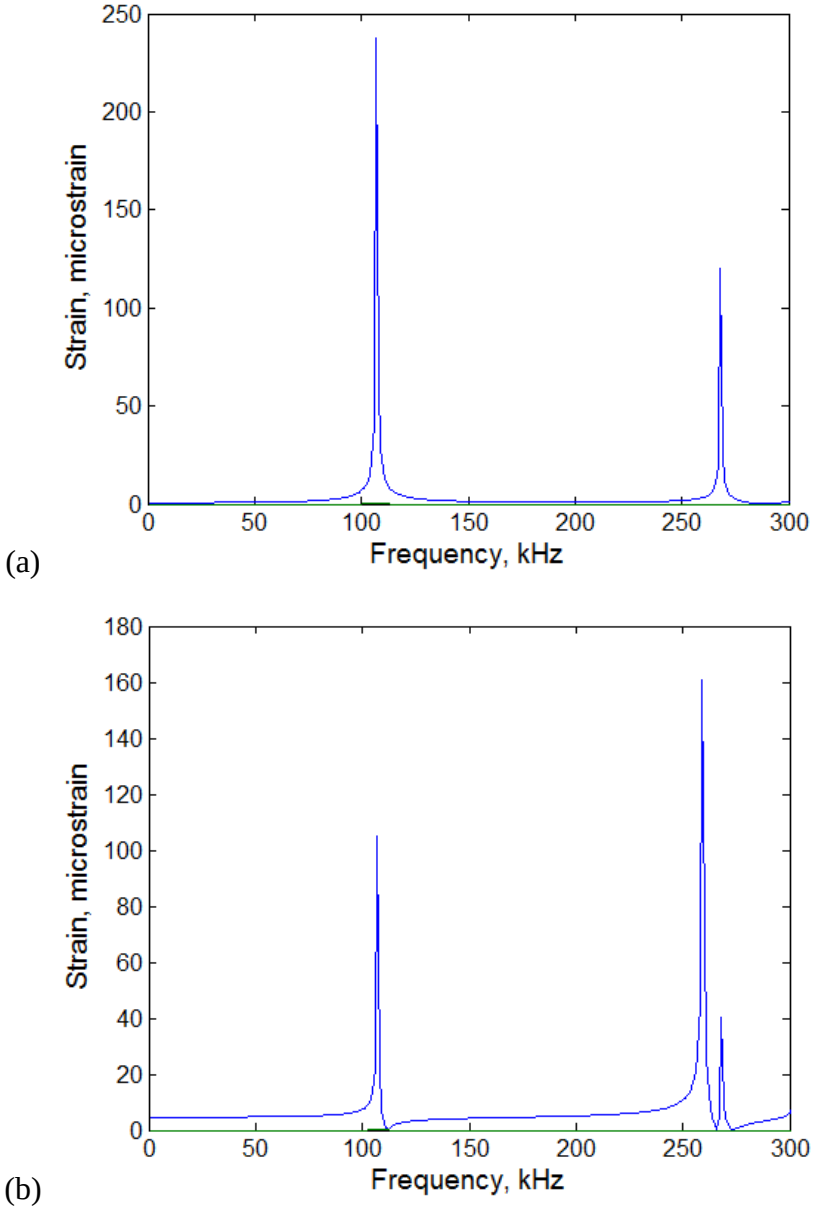

(a)

(b)

Figure 8.3: Harmonic response of the ring sensor to antisymmetric line force excitations via (a) nominal FBG strain calculated via differential displacement of the two ring sensor FBG holes, and (b) Von Mises strain at the top of the ring sensor

This is because the modes which were eliminated were near the fundamental resonance and would only serve to modifying the sensitivity in this range. Comparatively more important, there was still a large gap between approximately 100-268 kHz where a gap would be present in the ring sensor response.

8.2.5 FEM Evaluation of Broadband Ring Sensor Characteristics

To assess the potential for the ring sensor as a broadband ultrasonic sensor, a harmonic analysis was performed over a 0-1000 kHz frequency range. A 1 N out-of-plane harmonic force was distributed along the ring sensor's flat base. The average displacement was calculated on the curved face of the 0.25 mm FBG hole (only the longitudinal component was calculated – along what would be the FBG longitudinal axis). Two models were assessed, one for an aluminum 100 kHz ring sensor (Figure 8.4a), and one for a stainless steel 100 kHz ring sensor (Figure 8.4b).

It is notable that there were peaks at the same resonance frequencies for each sensor. Not only that, but the relative amplitude and shape of each of the peaks were preserved. This was because even though the density and elastic modulus were substantially different between the aluminum and stainless steel, the wave speeds given by $c = \sqrt{E / \rho}$ were nearly the same.

As can be observed in Figure 8.4, there were several closely spaced resonance peaks across the 100-1000 kHz sensing frequency range. The closely spaced nature of the resonance peaks indicated a strong potential for the ring sensor use as a broadband sensor, and needed further experimental confirmation.

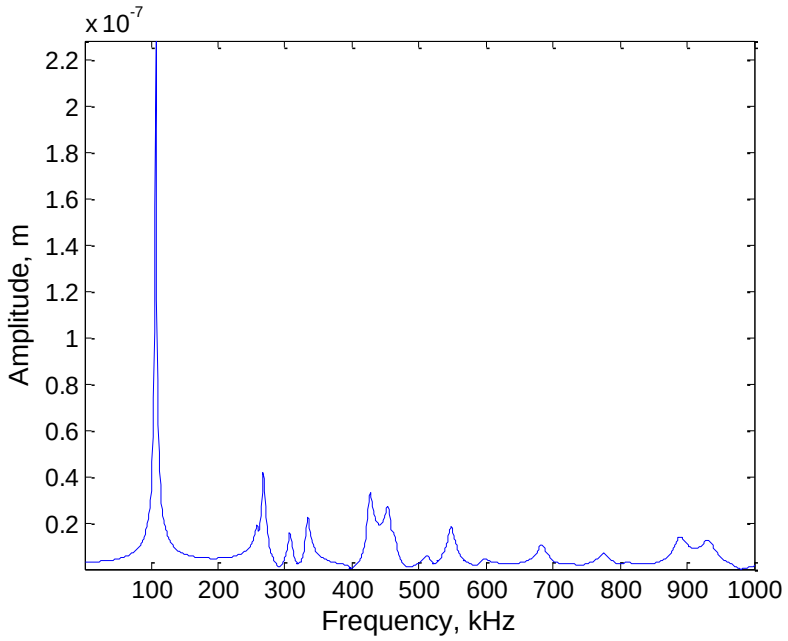

(a)

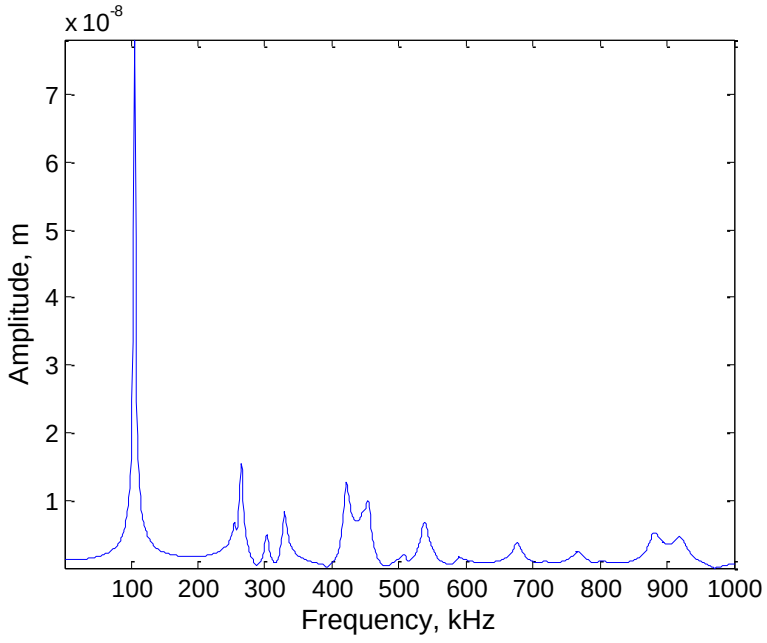

(b)

Figure 8.4: (a) Aluminum and (b) stainless steel broadband frequency response of the 100 kHz aluminum and stainless steel ring sensors

In this context, the utility of the frequency tunability feature of the 100 kHz ring sensor was actually the delineation of the lowest operating frequency just below 100 kHz where the fundamental resonance decayed. It should also be noticed that there were no

low-frequency resonance peaks, which may indicate insensitivity of the FBG to quasi-static strain. There was also a significant gap between 100 and 268 kHz with no resonance present; in this range, the roll off of the nearest two resonances may not merge, and a sharp drop might be seen in that portion of the ring sensor's frequency response.

In these models, no material damping was used. This means that the exact amplitude of frequency peaks, particularly the sharp fundamental frequency, is not entirely accurate; this does not negatively affect the assessment because only the presence and shape of resonance peaks are considered. This would not be affected much by small amounts of material damping. This was noted for the assessments in later chapters where a constant modal damping value was introduced for calculability of resonance peak amplitudes.

8.2.6 FEM Evaluation of Ring Sensor Mode Selectivity

To assess the mode selectivity of the ring sensor, a transient analysis of the ring sensor response to a Lamb wave was performed by modeling a ring sensor bonded to a 1.2 mm-thick aluminum plate. To excite only the S0 or A0 mode, a pair of 1 N peak-to-peak 3-count tone bursts were placed at a pair of top/bottom nodes across the thickness of the plate. These excitations were positioned 10 mm away from the center of the ring sensor base. By applying the excitations in phase, only the S0 wave mode was excited. By applying the excitations 180° out of phase, only the A0 wave mode was excited. The center frequency of the tone burst was lowered to 92 kHz, as the fundamental frequency of the ring sensor was lowered to this frequency due to plate-bonding effects described in Section 8.2.3 (the new ring sensor resonance frequency was found using a harmonic model with

NRBs). At the given frequency-thickness product, no higher order Lamb wave modes were excited in the plate. An NRB was placed on the plate to absorb edge reflections.

Figure 8.5 shows a sequence of events as a Lamb wave travels toward the ring sensor and interacts with it. As see in Figure 8.5a, the S0 mode excited shear-type resonance motion in the ring sensor which exists at a frequency close to that of to the breathing-type mode. The two holes of the ring sensor were almost entirely in-phase and would not substantially excite an FBG stretched across them. A node is also present at the top of the ring sensor such that a PWAS bonded to the top of it would sense no significant strain component.

Also seen in Figure 8.5b, the A0 mode excited both the shear-type motion and breathing-type motion. The component from the breathing-type motion excited the two holes of the ring sensor almost entirely out-of-phase to substantially excite the FBG. Although shear-type motion is present, it may be considered a superposition onto the breathing-type mode and does not substantially affect the response.

8.2.7 FEM evaluation of the potential for ring sensor mechanical amplification

The antisymmetric excitation model from section 8.2.6 was used to assess the ring sensor potential for mechanical amplification. A measure of ring sensor FBG strain in response to an A0 Lamb wave mode was calculated via differential displacement of the two holes in the ring sensor; this was compared to the surface strain at a location collocated with the ring sensor in a plate model that did not have the ring sensor, but was otherwise identical. The component of the surface strain longitudinal to the propagation path was used for comparison so it would reflect the strain observed by a plate-bonded FBG.

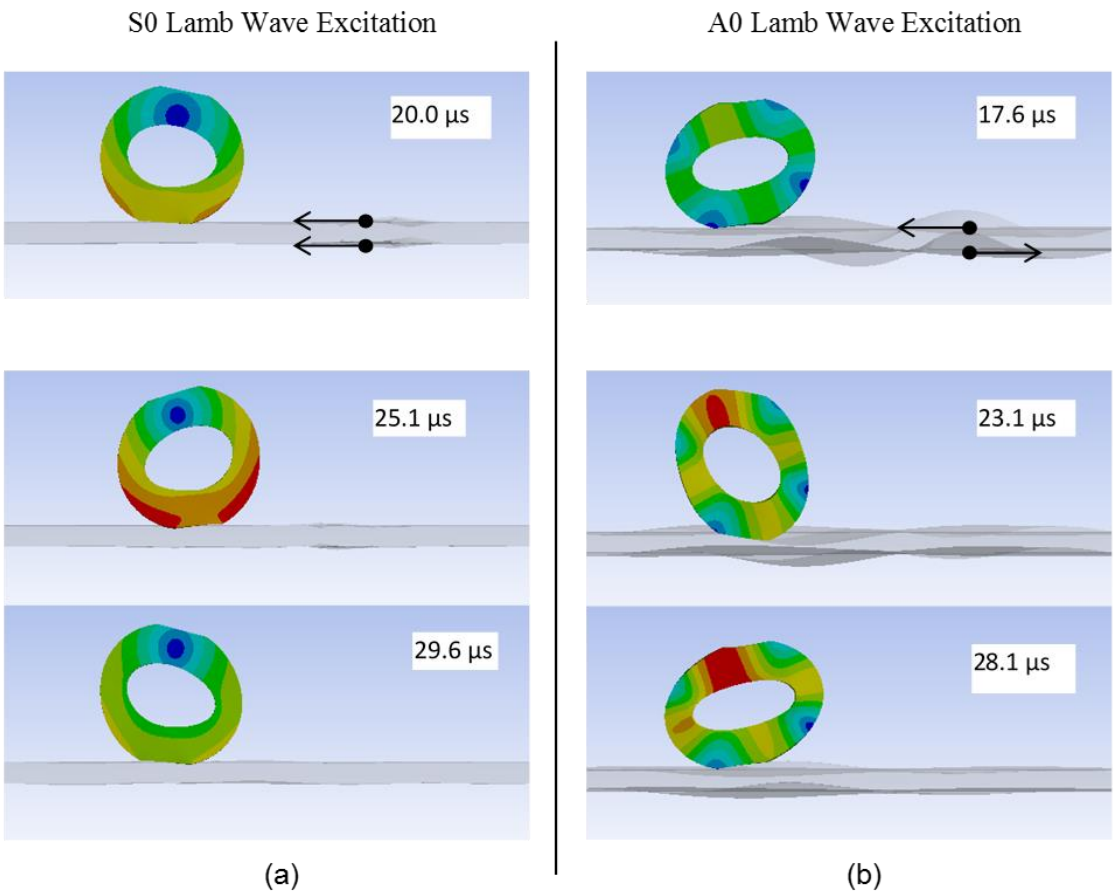

Figure 8.5: Mode selectivity feature of the ring sensor in capturing transient Lamb waves via (a) response to an incident S0 Lamb wave mode, and (b) response to an incident A0 Lamb wave mode

Seen in Figure 8.6, a larger strain was predicted by the FBG on the ring sensor, compared to the strain component available to the FBG on the plate. This result did not necessarily reflect what would be seen in experiment; the viscoelastic effect of the bonding layer is omitted in favor of modeling contact as a perfectly bonded sensor. Rather, it serves as baseline to indicate that theoretically a higher strain could be sensed using this ring sensor.

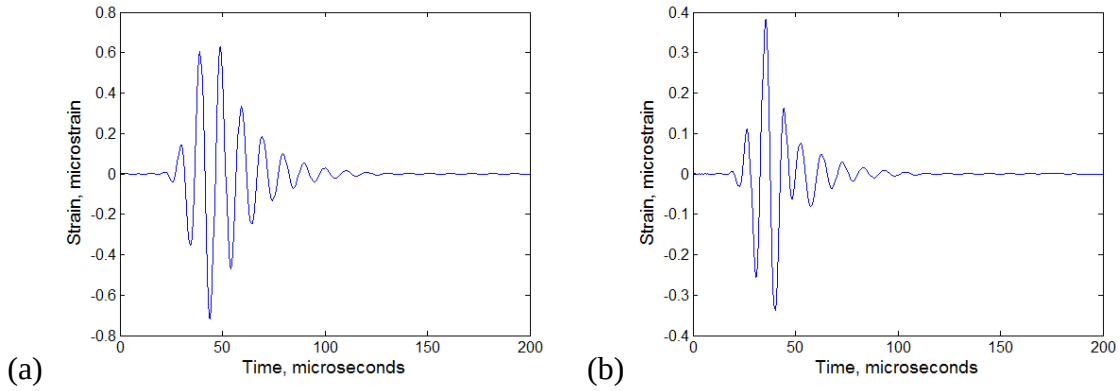

Figure 8.6: (a) Strain of a centrally-bonded FBG on a ring sensor shows a theoretical amplification over (b) longitudinal surface strain detectable by FBG at the same sensing location in a separate plate model

8.2.8 FEM evaluation of the ring sensor omnidirectionality

Assessment of the ring sensor directional response followed the same antisymmetric Lamb wave transient model from section 8.2.6. In each of seven models, the ring sensor was located 10 mm away from the excitation on the A0 Lamb wave mode. The ring sensor was rotated in place from 0° to 90° in 15° increments. The differential displacement between the two holes was used to calculate the strain sensed by the FBG. The predicted variation in maximum strain with incident angle was shown in Figure 8.7. There was a harmonic nature to the variation in amplitude with angle of excitation, shifted upwards by a constant. The mechanism of the ring sensor omnidirectionality was derived from the vibrational model, specifically looking at the base motion of the breathing-type mode. The out-of-plane excitation provided by the A0 Lamb wave mode was not directionally dependent, and therefore the ring sensor responds to it omnidirectionally. The in-plane sensitivity was larger along the FBG longitudinal axis rather than transverse to it. This provided the cosinusoidal-like shape to the motion. A likely explanation for the degree of the directional dependence is the finite transducer aperture effect. Because the sensor base was rectangular, rather than circular, the path length of the incident wave was a

function of orientation angle. Along the ring sensor FBG longitudinal axis, the width of the base is approximately 2.8 mm; along the transverse axis, the depth is 6.0 mm.

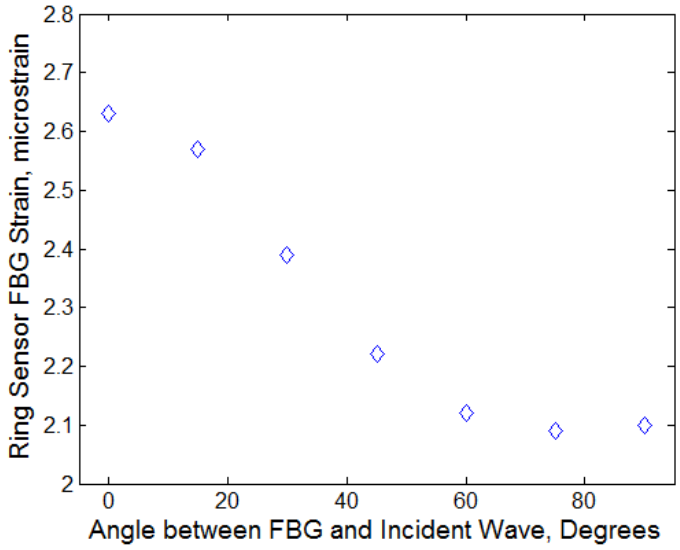

Figure 8.7: Ring sensor directional dependence. The ring sensor shows a cosinusoidal-like directional dependence, shifted upwards by a constant

This could be compared with the wavelength of an A0 Lamb wave mode in an aluminum 2024-T3 plate (Figure 8.8, obtained via the Disperse software phase velocity dispersion curve). If the ring sensor is bonded to a 1 mm plate, the wavelength of the A0 mode is approximately 9.5 mm at 100 kHz. This is significantly larger than the 2.8 mm path, but only slightly longer than the transverse 6.0 mm ring sensor path, which has the potential to cause a drop in amplitude due to the finite transducer aperture effect. The plate used in this study was 1.2 mm-thick instead of 1.0 mm, so the exact A0 mode wavelength was slightly different, but the effects were qualitatively the same.

The longitudinal and transverse components of the directional response were reproducible by experiment. In terms of ultrasonic and AE sensors which commonly measure sensitivity in decibels, the directional dependence of the response had only a 1.9

dB drop. Since response within 3 dB variation is often used to describe a nominally flat frequency response for AE sensors, this level of directional dependence was acceptable.

8.2.9 FEM Evaluation of Plate Thickness Effects

Although plate-bonding effects on the sensor have been observed, there were considerations that the sensor may perform differently for different plate thicknesses. This is particularly of note because calibration methods for AE sensors typically have been limited for Rayleigh waves in thick plates, and are nontransferable to Lamb waves in thin plates. As the frequency-thickness product increased with increasing plate thickness, parameters such as wave velocity, wavelength, and wave mode shape change. Also for thicker plates, a lower sensor response is expected for a given excitation, since the energy is present throughout the thickness and less energy is available at the sensor base.

A full study would require addressing effect of plate thickness on sensor frequency, wavelength, and sensitivity. To limit the complexity, only the effect of plate thickness on sensor sensitivity was assessed. This is not entirely without limitations; for example, the influence of bonded sensor on the plate mechanics is significant for the thinner plates assessed here. As far as wavelength considerations in a 1 mm plate, the A0 mode wavelength is approximately 9.5 mm at 100 kHz (Figure 8.8). This is sufficiently larger than the ring sensor base along the longitudinal axis of the fiber (approximately 2.8 mm). As plate thickness increases, the wavelength decreases such that it is closer to the width of the sensor base. At the wavelength to sensor length ratio decreases, finite transducer effects should become apparent.

Noting these limitations, an FEM study of plate thickness effect on sensitivity was performed using the transient analysis approach from Section 8.2.3. Two symmetric 1 N

3-count Hanning window point forces 10 mm away were used to excite an A0 Lamb wave mode across a plate to the ring sensor.

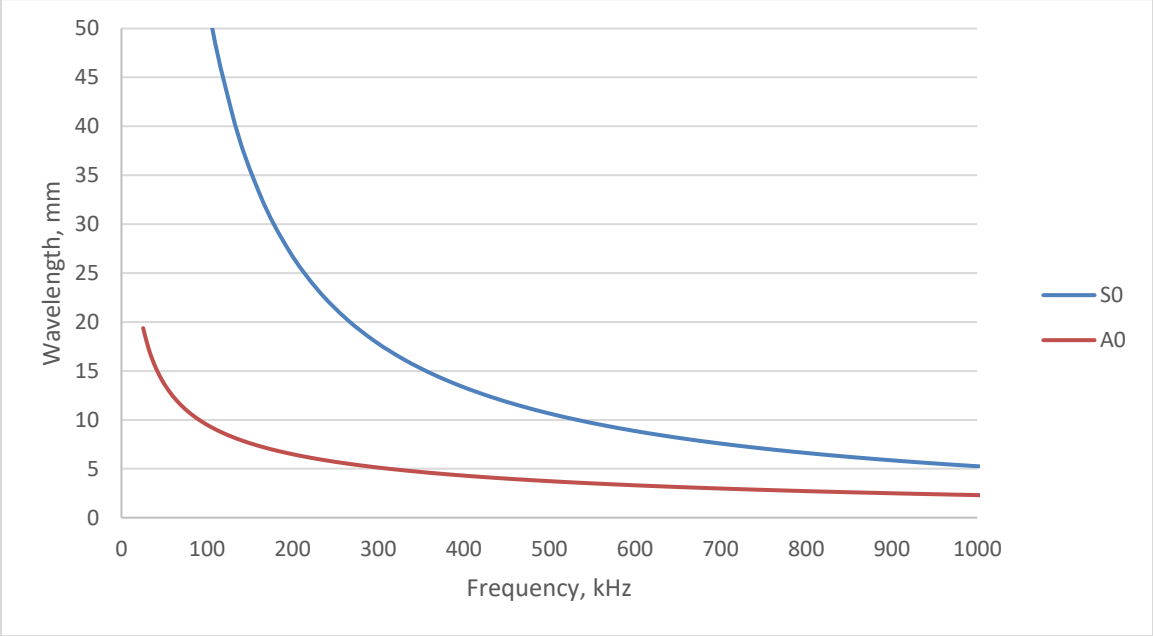

Figure 8.8: Wavelength of S0 and A0 Lamb wave modes for a 1 mm thick Aluminum 2024-T3 Plate

Three plate thicknesses were assessed: 1.2 mm, 3.0 mm, and 5.0 mm. The tone burst center frequency was set at the nominal 100 kHz resonance frequency of the ring sensor to intentionally omit the effect of changing sensor resonance. Since the tone burst had a frequency spread about its center frequency, overlap of the excitation frequency with the sensor resonance was expected.

Table 8.1: Ratio of sensor response to base displacement across plate thicknesses

Plate thickness, mm	Differential displacement between ring sensor holes, nm	Peak-to-peak out-of-plane sensor base displacement, nm	Normalized sensor response: (Differential displacement) / (peak-to-peak base displacement)
1.2	7.60	5.41	1.40
3.0	4.90	3.22	1.52
5.0	3.27	2.21	1.48

The out-of-plane displacement was obtained on a single node on the plate which joined the center of the ring sensor base. The average longitudinal displacement was obtained for the nodes inside both ring sensor FBG holes and, as a simplifying approximation, the maximum/minimum displacement between the two holes was subtracted assuming the two holes were moving completely out-of-phase.

The results, shown in Table 8.1, indicate that for a given excitation, out-of-plane surface displacement input to the ring sensor decreased with increasing plate thickness. However, the ratio between the base displacement and the sensor differential displacement remained nearly constant. It was surprising to get this consistent of a result due to the simplicity of the model and the simplifying assumptions made. Extension of this preliminary study may be useful for transitioning the sensor to different plate thicknesses.

8.2.10 Refinement of Sensing Elements on the Ring Sensor

From Section 8.2.4, it was noted that it is in theory possible to eliminate certain resonance modes to provide a more consistent ring sensor response. The best prospect was to exploit lines of symmetry and nodes of the resonance modes identified in the modal analysis. The FBG placement through the central hole was directly along a line of symmetry for each of these nodes.

It was not as clear that PWAS placement symmetrically across a line of symmetry would be sufficient to eliminate extraneous modes. However, it was possible that placing the PWAS symmetrically about vibrational nodes could be sufficient. To explore this, a coupled field FEM analysis was performed with a PWAS flush to the top of a ring sensor under free boundary conditions.

An FEM harmonic analysis was performed with a 1 V excitation on the top of the PWAS, and the bottom of the PWAS grounded. Using this approach, the effect of the PWAS could be assessed directly in FEM. The frequency response was sensed via differential displacement at the center holes for the FBG. As shown in Figure 8.9a, a single resonance response was obtained via a PWAS bonded flush with the top flat surface. This indicates that this was the ideal configuration for PWAS placement. However, a flush PWAS configuration was used in Chapter 7 and elicited multiple spurious resonance modes under experimental investigation. This was explained by the use of the "wrap-around" PWAS electrode, where the bottom electrode wrapped around to a portion of the top PWAS face. This caused a non-symmetric strain along the ring sensor top surface, which was then able to excite and receive these additional modes.

Following this line of thought, a second coupled field FEM model was developed with a PWAS overhanging by 1 mm, which would also generate a non-symmetric strain. It could also be experimentally validated. As shown in Figure 8.9b, this predicted two spurious modes which would be sensed by a centrally-bonded FBG (again, by subtracting the complex displacement of the two FBG holes, followed by calculating the magnitude).

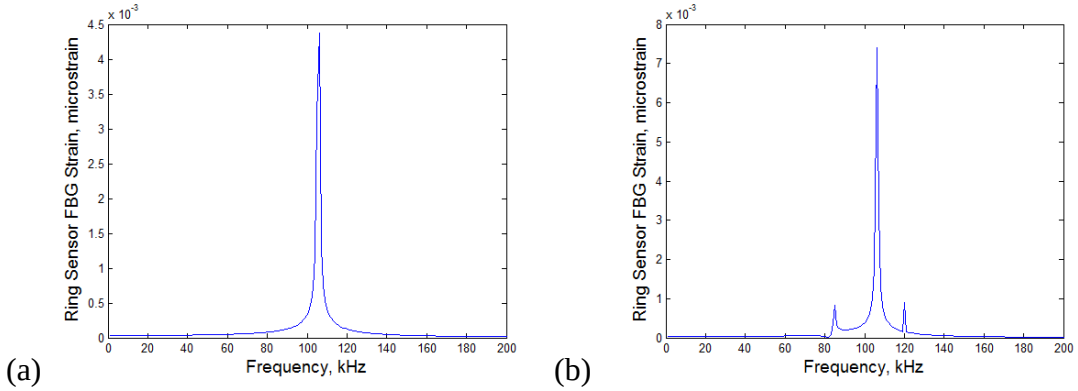

Figure 8.9: FEM simulation of ring sensor frequency response with (a) PWAS flush with the top surface, and (b) PWAS overhanging by 1 mm

8.3 Experimental Studies to Test Sensing Element Improvement

Sensing element configuration was assessed in two experiments by testing different FBG and PWAS configurations. The previous ring sensor configuration, as well as these new ones are shown in Figure 8.10. The same optical equipment used in Chapter 7 was used for these experiments with one exception; the old photodetector was replaced with a new one (New Focus 2053). The photodetector had an adjustable gain and built-in band pass filter which was convenient for this study. The band pass filter was set to 1-1000 kHz, and the gain was set to 30 times.

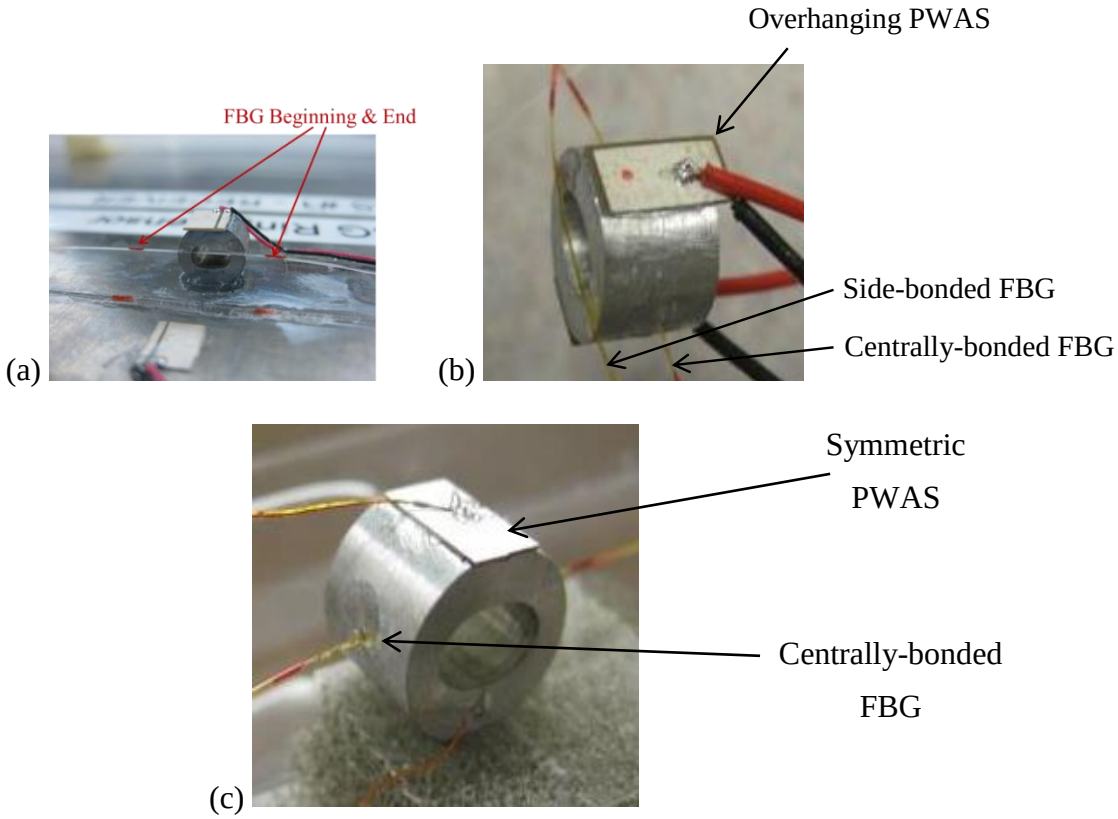

Figure 8.10 (a) Previous ring sensor configuration with a wrap-around electrode and a side-bonded FBG, (b) overhanging PWAS configuration with two FBG locations for comparison, and (c) ring sensor with flush PWAS and top/bottom electrodes flush with PWAS surface

In the first experiment, an FBG was threaded centrally through the holes of a stainless steel ring sensor and then bonded in place (Figure 8.11c). This was compared to an FBG bonded to the side of the ring sensor (Figure 8.11a,b). Two PWAS were bonded to the ring sensor, left overhanging by approximately 1 mm. These PWAS did not have a wrap-around electrode, and instead the PWAS electrodes were flush with their top and bottom faces. A 50 V_{pp} 50-150 kHz linear chirp excitation was performed by one of the PWAS. As seen in Figure 8.11a, the side-bonded FBG sensed multiple modes about 100 kHz. For the centrally-bonded FBG (Figure 8.11b), a single dominant resonance mode was present.

The same chirp experiment was performed over a larger 0-1000 kHz frequency range, transmitted from the overhanging PWAS and received by the centrally-bonded FBG (Figure 8.12). The ring sensor has a second harmonic at approximately 270 kHz with many closely spaced higher harmonics above 270 kHz. This is comparable to the FEM harmonic analysis from Section 8.2.5. This is further indication that the ring sensor may operate in a broadband frequency range.

In a second experiment, a PWAS with top/bottom electrodes was bonded flush with the top flat surface of an aluminum ring sensor. Since the bottom electrode could not be directly wired to a ground, conductive epoxy (CircuitWorks® CW2400) was used to bond a ground wire directly to the ring sensor. An EMIS experiment was performed to assess the interaction of this PWAS with the ring sensor. The response, seen in Figure 8.11c, showed only a single resonance peak.

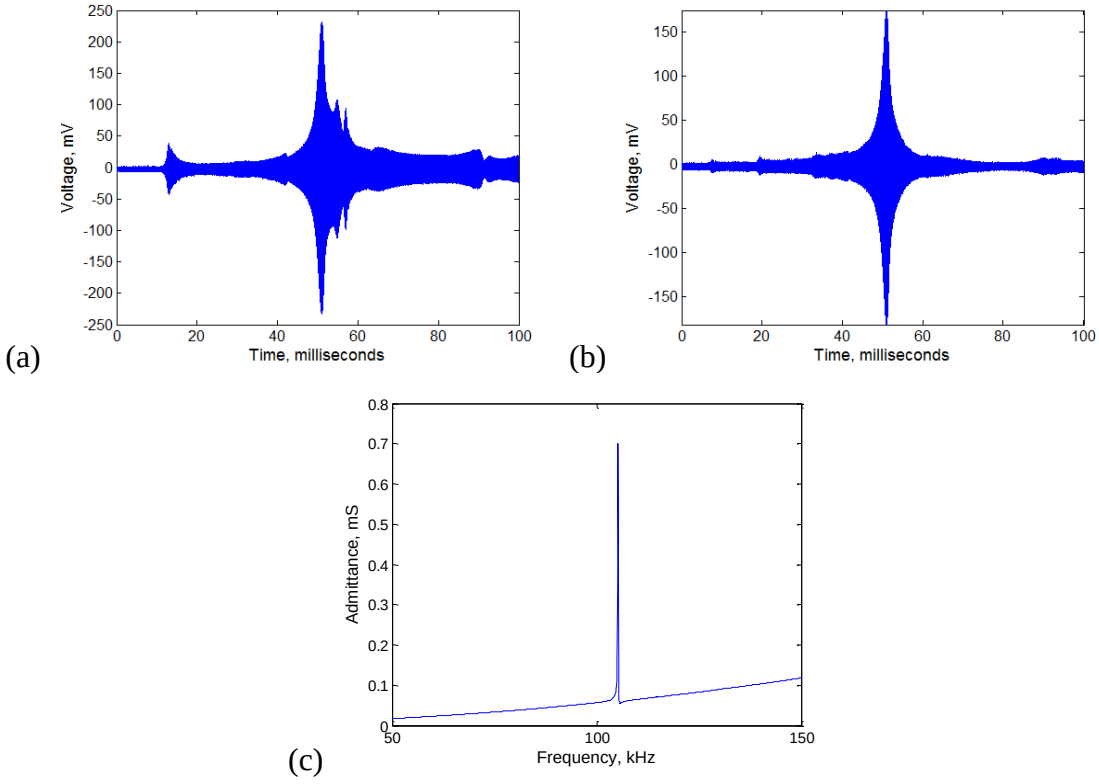

Figure 8.11: (a) Side-bonded FBG 50-150 kHz chirp response, (b) centrally-bonded FBG 50-150 kHz chirp response, and (c) flush top/bottom PWAS EMIS

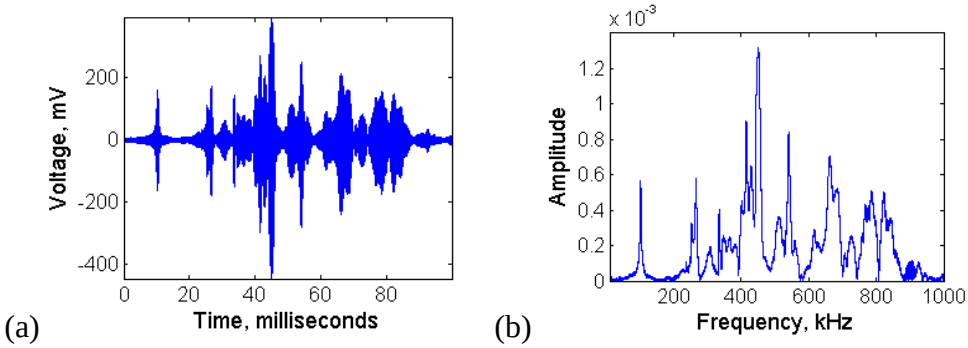

Figure 8.12 Chirp excitation of the 100 kHz aluminum ring sensor across a 0-1000 kHz frequency range, (a) time-domain response, and (b) frequency domain response

From these experiments, we concluded that a centrally bonded FBG was insensitive to the additional resonance modes near 100 kHz, but can still sense the fundamental ~100 kHz resonance. Additionally, a PWAS with flush top/bottom electrodes did not sense or receive spurious modes if it is flush with the top face of the ring sensor. Thus, this

PWAS/FBG sensing element configuration was taken to be the ideal candidate, and this aluminum ring sensor was used for Lamb wave sensing experiments.

8.4 Lamb Wave Experiments with Refined Sensor Configuration

8.4.1 Experimental Setup

The aluminum ring sensor with central FBG and top/bottom electrode PWAS was bonded to the same 1200 mm x 900 mm x 1.2 mm 2024-T3 aluminum plate as used in the Lamb experiments of Chapter 7 (Figure 8.13). The aluminum ring sensor was placed next to the stainless steel ring sensor during this comparison. The same plate-bonded experiments performed in Chapter 7 were performed again:

- Pitch-catch at the ring sensor's resonance frequency from PWAS 150 mm away. Propagation paths both longitudinal and transverse to the FBG axes were tested
- Tuning curves across the 50-150 kHz frequency range with both longitudinal and transverse propagation paths
- PLB-AE from 100 mm away with both longitudinal and transverse propagation paths.

In addition, the response to an impact via a steel ball drop was tested. Resonance amplification of a Lamb wave was also assessed with the same Hanning windows tone burst count variation scheme as Chapter 7; however, in this case it was performed for the plate-bonded aluminum ring sensor rather than a free ring sensor.

For this set of experiments, soft modeling clay was placed around the testing area for wave absorption. In the work of Poddar (Poddar and Giurgiutiu 2015), the use of this clay was capable of completely dampening out edge reflections, even on a significantly thicker 4.86 mm thickness aluminum specimen. The damping of edge reflections prevented

the development of standing modes during long-duration high-count tone burst and sinusoidal excitations. The clay was added to both the front and back sides of the plate, and only one reflection was observed, with a 96% reduction in amplitude compared to the first waveform arrival. This was sufficient to prevent the development of plate vibrational modes.

(a) 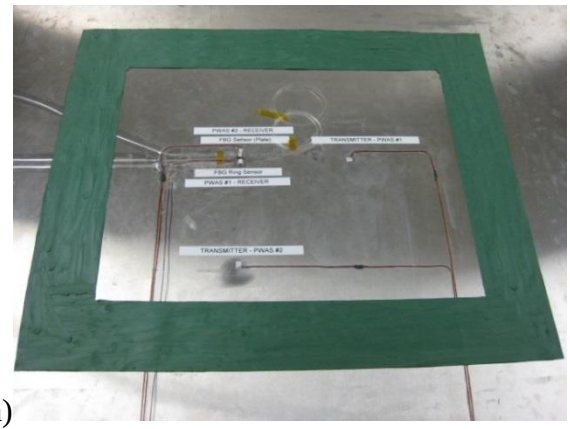 (b) 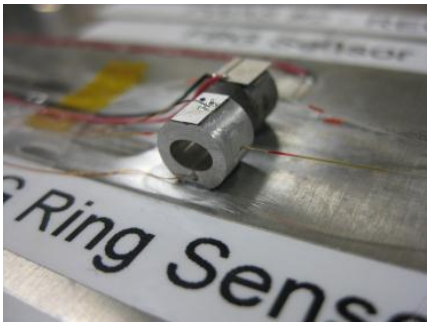

Figure 8.13: Plate used in ring sensor Lamb wave experiments showing (a) testing area surrounded by wave absorbing clay, and (b) close-up of aluminum (front) a stainless steel (back) ring sensors

8.4.2 Tuning Curves and Pitch-Catch Response

To measure tuning curves, a series of 20 V_{pp} 3-count Hanning windowed tone bursts was excited from the longitudinal and transverse 150 mm distance PWAS. Tuning curves for the PWAS on the plate, PWAS on the aluminum ring sensor, and FBG on the aluminum ring sensor are shown in Figure 8.14. The tuning curves were measured for the A0 Lamb wave mode. For amplitude measurements, the envelope was calculated via the magnitude of the signal's Hilbert transform and the maximum value of the envelope was used for each point of the tuning curve. This gave a more accurate response than calculating peak value; using this envelope approach made the amplitude result insensitive to waveform phase variations.

Comparing the tuning curves of the FBG on the ring sensor (Figure 8.14e,f) to the same results in Chapter 7, we note that the current curves are smoother with significantly less signal scatter. This was attributed to the change to the new photodetector which now filters out the low frequency noise below 1 kHz.

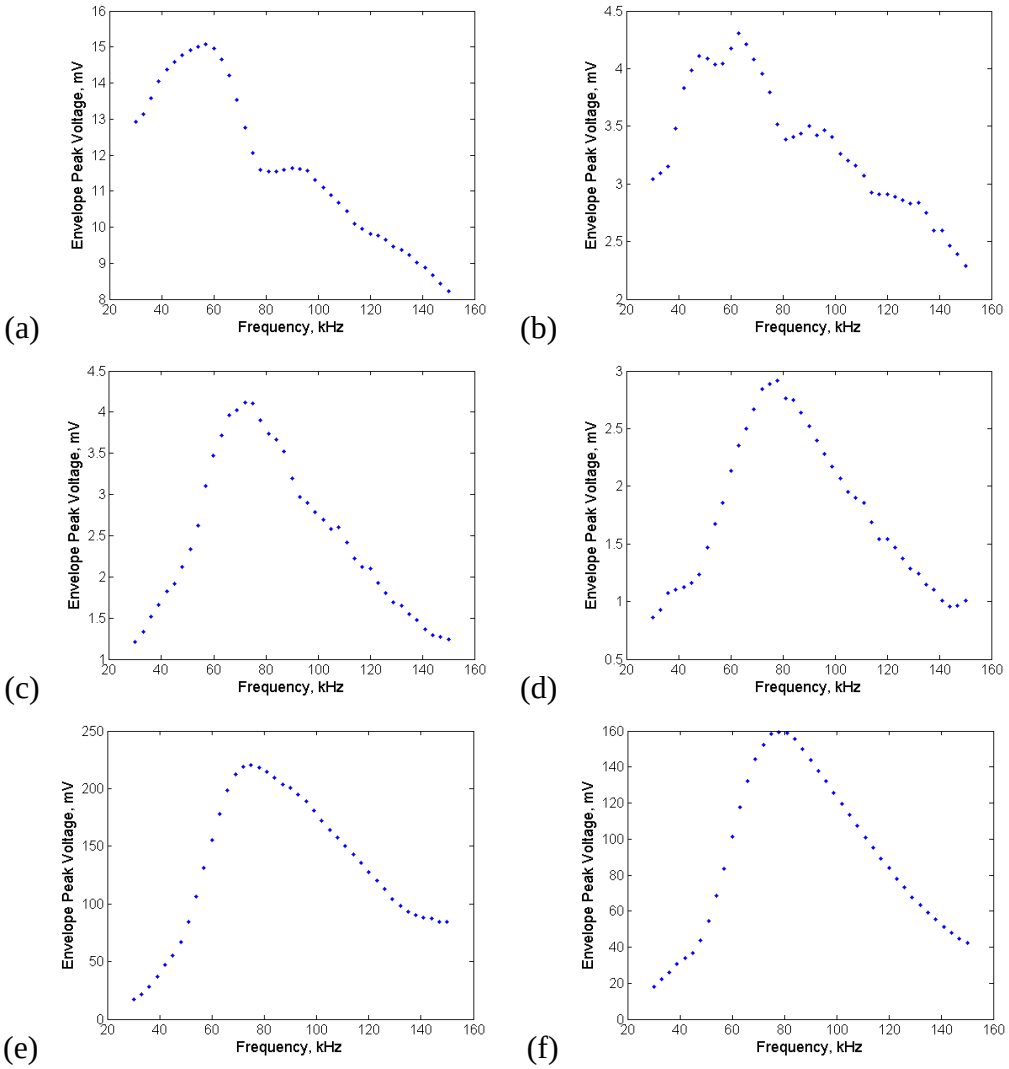

Figure 8.14: A0 mode tuning curves for (a, b) longitudinal and transverse propagation to plate-bonded PWAS, (c, d) longitudinal and transverse propagation to aluminum ring sensor PWAS, and (e, f) Longitudinal and transverse propagation to the aluminum ring sensor FBG

The PWAS on the ring sensor (Figure 8.14c,d) and FBG on the ring sensor (Figure 8.14e,f) had similar shapes in their tuning curves. Contrasting with the multiple resonances

observed on the stainless steel ring sensor with a side-bonded FBG and wrap-around PWAS, described previously, we note that a single peak was observed for the centrally-bonded FBG and flush top/bottom PWAS. This was in line with what was seen from the free ring sensor experiments. By way of comparison, the tuning curves for a plate-bonded PWAS are shown in Figure 8.14a,b.

Interestingly, the resonance frequency of the aluminum ring dropped from approximately 102.5 kHz to 82.1 kHz. This drop was larger than seen for the stainless steel ring sensor. One explanation is that this was caused by the decreased stiffness and density of the aluminum, i.e. a lighter compliant sensor may be more significantly affected by constraint to a plate of a given flexural rigidity and thickness.

The ring sensor FBG tuning curve was not symmetric about its fundamental resonance frequency. Rather, the drop off was shallower in the higher frequency range. This is due to a contribution from the ring sensor's second harmonic.

Individual pitch-catch signals excited at by the longitudinal and transverse PWAS at 75 kHz and sensed by the FBG on the aluminum ring sensor are shown in Figure 8.15c,d. These were compared to the stainless steel ring sensor FBG response excited at 99 kHz (Figure 8.15a,b). The aluminum ring sensor signal was significantly clearer, largely due to the use of the filtering out of low frequency noise below 1 kHz and high frequency noise above 1000 kHz.

8.4.3 Experimental Assessment of the FBG Ring Sensor for Strain Amplification

A resonance scheme was used in Chapter 7 to show that increasing tone burst counts caused the ring sensor response to approach its harmonic response. This experiment was performed here again, this time for a plate-bonded sensor. At first, this experiment was

done without the use of the wave absorbing clay, and no distinguishable trends could be seen. This was due to the presence of a standing wave on the plate, where the sensor response was influenced by its position relative to plate standing modes rather than reflecting the intrinsic sensor response. The addition of soft modeling clay prevented edge reflections sufficient for use of long-duration waves and harmonic waves.

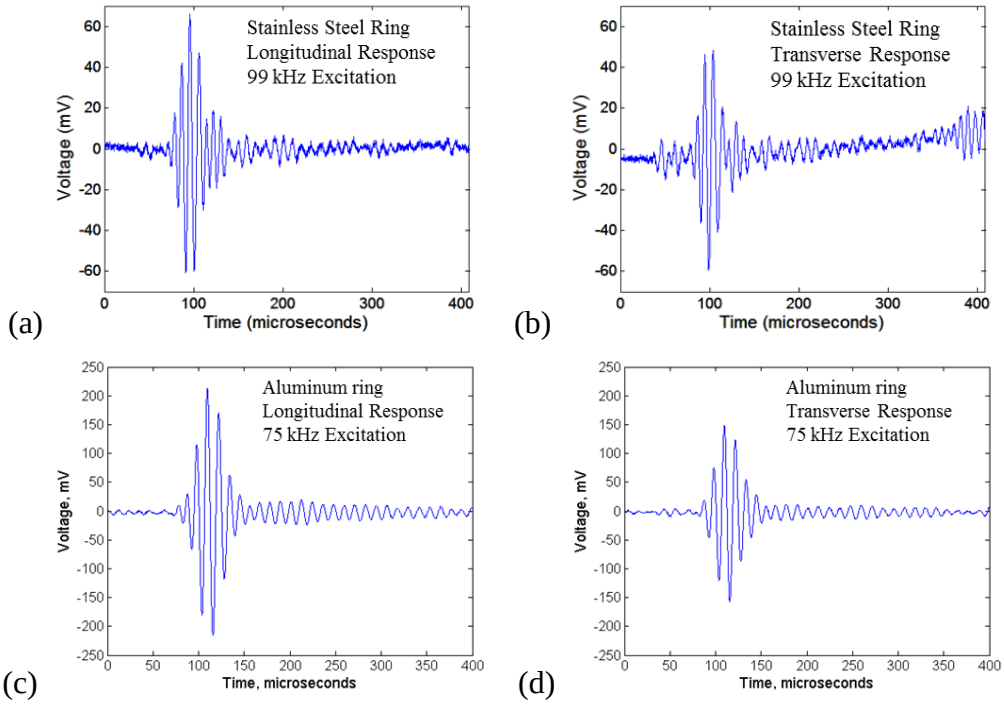

Figure 8.15: Longitudinal and transverse pitch-catch results for FBG on (a,b) a stainless steel ring sensor and (c,d) an aluminum ring sensor

In this case, just as in the tone burst count sweep experiments of Chapter 7, the resonance peak was found within 0.1 kHz by manually tuning the frequency of a sinusoidal excitation. The peak amplitude was additionally confirmed with a 3-count tone burst to negate any concerns that the sinusoidal excitation might cause a small degree of vibrational excitation. An 82.1 kHz center frequency 20 V_{pp} Hanning windowed tone burst was excited from the 150 mm longitudinal PWAS, with counts increasing from 1 to 128 by powers of 2 (a few additional counts were added manually to fill in the low count range). The peak-

to-peak amplitude of the A0 Lamb wave mode was calculated for the FBG on the plate and the FBG on the aluminum ring sensor, shown in Figure 8.16.

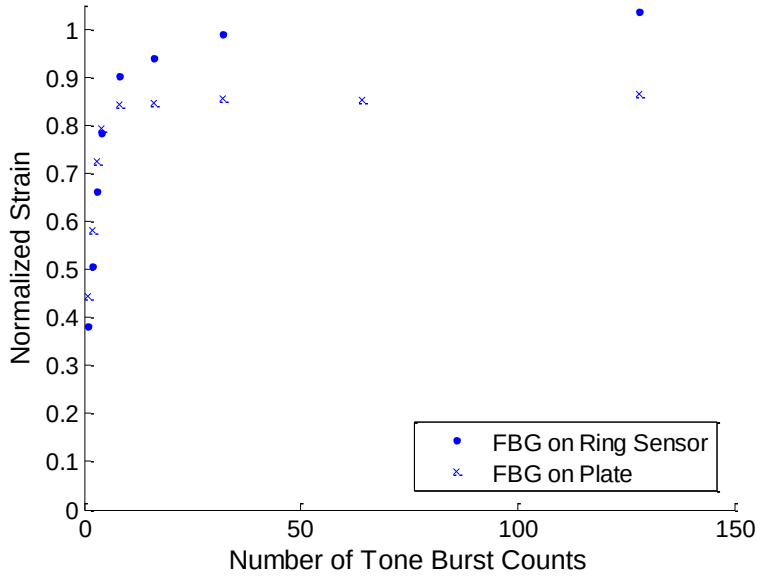

Figure 8.16: Tone burst count sweep experiment to assess the potential for resonance amplification via the fundamental resonance mode

When this experiment was performed using wave absorbing clay, the same trend seen in the free ring sensor resonance experiments was observed. With increasing counts, both the FBG on the plate and the FBG on the ring sensor approached the value of its harmonic response. The ring sensor FBG detected roughly a 20% higher strain associated with the A0 mode than the plate-bonded FBG. Comparing this to other sensor configurations in Chapter 6, this is in line with what has been seen in the literature. The mobile sensor head of Tsuada (2010) reported similar qualitative sensing enhancements as the ring sensor, but reported a 6 dB drop in SNR. In this sense, the detection of higher strain levels than a surface-bonded FBG is a positive effect, even though the increase is small.

This result must be interpreted carefully. The ring sensor FBG detected a higher strain from the A0 Lamb wave mode than the surface-bonded FBG. However, it was likely

due to the difference in sensing mechanism between the two sensors. The surface-bonded FBG was sensitive to in-plane surface strain; the ring sensor FBG was sensitive to out-of-plane motion (e.g. displacement), and that motion was detected by its conversion to its elongation by the ring FBG. As shown in Chapter 7, at 100 kHz in a 1.2 mm aluminum plate, the straight-crested A0 mode out-of-plane displacement was approximately 3 times higher than the in-plane displacement. This indicated that the ring sensor may just have sensed a higher amplitude because its sensing mechanism interacts better with the A0 mode, and not that it was amplifying the strain delivered to the FBG.

8.4.4 Pencil-Lead-Break Acoustic Emission Experiments

A series of PLB-AE tests were performed on the aluminum plate. The PLB-AE events were simulated by breaking 2H-hardness 0.3 mm lead on the front surface of the plate. PLBs were applied 100 mm away with both longitudinal and transverse transmission paths with respect to the axes of the FBGs. Figure 8.17 shows the waveforms and frequency spectra for longitudinal excitation of the plate-mounted FBG, longitudinal excitation of the aluminum ring sensor FBG, and transverse excitation of the aluminum ring sensor FBG.

Since the FBG is a broadband sensor, its response showed that the PLB excited predominantly in the 0-250 kHz frequency range, with the amplitude diminishing sharply with increased frequency (Figure 8.17b).

The frequency response of the FBG on the aluminum ring sensor (Figure 8.17d,f) had two resonance peaks – one at 77 kHz and a second at 270 kHz. These two peaks were also seen in the transverse ring sensor response. It is interesting to note that the 2nd harmonic experienced more directional dependence, dropping off more sharply in the transverse direction (Figure 8.17f). This can be explained by observing the mode shapes of

the 1st and 2nd resonance in Figure 8.1. The 2nd resonance mode shape has a depth-dependence to it, with two nodes at the edges in the depth direction. This alters how it interacted with waves with wavelength along the sensor transverse direction.

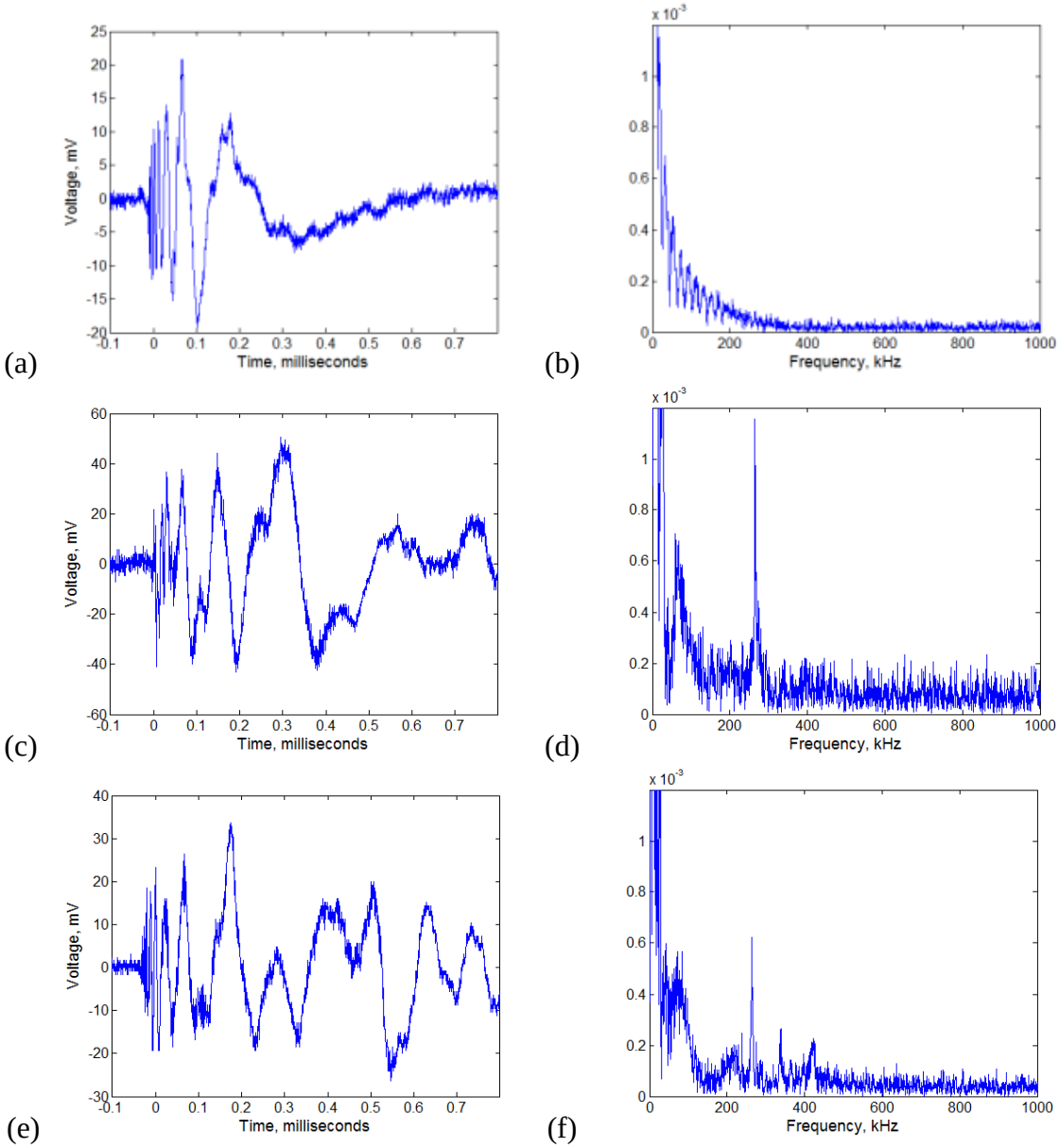

Figure 8.17: Response to 100 mm PLB-AE via (a, b) plate-bonded FBG longitudinal time and frequency response, (c, d) aluminum ring sensor FBG longitudinal time and frequency response, and (e, f) aluminum ring sensor FBG transverse time and frequency response

8.4.5 Impact Experiments

The ring sensor capability to sense impact events was assessed by dropping a 160 mg steel ball from a height of 100 mm 8.18. Impact locations were 100 mm away from the ring sensor, longitudinal with respect to the axes of the FBGs.

The response of the PWAS on the plate, the PWAS on the stainless steel sensor, the PWAS on the aluminum ring sensor, and the FBG on the aluminum ring sensor can be seen in Figure 8.18.

The PWAS showed on the plate (Figure 8.18b) the steel ball excited approximately in the 0-130 kHz range with the amplitude dropping off sharply at higher frequencies. Multiple peaks were seen for the stainless steel ring sensor near 100 kHz, and multiple in the 230-270 kHz range (Figure 8.18d). Both the PWAS and FBG on the aluminum ring has a peak at 77 kHz, although with a broader frequency spread about this peak (Figure 8.18f,h). A second peak can be seen at 270 kHz. The aluminum ring sensor has a distinctly less noisy response than the stainless steel ring sensor.

8.5 Summary and Conclusions

In Chapter 7, it was shown experimentally that the ring sensor had three enhancements over plate-bonded FBGs: omnidirectionality, mode selectivity, and frequency tunability. In this chapter, a series of FEM models were performed to explore these enhancements.

These included modal, harmonic, and transient analysis approaches using 3D elasticity and linear piezoelectricity. Both free boundary condition models and plate models were performed. The plate model used an NRB approach to simulate infinite plate conditions, thus using reduced computational resources.

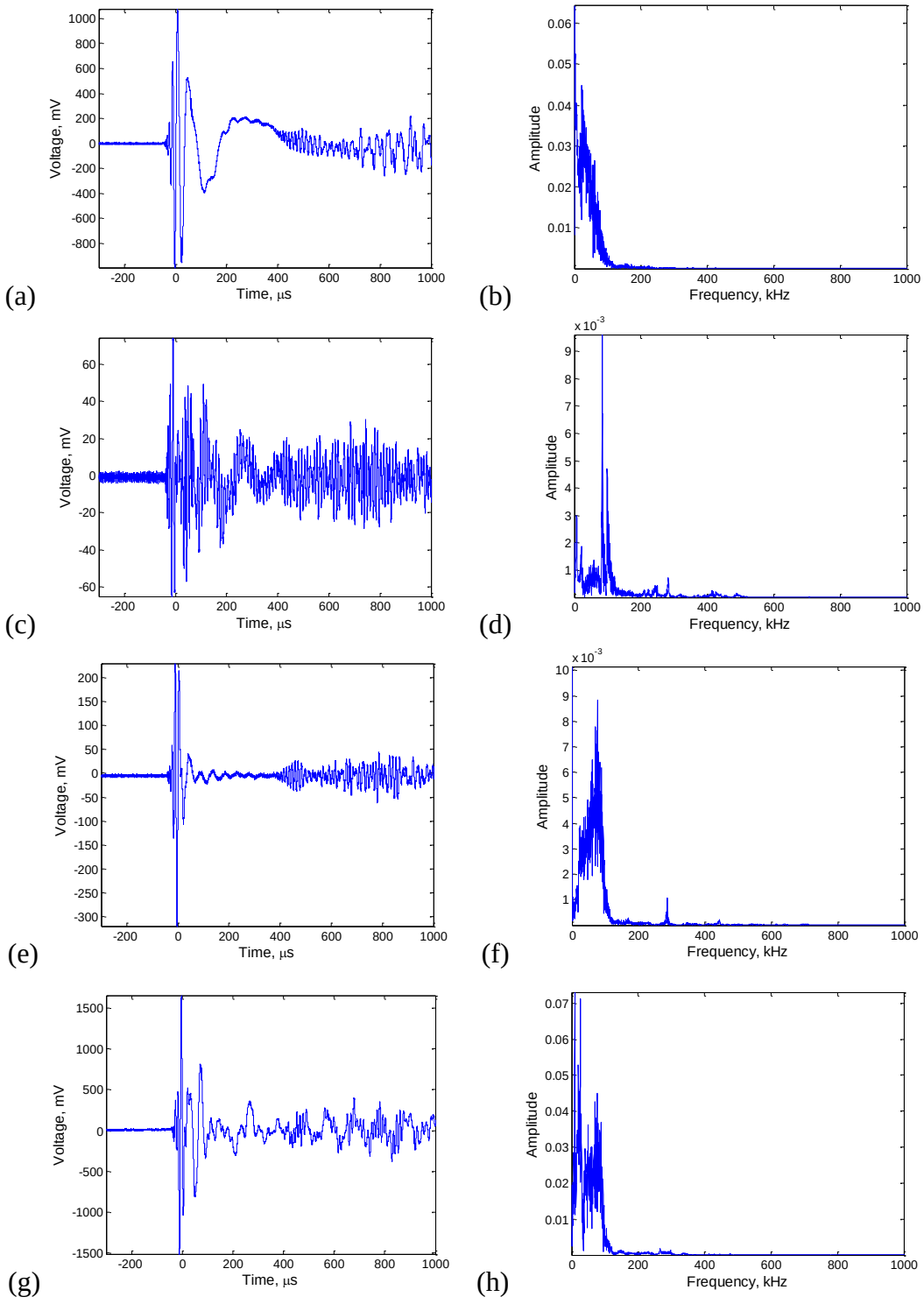

Figure 8.18: 100 mm longitudinal steel ball impact time and frequency response detected via (a, b) plate-bonded PWAS, (c, d) stainless steel ring sensor PWAS, (e, f) aluminum ring sensor PWAS, and (g, h) aluminum ring sensor FBG

Several conclusions can be drawn from the FEM studies:

- In FEM harmonic analysis, the ring sensor FBG responded in a broadband manner. Thus, the frequency tunability feature based on the ring sensor fundamental resonance was found to be too simplistic. Rather, the frequency tunability of the fundamental resonance specified the lowest operating frequency of the ring sensor.
- Transient FEM analysis demonstrated that it is theoretically possible for the ring sensor's FBG to detect a higher strain associated with the A0 Lamb wave mode than a plate-bonded FBG.
- In a plate thickness effect FEM analysis, the predicted ratio between FBG strain and out-of-plane sensor base displacement was constant across multiple plate thicknesses.
- An improved configuration consisting of a centrally-bonded FBG and a PWAS flush with the ring sensor top face resulted in a clear ring sensor configuration that had only one dominant resonance frequency near 100 kHz.

In free ring sensor and plate-bonded ring sensor experiments, the following observations were made:

- A side-bonded FBG, a wrap-around electrode PWAS, and an overhanging PWAS had additional resonance modes near 100 kHz. A centrally bonded FBG and a flush top/bottom PWAS grounded by conductive epoxy had only a single resonance mode.
- A chirp excitation performed over a 0-1000 kHz range experimentally confirmed that the free ring sensor had many closely spaced resonances across a broad frequency range, indicating a potential wideband response.

- Tuning curves showed a single-mode response of the plate-bonded aluminum ring sensor with the improved FBG and PWAS configuration.
- A resonance experiment with varying Hanning window tone burst counts showed that compared to a plate-bonded FBG, the ring sensor FBG detected a larger component of strain associated with the A0 Lamb wave mode.
- The aluminum ring sensor specimen responded well for both PLB-AE and impact passive sensing. The first two resonance modes identified in the free ring sensor testing were apparent. Other resonances were outside the frequency range predominantly excited by the PLB-AE and impacts.

From this work, three areas of improvement were found which require further analysis and redesign. First, the ring sensor should mechanically amplify the strain sensed by its FBG sensing element. This required an optimization for sensor amplitude. Second, there were limitations observed with the size of the sensor base relative to the wavelength of the A0 Lamb wave mode. It was beneficial to miniaturize the sensor to mitigate this effect by reducing the size of its base. Third, the potential for a broadband response was observed in free ring sensor experiments, but still needs to be demonstrated in plate-bonded experiments. These limitations are addressed in Chapter 9.

CHAPTER 9

DESIGN OPTIMIZATION AND EVALUATION OF THE RING SENSOR

9.1 MOTIVATION FOR RING SENSOR REDESIGN

The ring sensor studied in Chapters 7 and 8 showed beneficial improvements over a plate-bonded FBG. A slightly higher A0 Lamb wave mode amplitude was sensed by the ring sensor FBG compared to a plate-bonded FBG. This compared well with other FBG mechanical sensing configurations in the literature, as seen in Chapter 6. Thus, there were indications that a redesign with an emphasis on maximizing sensitivity may be fruitful.

Concurrently, it was considered beneficial to reduce the size of the ring sensor. Although the ring sensor was currently 8 mm in diameter, comparable in size of the smallest AE sensors on the market, the form factor of the sensor mechanical host is unappealing for use of this sensor in a permanently bonded configuration. Miniaturization also reduces the size of the sensor base and then possibly mitigates the finite transducer aperture effect. This miniature was attained through FEM optimization.

After miniaturization of the ring sensor, the frequency response, Lamb wave detection SNR performance, insensitivity to quasi-static strain, and waveform capture during structural loading were performed.

9.2 DESIGN OPTIMIZATION OF THE RING SENSOR

The ring sensor was optimized in ANSYS Workbench 15.0. For this work, the ANSYS DesignXplorer toolbox was used as it has built-in optimization features which

integrates directly with its FEM models. Features of the ring sensor geometry were used as parameters, and bounds were assigned to delineate a design space. Since FEM models were created automatically in the design space, the meshing was done automatically by ANSYS, with a specified number of elements across the wall thickness (Figure 9.1b). The initial model, three random intermediate models, and the final model all passed convergence checks.

The optimization scheme had the following steps:

1. Geometric features were identified for sensitivity analysis
2. The results of the sensitivity analysis were used to for creation of a response surface for visualization of the design space
3. A goal-driven direction optimization algorithm was used to identify optimized design candidates. Then, the geometry of the best performing candidate was modified for manufacturability and reassessed in FEM

9.2.1 Model Setup, Input Parameters, and Optimization Goals

A harmonic analysis was performed, with the mode proximal to 100 kHz (the breathing-type mode) amplitude and frequency tracked. For loading, a harmonic 1 N distributed force was applied to the flat face of the ring sensor in an out-of-plane direction (Figure 9.1a). Since there was only one mode proximal to 100 kHz, with higher harmonics not occurring until ~270 kHz, the mode was tracked by specifying a window between 50-200 kHz and then tracking the peak amplitude and frequency within the region. To widen the peak resonance amplitude to make calculations repeatable, a nominal 1% modal damping ratio was added to all modes. If no damping is used, the response amplitude at a resonance peak depends heavily on the frequency discretization. The aluminum material

properties used were density $\rho = 2770$ kg/m^3, elastic modulus $E = 71GPa$, and Poisson ratio $\nu = 0.33$.

A cluster algorithm was used which added more points around peaks in the frequency spectrum so the resonance frequency and amplitude could be accurately represented.

(a) 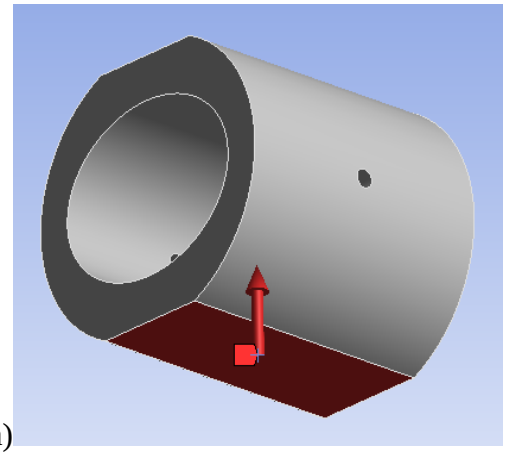 (b) 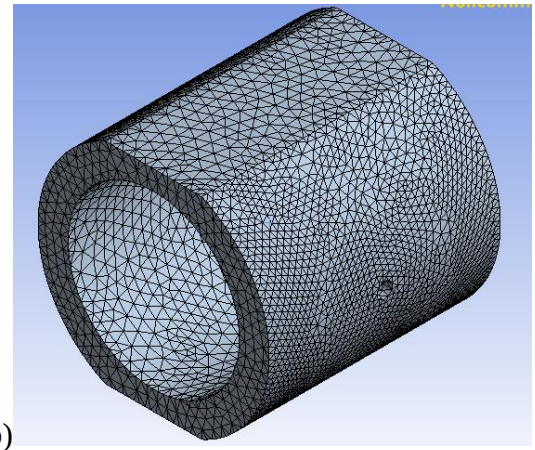

Figure 9.1: (a) 1 N distributed harmonic out-of-plane load applied at the base of the ring sensor, and (b) example mesh from sensitivity analysis and goal driven optimization

With each harmonic analysis, a modal analysis was performed and first resonance frequency compared with the harmonic analysis to ensure the correct mode was being used for the design.

The input parameters and bounds for the model were the following geometric features:

1. The outer diameter
2. The major diameter of the ellipse
3. The minor diameter of the ellipse
4. The "height" of the flat faces (distance from the line of symmetry)
5. The depth of the ring sensor

The optimization had three goals:

1. Maintain a target resonance frequency between 90 – 110 kHz
2. Maximize the amplitude of the dominant frequency's response
3. Reduce the outer diameter of the ring sensor

In the harmonic model, the average deformation along the entire curved face of the right FBG hole was used to determine the frequency and amplitude. The deformation was taken to be along the longitudinal axis where an FBG would be bonded (along the axis of the two ring sensor holes).

9.2.2 Sensitivity Analysis of the Ring Resonator

Two separate sensitivity analyses were performed, as new information was gleaned from the first analysis which warranted redefining the analysis method and input parameters. The sensitivity analyses were performed using the ANSYS Workbench Parameters Correlation toolbox.

For the first sensitivity analysis, only the major axis, minor axis, depth, and flat height were assessed. The outer diameter was omitted in the sensitivity analysis and fixed at a value of 8.00 mm, as it was known that the resonance frequency would increase with reduced outer diameter; this initial line of thinking was incomplete, as the relation with amplitude was not well known. However, this approach was still able to gather information about the response to the other parameters. 10 FEM models were run for each parameter. The sensitivity analysis was performed by holding the other parameters constant and varying one parameter at a time in a round robin fashion.

Scatter plots of the effect of each input parameter on frequency and amplitude as shown in Figure 9.2 and Figure 9.3, respectively. The effect of the input parameters on resonance frequency and amplitude are as follows:

- Depth: Frequency and amplitude are constant above a threshold value. This is interpreted as the ring responding in plane strain conditions.
- Flat height: Apparent quadratic relation with frequency and amplitude. Flat height had minimal effects on frequency, and a larger effect on amplitude.
- The ellipse major and minor diameters: Strong inverse linear proportionality with frequency. Correlated with amplitude, but with a higher variance.

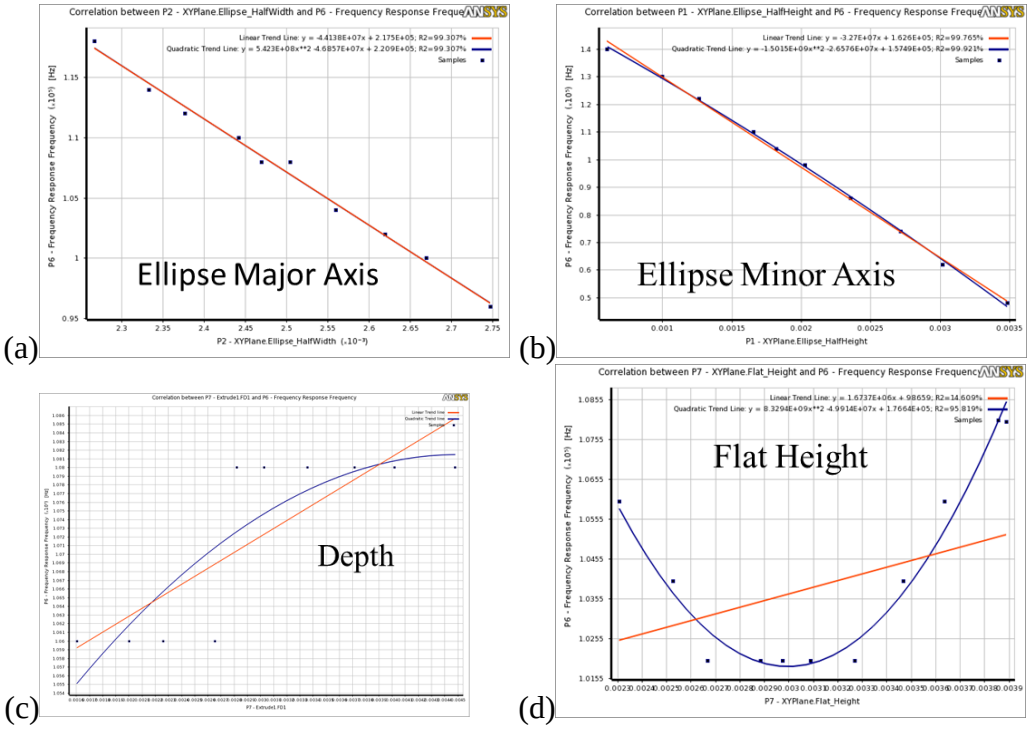

Figure 9.2: Effect of (a) ellipse major diameter, (b) ellipse minor diameter, (c) ring depth, and (d) flat height on 1st resonance frequency

The most interesting result was that the ellipse major and minor diameters had an almost equivalent effect on both frequency and amplitude. Because of this, the two parameters could be set equal and merged into a single parameter, given by the “wall

thickness" of the ring. There is a considerable manufacturing advantage to this, as a ring with a circular hole would not require costlier EDM processing like the ring with an elliptical hole.

The amplitude and frequency had a significant response to the flat height, but the relationship was roughly quadratic within the range assessed. This indicated that it should be used as a design parameter in later studies. Since the depth had no effect on frequency or amplitude beyond a certain threshold, the depth was maintained beyond that threshold in the optimization stage.

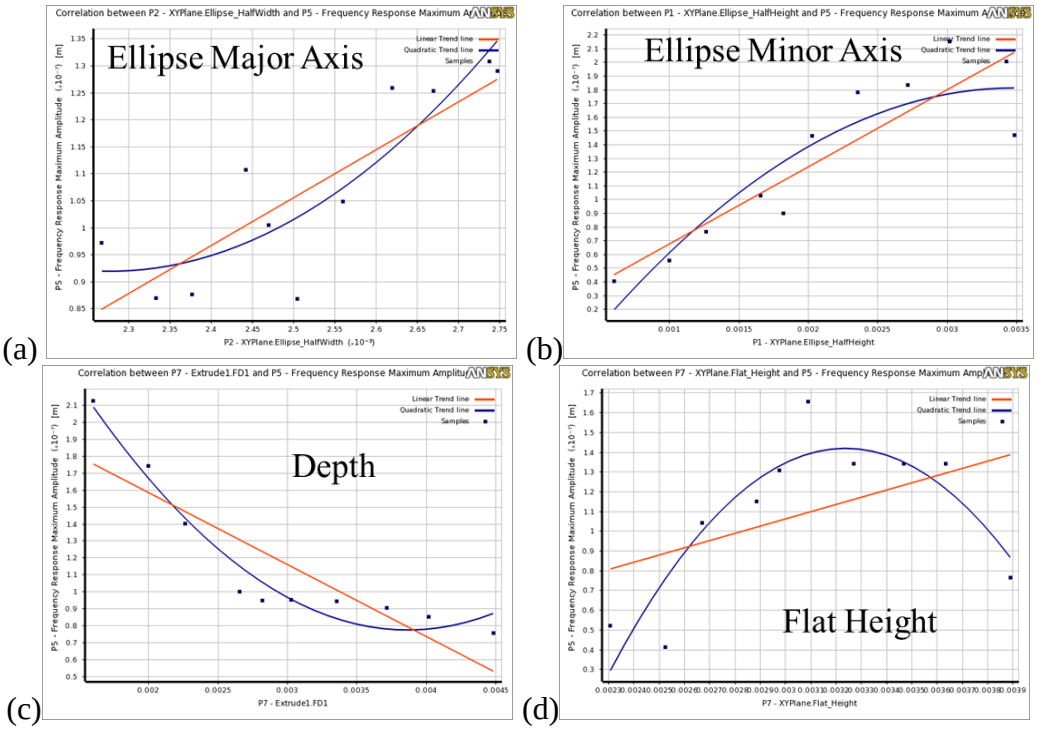

Figure 9.3: Effect of (a) ellipse major diameter, (b) ellipse minor diameter, (c) ring depth, and (d) flat height on 1st resonance amplitude

Upon gaining more experience and further reading of standard methods for performing sensitivity analyses, the sensitivity analysis approach was updated. Instead of varying each parameter individually, the parameters were varied simultaneously using a standard design of experiment (DOE) approach. This allows the relative strength of each

input parameter on the outputs to be observed, as its trends must be able to be seen through random noise of the other variables changing. This also helps ensure that the trends observed in the sensitivity analysis are independent of a fixed region in the design space, but rather tend to hold true over the entire design space. The result of the circularity of the ring sensor hole was maintained. All indications still pointed to the capability for the circular hole to provide a sufficiently strong response, and it was more important to remove the constraint that the ellipse had on manufacturing a miniature sensor.

For a second sensitivity analysis, the ANSYS built-in optimal space filling design method was used; this method uses a Latin Hypercube sampling method (i.e. a Monte Carlo sampling method with no repeated points) and then post processes it to maximize the distance between input parameters. The geometric parameters were the ring diameter, wall thickness, flat height, and depth. Again the 1st resonance frequency and amplitude used as output parameters, with the rest of the FEM harmonic analysis kept the same. In the parametric study, 100 FEM analyses were performed. A sketch of the ring with relevant parameters is given in Figure 9.4. Figure 9.5 shows the Spearman correlation coefficient values (sensitivities) between each input and output. The Spearman, rather than the Pearson correlation coefficient was used because it is more general. It quantifies monotonic relationships rather than just linear ones. Note that Spearman correlation coefficients below 0.25 are considered non-significant and not given a heigh on the graph.

The amplitude was found to be inversely correlated with wall thickness, and the other parameters had a negligible effect on amplitude. The ring diameter and flat height were negatively correlated with frequency, and the wall thickness was positively correlated with frequency.

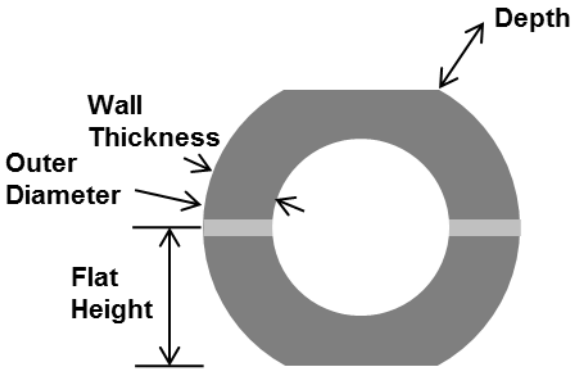

Figure 9.4: Sketch of ring sensor geometric parameters

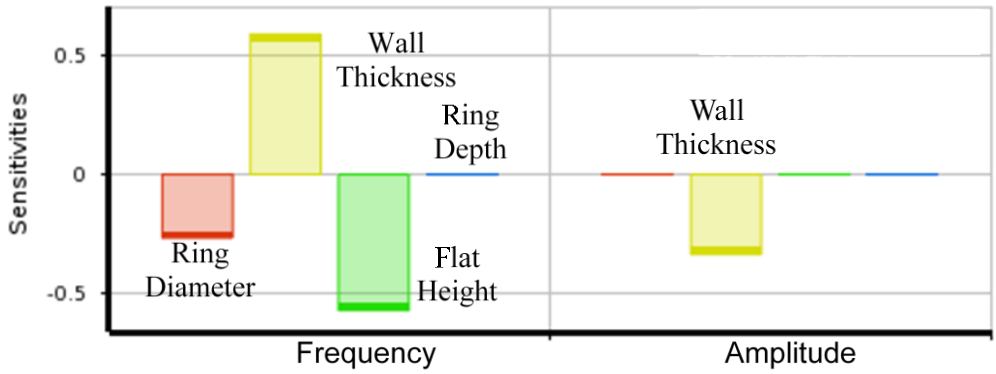

Figure 9.5: Spearmen correlation coefficients (sensitivities) between ring sensor geometric features and 1st resonance frequency and amplitude

Because of these correlations, a general design rule for optimizing amplitude while maintaining frequency was as follows:

1. Reduce the ring diameter and the wall thickness simultaneously. These counteracted each other's effect on resonance frequency, while a lower wall thickness increased the amplitude
2. Factor the flat height into the optimization algorithm, as it had a non-monotonic relationship with amplitude

3. Maintain the ring depth such that plane strain conditions are met (in the region where there is no relationship between ring depth and the 1st resonance frequency parameters). The ring depth and flat height ultimately factored bonding considerations into account as well.

Because of the counteracting tendencies of ring diameter and wall thickness, tradeoffs between amplitude and size criterion are not necessary (e.g. multi-objective optimization with weighted goals). Rather, maximizing amplitude will jointly minimize the size of the ring sensor.

9.2.3 Goal Driven Optimization

Based on the results of the sensitivity analysis, a goal-driven optimization was performed using the built-in ANSYS multi-objective genetic algorithm (this algorithm functioned well even though there was only a single objective). The ring diameter, wall thickness, and flat height were used as input parameters. The depth was maintained constant at 4.00 mm, as this was well within the plane-strain region for depth invariance of 1st resonance frequency and amplitude. The 1st resonance frequency was constrained between 90-110 kHz, with a nominal target frequency of 100 kHz. The single goal was the maximization of the longitudinal displacement for the ring FBG hole. There is an inherent supposition that maximization of the FBG hole displacement for the fundamental resonance mode would transfer to other resonance modes as well.

Observing the output of the optimization algorithm, it became readily apparent that the maximal amplitude occurred at the minimum bound of the outer diameter, with a wall thickness sufficiently tuned to reach the 100 kHz target frequency. Based on the

optimization with a lower outer diameter bound of 3.75 mm, the following “optimized” geometry was found:

- Outer Diameter: 3.75 mm
- Wall Thickness: 0.485 mm
- Flat Height: 1.70 mm
- Depth: 3.75 mm (manually matched to outer diameter)
- FBG Hole: 0.25 mm (size of the optical fiber)

A frequency sweep of the displacement of the FBG hole and the harmonic response at the 1st resonance frequency is given in Figure 9.6. To obtain rounded values, slight modifications were made from the original geometry, although the frequency (100 kHz) and amplitude of the response was not significantly changed.

It is important to note that the outer diameter was pushed to the lower bound of the design range, indicating that this is not a true optimum. Lowering the bound on the outer diameter could be used to generate a more optimized response. However, the restrictions become those of manufacturability. A smaller sensor could produce a more sensitive response, but would require precision manufacturing. In this current design, tolerances were on the order of 0.05 mm to maintain the frequency of the first resonance.

9.2.4 Sensor Prototyping with Geometry Modified for Manufacturing

To aid manufacturing, a commercially available piece of aluminum 6061 tubing was used. A piece of tubing was found at 0.125’’ (3.1* mm) outer diameter, with a 0.014’’ (3.56 mm) wall thickness. Since the wall thickness was quite small, half of the wall thickness was removed, providing a compromise between structural strength, manufacturability, and resonance frequency.

- (a)

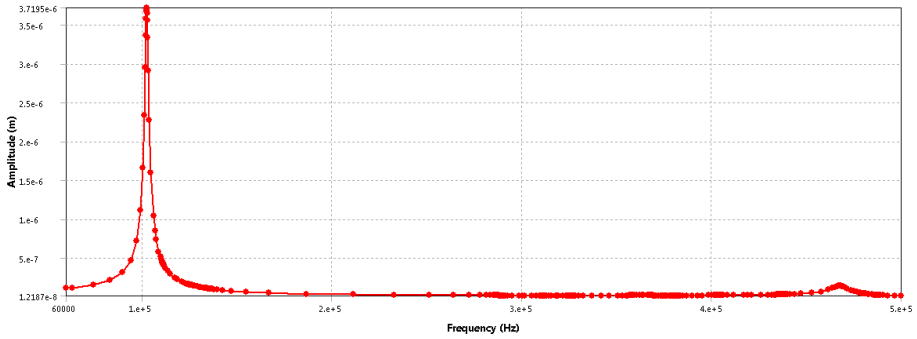

- (b)

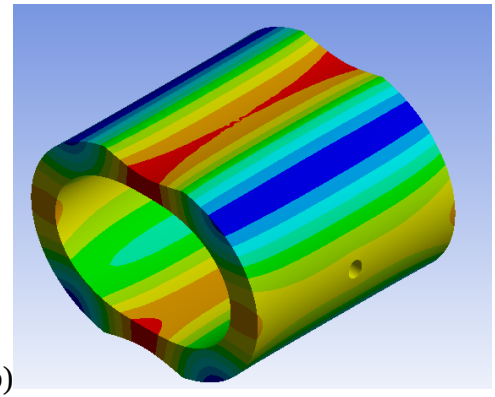

- Figure 9.6: Harmonic response of a 3.75 mm outer diameter ring sensor design, shown as (a) harmonic frequency sweep, and (b) resonant response at 100 kHz

A drawing of the modified ring sensor geometry is given in Figure 9.7. This final design also provided significant weight reductions over that of the original 8 mm aluminum ring sensor prototype (576 mg original, versus 23.9 mg miniaturized). The estimated resonance frequency was 102 kHz, very close to the 100 kHz target resonance. The motion at the fundamental 100 kHz resonance can be seen in Figure 9.8; the general breathing-type characteristic of the mode is still preserved. The harmonic response predicted that the amplitude of the modified ring sensor was 1.62 times larger than the optimization at the lower end of the bounds in Section 9.2.3.

This was attributed to a further reduction in wall thickness and outer diameter of the ring sensor. There were issues with manufacturability at small sizes. For example, the

new design of the ring sensor had a wall thickness of 0.36 mm. A ± 0.05 tolerance is ± 13.9% of the thickness, representing a significant error in resonance frequency.

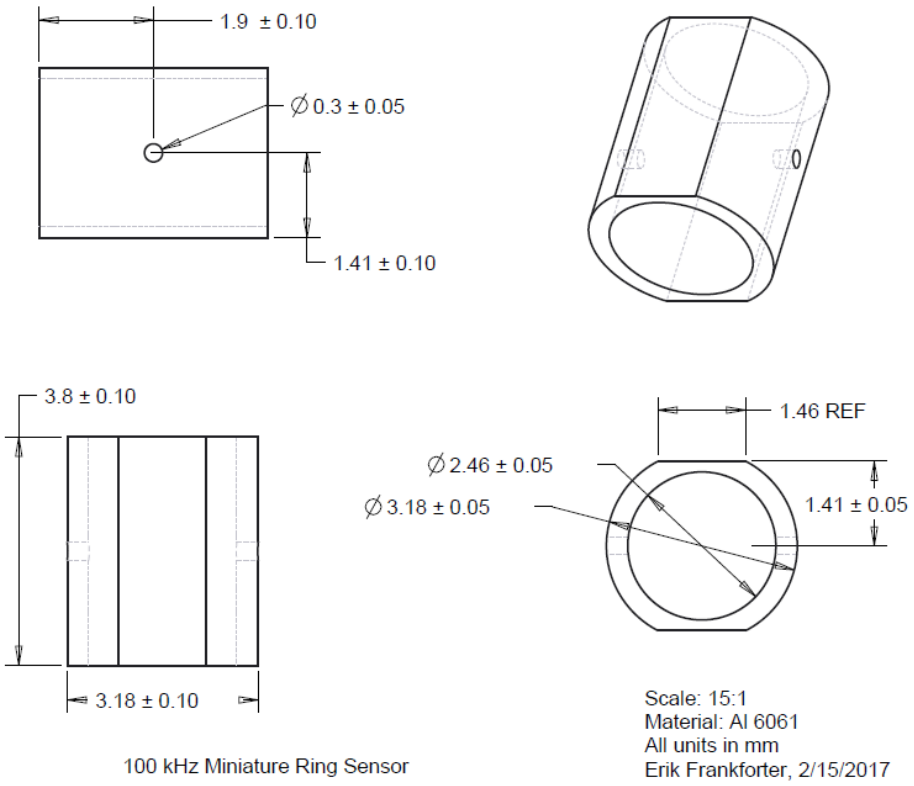

Figure 9.7: Geometry of a miniature 100 kHz ring sensor

Further amplitude and miniaturization optimization has a tradeoff of either higher variance in target frequency or the requirement for more expensive precision manufacturing methods. One workaround may be to design a fundamental resonance significantly lower than 100 kHz,

since the fundamental resonance only delineates the lower bound of the sensing frequency range. However, this kind of approach has drawback in terms of variability of sensor performance.

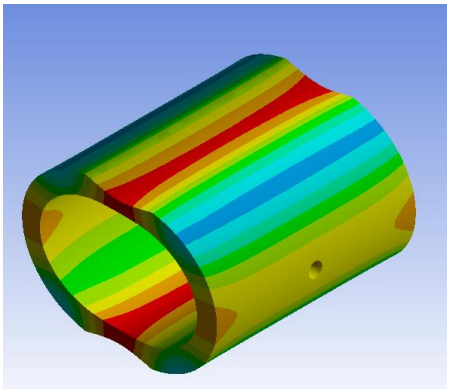

Figure 9.8: Harmonic response to out-of-plane motion at 100 kHz for a 3.2 mm outer diameter ring sensor design

9.3 Evaluating the Optimized Ring Resonator

9.3.1 Miniature 100 kHz Ring Sensor Prototyping

Prototyping was done in the University of South Carolina mechanical engineering machine shop. First, the inner diameter and wall thickness of the tubing were first measured to ensure they met specifications (Figure 9.9a). Next, a fixture was created with a channel that would snugly fit the tubing (Figure 9.9b). The fixture could be set in a vice to hold the tubing in place without permanently deforming the tubing. An aluminum rod was lathed to fit inside the tubing to reinforce the structure during machining. A vertical mill was used to make multiple passes along the top and bottom of the tubing until the flat height criteria was met. For the vertical mill pass over the second flat face, the tubing was aligned by pressing the flat milled surface against the bottom of the fixture channel. A 0.3 mm drill bit was used to create a series of holes along the side of the tubing. A horizontal mill with a thin cutting blade was used to cut the tubing between each hole to create multiple ring sensors in parallel (Figure 9.9c).

(a)  (b) 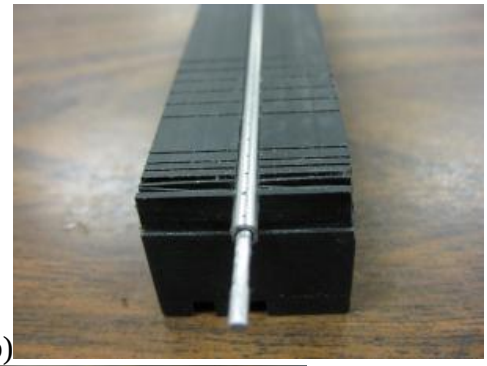

(c) 

Figure 9.9: (a) Thicker stainless steel tubing for prototype practice and aluminum tubing for prototyping, (b) aluminum tubing with flat faces milled and FBG holes drilled, and (c) final ring sensor prototypes

Since manual alignment of the ring sensor inside the fixture was difficult when a second round of prototyping was needed, a rotatable fixture with an internally threaded protrusion the size of the ring sensor was made. A screw was used to hold an unfinished ring in place for milling and drilling operations. Manufactured in this fashion, material and labor costs for a small batch order of 10 miniature ring sensors was approximately $150, including fixture creation. This makes this design very cost efficient.

9.3.2 Microscopic Geometry Measurements

Visual geometry measurements of one of the miniature ring sensor prototypes were made using a light microscope (Figure 9.10). The measurements were as follows:

- Outer diameter: 3.17 mm

- Inner diameter: 2.49 mm
- Ring depth: 3.13 mm
- FBG hole diameter: 0.33 mm
- Flat face length: 1.63 mm and 1.30 mm

(a) 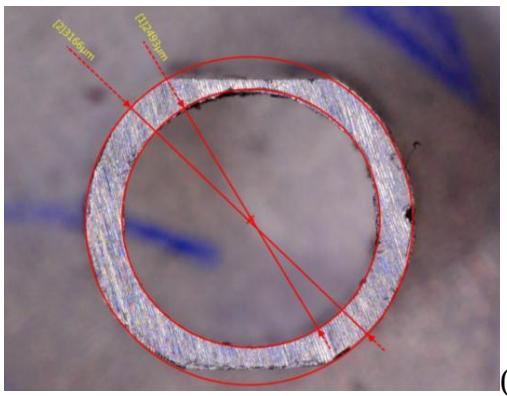

(b) 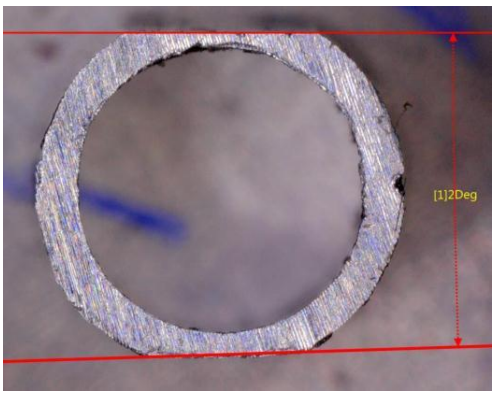

(c) 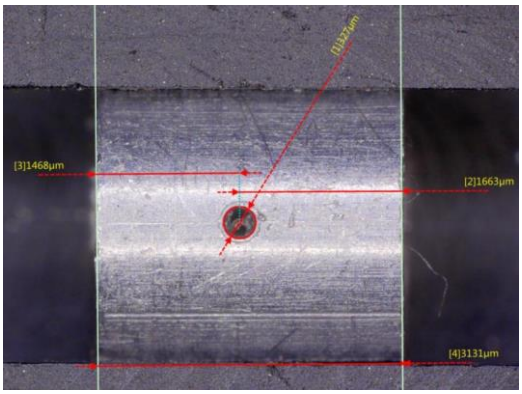

(d) 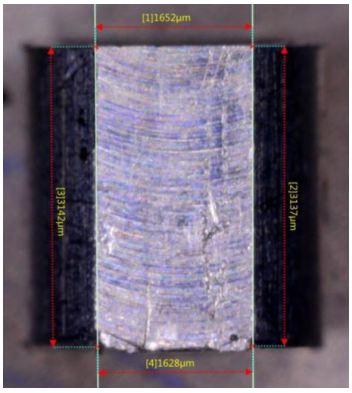

(e) 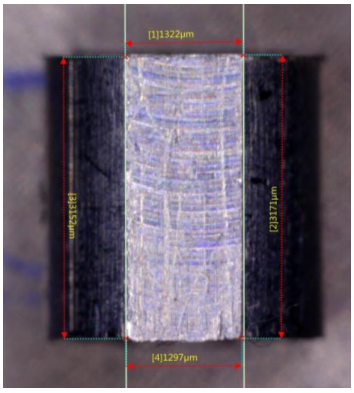

Figure 9.10: Miniature 100 kHz microscopic geometry measurements for (a) inner and outer diameter, (b) angle between the two flat faces, (c) ring depth, hole size, and hole placement, and (d, e) top and bottom flat surfaces

The inner and outer diameter were within specification. The ring depth was smaller than specified; however, this parameter only affects bonding considerations and finite transducer aperture effects, so this was considered acceptable. The height to the flat faces was out of specification due to the difficulty in machining such small features. A 2% offset in the angle between the two flat faces was observed, showing they were not entirely in alignment. This batch of ring sensors was self-manufactured in the machine shop; the second batch of ring sensors with a rotatable fixture had tighter tolerances, although these were not used until the calibration experiments in Chapter 11.

Because the prototype suffered issues with precision, the actual measured geometry was fed back into an FEM harmonic analysis to evaluate departures from desired conditions. The predicted harmonic response under ideal dimensions was compared to the predicted harmonic response of the ring sensor with measured geometry (Figure 9.11). The response at the 1st resonance is similar, although some asymmetry about the horizontal plane is seen for the FEM with the measured dimensions. There is a drop in the 1st resonance frequency prediction from 102 to 87 kHz. It is likely that the major factor contributing to this was the allowable tolerance in diameter and wall thickness, although the precision of the flat faces also plays a role. Further investigation would be needed to assess the influence of geometric tolerances on resonance frequency. Ultimately, a predicted resonance frequency at 87 kHz was acceptable for this prototype.

9.3.3 Material and Size Assessment

The effect of elastic modulus, density, and a scaling factor were assessed in FEM using the prototyped miniature ring sensor design as a basis. The scaling factor was created by multiplying each of the dimensions of the prototyped ring by a constant, except for the

FBG hole diameter which was maintained at 0.25 mm. Parametric sweeps of each of the three parameters was performed while holding the other two parameters constant.

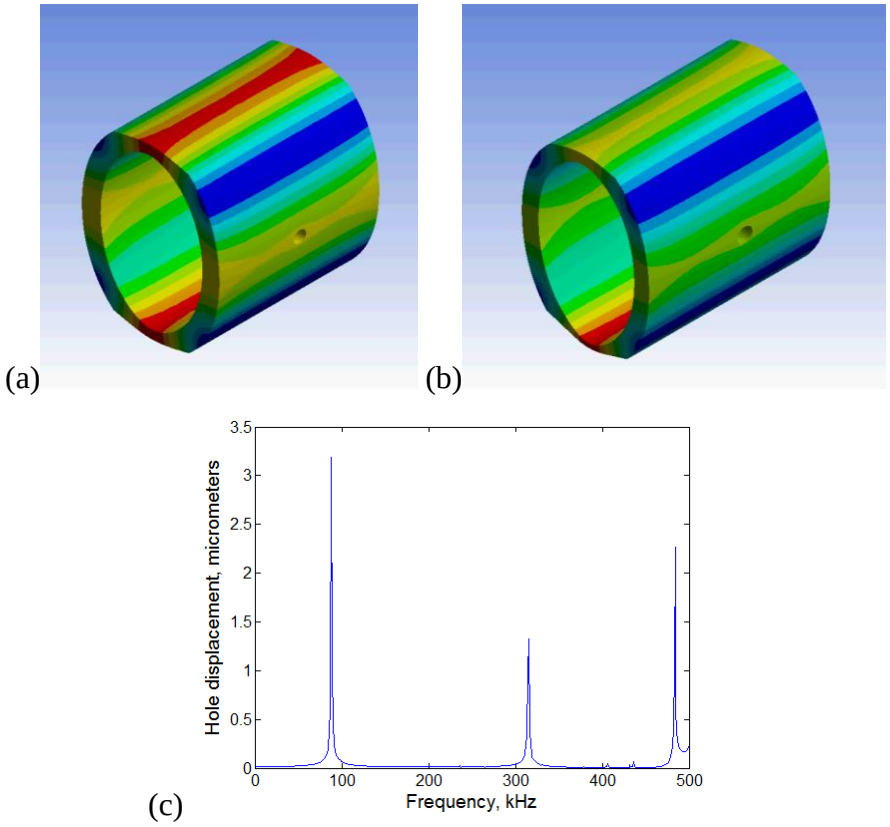

Figure 9.11 FEM modal and harmonic analyses of ring sensor with dimensions back-substituted from microscopic measurements

The results can be seen in Figure 9.12. With curve fitting, it can be shown that $f \propto \sqrt{\frac{E}{\rho}}$ and $f \propto \frac{1}{S^{1.008}}$ where f is the natural frequency in kHz, E is the elastic modulus, ρ is the density, and S is the scaling factor. The exponent on the scaling factor differs from unity because the size of the FBG hole was held constant. These two simple relations can be used as simple design guidelines for material selection and sensor sizing. Designs can quickly be made for different frequencies using these guidelines. For example,

a 200 kHz resonance frequency for an aluminum ring sensor is predicted with a scaling factor of 0.52 (1.625 mm outer diameter).

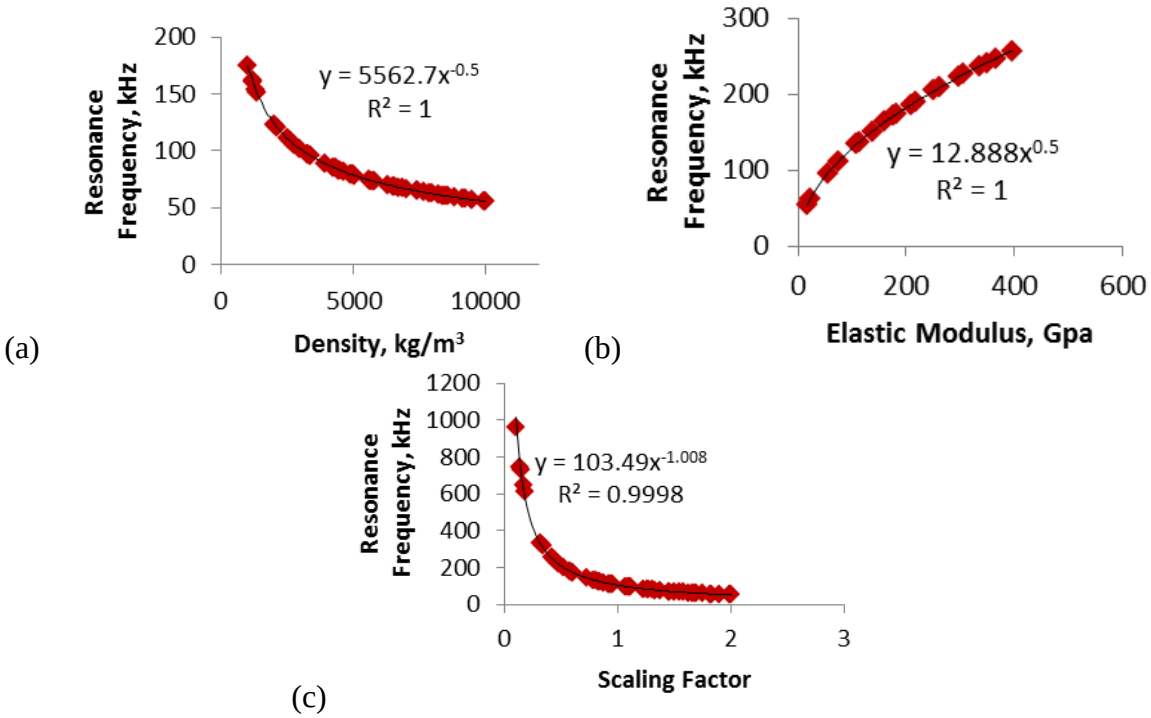

Figure 9.12: Effect of material properties and scaling factor on first ring sensor resonance frequency

In practice, the acoustic impedance should also be considered when switching materials. So far, when using aluminum, the acoustic impedance was matched with the host structure (although the effect of the bonding layer may somewhat mitigate this). If maximal transfer to a PWAS is necessary, the use of a brass ring sensor with an impedance matching layer at the sensor base may be helpful.

9.3.4 Frequency Response of the Ring Sensor

An aluminum miniature ring 100 kHz sensor was instrumented with a top/bottom electrode PWAS and an optical fiber with a 3 mm length FBG (Figure 9.13). The cyanoacrylate adhesive for the FBG was dispensed by a micropipette placed on the outer surface of the ring sensor. The optical fiber was bonded to one side at a time. When the

FBG was bonded on the second side of the ring sensor, a small pretension was applied by hand and held throughout the curing.

(a) 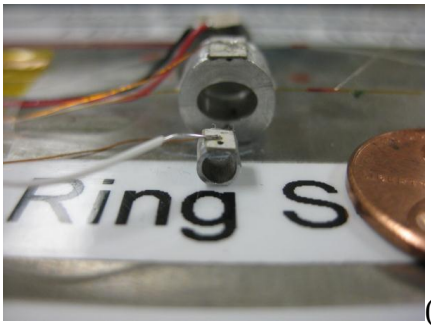

(b) 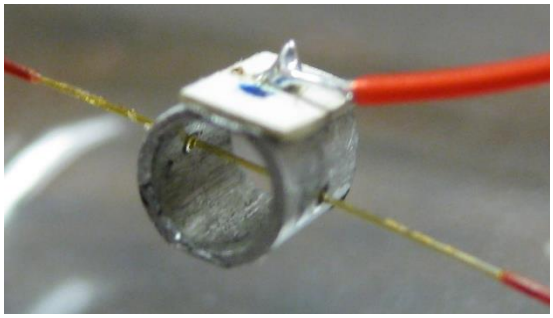

Figure 9.13: Miniature ring sensor and original 100 kHz ring sensor comparison and instrumentation

The EMIS, chirp, and pitch-catch responses were assessed for the free ring sensor. The plots for each can be seen in Figure 9.14 alongside the same experiments performed on the 8.00 mm diameter (old) aluminum ring sensor. The EMIS showed a fundamental resonance at 83.5 kHz, slightly lower than the 87 kHz resonance frequency predicted by the FEM updated with microscopic dimension measurements from Section 9.3.2. It is hypothesized that at this small sensor size, the presence of the PWAS was sufficient to additionally drop the resonance frequency. The chirp excitation was 0-200 kHz, 0-50 V_{pp}.

The response shows 3 distinct peaks – the cause of the two additional peaks is unclear. The pitch-catch excitation was performed at the sensor resonance frequency of 83.5 kHz, showing a clear transient response without excessive ringing.

The ring sensor was bonded to a 1.2 mm thick aluminum 2024-T3 plate, and the chirp experiment was repeated. The resonance frequency dropped from 83.5 kHz to 52.2 kHz. This was attributed to the change in boundary conditions from bonding of the ring sensor. This effect was also observed in the original ring sensor prototype in Chapter 7, but to a lesser degree. If future miniature ring sensors are prototyped, it may be useful to increase

the resonance frequency to values at least in the range of 150 kHz, accounting for a drop in resonance frequency with bonding.

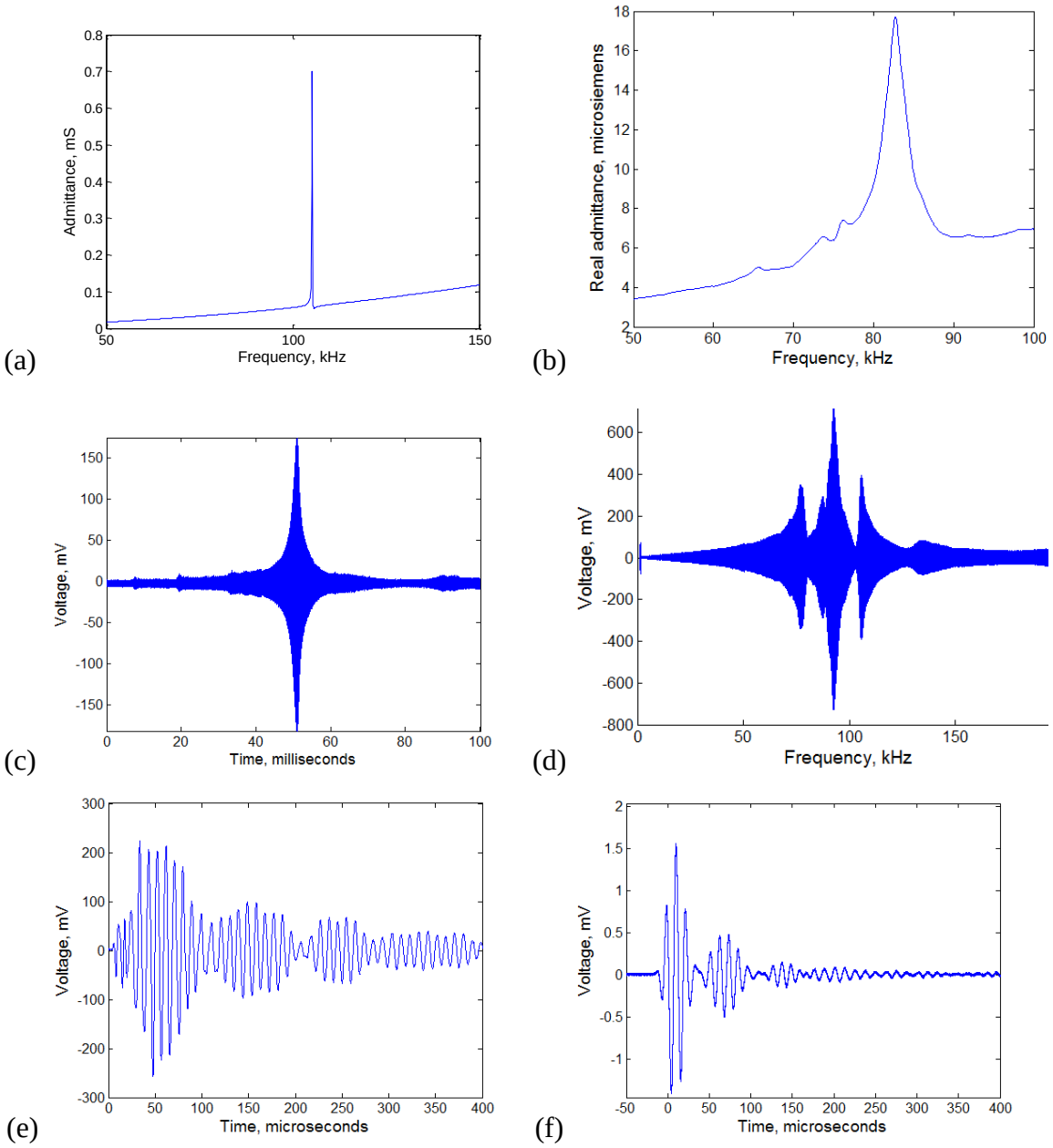

Figure 9.14 Electromechanical admittance of the (a) 8.0 and (b) 3.2 mm ring sensors, chirp response of the (c) 8.0 and (d) 3.2 mm ring sensors, and pitch-catch response of the (e) 8.0 and (f) 3.2 mm ring sensors, respectively

However, the drop in resonance frequency to 52.2 kHz does not cause major problems in sensor operation. A lower bound to the sensor response near 50 kHz is suitable for AE detection, particularly if the sensor responds in a broadband manner.

9.3.5 Lamb Wave Pitch-Catch Experiments

The miniature 100 kHz ring sensor was bonded to the 1.2 mm thick aluminum 2024-T3 plate setup from Chapters 7 and Chapters 8, allowing direct comparison to the 8 mm ring sensor prototype (Figure 9.15). The experimental setup is as follows:

- PWAS transmitters were located 150 mm away from the cluster of receivers, wave transmission paths longitudinal and transverse to each FBG axis
- A plate-bonded PWAS, plate-bonded FBG, 8 mm aluminum ring sensor (original prototype), and 3.18 mm aluminum ring sensor (optimized design) were bonded to the plate. Both ring sensors were outfitted with PWAS and FBG.

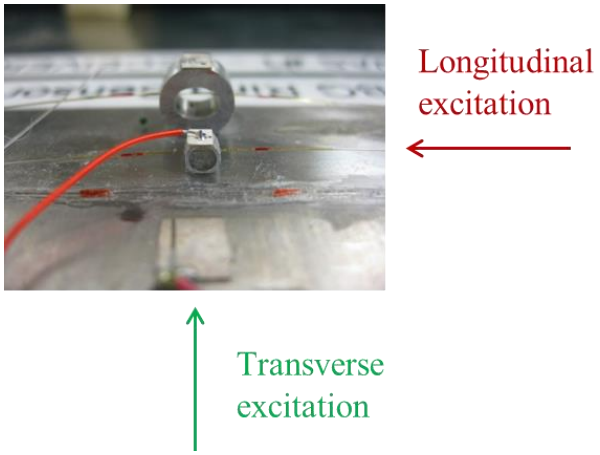

Figure 9.15: Sensor cluster for sensor evaluation via Lamb wave testing

Tuning curves from both longitudinal and transverse excitations were assessed for original ring sensor and the optimized ring sensor. To determine if the sensors would exhibit a broadband response in Lamb wave experiments, a series of 20 V_{pp} 3-count

Hanning windowed tone bursts were excited, ranging from 3-600 kHz in 3 kHz increments. The longitudinal and transverse tuning curves for each ring sensor can be seen in Figure 9.16. The miniature ring sensor had a fundamental resonance at 52.2 kHz, a second resonance in the 120 kHz range, and a third resonance in approximately in the 380 kHz range. The original ring sensor prototype had multiple resonances about to 100 kHz and a higher harmonic in approximately the 350 kHz range.

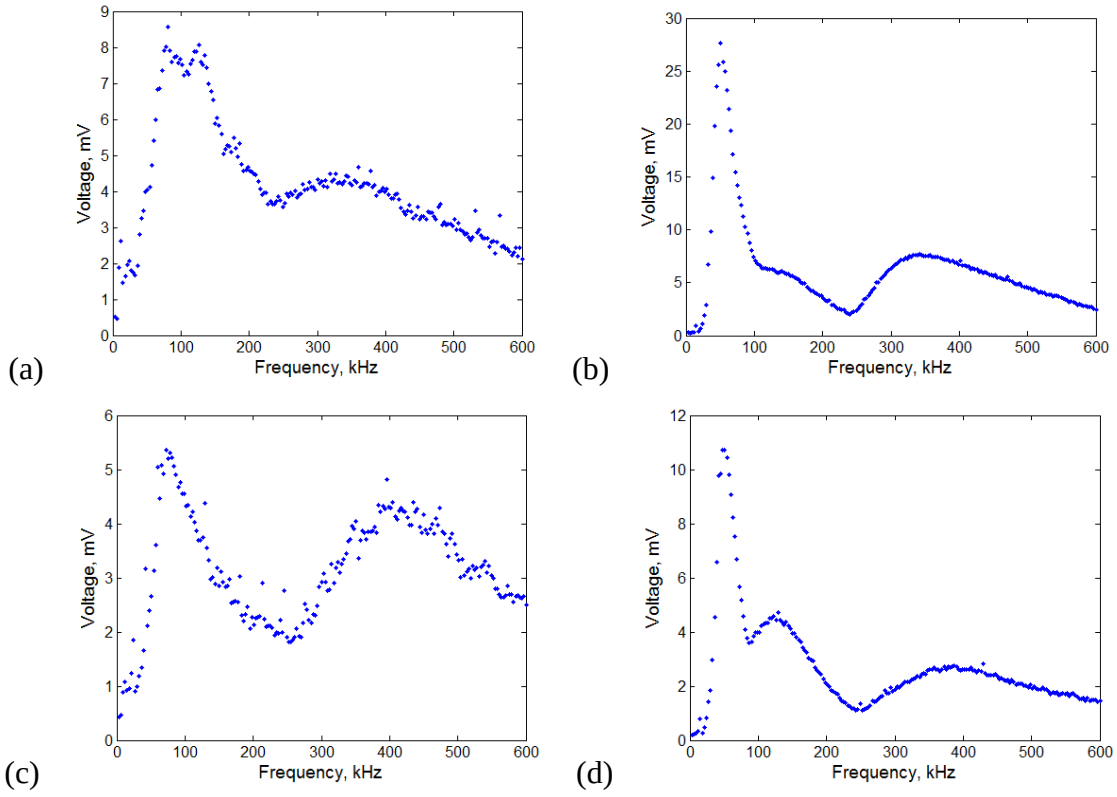

Figure 9.16 Longitudinal tuning curves of (a) the original ring sensor and (b) the miniature mm ring sensor, and transverse tuning curves of the (c) original ring sensor and (d) the miniature ring sensor

Comparing the tuning curves of the 8 mm aluminum ring sensor in Figure 9.16 to those produced in Chapter 8, we notice that the data points are now more scattered. This is because these tuning curves were taken without any averaging to reduce noise. Another

notable difference is a second resonance peak in the original 8 mm ring sensor tuning curve near 100 kHz. This may be due to a rebonding that was performed for this sensor.

For the miniature 3.2 mm ring sensor, although the fundamental resonance frequency is somewhat low, there is a non-negligible response at all frequencies across the 0-600 kHz range. It is also notable that the tuning curves of the miniature ring sensor are much smoother. This is due to the miniature ring sensor's higher signal-to noise ratio, which can be seen in an individual pitch-catch measurement.

The transverse response of the 3 mm ring sensor was much smaller than the longitudinal response. This was surprising since the reduction in sensor size should have reduced the finite transducer thickness effect, particularly at the fundamental resonance where the wavelength is significantly longer than the length of the sensor in any direction. This was not due to in-plane sensitivity, as no presence of the S0 Lamb wave mode was observed in the ring sensor response. The second harmonic was also more pronounced in the transverse excitation. These effects may warrant further theoretical investigation.

The tuning curves of Figure 9.16 have an artificially induced appearance of a wideband-type response. This can be seen by contrasting them with the chirp response of the free ring sensors from Chapter 8 which has numerous closely spaced resonance modes. This is because in the chirp, frequency components are directly calculated via FFT (or in the time-domain, the response has the same shape as the FFT). In contrast, each frequency data point in a tuning curve contains a significant portion of energy from a nearby frequency range. The bandwidth is inversely proportional to the time-duration of the signal (Giurgiutiu 2014); increasing the number of tone burst counts decreases the bandwidth, and increasing the excitation frequency increase the bandwidth. Therefore, each data point

in the tens of kHz averages frequency content in a local neighborhood that is tens of kHz wide. It becomes more predominant in the higher frequency ranges, where frequency content from a region hundreds of kHz wide is averaged to obtain a single nominal frequency point of a tuning curve.

This indicates that, although a tuning curve approach can identify the ring sensor's wideband characteristics, it is not able to assess the granularity of the frequency response. This is corrected in the calibration experiments of Chapter 11.

9.3.6 Pitch-Catch Experiment and Miniature Ring Sensor Fundamental Resonance

The performance of the miniature ring sensor was assessed at its resonance frequency. A 20 V_{pp} 3-count Hanning windowed tone burst was transmitted by the 150 mm longitudinal PWAS at 52.2 kHz. No signal averaging was performed to assist in measuring an accurate assessment of sensor signal-to-noise ratio. The PWAS on the plate, the FBG on the plate, and the FBG on the miniature ring sensor were used as receivers. The response of each sensor is shown in Figure 9.17. The FBG on the miniature ring sensor had a visibly higher SNR compared to the other two sensors.

9.3.7 Testing for FBG Buckling in a Two-Point Bonding Configuration

One concern about the use of a two-point bonding FBG technique was that it may buckle in compression, or otherwise exhibit nonequivalent FBG response in tension and compression. To assess this, the pitch-catch was repeated, with the PWAS excited with the negative of the tone burst. This caused the flipping of the compression and tension in the propagating wave, ring sensor, and optical fiber. The response of the FBG on the miniature ring sensor to both waveforms is shown in Figure 9.18. When the excitation was inverted, the response was inverted without any phase shifts, loss in amplitude, etc. This indicated

that the optical fiber did not suffer from buckling or nonequivalent tension and compression response. This may be due to the pretension applied. It was also possible that longitudinal waves propagate down the fiber, and even if the fiber can buckle, it was not a concern from a wave propagation perspective.

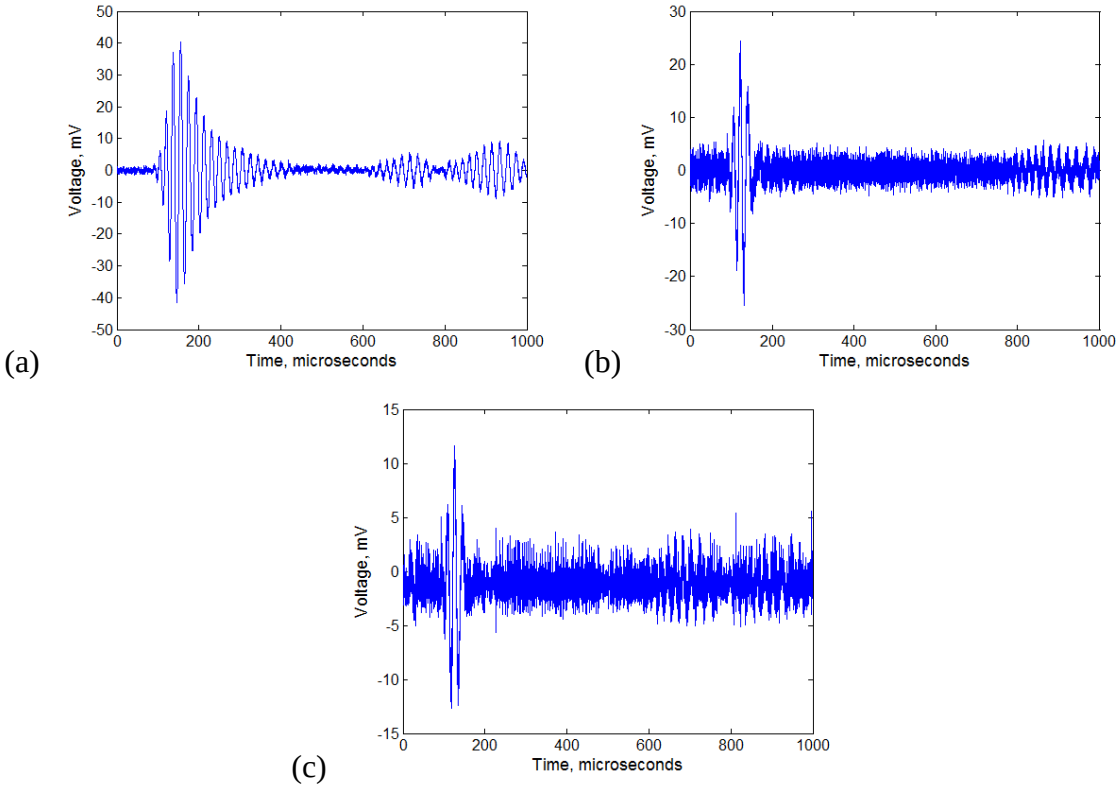

Figure 9.17: A high SNR is observed for sensors responding to a 150 mm PWAS excitation for (a) the miniature mm ring sensor FBG, as compared to (b) the plate-bonded FBG and (c) the plate-bonded PWAS response

9.3.8 Pencil-Lead-Break Response

PLB-AE events were excited using 0.5 mm 2H lead, 100 mm away from the sensor cluster in the longitudinal direction. The response of each sensor can be seen in Figure 9.19. The PWAS had an initial high frequency burst, followed by a low-frequency flexural component commonly seen in PLB on plate faces (caused by a release in downwards pressure). The FBG on the plate sensed primarily in the low frequency range, below 200

kHz, and had a small flexural component. It had a visibly low SNR, and several noise peaks are apparent in the frequency domain. The FBG on the 8 mm ring sensor had a number of peaks near 80 and 260-350 kHz. The FBG on the miniature ring sensor had one sharp resonance at approximately 50 kHz, with other peaks approximately at 200 and 390 kHz.

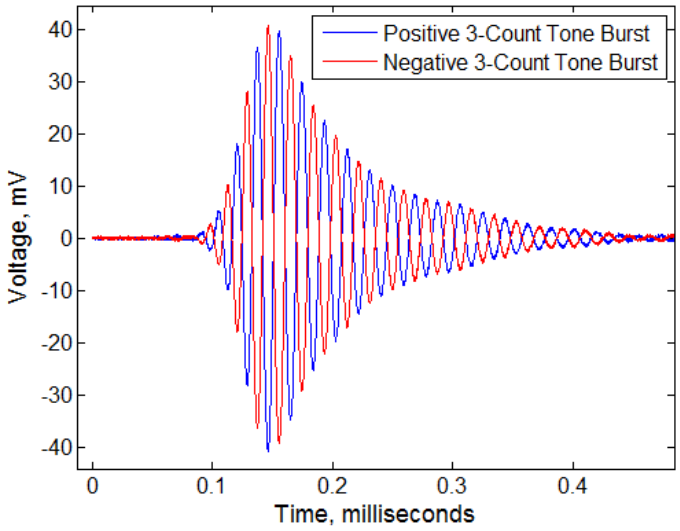

Figure 9.18: No difference in miniature ring sensor FBG tension/compression behavior was observed when comparing two Hanning windowed tone burst excitations, one the negative of the other

The miniature ring sensor filtered out the flexural component of the AE event (Figure 9.19g,h), where the other sensors, even the original mm ring sensor, did not. The SNR of the miniature ring sensor was also much higher than the other sensors. This is quantified in Section 9.4.

9.3.9 Lumped Parameter Model of the Ring Sensor

The response of the ring sensor near its fundamental resonance frequency is well-characterized by a 1 DoF model of a mass-spring-damper. Initially, the purpose was to add damping. Although later comparisons found the degree of ringing comparable to a commercially available R15α AE sensor in a Lamb wave response on a 1 mm plate.

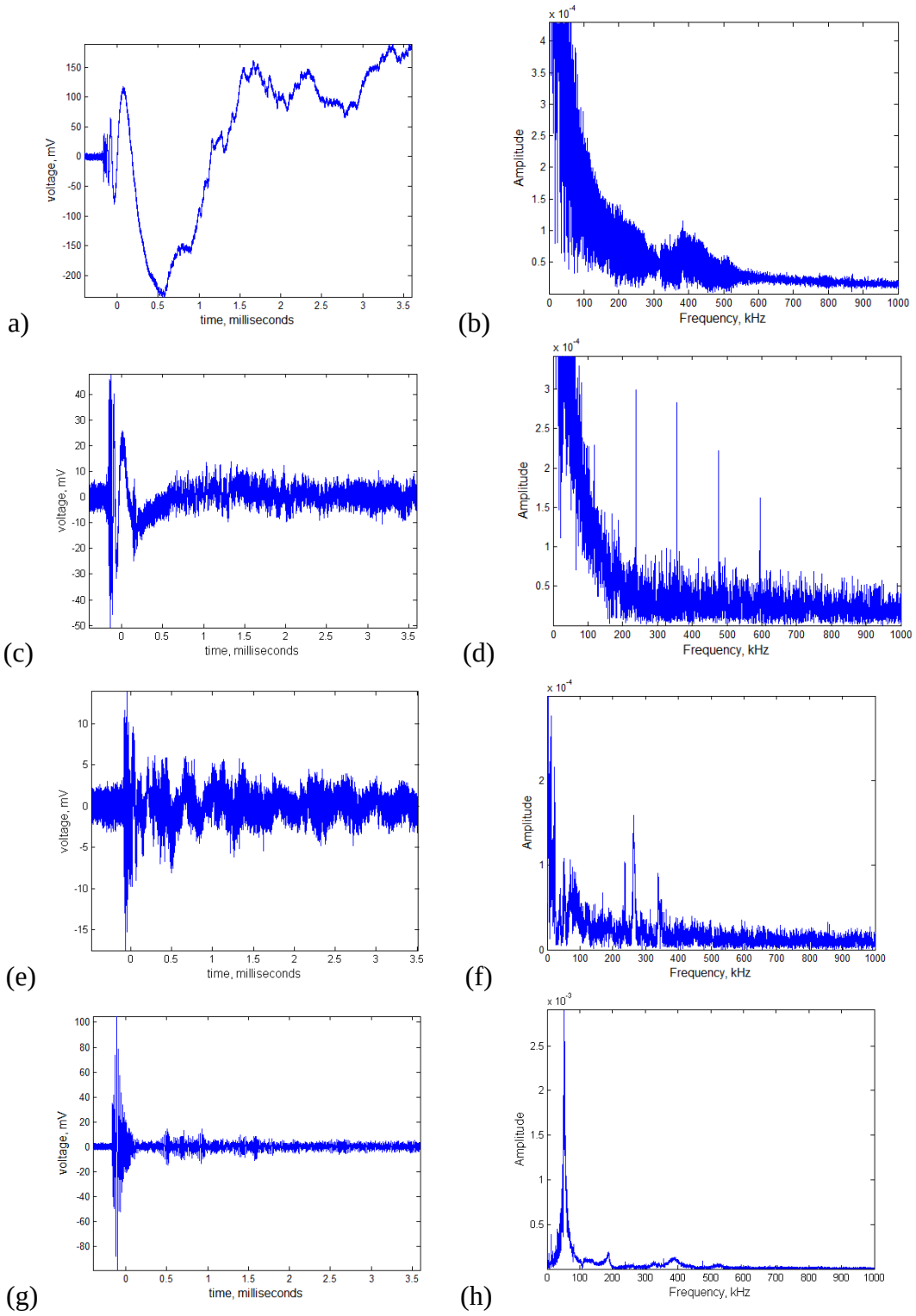

Figure 9.19: longitudinal PLB-AE waveforms sensed by (a, b) PWAS on the plate, (c, d) FBG on the plate, (e, f) original ring sensor FBG, and (g, h) miniature ring sensor FBG

Perhaps more pertinently, the sensitivity advantages of the ring sensor are important for improving the sensitivity limitations of the FBG, and these improvements would be mitigated by added damping.

The choice was to maintain the ring sensor as a resonant sensor to maintain improved sensitivity (refer the review of AE sensors in Chapter 4 for further detail on resonant versus broadband AE sensor design concepts).

The 1 DoF lumped parameter model is useful for understanding ring sensor characteristics, particularly near its fundamental resonance frequency. Most notably, it permits experimental measurement of the modal damping ratio. The model used was

$$\ddot{x} + 2\varsigma\omega_0\dot{x} + \omega_0^2 x = F(t) \tag{9.1}$$

where x is the ring sensor response. Nominally in a 1 DoF mass-spring damper model, x would be displacement, although it is normalized for comparison with voltage in experiments. The parameters ζ, ω_0, and $F(t)$ are the modal damping ratio, natural frequency, and forcing function, respectively. The input damping ratio was obtained using the logarithmic decrement approach:

$$\delta = \frac{1}{n}\ln\frac{x(t)}{x(t+nT)} \quad , \quad \zeta = \frac{1}{\sqrt{1+(2\pi/\delta)^2}} \tag{9.2}$$

where $x(t)$ is the amplitude of a given local peak, and $x(t+nT)$ is the amplitude of a peak n periods T away. Approximations for the damping ratio were used by calculating the damping ratio estimates associated with an initial peak $n=0$ and subsequent peaks $n=1,2,...$. It was found that using peaks too close to the peak associated with the maximum response caused high discrepancies between damping ratio estimates. When referencing each damping ratio estimate to the 6th peak after the initial maximum, the

variance was low. The average of the estimates until signal decay was used to calculate the damping ratio. It was found to be $\zeta = 3.3\%$ which is rather high if aluminum alloy and fused silica are to be considered. The high degree of damping most likely comes from the cyanoacrylate adhesive used to bond the FBG and PWAS to the ring sensor, and the sensor to the plate. It is also generally observed with commercial AE sensors bonding decreases the amount of ringing (i.e. increases modal damping).

The excitation frequency was 52.2 kHz with a 3-count Hanning window tone burst input given by

$$F(t) = \frac{1}{2}(1-\cos(2\pi ft / N_b))*\sin(2\pi ft) \tag{9.3}$$

where N_b is the number of counts. The analytical response was calculated by taking the multiplying the transfer function of (9.1) in the Laplace domain by the Laplace transform of (9.3). This was followed by taking the inverse Laplace transform. The excitation frequency f was set to 52.2 kHz to match the pitch-catch experiment shown in Figure 9.17. The natural frequency was modified by trial and error to be 53.0 kHz to best match the analytical and experimental signals. A normalized comparison between the experimental and analytical signals is shown in Figure 9.20. The two waveforms match very well, particularly since the dispersion effects of the Lamb wave along the 150 mm propagation path were not taken into consideration.

This model does not account for the directional dependence of the ring sensor response, although a directional correction factor could be incorporated into it. Additionally, it only models the ring sensor's fundamental resonance and does not account for its higher harmonics. It provides a simplified basis for ring sensor conceptualization; for example, in the 1 DoF model, reducing stiffness increases the value of the forcing

function (in the forced mass-spring damper model, the forcing function is stiffness-normalized). The stiffness parameter is related to the ring sensor wall thickness. To maintain a given resonance frequency, the mass, i.e. the ring outer diameter must be reduced. This gives an intuitive means for understanding why miniaturization combined with reducing wall thickness increased the sensor response.

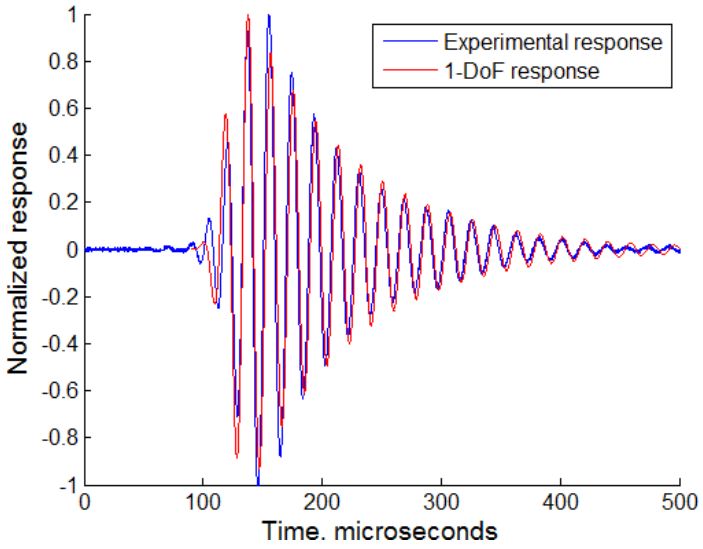

Figure 9.20: Normalized 1-DoF system response of the ring sensor and comparison to experimental 3-count Hanning windowed tone burst A0 mode response

9.4 Quantitative Assessment of Ring Sensor Noise

9.4.1 Signal-to-Noise Ratio for Characterizing Noise Levels

The SNR is a simple and useful way of obtaining a characterization of sensor amplitude. Sensitivity characterization (sensor output per unit input motion) does not entirely account for the sensor performance as noise sources can dominate even for a high-sensitivity sensing configuration. For example, using an intensity modulation approach, a pi-FBG has a much higher sensitivity than a standard FBG. However, when the tunable laser source noise is the dominant noise source, the noise increases proportionately with

sensitivity as shown in Chapter 7. In this case the SNR would show no change in performance, whereas increasing sensitivity values would not correlate to improved sensing capabilities.

Sensor resolution is another useful metric. It is defined as the smallest amplitude (e.g. strain) that the sensor can resolve. This is commonly taken as the amplitude which produces a SNR of 1.

The SNR is the ratio of signal power to noise power, i.e.

$$SNR = \frac{P_{Signal}}{P_{Noise}} = \left(\frac{V_{Signal}}{V_{Noise}} \right)^2 \tag{9.4}$$

where P represents power and V represents voltage. The voltage ratio holds true if the signal and noise are calculated across the same impedance. SNR can also be defined in decibels, as

$$10\log_{10}\left(\frac{P_{Signal}}{P_{Noise}} \right) = 20\log_{10}\left(\frac{V_{Signal}}{V_{Noise}} \right) \tag{9.5}$$

Although not difficult, care must be taken to accurately represent the SNR in a repeatable manner. The difficulty comes in defining the signal and noise amplitude. Different definitions are admissible. For the signal voltage one can use maximum absolute value of voltage, peak-to-peak voltage, height of the signal envelope, etc. For noise voltage, RMS voltage is commonly used, although peak to peak noise has been used. The vertical distance, in dB, between the noise floor and the largest peak in the frequency spectrum has even been used. None of these approaches are inappropriate if they are properly defined. However, frequently SNR calculations are given in sensor literature without context, which makes replicating them unfeasible. For SNR calculations in this research, the signal is taken as the full peak-to-peak of the signal, and the noise is taken as the RMS of the noise. The

noise is calculated from the pre-trigger region of the signal prior to arrival of the first waveform.

9.4.2 Effect of Bandwidth Reduction on Noise Levels

As seen in Chapters 5 and 6, it is common to represent sensitivity and resolution normalized by a $\sqrt{Bandwidth}$ factor. This is because in the presence of white noise, noise levels per unit $\sqrt{Hz}$ are constant. Because of this, noise levels can be measured over a smaller bandwidth, e.g. through digital or analog filtering. An experiment was performed to verify this effect for our optical system. The optical system was powered at 10 mW excitation, reflecting off the half-maximum point of an FBG in the absence of an excitation signal. The Thorlabs PDA10CF photodetector was used to convert the optical power to voltage, and the oscilloscope was AC coupled to detect the AC component of the noise. The sampling rate was set to 12.5 MHz. At lower sampling frequency, the noise level varied with sampling frequency. A 12.5 MHz sampling rate was high enough that the noise level did not significantly vary with changes in sampling rate. A noise sample of 200 μs of noise was captured. The signal and its single-sided amplitude spectrum in the frequency domain can be seen in Figure 9.21a,b.

A MATLAB program for a 3rd order Butterworth band pass filter with a variable bandwidth and center frequency was created. A Monte Carlo simulation was performed where the bandwidth and center frequency were randomly chosen within a uniform probability distribution. The filter with each given bandwidth and center frequency was applied to the noise capture, and the RMS value of the noise was calculated. Figure 9.21c shows the relationship between $\sqrt{Bandwidth}$ and RMS noise voltage. A highly linear

relationship ($r^2 = 99.9$) between the two demonstrates the capability to reduce noise levels by reducing the bandwidth of data acquisition.

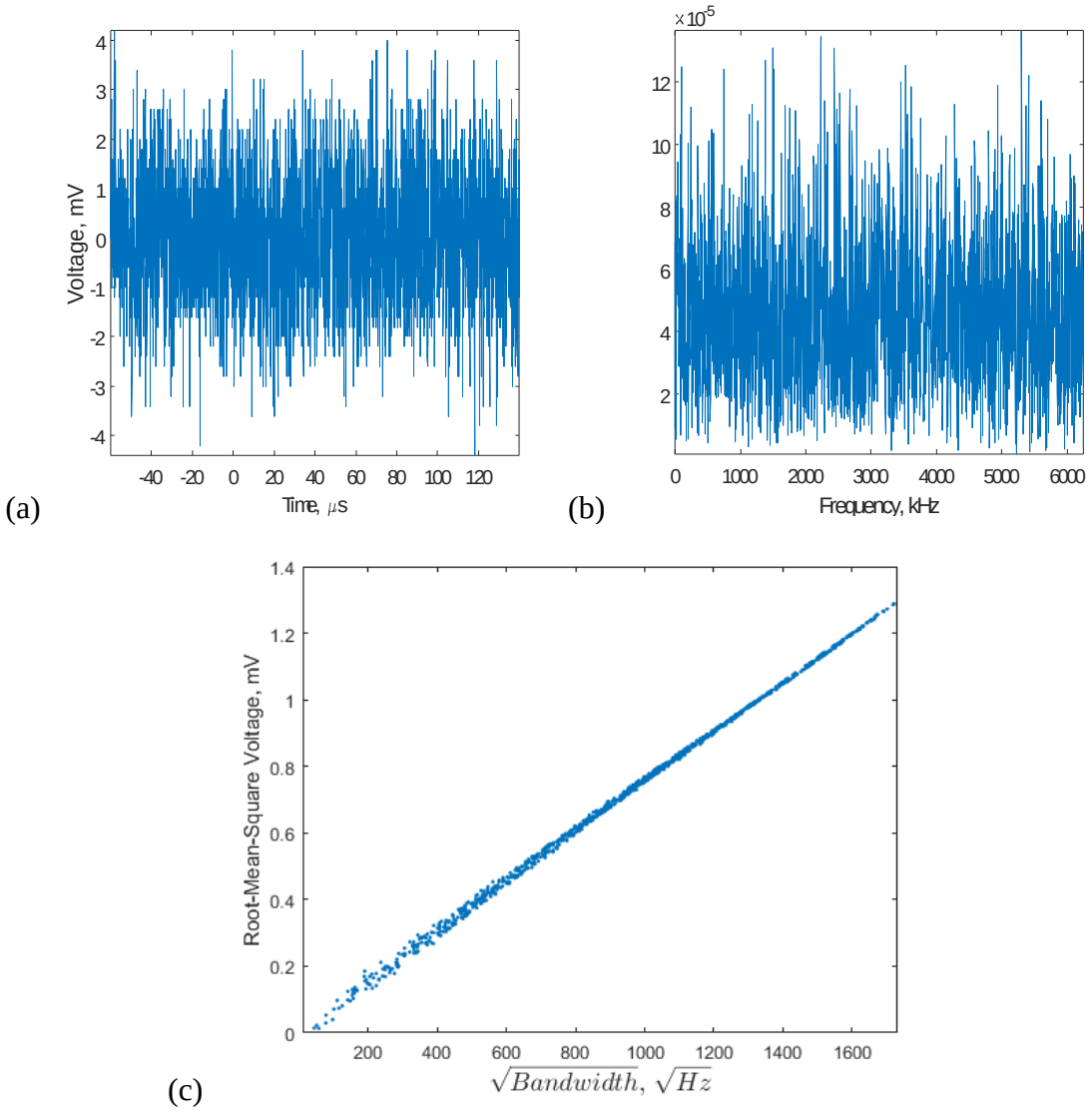

Figure 9.21: (a,b) Time and frequency optical system noise, and (c) effect of sensing bandwidth on optical system noise

The reduction of noise levels with reduced sampling bandwidth is a feature that should be implemented when sensing occurs in a pre-established and narrowband frequency range. When mechanical amplification occurs within a limited frequency range, an analog or digital filter can be used to improve sensor resolution and SNR.

Applying this principle to the PLB-AE signals, a 3rd order Butterworth 20-80 kHz band pass filter was applied to the pitch-catch response of the FBG on the 3.2 mm ring sensor (Figure 9.22). A large reduction in noise was seen with little reduction in signal amplitude. This is because this response is dominated by the ring sensor's fundamental resonance.

The PLB-AE waveforms from Figure 9.19 were also filtered. The filtered waveforms are shown in Figure 9.23. The noise was reduced for all four signals. For the PWAS on the plate and the FBG on the plate, the signal amplitude was also reduced as the frequency response was more broadband. For the FBG on the 8 mm ring sensor (Figure 9.23c), the signal amplitude was slightly reduced, which can be attributed to filtering out the sensor's second resonance. For the FBG on the miniature mm ring sensor (Figure 9.23d), the reduction in signal amplitude was quite small.

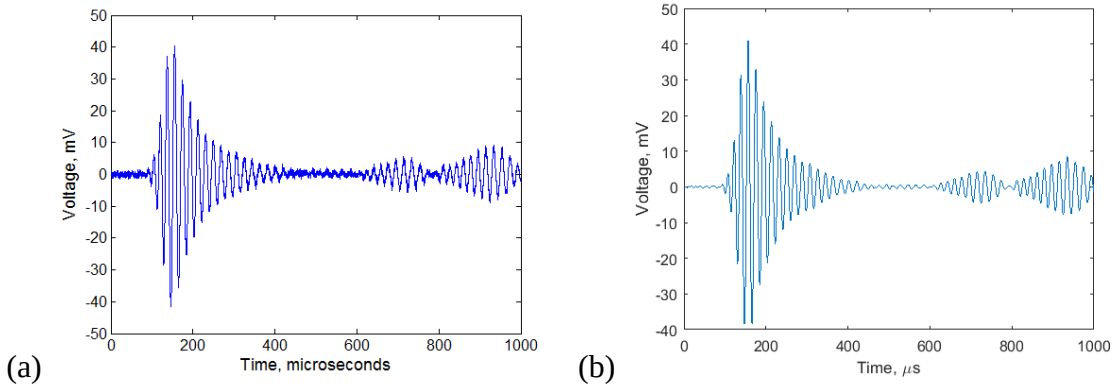

Figure 9.22: Effect of filtering on the miniature ring sensor FBG pitch-catch response, (a) raw signal and (b) filtered signal

9.4.3 Pitch-Catch and Pencil-Lead-Break Signal-to-Noise Ratio Calculations

The SNR was calculated for the pitch-catch and PLB experiments from Section 9.3.4, as well as the filtered signals from Section 9.4.2. Table 9.1 shows signal, noise, and SNR calculations for the pitch-catch excitations. Both the filtered and unfiltered waveform

for the FBG on the 3.2 mm ring sensor were used. The FBG on the 3.2 mm ring sensor had an SNR 19.2 dB higher than the plate-bonded PWAS, and 14.1 dB higher than the plate-bonded FBG.

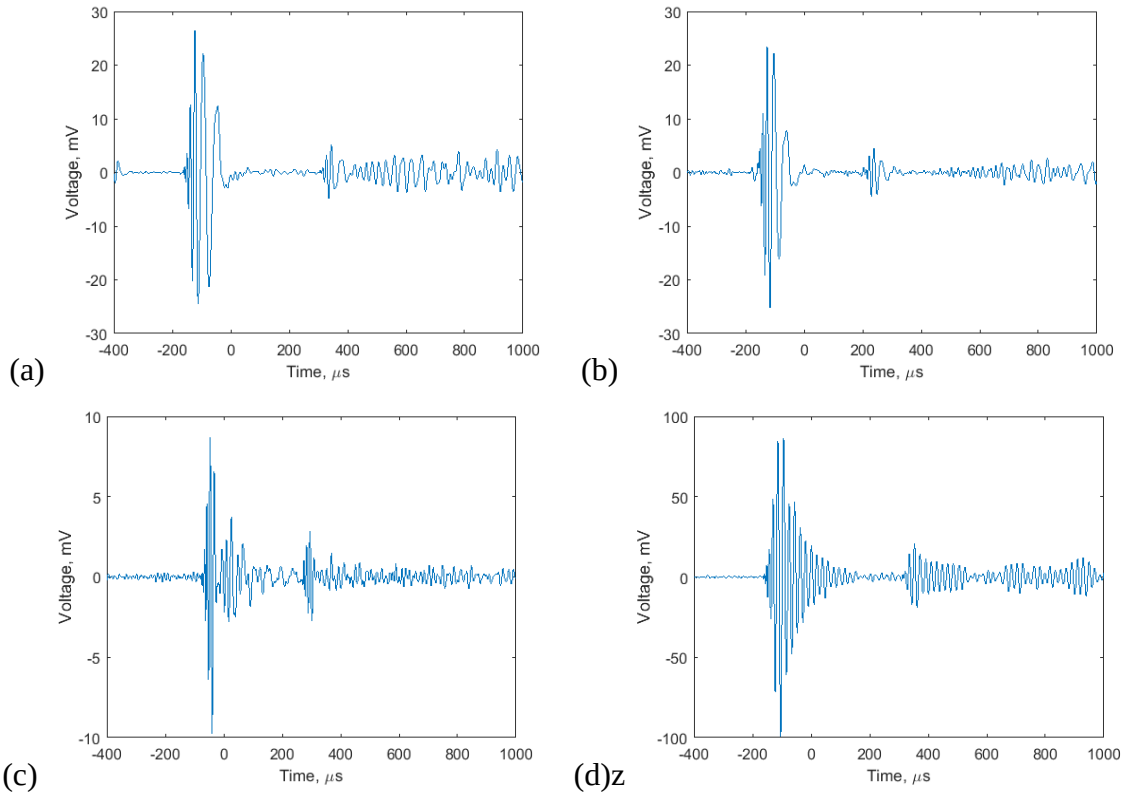

Figure 9.23: Filtered PLB-AE responses for (a) PWAS on the plate, (b) FBG on the plate, (c) FBG on the 8 mm ring, and (d) FBG on the 3.2 mm ring.

Table 9.1: Signal, noise, SNR, and SNR_{dB} for longitudinal pitch-catch waveforms

Sensor	Peak-to-Peak Signal, mV	RMS Noise, mV	SNR	SNR, dB
PWAS on Plate	24.3	1.32	338	25.3
FBG on Plate	49.9	1.50	1,108	30.4
FBG on 3.2 mm Ring (unfiltered)	81.9	0.49	28,173	44.5
FBG on 3.2 mm ring, (filtered)	79.42	0.11	568,671	115.1

This is significant enough that it can be attributed to mechanical strain amplification via the ring sensor. When the band pass filter was applied, the filtered signal has an SNR which is 70.6 dB higher than the unfiltered signal.

Table 9.2 shows signal, noise, and SNR calculations for the PLB-AE excitations. For the PLB-AE excitation of the PWAS, the peak-to-peak signal was taken only from the initial burst, and this is closer to the burst-type AE received during damage-induced AE experiments. The FBG on the 3.2 mm ring sensor had SNRs 22.1 dB, 11.9 dB, and 14.5 dB higher than the PWAS on the plate, FBG on the plate, and FBG on the 8 mm ring sensor, respectively. The performance was better for the PLB-AE than for the pitch-catch excitation. This was surprising, as the PLB-AE was a broadband excitation. One possible explanation for this behavior was that the time duration of the PLB-AE is longer, such that more mechanical amplification occurs due to ring sensor resonance effects.

Table 9.2: Signal, noise, SNR, and SNR_{dB} for longitudinal unfiltered PLB-AE

Sensor	Peak-to-Peak Signal, mV	RMS Noise, mV	SNR	SNR, dB
PWAS on Plate	54.4	3.30	272	24.4
FBG on Plate	98.9	1.84	2,894	34.6
FBG on 8.0 mm Ring	31.4	0.78	1,590	32.0
FBG on 3.2 mm Ring	203.7	0.95	45,173	46.5

Table 9.3 shows signal, noise, and SNR calculations for the filtered PLB-AE excitations. Gains in SNR from filtering were significant, with increases of 56.0 dB (plate-PWAS), 59.6 (plate-FBG), 57.2 dB (8 mm ring-FBG), and 67 dB (3 mm ring-FBG). The FBG on the 3.2 mm ring sensor had the highest gain in performance with filtering, as its

response is dominated by the fundamental resonance, where the other sensors detected more broadband frequency content.

Table 9.3: Signal, noise, SNR, and SNR_{dB} for longitudinal filtered PLB-AE

Sensor	Peak-to-Peak Signal, mV	RMS Noise, mV	SNR	SNR, dB
PWAS on Plate	50.8	0.50	10,495	80.4
FBG on Plate	48.7	0.21	51,520	94.2
FBG on 8.0 mm Ring	18.4	0.11	28,913	89.2
FBG on 3.2 mm Ring	189.4	0.28	471,447	113.5

With filtering applied, the FBG on the 3.2 mm ring sensor response was 19.3 dB higher than the FBG on the plate; a large proportion of this is due to the degree of mechanical strain amplification, as it is too large to be accounted for by the difference in sensing mechanism. In practice, the particular waveform detected will modify this effect.

9.5 Ring Sensor Experiments on a Specimen Under Load

In two experiments, fiber-optic and piezoelectric sensors were assessed on 100 mm x 300 mm x 1 mm Al-2024 T3 specimens (Figure 9.24). The first specimen was instrumented with PWAS (0.7 mm diameter, 0.2 mm thick) and FBG; the second specimen was instrumented with a miniature ring sensor, a PWAS, and MISTRAS R15α sensor.

The specimen was loaded in MTS grips, and it allowed for testing three things:

- Determining whether the miniature ring sensor is insensitive to quasi-static strain, compared to surface-bonded FBG which are sensitive to quasi-static strain.
- Determining if the miniature ring sensor detects waveforms in the presence of large structural strains
- Determining if the miniature ring sensor can detect waveforms from fatigue crack-generated AE events.

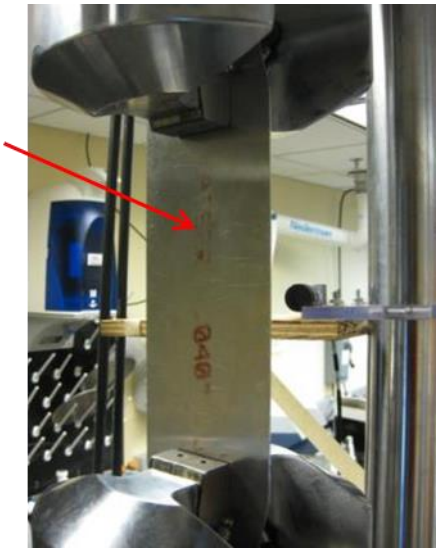

Figure 9.24: Aluminum test specimen in MTS grips for fatigue test

The optical and data acquisition instrumentation used in this experiment is shown in Figure 9.25. The fiber-optic data acquisition was performed using the MISTRAS Micro-II digital AE system.

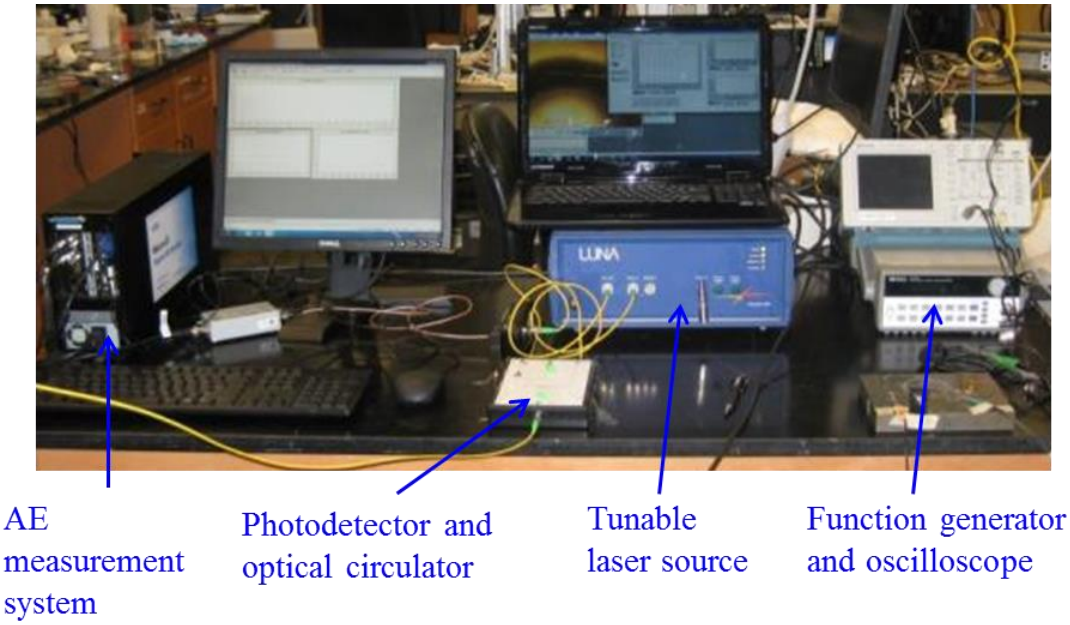

Figure 9.25: Data acquisition system setup for fiber-optic static strain and AE tests

9.5.1 Surface-Bonded FBG –Static Strain Effect

First, a 1 mm central hole was drilled in the aluminum specimen, and it was loaded in low cycle fatigue ($R = 0.1$, $\sigma_{\max} = 0.65\sigma_{Yield} = 0.65 \cdot 345$ MPa) to grow an approximately 20 mm long fatigue crack. Microscopic measurements indicated that the fatigue crack length was 17.6 mm (Figure 9.26). The fatigue crack was a butterfly crack, with half of the crack extending from each side of the 1 mm hole, perpendicular to the loading axis. After the fatigue crack was generated, two PWAS and two FBG sensors were bonded (Figure 9.27). The FBG were bonded perpendicular to the loading axis to bond the best case scenario for sensor operation, where static strain along the longitudinal FBG axis was minimized.

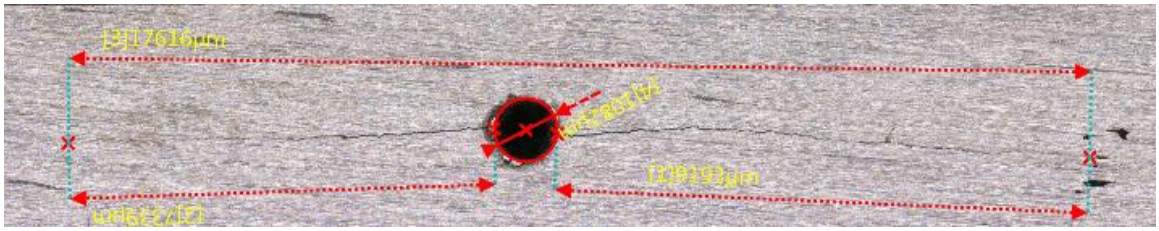

Figure 9.26: Microscopic measurements indicated the fatigue crack length was 17.6 mm.

Static tensile tests were conducted to calculate the FBG peak wavelength shift under load and verify that the FBG wavelength shift would be sufficient to cause the plate-bonded FBG to cease measurement of dynamic strain measurement. This was done by measuring the FBG peak wavelengths at 0 kN and 12.3 kN tensile load. A rough calculation on the stress levels was performing by calculating $\sigma = F / A$ for an area reduced by the 20 mm crack length, i.e. 80 mm x 1 mm. This put the stress for this load approximately at 45% of the yield stress (with this approach, 65% of the yield stress was associated with 18.0 kN). Wavelength shifts were measured in experiment by measuring the FBG peak

wavelengths at 0 and 12.3 kN tensile load. The measured wavelengths at each load were subtracted to obtain a wavelength shift.

To obtain theoretical predictions of strain and FBG wavelength shift, a static FEM analysis was performed on a 100 x 300 x 1 mm aluminum 2024-T3 plate with a 1 mm hole and a 20 mm butterfly crack (this model was run concurrently with crack length measurements, so the exact crack length was not used). The butterfly crack was modeled by a 1 µm wide notch. A pair of 12.3 kN loads was applied to the faces on each side of the plate, and the transverse surfaces strain was measured at 5 mm and 25 mm away where the FBG were located.

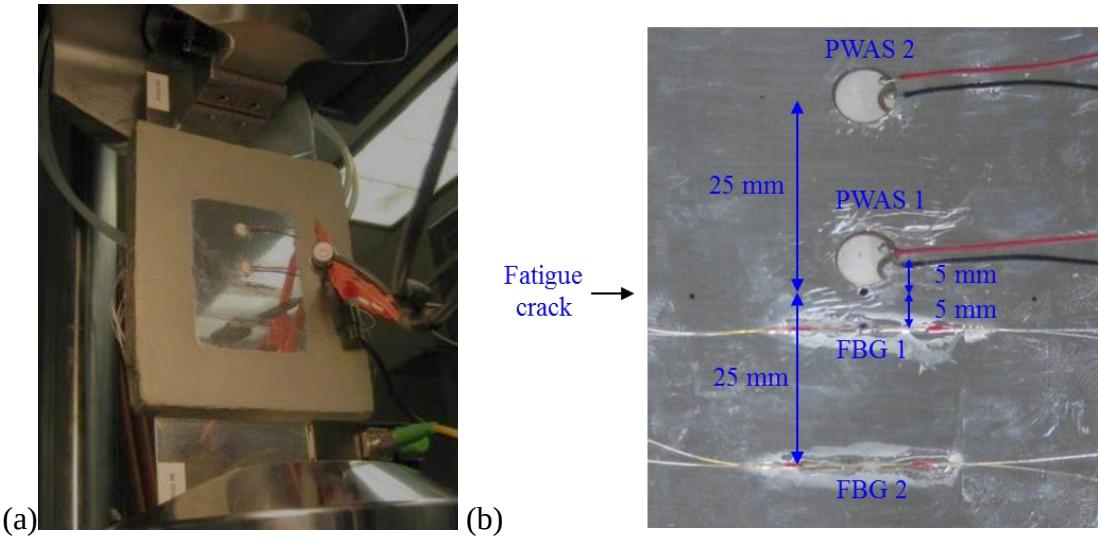

Figure 9.27: (a) Aluminum specimen outfitted with sensors in tensile loading frame, and (b) FBG and PWAS bonded symmetrically about a fatigue crack

The model setup is shown in more detail in Figure 9.28. The transverse strains were converted into wavelength shift predictions using the equation:

$$\frac{\Delta\lambda_B}{\lambda_B} = \left(1-\rho_e\right)\varepsilon \tag{9.1}$$

The experimental wavelength shifts were on the same order of magnitude as the FEM predictions (Table 9.4), although FEM over predicted the shift for the FBG 5 mm

away from the crack. This is believed to be due to the discrepancy in experimental (17.1 mm) and FEM crack length (20 mm).

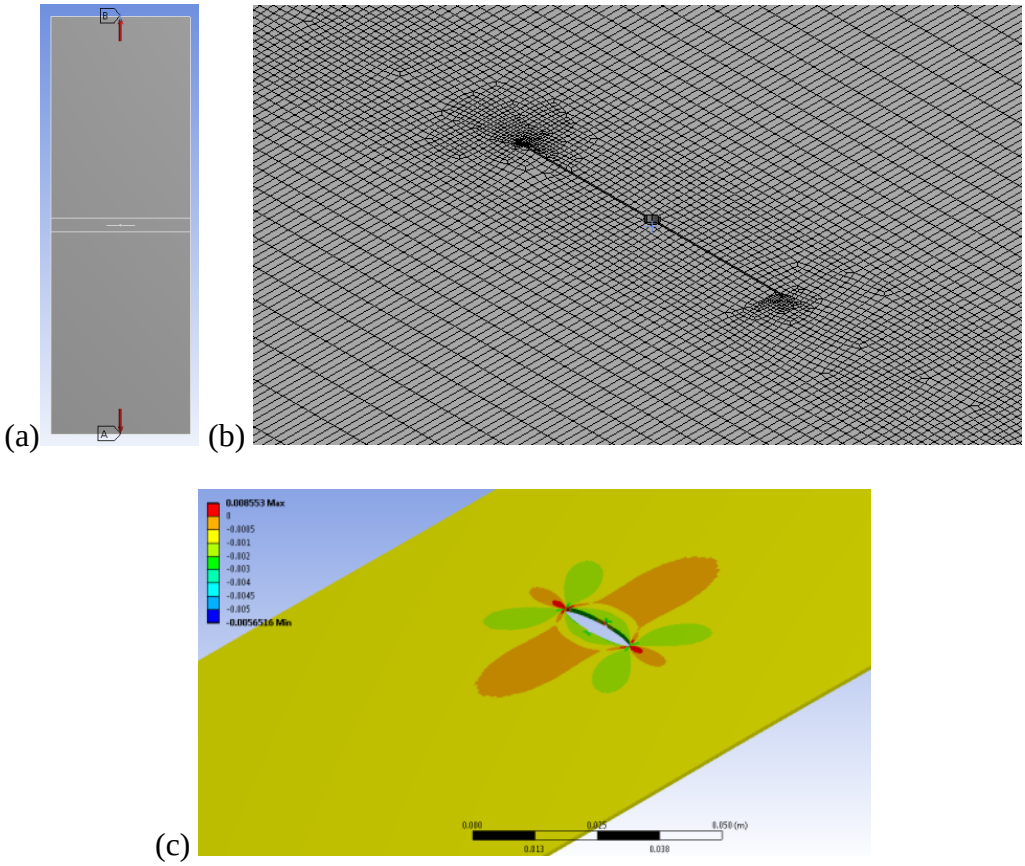

Figure 9.28: Static FEM of the aluminum plate fatigue-AE specimen

The FEM simulation also predicted a significant variation in strain across the length of the 5 mm away FBG (Figure 9.29). This was seen in the experiment by perturbations in the shape of the FBG spectrum, although the spectrum still had a monotonic increase and decrease with a single peak.

Table 9.4: FEM-Predicted and Experimental Bragg Wavelength Shift

FBG Distance from Crack, mm	FEM Transverse Strain, με	Predicted Wavelength Shift, nm	Experimental Wavelength Shift, nm
5	-402	0.49	0.34
25	-355	0.43	0.51

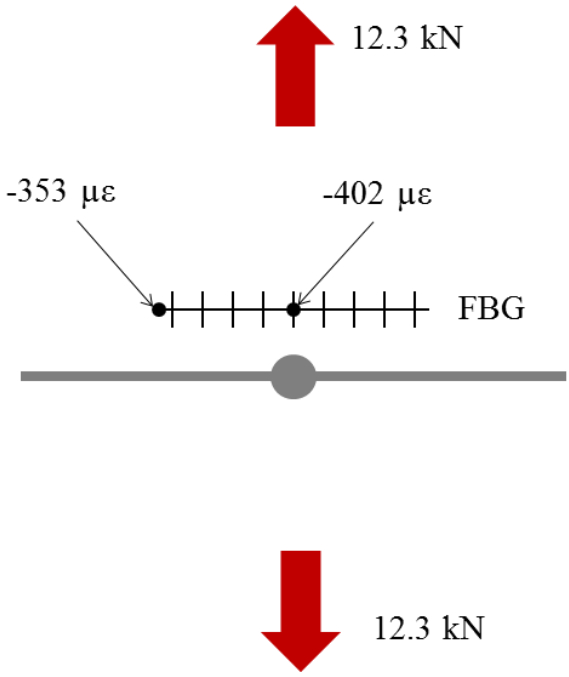

Figure 9.29: FEM calculations of transverse strain variation explain the deviations in the FBG spectrum observed at high loads

From the experimental wavelength shifts of 0.34 and 0.51 for the FBGs 5 mm and 10 mm away from the crack, these FBGs could sense waveforms only within a ±0.9 kN and ±0.6 kN range. This was an extremely narrow window of strains that could be calculated if these sensors were to be used in fatigue tests.

9.5.2 Surface-Bonded FBG – Pencil Lead Break AE Capture

A series of PLB-AE experiments were performed at 0 kN, 1.23 kN, 5.54 kN, and 12.3 kN tensile loads with their respective laser wavelength set at half-maximum calibration point. The PLB were applied to the front face of the plate and were easily detected from over 50 mm away. This verified the functionality of the optical setup (Figure 9.30).

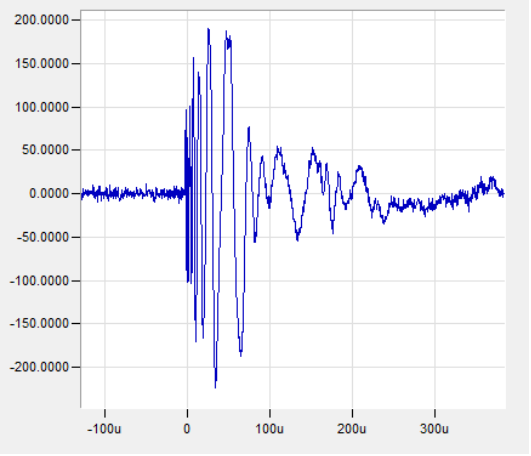

(b)

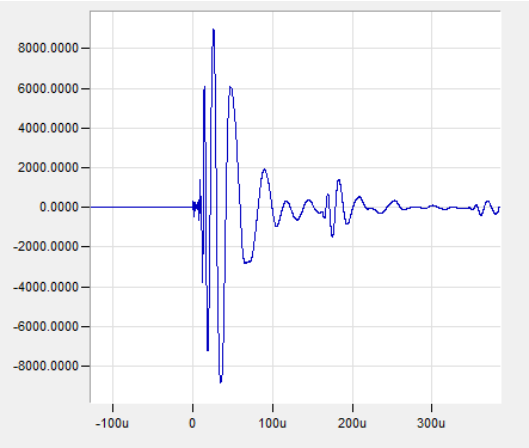

Figure 9.30: PLB waveforms to establish functionality of the FBG equipment for (a) FBG 5 mm away from the crack, and (b) PWAS 5 mm away from the crack

9.5.3 Surface-Bonded FBG – Attempts at Fatigue-AE Capture

An AE experiment was attempted. The wavelength where the FBG would get maximum coverage at the peak tensile load during cycling was calculated and used to set the half-maximum calibration point for the FBG spectrum (Figure 9.31). 600 fatigue cycles with sinusoidal loading between 1.23 – 12.3 kN at 4 cycles/second yielded thousands of AE waveforms detectable by the PWAS, but not by the FBG. For example, over an arbitrarily chosen 150 fatigue cycles, the PWAS 5 mm away captured 1130 AE waveforms and the PWAS 25 mm away captured 571 AE waveforms. Then, the laser wavelength was set so the FBG could capture several different windows at the top, bottom, and middle loads of the tensile test, but no AE signals were captured. 50 cycles with a slower loading rate (1 cycle / 20 seconds) was tested so it could be observed that AE waveforms received by each PWAS were excited while the FBG wavelength was in a range capable of dynamic sensing. Most of the AE events occurred close to the peak load.

The orientation of the FBG longitudinal axes was another consideration which may have affected sensing. The FBGs were 90° off-axis from the maximum sensing direction

for the AE events. However, the FBGs were still capable of detecting a significant strain component due to Poisson effects, with the Poisson ratio at 0.33 in aluminum 2024-T3. The reduction in amplitude due to off-axis sensing would not have prevented the FBGs from detecting AE events if they were sufficiently sensitive for this application. Since the FBG and optical system were performing as expected, and the laser wavelength calibration was appropriately configured to detect AE events within its narrow window, it could be concluded that the plate-bonded FBG was not sufficiently sensitive to detect AE events.

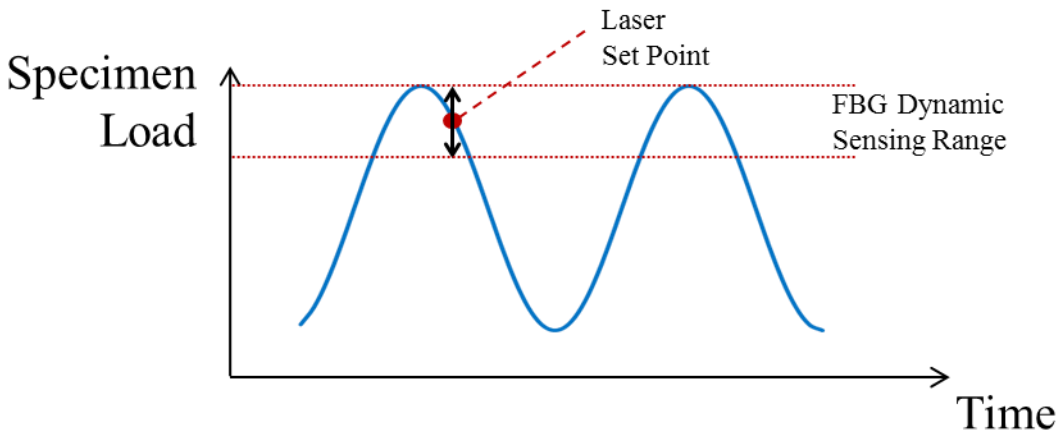

Figure 9.31: Tunable laser fixed wavelength set slightly off maximum load for maximum FBG sensing coverage during fatigue loading

9.5.4 Ring Sensor FBG –Static Strain Effect and Attempts at Fatigue-AE Capture

Static strain, pitch-catch, and fatigue-AE tests were performed with the ring sensor on an identical fatigue specimen with a 20 mm fatigue butterfly crack (Figure 9.32). Again, the fatigue crack was grown without the sensors present to ensure the sensor bonding was pristine at the beginning the experiments. A miniature ring sensor (with FBG and PWAS), a PWAS, and a commercially available MISTRAS R15α resonant-type sensor were bonded 25 mm away from the crack (the R15α sensor was bonded on the opposite side of the plate from the PWAS).

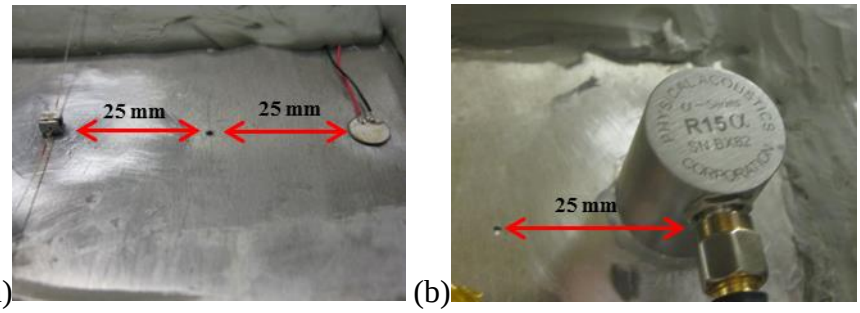

(a) (b)

Figure 9.32: (a) Front side of specimen with ring sensor and PWAS, and (b) back side of specimen with R15α sensor

Just as for the previous specimen, the FBG wavelength shift was calculated under static tensile loading, this time between 0 kN – 16.0 kN. A 0.070 nm shift was measured. This is comparable to the 0.20 nm linear portion of the FBG curve. A screenshot of the user interface (Lin and Giurgiutiu 2014a) for the FBG optical system is shown in Figure 9.33.

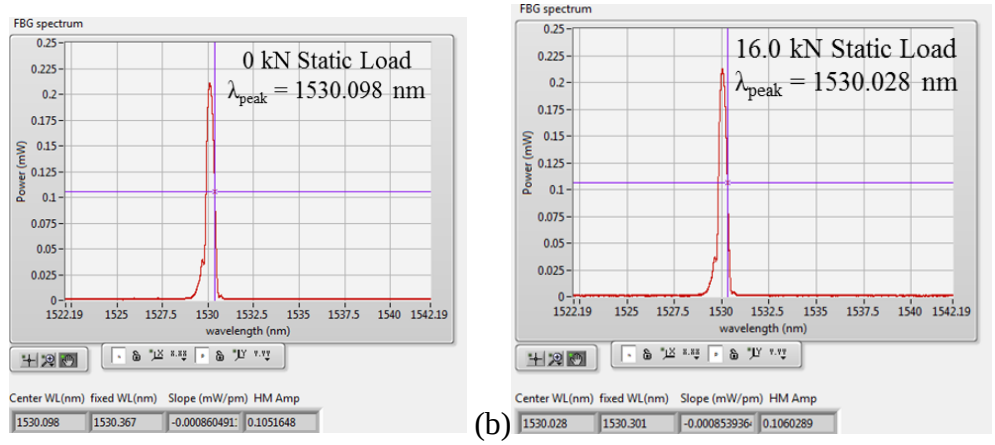

(a) (b)

Figure 9.33: 0.070 nm wavelength shift observed from miniature ring sensor FBG (a) under 0 kN load, and (b) under 16.0 kN load

The wavelength shift comparison between the ring sensor FBG and plate-bonded FBG were performed with the same sensor location, same FBG orientation, and same crack length. After compensating for difference in load, it was calculated that the ring sensor FBG sensed a quasi-static strain that was 9.5 times smaller than for the plate-bonded FBG. This indicates that the ring sensor reduces severity to quasi-static strain, but does not

completely provide quasi-static strain insensitivity; however, it allows the ring sensor FBG wavelength to be calibrated at zero load, and to function at least up to the point of yielding in aluminum. However, the FBG must be chosen carefully. The size of the linear range observed with the 10 mm FBG would not be sufficient for sensing with this level of quasi-static strain reduction. However, the miniature ring sensor used in this experiment required the use of a 3 mm FBG; the smaller FBG served as a wider wavelength filter, providing a sufficiently large linear portion of the curve.

Just as for the other specimen, the PLB response was tested at 0 kN, 5.54 kN, and 12.3 kN. The difference here is that the laser wavelength was calibrated at the 0 kN load only. Each sensor, including the ring sensor FBG registered a response. AE tests were also performed at 4 seconds/cycle and 20 seconds/cycle with loading between 1.23 – 12.3 kN. Just as with the plate-bonded FBG, no AE events were captured by the ring sensor FBG.

To determine if AE events could be detected, a PWAS and ring sensor were placed in the immediate vicinity of the crack (Figure 9.34). The specimen was loaded between 1.8 – 18 kN with a loading rate of 1 cycle/second. Laser wavelength calibrations were performed at 1.8 kN, 9.9 kN, and 18 kN to reconfirm that this was not causing any problems with AE detection.

Only one anomalous high-amplitude AE event was clearly detected by the ring sensor FBG over the course of this experiment. This event was verified through detection by the other sensors. The waveform is not shown in this dissertation as it could not be replicated with further testing.

A chart displaying AE hits over time on a dB scale (referenced to 1 mV) over a 15 minute test is shown in Figure 9.35. Perhaps the most interesting note is that the ring sensor

PWAS only detects 4 AE events (the individual waveforms were observed to ensure they were not noise signals).

(a) 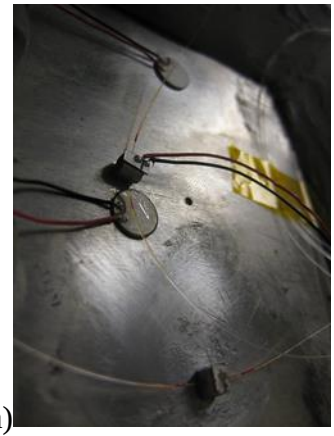 (b) 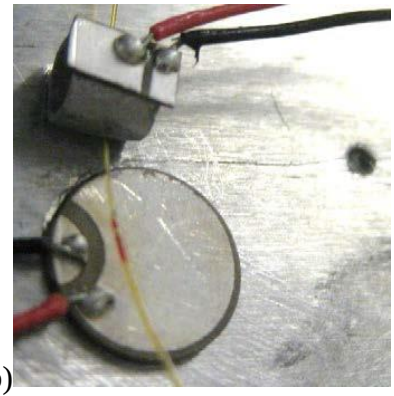

Figure 9.34: An additional ring sensor and PWAS bonded within 1 mm of the crack tip and further fatigue experiments were performed

At first, it was considered that the ring sensor bonding was damaged during fatigue loading. A pitch-catch tone burst at 100 kHz transmitted from the PWAS 25 mm away from the crack during fatigue loading established that the ring sensor was operating as expected. Next, it was hypothesized that the ring sensor PWAS may not be as sensitive as a plate-bonded PWAS. However, after calibrating both a plate-bonded PWAS and ring sensor PWAS in Chapter 11, this was not the case, and this hypothesis was rejected. The PWAS on the ring sensor should have served as an external validation of the ring sensor motion. Even if the ring FBG was too noisy to detect AE events, if the ring sensor was excited by AE events it should still excite a sufficiently sensitive PWAS. One possible explanation is if AE waves generated by the fatigue crack generated predominantly in-plane motion associated with S0 wave modes. In this case, the plate-bonded PWAS could then detect these, but not the ring sensor. The R15α sensor would still be able to detect

these modes due to its high level of sensitivity. After a search of AE literature, a conclusive answer to this hypothesis was not found, and the question is still open.

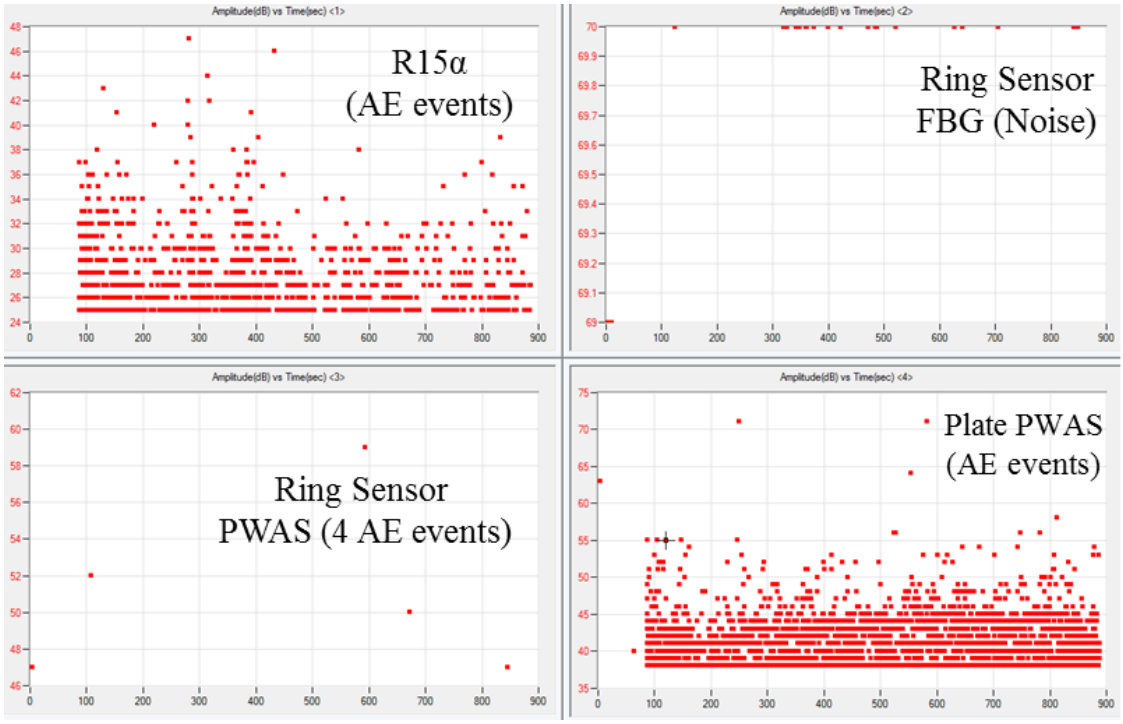

Figure 9.35: Chart of AE hits, with waveform amplitude (dB_{mV}) on the vertical scale and time (seconds) on the horizontal scale

9.6 Summary and Conclusions

The design of the ring sensor was optimized using ANSYS Workbench. A pair of sensitivity analyses were performed to assess the effect of ring sensor dimensions on fundamental resonance frequency and amplitude. It was found that the ring ellipse could be changed to a circular hole without loss in performance. This greatly simplified manufacturing and design. The optimization process had an underlying supposition that optimizing the ring sensor fundamental resonance amplitude would increase the amplitude of other resonance frequencies as well. This ended up being accurate; the increased compliance due to reduced wall thickness was experimentally verified to increase ring sensor sensitivity at higher modes.

A general design rule was developed: reducing wall thickness and outer diameter simultaneous allowed for maintaining a target fundamental resonance frequency while increasing sensitivity. The depth and flat height parameters were designed primarily with bonding characteristics in mind. Previously, it was thought that the elliptical hole forced the motion along the ellipse major axis. However, having flat surfaces on a circular ring was sufficient to induce directionality. Also, in a practical sense, it does not matter if directional preference is enforced, e.g. a ring with high amplitude dilatational motion would be preferred over a ring with low amplitude breathing-type motion.

A goal driven optimization algorithm was used to develop a sensitivity and miniaturization optimized design. The design bounds, and particularly the minimum ring diameter, were a limiting factor on optimization. An optimized design was created with an outer diameter of 3.75 mm. At the prototyping stage, a second design was made at 3.18 mm based on using a commercially available length of tubing as a basis for developing prototypes. This was found to have a superior performance, as its outer diameter and wall thickness was lower than the bounds given in optimization. In principle, more sensitive designs could be made by making smaller ring sensors, but there are limits in terms of manufacturability and cost.

Several ring sensor prototypes were fabricated in the USC machine shop. Microscopic optical measurements of the dimensions were made. Since some of the dimensions were slightly out of specification, the geometric measurements were back-substituted into the FEM models and the predicted resonance dropped from 100 kHz to 87 kHz. The variation of wall thickness and ring diameter were the major contributors to the

drop in resonance frequency from the designed value, even though these were within specification. This was a natural effect of designing at such a small size.

General design rules were created by curve fitting the results from parametric sweeps; the effect of varying elastic modulus, density, and scaling factor were observed on fundamental resonance frequency and amplitude, calculated in FEM harmonic analyses. These can be used for rapid design of the ring sensor with different materials and target frequencies. A 1 DoF model was also created for the ring sensor. Calculating the damping based on a logarithmic decrement method, and manually adjusting the resonance frequency, the normalized curve for the 1 DoF model matched the response of the ring sensor near the 1st resonance frequency.

Frequency testing of the ring sensor was performed for free and plate-bonded conditions. Three resonances were found in the free response, with a dominant response at 84 kHz. Upon plate bonding, the response dropped to 52 kHz due to changing boundary conditions. Tuning curves, pitch-catch waveforms, and PLB-AE waveforms were assessed. It was demonstrated that the ring sensor responded equally well in tension and compression. The pitch-catch and PLB-AE response both showed a significantly higher SNR than the other sensors.

SNR calculations for pitch-catch and PLB-AE experiments showed that the FBG on the 3.2 mm ring sensor provided mechanical strain amplification to the waveforms. This was reflected by SNR_{dB} increases of the 3.2 mm ring sensor over that of the plate-FBG. Quantitatively, these were 14.1 dB (pitch-catch), 11.9 dB (PLB-AE), and 19.3 dB (filtered PLB-AE).

Both plate-bonded FBG and the 3.2 mm ring sensor were tested for AE detection on a plate loaded for low cycle fatigue in a load frame. Quasi-static strain tests indicated that the ring sensor FBG reduced the quasi-static strain sensed in comparison to plate-bonded FBG by a factor of 9.5. This is sufficient for ring sensor insensitivity to quasi-static strain for most applications if the width FBG linear range is considered appropriately in the sensor design phase. Functionality of the optical equipment was established by PLB-AE tests during quasi-static strain. The ring sensor was capable of detecting Lamb wave during low cycle fatigue loading. This is a positive indicator for the use of the ring sensor as a general ultrasonic guided wave sensor, and not just as an AE sensor.

The FBG and ring sensor did not detect AE waveforms, whereas plate bonded PWAS and R15α sensors detected numerous AE waveforms. The plate-bonded FBG was not sensitive enough to detect the AE waveforms. The use of the PWAS on the ring sensor exposed an additional factor – we believe the metallic ring itself was not substantially excited by symmetric AE waves produced by a crack in a thin plate. We additionally believe that most of the energy is in the S0 wave mode due to the symmetry of the crack extension across the plate thickness; the relative amplitudes of the sensors studied, particularly the R15α sensor, as the AE hit chart shows that its SNR performance was about the same as a surface-bonded PWAS.

Several long-term research goals have been achieved by the results in this chapter:

- The ring sensor was miniaturized from 8 mm to 3.2 mm, and weight from 576 mg to 23.9 mg. The size of the sensor base was reduced as well, reduce the effect of the finite transducer aperture.

- The ring sensor was optimized for maximal amplification. Performance improvements were measured experimentally by SNR increases on the order of 12-19 dB. This is enough to demonstrate mechanical strain amplification to an FBG via the ring sensor.
- Both the 8 mm ring sensor and 3.2 mm optimized ring sensor were shown to have broadband sensing characteristics in response to Lamb wave excitation over at least a 50-600 kHz sensing range. The exact nature of the frequency response still needs to be assessed, as the tuning curve method smoothed out an otherwise jagged frequency spectrum associated with resonant-type sensors.
- The ring sensor was demonstrated to be largely insensitive to quasi-static strain, reducing quasi-static strain sensed by a factor of 9.5.

To follow up on the capabilities demonstrated in this work, the optimization framework developed in this chapter is used in Chapter 10 with a new sensing architecture. In Chapter 10, a wave trapping geometric feature to further improve FBG sensitivity. It also complements the ring sensor by providing the potential for both in-plane and out-of-plane fiber-optic sensing within a single sensor. Limitations in the tuning curve approach for assessment of a frequency response were also noted in this chapter. To address this, the ring sensors will be calibrated in Chapter 11 to provide absolute measurements of motion and provide a sufficient level of granularity in the sensor frequency response.

CHAPTER 10

FIBER-OPTIC ACOUSTIC BLACK HOLE SENSOR

10.1 CONCEPT AND MOTIVATION FOR AN ACOUSTIC BLACK HOLE SENSOR

The acoustic black hole (ABH) is a concept in which acoustic waves, traveling in a waveguide of diminishing cross-section, travel towards a point-like tip where they are trapped without reflection. Since all of the incident energy is focused into a very small region, large local vibrations are present at the waveguide tip.

Following the approach of using mechanical amplification to increase fiber-optic sensor sensitivity, the ABH seems like it may provide significant advantages due to its high local vibrational response. A sensing configuration is proposed which involves one or more ABH waveguides. These features provide high displacement amplification and wave trapping mechanisms.

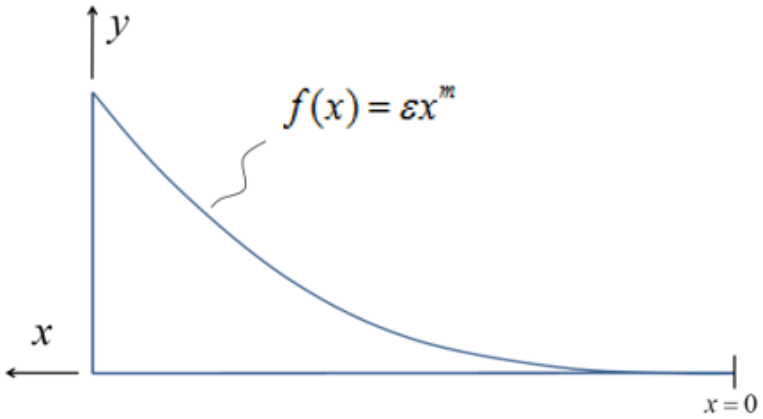

Figure 10.1: The ABH geometry with its thickness following a power law profile approaching a zero-thickness tip

An ABH is a geometric feature where an incident flexural wave originating from an arbitrary internal point is isolated to the neighborhood of its tip, producing a zero-reflection condition. In this manner, it is the acoustic analogy to the astronomical black hole which traps optical waves. Geometrically, an ABH is a variable thickness feature where the thickness follows a power law profile described by the equation

$$f(x) = \varepsilon x^m \tag{10.1}$$

where c is a constant and m is a positive rational number ≥ 2 if the ABH is in vacuum. For $x = 0$, the power law approaches a zero-thickness tip (Figure 10.1). In practice, it must be truncated to a finite thickness tip, so a degree of reflection is permitted.

For a flexural wave propagating from a point x within an ABH surrounded by vacuum, the wavenumber is given by

$$\gamma(x) = \frac{\sqrt[4]{12}\sqrt{k_P}}{\sqrt{\varepsilon x^m}} \tag{10.2}$$

Approaching the tip of the ABH at $x = 0$, the wavenumber approaches infinity. Since the wave speed is inversely proportional to the wavenumber, the wave speed approaches zero. This offers an explanation for the zero-reflection condition, as the incident wave asymptotically approaches the ABH tip but does not reach it, and thus cannot interact with the free edge of the tip to reflect.

An ABH waveguide has three major practical benefits for sensing applications:

1. The zero-reflection condition of the ABH concentrates energy at the ABH tip, such that most or all of the incident wave can be channeled into a sensing region
2. The ABH has high displacement amplification at its tip. When no truncation is present, a finite input produces a theoretically infinite displacement at the ABH

tip. In practice, with an ABH tip-thickness truncation, a finite but large displacement can be achieved.

3. As a wave propagates along an ABH, its wavelength sweeps from an initial value towards zero, offering a wide range of wavelengths to maximize energy transfer to an external transducer

This chapter describes the development a guided wave sensor built around the ABH idea. First, the geometric acoustics approximation for modeling an ABH is described, followed by a review of relevant ABH literature. Next, several obstacles specific to developing a sensor with a diminishing thickness tip are addressed. A scaled-up prototype is developed to validate sensor resonance modes, and a small-scale circular ABH-like tapered sensor is developed for fiber-optic guided wave sensing applications. Next, a sensor design with a true power law ABH geometry is optimized and prototyped. Free sensor experiments were conducted for the circular ABH sensor; it is also calibrated in the next chapter. Preliminary studies have been performed on the power law ABH sensor's directional response and its in-plane and out-of-plane sensitivity. From our search of the literature, we believe that this work is the first use of an ABH for sensing applications. We have submitting a US patent application (Giurgiutiu and Frankforter 2017) entitled "Acoustic Black Hole for Sensing Applications" to this effect.

10.1.1 Geometric Acoustics Approach to Modeling an Acoustic Black Hole

The modeling framework for an ABH waveguide is based on the geometric acoustics formulation. It is also known as the eikonal approximation or the WKB approximation. It has been applied broadly in other fields as well such as optics, seismology, and electromagnetic waves. The defining feature of the geometric acoustics

approximation is that constant-parameter differential equations can be used to approximate variable parameter differential equations if those properties vary gradually with sufficient smoothness. As long as parameters are nearly constant in a local neighborhood, a propagating wave continues to be a propagating wave, and an evanescent wave continues to dampen at the same rate with increasing distance. The assumption can be thought of as one of length scales, where properties change on a larger length scale than the wavelength of the wave.

The derivations here follow the works of Pierce (1969), who introduced the geometric acoustics approximation for flexural waves in Euler-Bernoulli beams and Kirchoff-Love plates; Mirinov (1988) who discovered the ABH effect; and Krylov (1990) who investigated localized acoustic modes at the tip of an ABH. Although the geometric acoustics approximation can be used to model wave propagation with any property varying smoothly, such as material properties, the treatment here is limited to plate thickness variations as those are most pertinent to the ABH waveguide and easiest to effect in application.

Plate thickness and subsequently plate flexural stiffness are considered a sufficiently smoothly varying function of position, and are used as dependent variables within the differential equation for a thin isotropic constant-thickness plate, i.e.

$$D\nabla^4 w + \rho h\ddot{w} = 0 \tag{10.3}$$

where $D(x) = \frac{Eh(x)^3}{12(1-\nu^2)}$ is the plate flexural stiffness and $h(x)$ is plate thickness at a position x. E is the Young's modulus, ν is the Poisson ratio, and ρ is the density of the plate material. The equation (10.3) is solved using the eikonal approximation solution

$$w(x,y,t) = \hat{w}(x,y)e^{-iwt}e^{iS(x,y)} \tag{10.4}$$

where S is known as the eikonal, given by

$$S(x,y) = x\gamma_x(x,y) + y\gamma_y(x,y) \tag{10.5}$$

with $\gamma_x(x,y)$ and $\gamma_y(x,y)$ are the wavenumbers in the x and y directions, respectively. Substituting (10.4) into (10.3) yields

$$D\left[\left(\frac{\partial S}{\partial x}\right)^2 + \left(\frac{\partial S}{\partial y}\right)^2\right]^2 = \rho h\omega^2 \tag{10.6}$$

Note that $\hat{w}$ was considered constant due to the gradual change in geometric parameters. If the wave is considered straight-crested with the wave propagating in the x direction, derivatives with respect to y become zero and $\partial S/\partial x$ is the flexural wave speed in the x direction, denoted by γ where the subscript from γ_x is removed for brevity:

$$D\gamma(x)^4 = \rho h(x)\omega^2 \tag{10.7}$$

The rest of the formulation follows that of flexural waves in beams and straight-crested plates as presented in Chapter 1, with the caveat that the values of height and therefore plate flexural stiffness depend on position. Defining

$$a(x)^4 = \frac{D(x)}{\rho h(x)} \tag{10.8}$$

The four solutions for the wavenumber γ are given by

$$\pm\frac{\sqrt{\omega}}{a(x)},\ \ \pm i\frac{\sqrt{\omega}}{a(x)} \tag{10.9}$$

The out-of-plane displacement is obtained by back-substituting the wavenumbers γ from (10.9) into equations (10.4) and (10.5), given by

$$w(x,t) = A(x)e^{i(\gamma x+\omega t)} + B(x)e^{-i(\gamma x-\omega t)} + C(x)e^{\gamma x}e^{i\omega t} + D(x)e^{-\gamma x}e^{i\omega t} \tag{10.10}$$

The flexural wave speed $c_F = \dfrac{\omega}{\gamma_F}$ is given by

$$c_F = \sqrt{\omega}\left(\frac{Eh(x)^2}{12\rho\left(1-\nu^2\right)}\right)^{1/4} \tag{10.11}$$

The flexural wavenumber can be expressed as

$$\gamma = \sqrt{\omega}\left(\frac{12\rho(1-\nu^2)}{Eh(x)^2}\right)^{1/4} \tag{10.12}$$

Note that as long as the condition of sufficient smoothness is met, the waves propagate as if they were propagating in a beam or plate, without reflection, even though there are gradual changes in plate thickness.

10.1.2 Power Law Satisfying the Condition of Sufficient Smoothness

Insofar, the condition of sufficient smoothness has been stated qualitatively. In a quantitative sense, for the geometric acoustics approximation to be valid, the change in wavenumber over the span of a wavelength must be small compared to the magnitude of the wavenumber. Expressing this formally, and keeping in mind the wavelength-wavenumber relation $\lambda = 2\pi/\gamma$, the condition of sufficient smoothness is given by

$$\frac{d\gamma}{dx}\frac{1}{\gamma} << \gamma \quad \text{or} \quad \frac{d\gamma}{dx}\frac{1}{\gamma^2} << 1 \tag{10.13}$$

Mirinov (1988) was the first to identify that this condition is uniquely satisfied at all locations when the plate thickness $h(x)$ is prescribed by a power law profile, later termed as an ABH

$$h(x) = \varepsilon x^m \quad m \geq 2 \tag{10.14}$$

Substituting (10.14) into (10.12), the flexural wavenumber is given by

$$\gamma = \sqrt{\omega}\left(\frac{12\rho(1-\nu^2)}{E}\right)^{1/4}\left(\frac{1}{\varepsilon x^m}\right)^{1/2} \tag{10.15}$$

This equation can be further simplified using the longitudinal wavenumber in a plate given by

$$k_L = \frac{\omega}{c_L} = \omega\sqrt{\frac{\rho}{E}(1-\nu^2)} \tag{10.16}$$

Substituting (10.16) into (10.15) yields

$$\gamma = \frac{\sqrt[4]{12}\sqrt{k_L}}{\sqrt{\varepsilon x^m}} \tag{10.17}$$

10.1.3 Verification of a Power Law Satisfying the Condition of Sufficient Smoothness

To ensure that the power law profile satisfies the condition of sufficient smoothness, we can back-substitute (10.17) into (10.13). to find

$$\begin{aligned} \frac{d\gamma}{dx} &= -\frac{m\sqrt[4]{12}\sqrt{k_L}}{2x\sqrt{\varepsilon x^m}} \\ \frac{d\gamma}{dx}\frac{1}{\gamma} &= -\frac{m}{2x} << \frac{\sqrt[4]{12}\sqrt{k_L}}{\sqrt{\varepsilon x^m}} \end{aligned} \tag{10.18}$$

Rearranging:

$$-m\sqrt{\varepsilon x^{m-2}} << 2\sqrt[4]{12}\sqrt{k_L} \tag{10.19}$$

The value under the radical on the left-hand side of the equation must be greater than or equal to zero, giving the condition that $m \geq 2$. For a power law with $m = 2$, and eliminating the negative sign via an argument of geometric equivalence with the positive term, (10.19) simplifies to

$$\sqrt{\varepsilon} << \sqrt[4]{12}\sqrt{k_L}$$
$$1 << \left(\frac{2\sqrt{3}k_L}{\varepsilon} \right)^{1/2} \tag{10.20}$$

This condition can be found in some of the early literature on the ABH (Krylov 1990). Equation (10.20) indicates that the coefficient ε of the power law must be sufficiently small, depending on the frequency and elastic properties, for the geometric acoustics approximation of an ABH to hold. For a 50 kHz excitation frequency, with the material used being SS-304 ($E = 200$ GPa , $\rho = 8,000$ kg/m^3, $\nu = 0.29$), $\varepsilon << 208$ 1/m . For a 200 kHz excitation frequency, one gets $\varepsilon << 833$ 1/m .(As a reference, using a rather small sensor design with 5 mm length, 5 mm height and 0.1 mm tip thickness gives $\varepsilon = 196$ 1/m). Therefore, when designing sensors with an ABH, particularly the lower end of the frequency range, one should be aware that there is a potential for the geometric acoustics approximation to be invalid. This does not necessarily mean that the design will perform poorly; as a counterexample, when Ferutado (2014) utilized the normalized wavenumber variation

$$\left(\frac{d\gamma}{dx} \frac{1}{\gamma^2} \right) \tag{10.21}$$

as a design criterion for wave absorbing applications, he found that simulations of higher order ABH tended to violate the criteria that the normalized wavenumber variation is much less than one. However, these ABH still had potential better wave absorbing properties. However, the wave propagation features of the geometry such as wave absorption, wavelength, etc. may change. Higher excitation frequencies and more gradual ABH slopes make the geometric acoustics approximation more accurate and valid.

10.1.4 Zero-Reflection and Wavelength Sweep Characteristics of an ABH

Noting that k_L is frequency dependent, propagation within a power law wedge is still dispersive. However, approaching the tip of the power law as x approaches zero, the wavenumber approaches infinite. Since the wave speed is inversely proportional to the wavenumber, the wave speed approaches zero and the wave asymptotically slows down while never reaching the end a power law waveguide with a zero-thickness tip. Additionally, since the waves are governed by the same solution as straight-crested flexural waves in plates (albeit, with positional variation in its independent variables), the waves will not reflect off any internal portion of the power law curve. Stated more formally, a straight-crested flexural wave originating within an arbitrary position within a power law and directed towards its zero-height origin will propagate with asymptotically diminishing speed and without reflection.

Another useful feature of the ABH is the wavelength sweep characteristic. Since wavelength is also inversely proportional to wavenumber, the wavelength sweeps from an initial value towards zero regardless of the excitation frequency. This is a useful feature for energy transduction applications as energy transfer into a transducer is often wavelength-dependent. Figure 10.2 shows the ABH test case from Section 10.1.3, stainless steel 304 with 5 mm length and maximum height. To clearly demonstrate the ABH effects, a zero-thickness taper was modeled for a 50 kHz wave propagating from left to right. Figure 10.2a shows the height profile, Figure 10.2b shows the wavenumber, Figure 10.2c shows the wave speed, and Figure 10.2d shows the wavelength. A linearly diminishing wave speed and wavelength is seen, showcasing the zero-reflection effect for a zero thickness taper and the frequency sweep effect.

10.1.5 Reflection Coefficient of a quadratic ABH with a Finite Thickness Taper

In Mirinov's initial discussion of a power law ABH (Mirinov, 1988), a relation for reflection coefficient was produced for a finite length wedge truncating to a finite thickness. For a quadratic wedge with a height h_0 at its thicker end and h_1 at its thinner edge, the amplitude reflection coefficient is given by

$$W = \left(\frac{h_1}{h_0}\right)^{\frac{1}{2\sqrt{\varepsilon}Q}\left(\frac{3\rho\omega^2}{E}\right)^{1/4}} \tag{10.22}$$

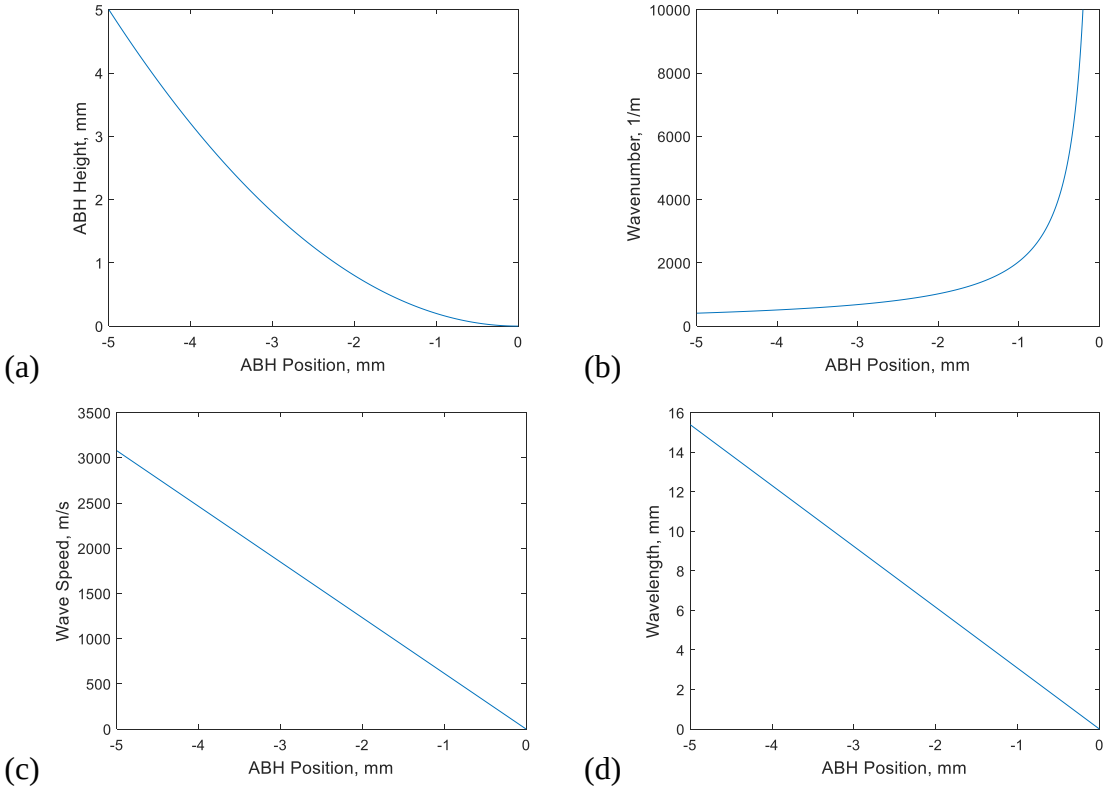

Figure 10.2: (a) ABH height, (b) wavenumber, (c) wave speed, and (d) wavelength calculations for a 50 kHz flexural wave propagating in a 304 stainless steel quadratic ABH

Q is the material quality factor with a complex Young's modulus $E \to E(1+\frac{i}{Q})$. Mirinov (1988) gave the example of a three order of magnitude ratio h_1/h_0, $Q=10^2$, and

$(3\rho\omega^2/(\varepsilon^2 E))^{1/4}$ =10. Using these values, it was found that $W = 0.708$, indicating that a large proportion of the wave energy is reflected. Further experimental studies for relatively low frequency vibration have validated this for metallic and composite ABH wave absorbers (Krylov 2002; Krylov and Tilman 2004; Bowyer and Krylov 2014b).

To see if this is a concern for ultrasonic wave sensing applications, we construct the scenario of a 304 stainless steel sensor with the same material properties as Section 10.1.3. Using a height of 5 mm, tip thickness of 0.1, $\varepsilon = 196\ \ 1/m$. The same quality factor as Mirinov (1988), $Q = 10^2$ was used. The variation in reflection coefficient with excitation frequency is shown in Figure 10.3a. Similarly, the excitation frequency was fixed at 50 kHz and the sensor height at 5.0 mm, and the variation in reflection coefficient with ABH length is shown in Figure 10.3b.

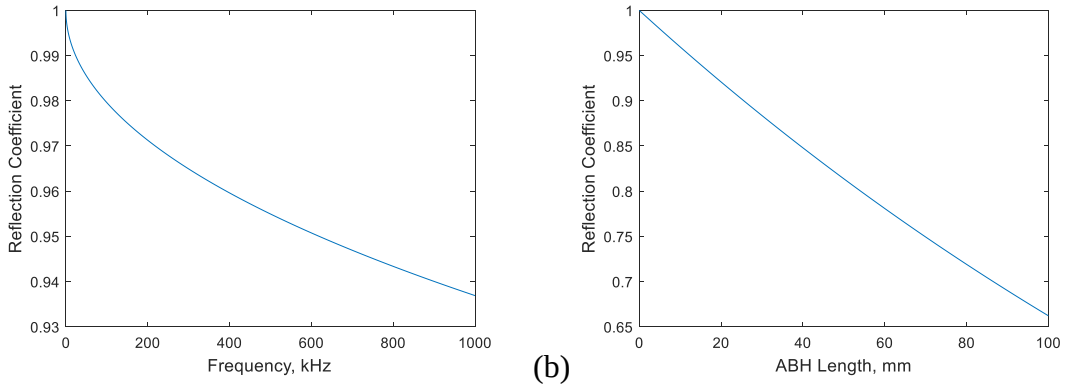

(a) (b)

Figure 10.3: (a) Reflection coefficient as a function of frequency for a 5 mm length and 5 mm height ABH, and (b) reflection coefficient as a function of ABH length for a 5 mm height ABH and an excitation frequency of 100 kHz

The relatively small ABH waveguide has a high reflection coefficient across a 0 – 1000 kHz frequency range, with a slightly decreasing reflection coefficient with increasing frequency. For the ABH length assessment, a reflection coefficient of 66.2% is seen for a 100-mm ABH length with 5-mm ABH height. However, for the case with the lowest

reflection coefficient, the dimensions are large and the rather squat aspect ratio makes manufacturing difficult. The high reflection coefficients are not an indicator of poor sensor performance; rather that the sensor will perform as a resonant-type sensor. Additional damping will be needed to flatten the frequency response if a broadband ABH sensor is required.

10.1.6 Increased Displacement Amplitude at the tip of an ABH

Most applications of an ABH are for vibration absorption, and thus the amplitude characteristics are often ignored. Returning to one of the seminal works on the ABH (Krylov 1990), if a straight-crested wave approaches towards an ABH tip with normal incidence, the transverse flexural wave amplitude is given by

$$\hat{w}(x) = \frac{G}{x\sqrt{\gamma}} \tag{10.23}$$

where G is a constant determined by the transverse displacement amplitude at a point x_0. Referring back to (10.17), one gets

$$\sqrt{\gamma} \propto \frac{1}{x^{m/4}} \tag{10.24}$$

Substituting (10.24) into (10.23):

$$\hat{w}(x) \propto \frac{1}{x^{(4-m)/4}} \tag{10.25}$$

This gives the condition that for values $m < 4$, the displacement becomes singular approaching the ABH tip (approaching $x = 0$), but for values $m \geq 4$, the displacement approaches zero at the ABH tip. Analysis of (10.25) indicates that smaller values of m increase the rate at which $\hat{w}(x)$ approaches infinite, indicating that smaller values of m are preferred for displacement amplification. Since the ABH phenomenon requires $m \geq 2$

for the geometric acoustics modeling to be admissible (e.g. lacking reflection off the ABH curvature), a value of $m = 2$ is expected to be not only easier to manufacture than higher order power laws, but better for sensing applications. This is in contrast to wave and vibration damping applications where higher order power laws provide better performance through a lower reflection coefficient (Ferutado, 2014).

10.2 State of the Art in Acoustic Black Holes

10.2.1 Wedge Acoustic Waves

Prior to the discovery of the ABH geometry by Mirinov (1988), Moss (1973) studied the similar effect of vibrational edge modes at the tip of wedges with diminishing interior angle. Moss found that vibrational edge modes for wedges with an apex less than 100° are antisymmetric flexural modes, with the number of edge modes localized near the apex of a wedge increasing as the wedge angle decreased. This is similar in effect to the ABH, although non-reflection is not guaranteed for an interior angle wedge a similar framework has been developed for ABH as wedge-acoustic waves with both normal incidence and waves guided along the ABH ridge. Krylov (1990) developed a modeling framework for ABH as wedge-acoustic waves, demonstrating the presence of localized modes at the tip of an ABH, and the capability for waves to travel along the ABH ridge. Cardonne (2008) has studied elastic wave processes in beak-shaped irregularities, where a 1D ABH is supplemented in the thickness direction with arced tapers, terminating in a finite point.

Krylov (2012) has also developed a geometric acoustics model for Rayleigh and Lamb waves in gradually varying thickness medium, an important step into extending the

ABH concept, although the derivation is somewhat cumbersome and outside the scope of this work.

10.2.2 ABH as Vibration Absorbers

Krylov (2002; Krylov and Tilman 2004) proposed the use of acoustic black holes as passive vibration absorbers, this work's theoretical analysis indicating that a thin viscoelastic absorbing layer can dramatically reduce the reflection coefficient. This has interesting promise for sensor development, as the development of a broadband sensor corresponds to adding sufficient damping, and a thin adhesive layer is easier to apply and significantly less bulky than traditional epoxy damping "backing" media. Krylov (Krylov and Winward 2007) followed this up with experimental studies of ABH tapers at the end of plates subject to vibration excitation with frequency ranges below 7 kHz. It was shown that with the use of a thin adhesive strip, the reflection coefficients were as low as 1-3% compared to free wedges with reflection coefficients from 50-70%. Reductions in resonance peaks, with up to 20 dB maximum attenuation compared to a conventional plate was observed. Denis (Denis et al. 2015) used LDV to measure the reflection coefficients of an ABH taper, finding it matched well with theoretical calculations.

Bayod (Bayod 2011) found that modifications to the traditional ABH setup could improve performance; the small tip of the ABH is the most difficult component to manufacture, and Bayod (Bayod 2011) found that extending the tip in a straight line allowed for sufficient vibration absorbing with a slightly larger ABH tip, much more easily machined by conventional manufacturing methods such as CNC milling.

Bowyer (Bowyer and Krylov 2014a) found that ABH manufactured into turbofan blades reduced resonance beaks by as much as 10-12 dB, and wind tunnel tests indicated

diminishment of airflow-induced vibrations. Bowyer (Bowyer and Krylov 2014b) also found that ABH performed similarly in glass-fiber composites as they do in metallic plates, showing that incorporating ABH into the plate sandwich component of honeycomb sandwich structures reduced vibration amplitude.

10.2.3 Use of Acoustic Black Holes for energy transduction

Zhao (2014) presented the concept of an energy harvester based on an ABH, with numerical modeling indicating theoretical benefits of an ABH/piezoelectric energy harvester. The wavelength sweep effect presented in Section 10.1.4 is of particular interest, as certain wavelengths may couple better with the piezoelectric transducer. The downside is that the piezoelectric transducer adds a significant thickness to the ABH, particularly compared to the order of a practical ABH taper. Experimental verification has not yet been performed. Remilleux (2014) demonstrated a numerical study where an ABH was predicted to improve the radiation efficiency of an air coupled piezoelectric transducer. This study was performed up to 100 kHz and the piezoelectric transducer need not be placed directly onto the ABH and would not interfere with its response. Anderson (Anderson et al. 2015) demonstrated experimentally that an ABH could increase the radiation efficiency of an air coupled piezoelectric transducer, measuring the effect up to 100 kHz.

10.3 Finite Element Analysis of a Diminishing Thickness Sensor

Through FEM modeling of the 8-mm ring sensor, a half-ring, and a comparable sized ABH sensor, dynamics of the ABH sensor can be understood. This leads to the assessment of practical considerations for sensing element configuration and the design of an ABH sensor prototype.

10.3.1 Harmonic Analysis of a Tapered Thickness Sensor

The 8 mm ring sensor, a half-ring sensor, and a parabolic ABH sensor was modeled in ANSYS Workbench (Figure 10.4). It was later found that the orientation of the parabola needed to be changed from vertically oriented to horizontally oriented to localize the tip of an ABH at the sensor tip. Thus, the results in this section are applicable to a sensor with a tapered thickness, and subsequently transferrable to an ABH sensor because they share the quality of high compliance at a sensing region.

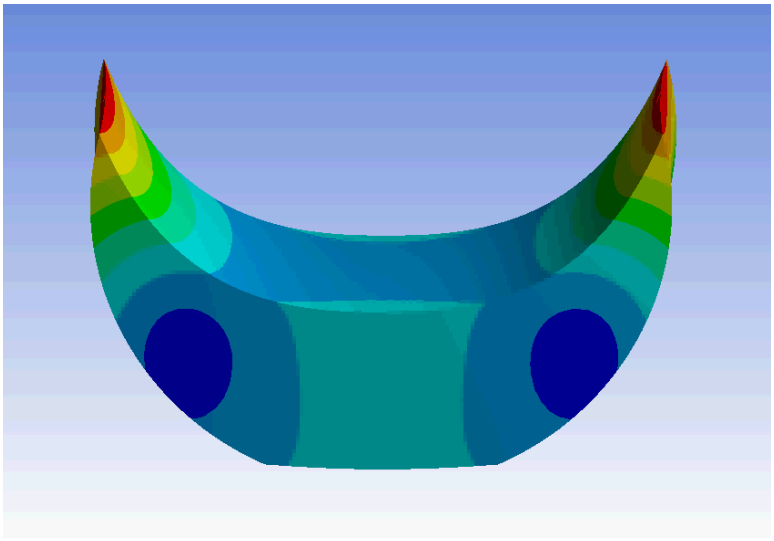

Figure 10.4: 1st resonance frequency of a parabolic tapered sensor

The quadratic curve was made to intersect with the outer circular profile at the point where the tangent of the circle was perpendicular with the sensor base. A harmonic analysis was performed with a 1 N out-of-plane distributed harmonic load on each sensor base.

A model was developed with an optical fiber incorporated into the ABH sensor. The optical fiber was treated as an isotropic elastic solid with elastic modulus $E = 70 GPa$ and Poisson ratio $\nu = 0.20$. Density values were found for fused silica and polyurethane

acrylate from Corning at $\rho = 2200\,kg/m^3$ and $\rho = 1020\,kg/m^3$, respectively. The density under a homogeneous assumption was then be calculated via a rule of mixtures approach:

$$\rho = \frac{m}{V} = \frac{m_1 + m_2}{V} = \frac{\rho_1 V_1 + \rho_2 V_2}{V_1 + V_2} \tag{10.26}$$

where m is the mass, V is the volume. The subscripts represent the mass, density, and volume of a given material within the optical fiber. Using this approach, the density was calculated to be $\rho = 1315\,kg/m^3$. Incorporating the optical fiber into the ABH model, the resonance peak can be seen to spread compared to the ABH model without the FBG. The displacement amplitude also drops from ~140 μm to ~2.4 μm (Figure 10.5).

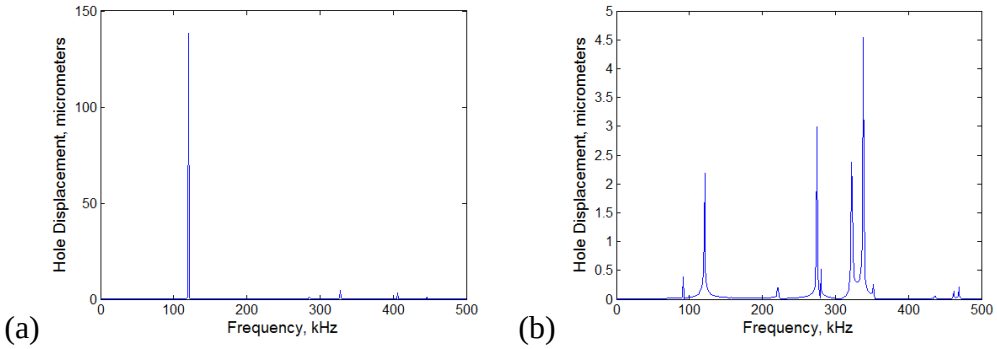

Figure 10.5: (a) High displacement observed in harmonic analysis without optical fiber and (b) diminished displacement observed in harmonic analysis with optical fiber

To aid understanding of amplitude drop in the presence of the optical fiber, an approach was formulated based on the dynamic stiffness of the resonator and the FBG.

Given a harmonic excitation

$$F = F_0 e^{i\omega t} \tag{10.27}$$

the dynamic stiffness can be written as

$$k(\omega) = \frac{F_0}{\Delta u(\omega)} \tag{10.28}$$

The half-ring sensor was used for this analysis, as the width could be varied to change the dynamic stiffness parameter. The force F_0 was 1 N. The dynamic displacement $\Delta u(\omega)$ was calculated for both the FBG and half-ring at the half-ring's resonance frequency. On the FBG, the loads were distributed across the circular ends. On the ring sensor, the loads were distributed as line forces along the top-inner surface of the half-ring (Figure 10.6).

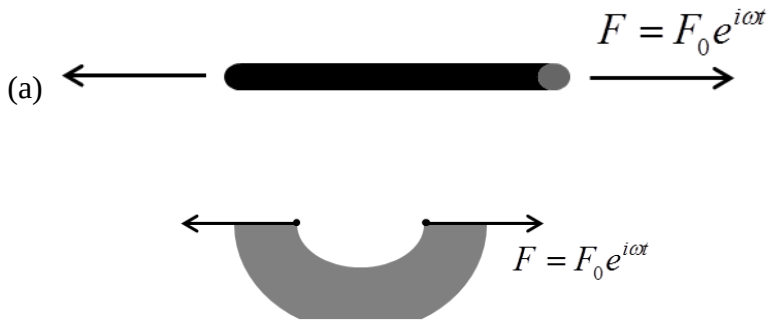

Figure 10.6: Load application for dynamic stiffness exploratory FEM models as (a) distributed harmonic load per unit area applied along the circular cross sections of the optical fiber, and (b) distributed harmonic load per unit length applied along an inner line across the ABH sensor depth

Three cases were assessed, where the half-ring width was modified such that:

- The half-ring had a higher stiffness than the FBG
- The half-ring had a matched stiffness with the FBG
- The half-ring had a lower stiffness than the FBG

The three half-rings which satisfied these criteria, along with the FBG, are shown in Figure 10.7. The tip width, dynamic stiffness, and dynamic displacement amplitude with and without the FBG are shown in Table 10.1. Looking at the dynamic displacements, there is a tradeoff between high stiffness and low stiffness designs. If the sensor stiffness is too

high, the sensor displacement is too low to excite the FBG. If the sensor stiffness is too low, the sensor without the FBG has a high displacement, but the presence of the FBG lowers the response.

Table 10.1: Influence of dynamic stiffness matching on sensor performance

Sensor	Tip Width, mm	$k(\omega)$,N/mm	Δu ,µm At Resonance No FBG	Δu ,µm At Resonance With FBG
Higher	1.50	154	6.5	6.4
Matched	0.13	58	17.4	12.9
Lower	0.05	52	19.4	11.9

The case of matched stiffness had the highest displacement for the sensor + FBG configuration. The frequency sweep of the matched stiffness sensor configuration is shown in Figure 10.8, with and without the FBG. There is an additional resonance mode near the

If this study is to be extended for application, the material properties should be changed from an isotropic model to a two-material model. This will likely change the numerical calculations, but the overall conclusions would still be preserved.

10.3.2 Design of a 100 kHz ABH Sensor Prototype

To design a 100 kHz ABH sensor, the power law was changed to a circular profile to simplifying manufacturing. Although this is not a true ABH, it incorporates the diminishing thickness effect of the sensor. In this dissertation, it is called an ABH sensor for simplicity, as the gradually tapering thickness gives it sensing characteristics similar to an ABH sensor.

A harmonic analysis was conducted similar to the design optimization of the rings sensor in Chapter 9. The 1st resonance frequency and displacement amplitude at the ABH tip were measured, with a nominal 1% modal damping used. A meshing scheme with hexahedral elements was defined entirely by number of elements at various key points such

as the sensor base and the ABH tips. An example of the mesh used is seen in Figure 10.9a,b. A 1 N distributed base force load was applied along the base of the sensor in an out-of-plane direction (Figure 10.9c).

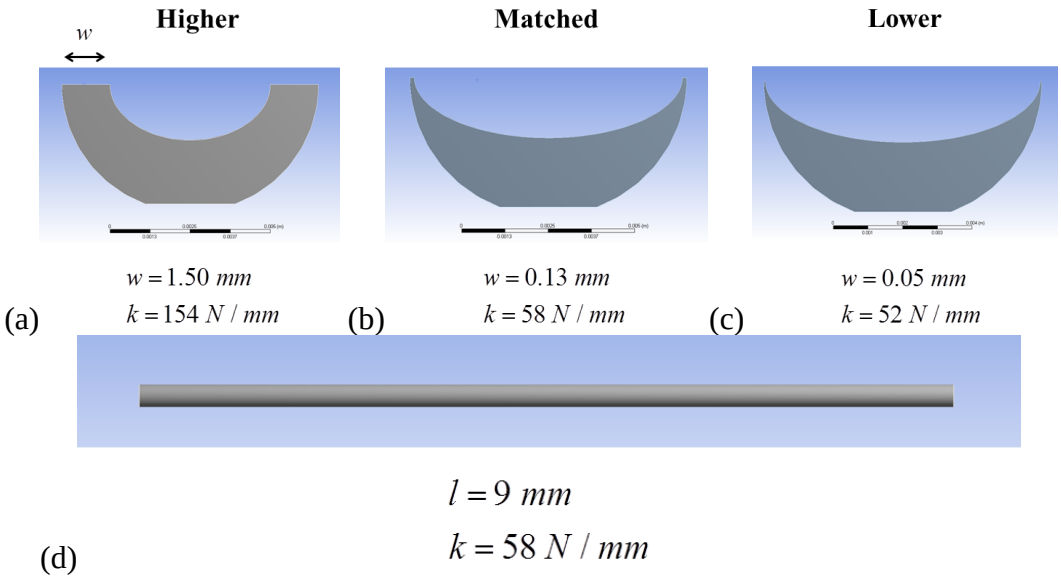

Figure 10.7: Dynamic stiffness exploratory FEM models where (a) a half-ring sensor had a higher dynamic stiffness than optical fiber, (b) a half-ring had a dynamic stiffness matched with the optical fiber, and (c) a half-ring with dynamic stiffness lower than the optical fiber

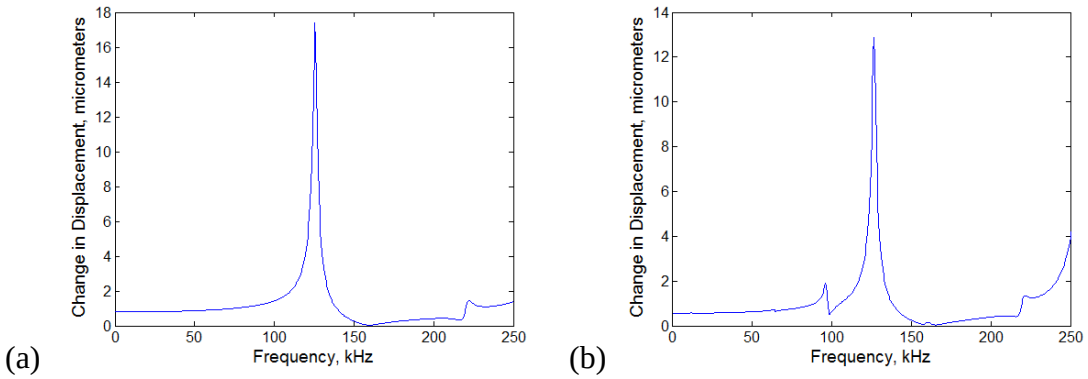

Figure 10.8: Harmonic response of the half-ring geometry with tip thickness tuned for matched dynamic stiffness, (a) without the optical fiber, and (b) with optical fiber

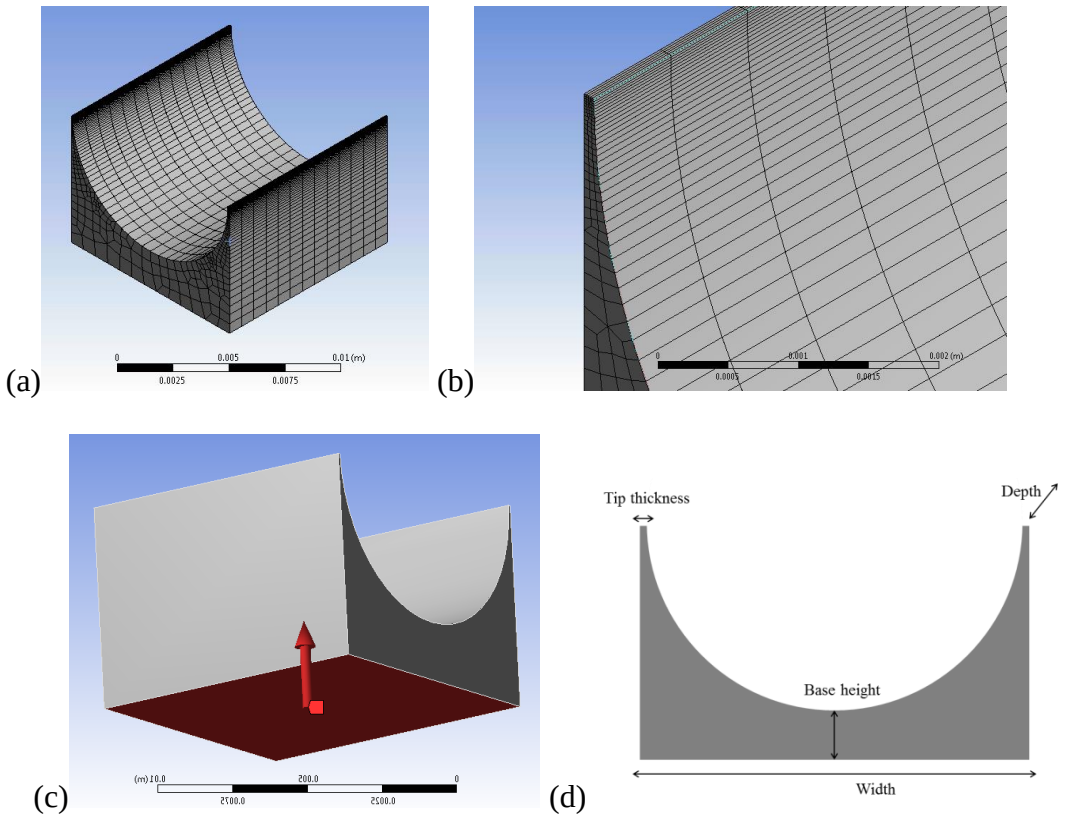

Figure 10.9: (a,b) Sample mesh for a circular ABH sensor variable meshing scheme, (c) 1 N distributed out-of-plane harmonic load along the sensor base, and (d) geometric parameters for a circular ABH sensor optimization

The four geometric parameters used in optimization (shown in Figure 10.9d) are: width, base height, tip thickness, and depth. A sensitivity analysis was performed starting with an initial design of 10.0 mm width, 5.0 mm depth, 2.0 mm base height, and 100 μm base thickness. The bounds of the sensitivity analysis were given as $\pm$ 10% of each parameter value (at the time, technical difficulties with the software precluded using larger bounds). The Spearman correlation coefficients (global sensitivities) between each parameter are shown in Figure 10.10. The amplitude correlated positively with the width and the base height. The frequency correlated negatively with the width. Both the depth and tip thickness had no correlation with either output parameter. This was expected for

the depth, as it was sufficient for plane strain conditions. It is surprising that the ABH tip thickness was not significant.

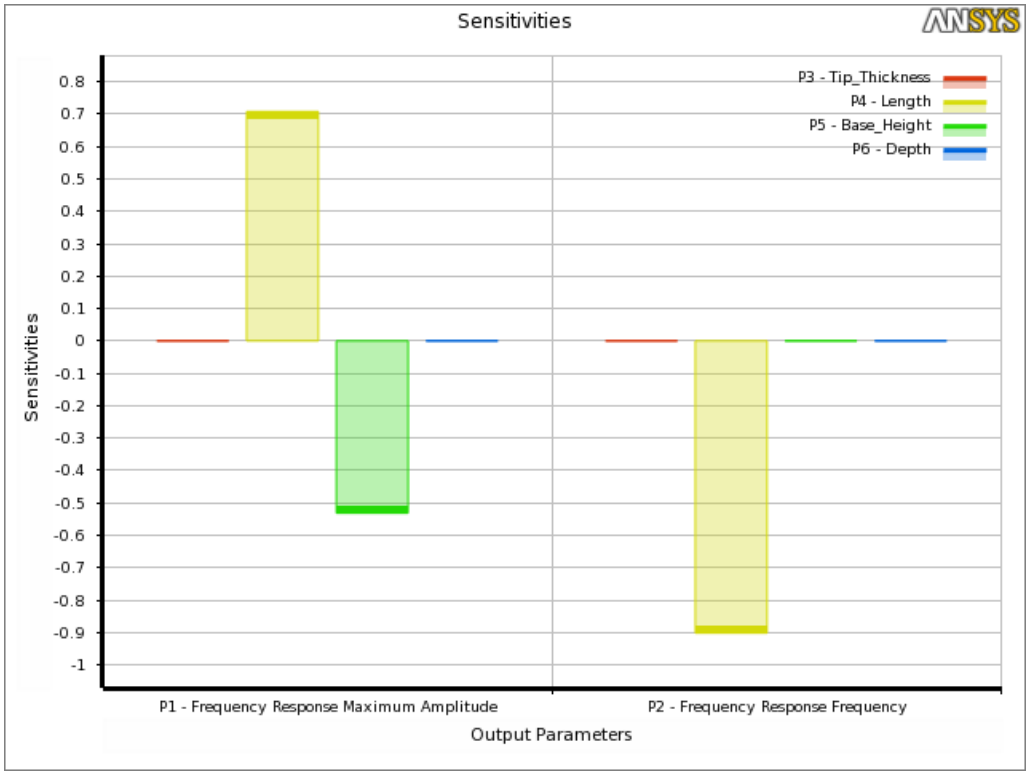

Figure 10.10: Pearson correlation coefficients (sensitivities) for a sensitivity analysis with bounds ±10% of an initial design with 10.0 mm width, 5.0 mm depth, 2.0 mm base height, and 100 µm tip thickness

Next, a response surface was created in ANSYS using a central composite design-of-experiments (DOE) method. The central composite design seeks to minimize the degree of non-orthogonality between the regression coefficients of each parameter and minimize the chance of using sample points with influences non-representative of overall trends. With 3 input parameters, a total of 15 models were used to create the response surface. Response surfaces themselves were created by curve fitting the data by quadratic surfaces.

Figure 10.11 shows local sensitivity plots generating during the response surface analysis. Local sensitivity values are calculated for a given sensor geometry. They are a normalized partial derivative of the output with respect to the input at that point on the

response curve. A tip thickness of 150 µm, width of 12 mm, base height of 2.0 mm, and depth of 5.0 mm was used to calculate a local sensitivity plot (Figure 10.11a). When the sensor width is reduced from 12 mm to 6 mm, the sensitivity of tip thickness on amplitude roughly triples. This shows that the effect of ABH tip thickness depends on it its proportional size with the width of the sensor. It also depends on a lesser effect to the base height. From this observation, the tip thickness is still a significant feature which should be minimized.

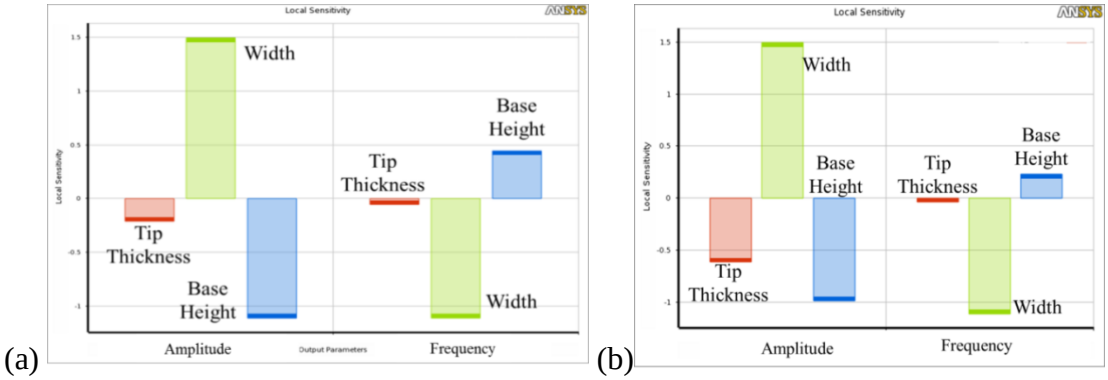

Figure 10.11 Local sensitivity plots for ABH sensors with (a) 12 mm width and (b) 6 mm width

3D response surfaces, representing the effect of sensor length and base height on both frequency and amplitude are shown in Figure 10.12a,b. As seen in Figure 10.12a, to obtain a resonance frequency of 100 kHz, a sensor width in the 6.0 – 8.0 mm range must be chosen. It seems there are counter directional trends between frequency and amplitude. From Figure 10.12b, increasing both base height and sensor width leads to higher amplitude designs. However, this also moves the sensor into the low frequency range, e.g. 30 kHz for a 12 mm wide sensor with a 1.6 mm high base.

Both a response surface optimization and a multi-objective genetic algorithm were used to search for an optimized sensor design. The constraints were set at a resonance

frequency between 90 kHz – 110 kHz. The resonance displacement amplitude was set to be maximized. The direct multi-objective genetic algorithm produced higher amplitude final results, as it did not rely on interpolations between design points. The downside is that it required the evaluation of 415 separate FEM models. The optimization history is shown in Figure 10.13. In Figure 10.13a, the amplitude rose sharply around model #50, but was followed with a subsequent drop in resonance frequency (Figure 10.13b). This was caused by a rise in sensor width (Figure 10.13c). Eventually, the algorithm settled on a width around 0.6 – 0.7 mm which satisfied the frequency constraint. The base height (Figure 10.13d) and tip thickness did not follow such a clear pattern.

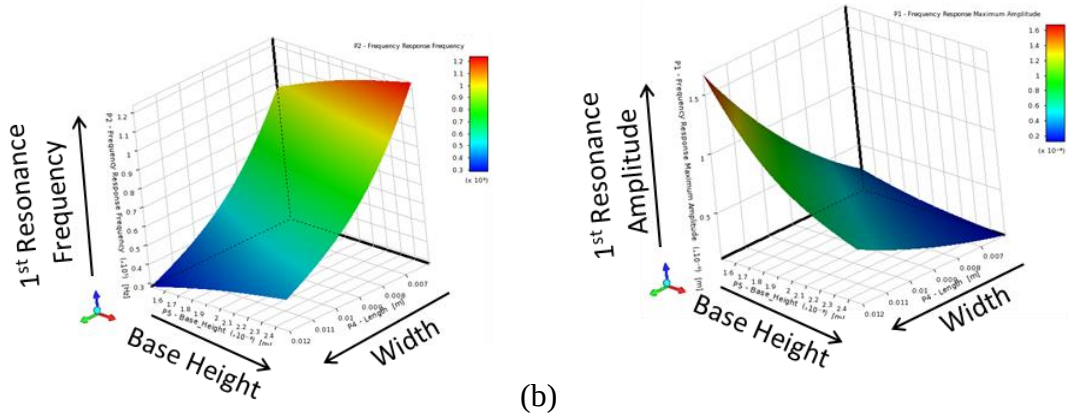

(a) (b)

Figure 10.12: Effect of width and base height on (a) 1st resonance frequency and (b) 1st resonance amplitude

From this analysis, we see that the optimization of this ABH sensor design is highly constrained by its target resonance frequency. For a given target frequency, increases in amplitude can be made by subtle variations in dimensions. However, counter directional trends do not allow for major increases in amplitude from the original designs. This is in contrast to the ring sensor, where large amplitude increases could be made by joint

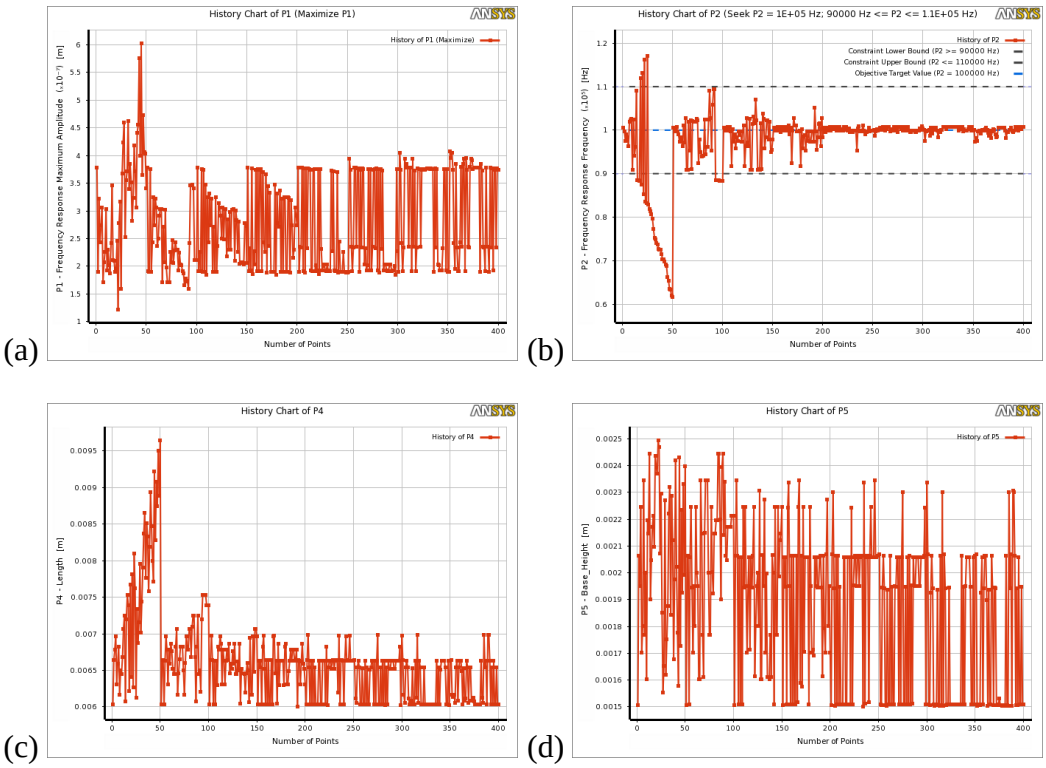

Figure 10.13: Analysis history of (a) Amplitude output, (b) frequency output, (c) width input, and (d) base height input with number of models

reduction of outer diameter and wall thickness. The problem seems to be that there are not enough design features to be able to separately control frequency and amplitude for optimization. It is hoped that the effect of reduced tip thickness is sufficient to provide high amplitudes. A design candidate for the circular ABH sensor is shown in Figure 10.14a. The width and depth are both at 6.5 mm, with a tip thickness of 150 µm and a base height of 1.95 mm. The harmonic analysis shows a resonance frequency at 99.8 kHz. This was used as the final design for sensor evaluation.

10.4 Sensing Element Concepts for the ABH Sensor

Since added stiffness is expected to reduce the effectiveness of the ABH sensor, a minimally intrusive or noncontact sensing element is required. Two of the sensor

configurations presented in Chapter 6 are well-suited to this task: the FPI and the single-point bonded FBG.

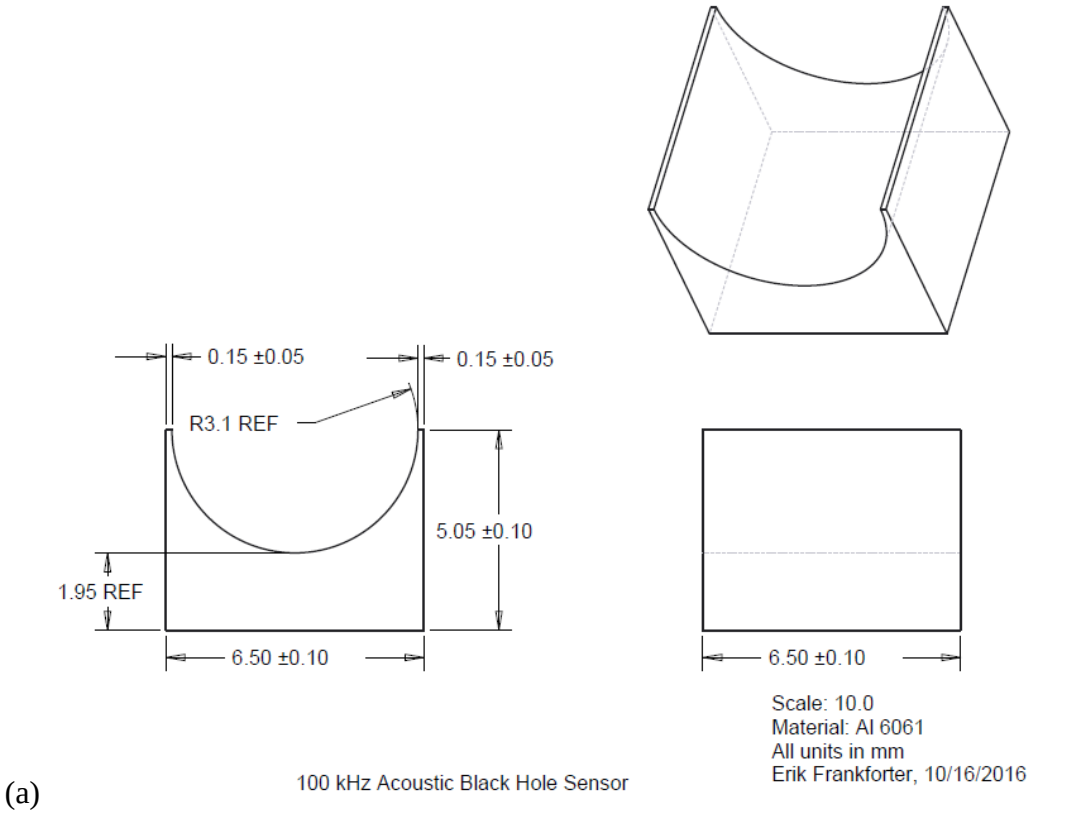

Figure 10.14: Final ABH sensor design shown via (a) CAD drawing of 100 kHz ABH sensor, and (b) harmonic analysis frequency sweep of directional deformation of the ABH tip

An FPI is a noncontact displacement sensor where reflected light intensity is proportional to the length of a gap between two reflective surfaces. A concept sketch for a FPI-ABH sensor is shown in Figure 10.15a. In response to either in-plane or out-of-plane

base excitation, each sensor tip will move in a longitudinal direction (parallel to the longitudinal axis of the optical fiber).

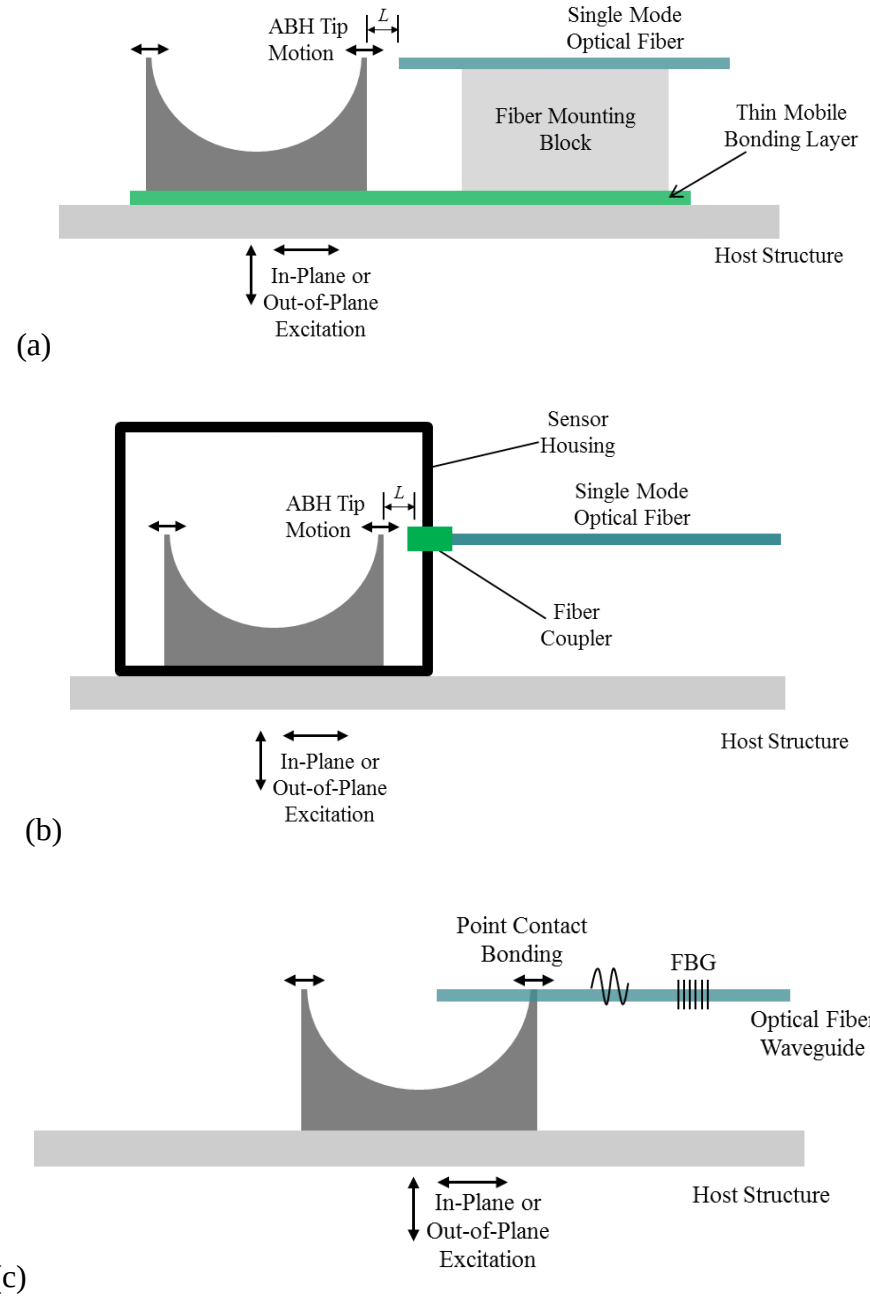

Figure 10.15: Conceptual sketch of (a,b) noncontact FPI ABH sensor configurations and (c) point-contact FBG configuration

The distance L between the ABH sensor and the optical fiber serves as the Fabry-Pérot optical resonance cavity. Modifications to the ABH setup may be necessary for this configuration. The optical fiber will need to be mounted to an external structure (e.g. a "mounting block"). Both the mounting block and the ABH sensor will need to be bonded to a thin mobile bonding layer so their precise alignment is maintained. This bonding layer is what would be bonded to a host structure.

An alternate configuration is shown in Figure 10.15b. Instead of a mobile bonding layer, a sensor housing is used as the common structure. The optical fiber is attached to the sensor housing through the use of a commercially available fiber coupler.

A conceptual sketch for a single-point bonded FBG ABH sensing configuration is shown in Figure 10.15c. In this approach, the FBG optical fiber is bonded to the tip of the ABH, and the motion of the ABH induces elastic waves in the optical fiber. The point-contact bond is able transfer motion into longitudinal wave modes that propagating along the optical fiber for sensing by a distant FBG (see Chapter 5). The benefit of this method is its simplicity. This sensing configuration can be quickly realized and assessed using the equipment and methods developed in previous chapters. The downside is that there is a possibility that by bonding the fiber to the tip of the ABH, the ABH performance will be diminished.

10.5 Dual In-Plane and Out-of-Plane Sensing ABH Sensing

For a two-point bonded FBG, antisymmetric motion of the two ABH tips was necessary to produce a response (i.e. the two sides moving 180° out of phase with each other). Since the sensing concepts in Section 10.3 require the motion of only one side of the ABH, symmetric motion of the two ABH tips can also produce a response (i.e. the two

sides moving in phase with each other). Figure 10.16 shows such a mode shape resulting from a modal analysis on the 6.5 mm ABH sensor design. The resonance frequency of this mode is at 138 kHz. Because of this, the ABH sensor may have dual in-plane and out-of-plane sensing capabilities. This is significant, particularly for AE sensing. Conventional piezo AE sensors only sense out-of-plane components of waves, and in-plane sensing is highly desirable to obtain additional damage-related information from AE signals.

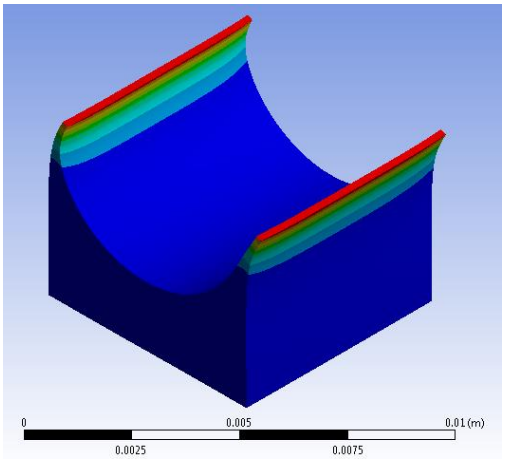

Figure 10.16: 138 kHz mode of in-plane sensitive mode with ABH tips vibrating in phase

10.6 Sensor Concept Validation with a Scaled-Up Prototype

Since the design of the ABH sensor followed vibrational concepts in its analysis, validation of its resonance modes can add additional assurance of its mechanisms of action. LDV, a non-contact method for measuring out-of-plane motion using the Doppler effect, is well-suited to this task. However, the small size of the 6.5 mm ABH sensor prototype makes mode shape assessment difficult. To perform this study, a scaled-up ABH resonator was designed using the methods described in section 10.2.3. A circular profile is used to generate a tapered tip. The width and depth were 50 x 50 mm (Figure 10.17a). The sensor designed for a resonance frequency of 10 kHz. Figure 10.17b,c show the final prototype.

A 5/16’’ hole with a counterbore were included for sensor mounting to a Brüel & Kjaer type 4809 vibration exciter (shaker table). The shaker table documentation reported a linear range up to 20 kHz. A Polytec OFV-505 LDV was used for sensing the out-of-plane velocity of the ABH resonator.

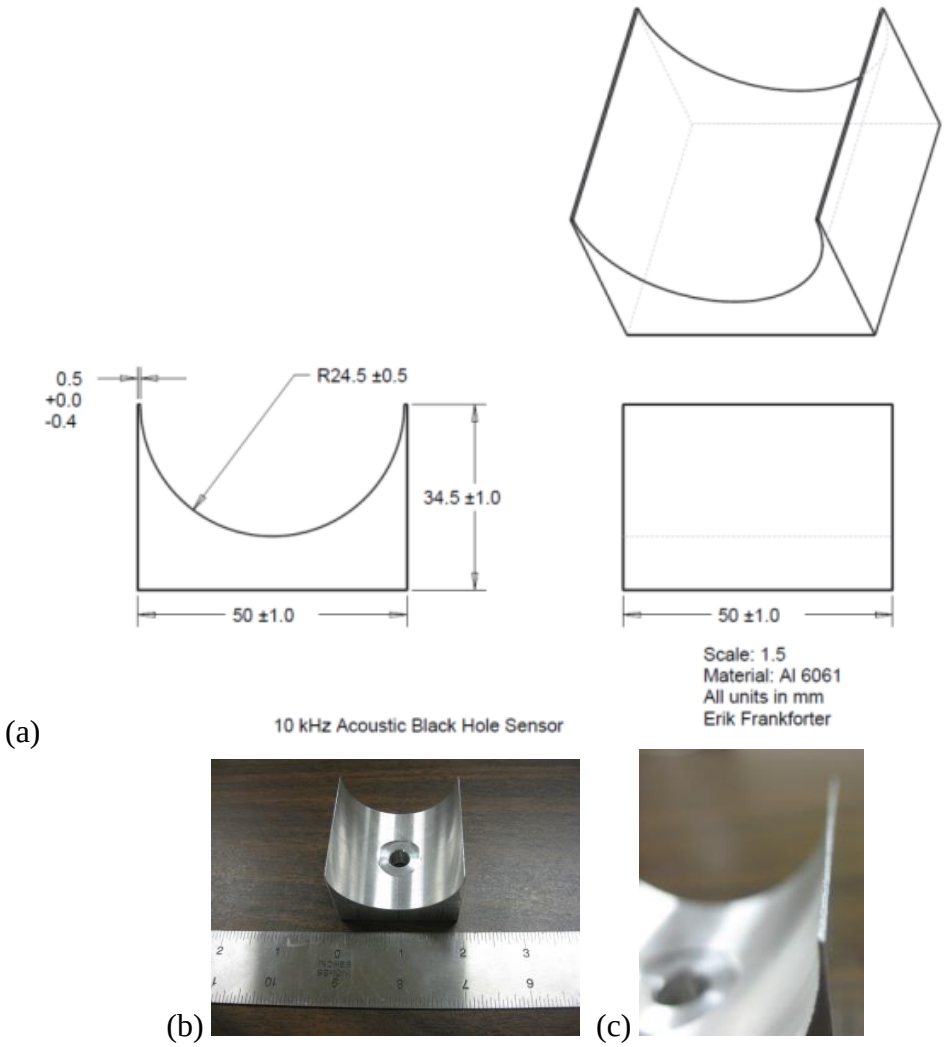

Figure 10.17: (a) CAD drawing of a 10 kHz ABH resonator, and (b,c) ABH resonator prototyped in USC machine shop

The shaker table was placed inside a fixture designed to rotate it by 90° so the ABH motion was out-of-plane with respect to the LDV. The LDV was mounted to a 2D

translational stage controllable via OKOS ODIS 3.16 software which integrated waveform capture with motor control. The experimental setup is shown in Figure 10.18.

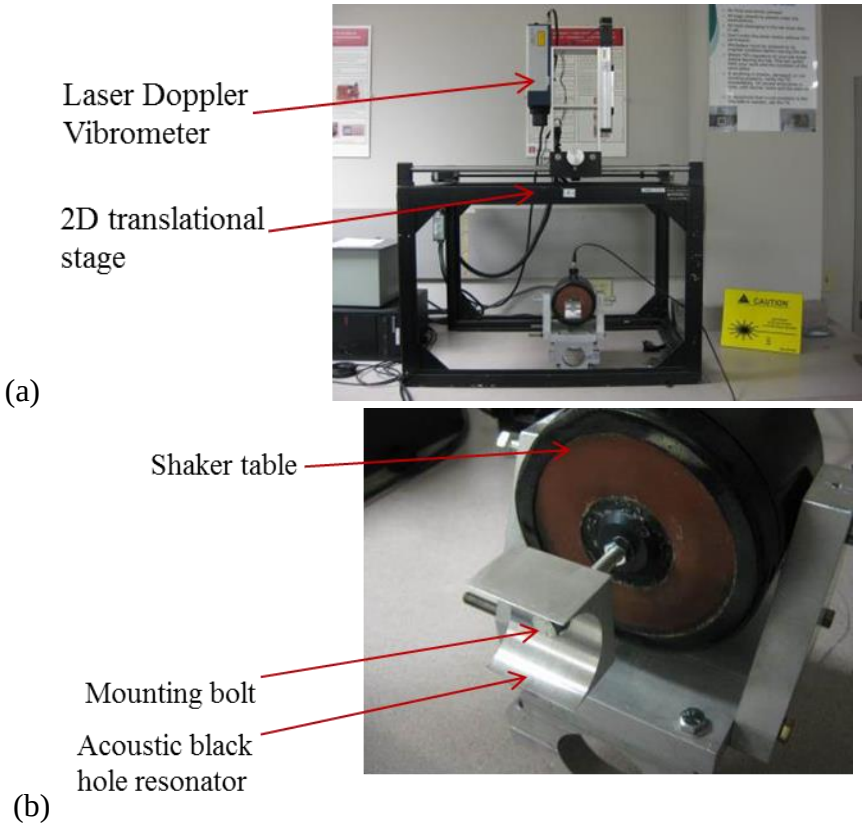

Figure 10.18: (a) Sensing performed by an LDV mounted to a 2D translational stage, and (b) a shaker table mounted on a rotatable fixture to obtain velocity data from different directions

In a first set of experiments, the shaker table was excited with a 1-20 kHz chirp excitation to determine resonance frequencies. Figure 10.19a,b shows the chirp response of the bolt used to mount the ABH resonator the shaker table. Unfortunately, the shaker table motion measured at the bolt head had a resonance frequency at 11 kHz, very close to the ABH sensor resonance frequency.

The resonance could be caused by either the bolt or the shaker table (the shaker table had been previously repaired). This does not preclude analysis, but meant that the sensor response needed to be carefully calibrated with respect to the input velocity. A nut

and lock washer were used to hold the ABH resonator rigidly to the mounting bolt, and the chirp excitation was performed again (Figure 10.19c,d). Additional resonances caused by the ABH can be seen in the velocity response. This velocity frequency response was taken as the input velocity and used for calibration of the ABH resonator.

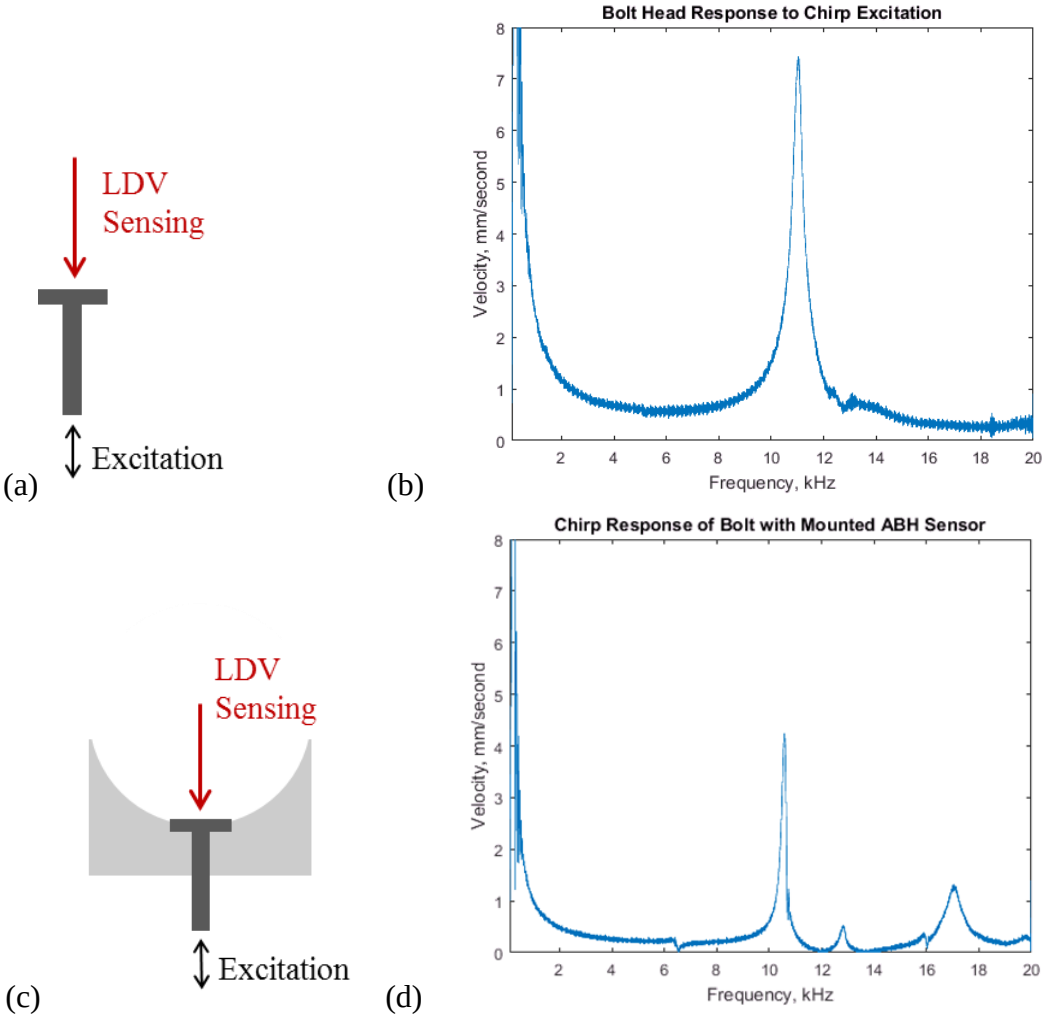

Figure 10.19: (a,c) Direction of bolt excitation and sensing, and (b,d) frequency sweep of measured bolt velocity

The shaker table fixture was rotated by 90° to measure the sensor tip velocity (Figure 10.20a). The laser was pointed as close as possible to the corner of the ABH. The amplitude of the ABH resonator velocity was divided by the amplitude of the input velocity to obtain a calibrated response (Figure 10.20b,c). Because of artifacts induced by regions

of near-zero input velocity, results are split into two regions: 100 Hz – 11 kHz and 14.5 kHz to 20 kHz. Clear resonances are present in the calibrated response at approximately 6.0, 10.5, 15.9, and 17.5 kHz. Significant mechanical amplification is present at 6.0 and 15.9 kHz – approximately 30 and 80 times amplification.

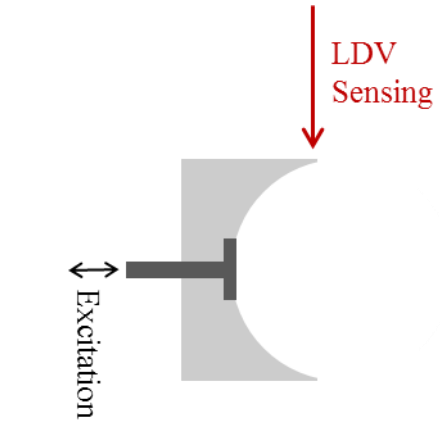

(a)

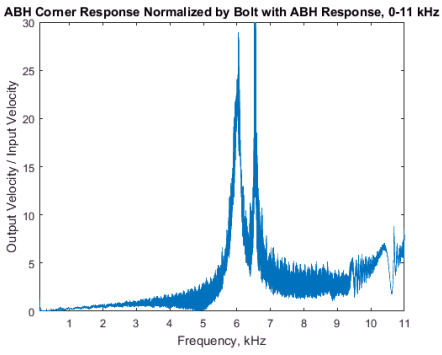

(b)

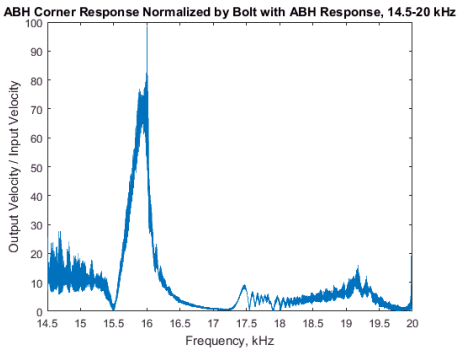

(c)

Figure 10.20: (a) Direction of excitation and LDV sensing, (b) calibrated response from 100 Hz – 11 kHz, and (c) calibrated response from 14.5 kHz – 20 kHz

Harmonic excitations were performed at the four resonance frequencies identified. The velocity was calculated at the bolt head with the ABH resonator attached. Then, the shaker table fixture was rotated by 90° to measure the sensor tip velocity at 10 points spanning the sensor tip (Figure 10.21a). The ABH tip velocity was divided by the input velocity of the bolt head to get a calibrated response at each resonance frequency (Figure

10.21b). The amplification values (output velocity / input velocity) were different from those seen in the chirp response. In particular, the 10.5 kHz resonance had a 5 times amplification, and the 17.5 kHz resonance had a 20-30 times amplification depending on the position along the tip of the sensor.

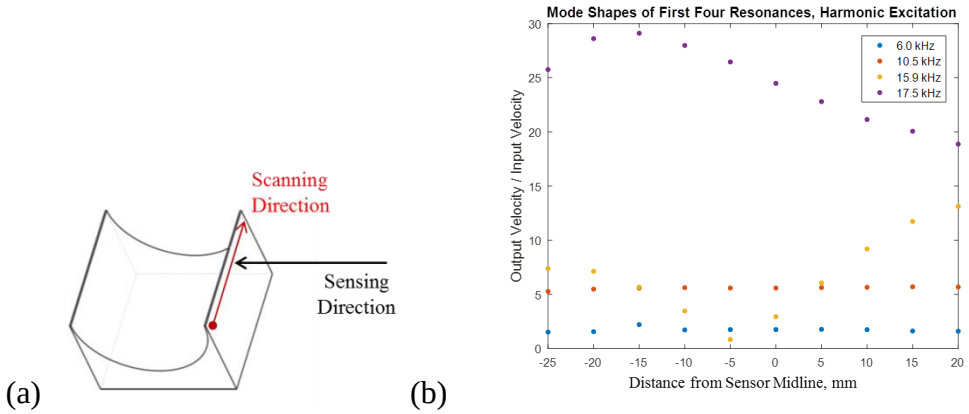

Figure 10.21: (a) Scanning direction of LDV sensing, and (b) four mode shapes across the span of the ABH tip

Area scans across the side of the ABH (Figure 10.22a) were used to determine sensor mode shapes which could be matched to mode shapes from a FEM modal analysis. At each scanning point, a 100 Hz – 20 kHz, 200 μs linear chirp burst was excited. In Figure 10.22b, the FFT amplitude is plotted for the point in the area scan where its amplitude is a maximum. For every frequency, this was somewhere along the tip of the ABH.

A mode shape retrieval method was performed, consisting of the following steps:

- The FFT was taken at each scanning point to isolate motion at a given frequency. At a given frequency, the real part of the complex number represents an arbitrary point throughout the phase of the vibration
- For a given frequency, the complex number was multiplied by the phase factor $e^{i\varphi}$ where $0 < \varphi < 2\pi$ is the phase angle in radians. By sweeping the phase factor from

0 to 2π, a video was created. This is the experimental analogue to an FEM video of a harmonic response at a given frequency

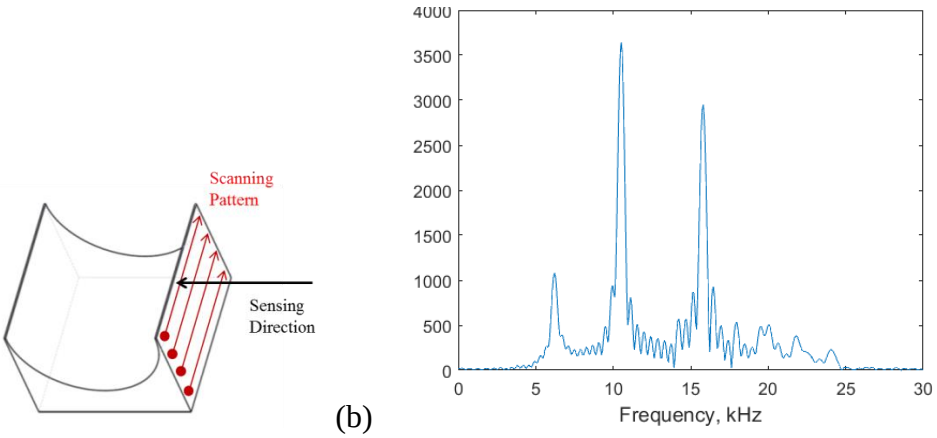

Figure 10.22: (a) An area scan was used for experimentally evaluating mode shape comparison, and (b) FFT amplitude at its maximum point for each frequency

The mode shape videos were matched with ANSYS modal analysis mode shape videos to identify given modes. Experimental modes at 6.2 kHz, 10.5 kHz, 15.8 kHz, and 24.1 kHz (Figure 10.23) corresponded to FEM calculated modes at 10.0 kHz, 19.1 kHz, 17.1 kHz, and 22.9 kHz, respectively. Modes with a "flexural" type motion of the ABH tip corresponded well to calculated modes. The modes with an "axial" type motion of the ABH tip were lower for the experimental cases, lowering from 10.0 kHz to 6.2 kHz and 19.1 to 10.5 kHz. This is likely due to the difference in boundary condition. In the FEM, the model was formulated under free boundary conditions. Experimentally, the boundary condition could be considered closer to an elastic foundation.

From this study, the experimental mode shapes of the ABH resonator correspond well to mode shapes of the mode shapes observed in FEM. There were discrepancies in the resonance frequency of the axial type modes due to changes in boundary conditions.

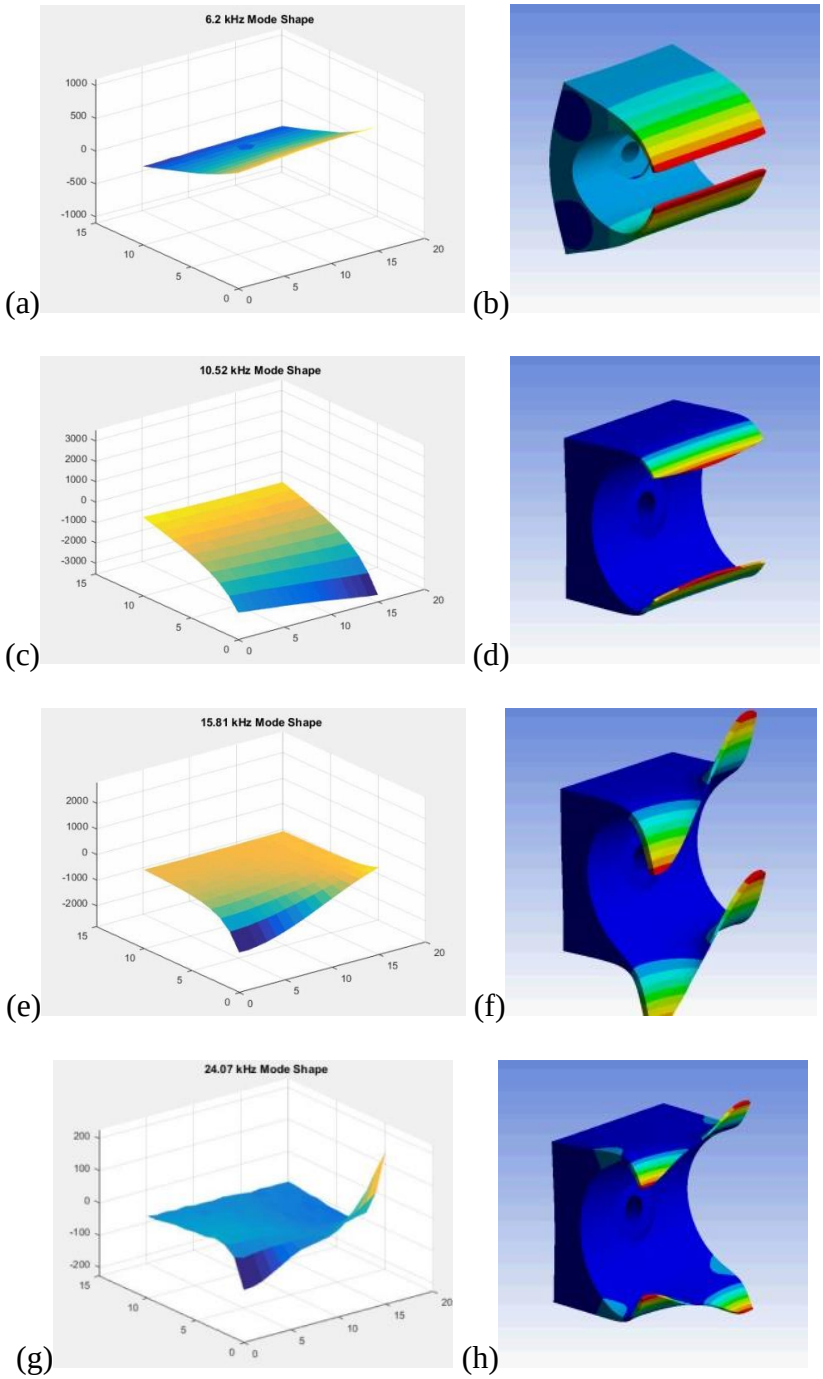

Figure 10.23 (a, b) “Axial” mode predicted at 10.0 kHz and measured at 6.2 kHz, (c, d) “axial” mode predicted at 19.1 kHz and measured at 15.8 kHz, (e, f) “flexural” mode predicted at 17.1 kHz and measured at 15.8 kHz, and (g, h) “flexural” mode predicted at 22.9 kHz and measured at 24.1 kHz.

However, this visualization adds a degree of confidence that the FEM design and analysis well-predicts the physical structure. This confidence extends to the 100 kHz ABH prototype, in that the vibrational modes identified should be indicative of the sensor motion.

10.7 Evaluation of a 100 kHz ABH Sensor under Free Conditions

The 100 kHz ABH sensor designed in section 10.2.3 (Figure 10.14a) was prototyped at the USC machine shop (Figure 10.24). It was decided that the point-contact bonded FBG sensing configuration would be tested, as FBG sensing capabilities were already available in the laboratory.

Figure 10.24a shows a prototyped ABH sensor with a bonded PWAS and FBG. The FBG was bonded along the side of the ABH sensor at the very tip of the ABH. Microscopic measurements of sensor dimensions were made, shown in Figure 10.24b. The designed and actual dimensions were:

- Sensor width: 6.50 mm design, 5.75 mm measured
- Base height: 1.95 mm design, 2.26 mm actual
- Tip thickness: 150 μm design, 200 μm actual

The measurement indicated a decreased width and increased base height; thus, an increase in the 1st resonance frequency is expected from the sensitivity curves of Figure 10.10 and Figure 10.11.

Three experimental assessments of the free 100 kHz ABH sensor were performed: a 1-500 kHz 20V_{pp} linear chirp (Figure 10.25a,b), EMIS (Figure 10.25c), and a pitch-catch at 150 kHz (Figure 10.25d). By tuning the excitation frequency of the pitch-catch, 150 kHz was found to be the point where the FBG had the largest response.

In the EMIS experiment (Figure 10.25c), the 1st resonance frequency is at 118 kHz, 18% larger than the design frequency. Higher harmonics start at 118 kHz, with a large peak at 365 kHz. In the chirp experiment (Figure 10.25a,b), there were a large number of closely spaced resonance modes across roughly the 100 – 400 kHz range.

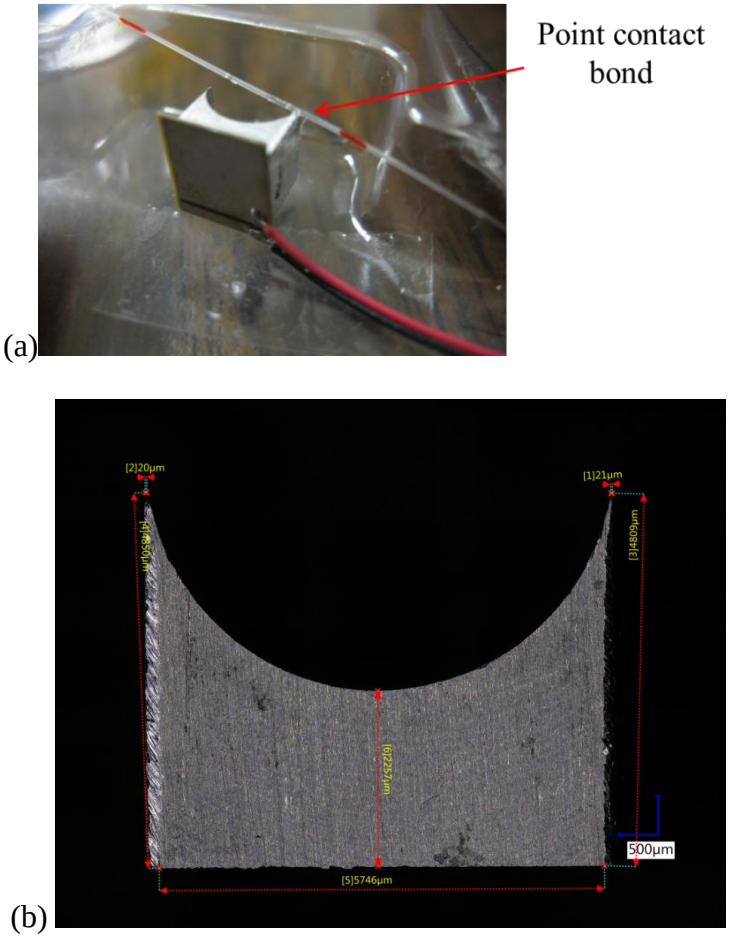

Figure 10.24: (a) Sensor prototype with bonded PWAS and point-contact bonded FBG, and (b) microscopic sensor geometry measurements

This indicated that the ABH sensor may actually be a broadband sensor in that range. This was not intentional, as higher order modes were not considered in the analysis; however, it is a welcome result.

The pitch-catch response (Figure 10.25d is the first experimental indication that the ABH sensor with a point-bonded FBG optical fiber may be a highly sensitive design. Looking at the received waveform, the signal amplitude is so large that a noise floor cannot be determined.

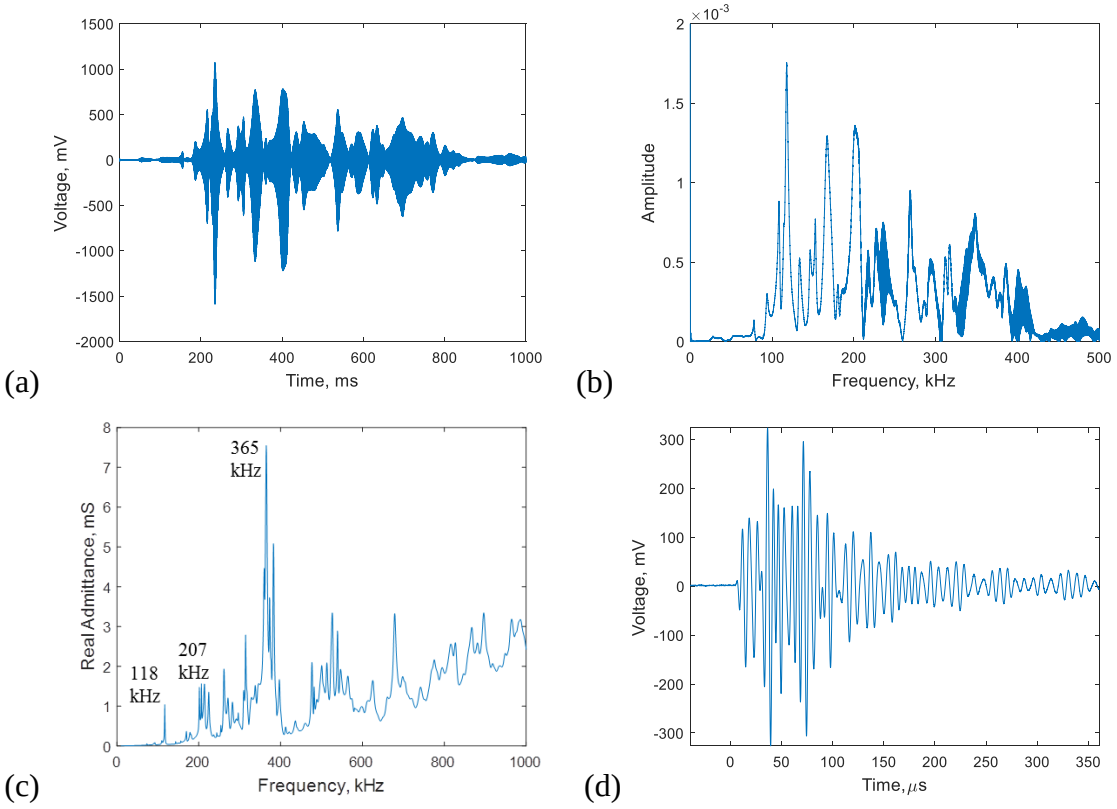

Figure 10.25: Circular ABH sensor (a,b) chirp response time and frequency domain, (c) PWAS EMIS response, and (d) FBG response to 150 kHz excitation via PWAS on the sensor base

Rather, the noise in the pre-waveform portion of the signal is digitization noise and thermal noise from the oscilloscope only. Comparing this to similar experiments on the 8.0 and 3.2 mm ring sensor, the signal to noise ratio is clearly better than the other two signals. An exact quantification cannot be determined, as only a lower bound on the SNR can be obtained for the ABH sensor. It is a positive indicator that testing and development should be continued for the ABH sensor.

10.8 FBG Effect on ABH Sensor Dynamics

Since there were concerns about the ABH effect on sensor dynamics, LDV measurements were taken at the tip the ABH sensor with and without the optical fiber bonded. A $5V_{pp}$ 0-1000 kHz chirp excitation was performed using the PWAS bonded to the ABH sensor base for excitation. The LDV was pointed at the corner of the ABH, and a screw-adjusted mechanical stage was used to adjust the laser point to the tip of the ABH (Figure 10.26). The tip of the ABH sensor was found by identifying the point where the ABH sensor velocity was a maximum in response to the chirp excitation. The 0-1000 kHz chirp responses of the ABH without and with FBG bonded are shown in Figure 10.27.

(a) 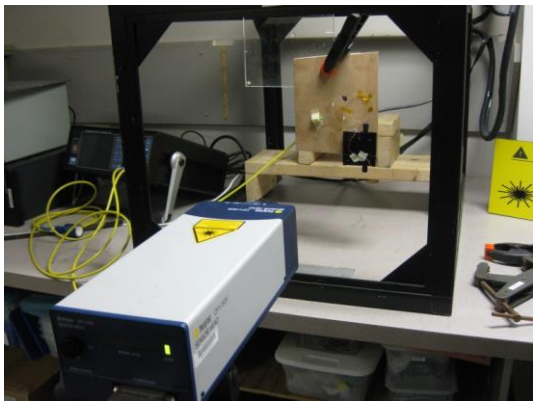 (b) 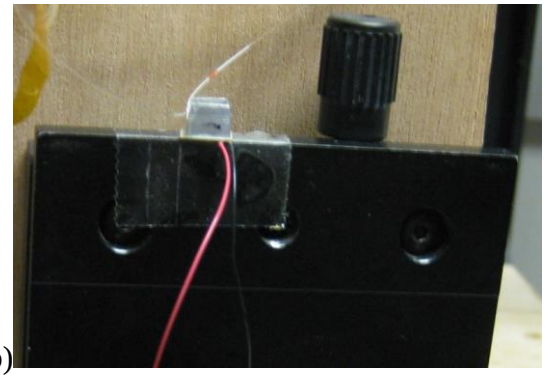

Figure 10.26: (a) LDV measurement at the tip of the ABH sensor, and (b) ABH sensor attached to screw-adjusted mechanical stage

(a) 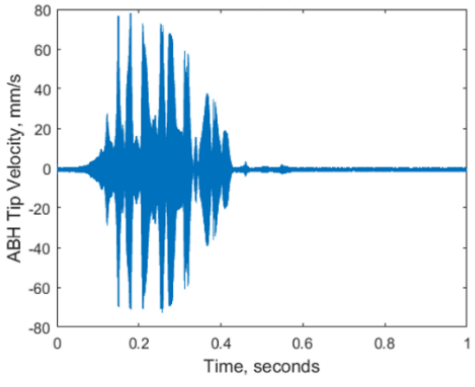

(b) 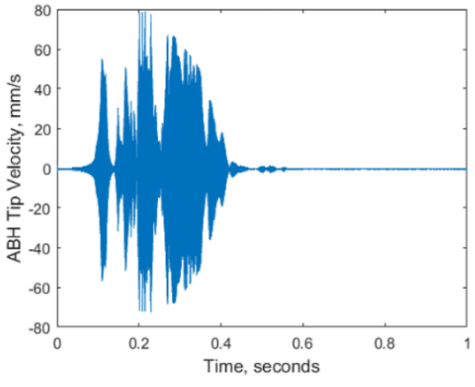

Figure 10.27: ABH tip velocity in response to 0-1000 kHz chirp excitation (a) with no optical fiber, and (b) with an optical fiber bonded

There was no significant reduction in amplitude, however there was a spread in its frequency components. One possible explanation for this is that the cyanoacrylate adhesive added damping near the tip of the ABH. From the literature survey, the tip of an ABH is very sensitive to small amounts of damping, even a small amount of adhesive could influence this aspect of the response.

10.9 Development of a Power Law ABH Sensor

10.9.1 FEM Performance Comparison Between Circular and Power Law ABH Sensors

The ABH sensor assessed so far did not have a true power law ABH, but instead used a more easily-manufactured circular taper. To determine if it was worth the development time of a power law ABH sensor, a FEM comparison of a circular versus a quadratic taper was performed first.

The geometry of the 100 kHz circular ABH sensor was used as a reference. The same width, tip width, height, base height, and depth were used. The only difference was the use of two quadratic tapers, one for each ABH tip. The taper is prescribed by one half of a parabola oriented horizontally (i.e. by $x = c(y-h)^2, y \le h$). The FEM meshes are shown in Figure 10.28.

A harmonic analysis was performed with a prescribed 1 μm out-of-plane displacement at each sensor base. The harmonic responses of the 1st resonance frequencies are shown for each in Figure 10.29. The circular profile had a 38 times displacement amplification, whereas the quadratic ABH sensor had a 53 times displacement amplification. A significant frequency shift was also present. The character of the 1st resonance mode shape (both tips vibration 180° out of phase) was not changed (Figure 10.30).

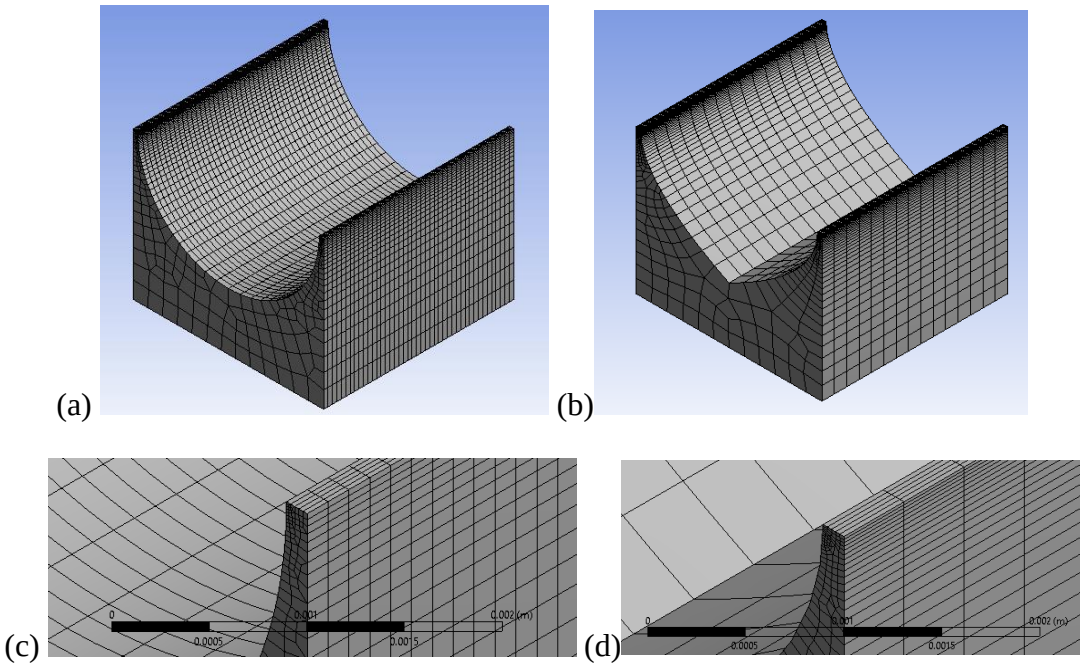

Figure 10.28: (a,c) Circular ABH senor mesh and (b,d) quadratic ABH sensor mesh

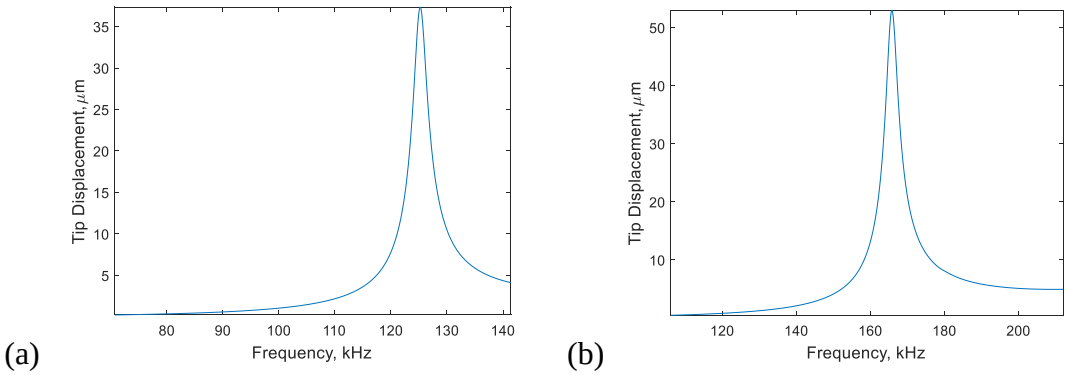

Figure 10.29: (a) 1st resonance of circular ABH sensor, and (b) 1st resonance of quadratic ABH sensor

In practice, the sharp intersection of the two quadratic ABH profiles at the midline of the sensor would be rounded during manufacturing. Because of this, a separate harmonic analysis was performed, where this sharp intersection was replaced with a 1 mm round. There were no changes in sensor performance for this model.

10.9.2 Design of a Power Law ABH Sensor

Because the power law ABH sensor was predicted to perform better than the circular ABH sensor, it was decided that one should be designed and prototyped. A design optimization was performed using ANSYS Workbench. Just as in previous sensor designs, an adaptive meshing approach was created by specifying the number of elements across several landmarks.

(a) 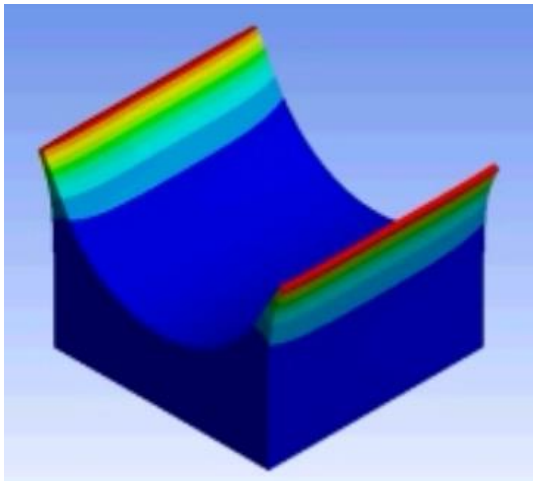 (b) 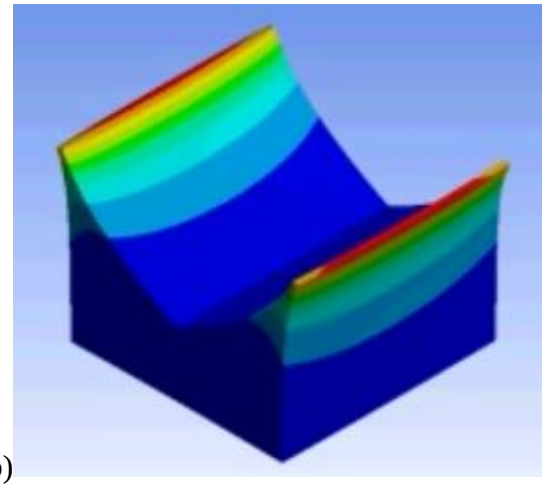

Figure 10.30: 1st resonance mode of (a) the circular ABH sensor and (b) the quadratic ABH sensor

The geometry creation itself required special attention. The ANSYS Workbench built-in CAD suite (ANSYS DesignModeler) did not support the specification of a parametric curve which was required to create the two parabolic ABH sensor profiles. The most recent version of ANSYS SpaceClaim has this feature, but we were unable to update to that version for this research. To model the ABH sensor, the bidirectional CAD associativity feature between ANSYS Workbench and Creo Parametric 3.0 was used. The geometry was fully parameterized in Creo so that both dimensions and order of the power law could be specified directly. These parameters were exposed to the ANSYS Workbench working environment, where ANSYS can request a model with new parameters, followed by Creo

updating the CAD model and passing it back to ANSYS. This allowed geometric values specified in ANSYS Workbench DOE and optimization algorithms to automatically update a Creo model, which automatically transferred the model back to ANSYS Workbench. After configuration, the entire DOE and optimization process required no further human input.

The following parameters and bounds were considered in the design exploration:

- Base Width: 5-12 mm
- Base Height: 1.5-4.5 mm
- Sensor Height: 4.6-8 mm
- Tip Width: 150-500 μm
- ABH Power: 2-5

The relaxation of a circular profile to a power law curve allowed for an additional geometric design feature, as the base height and sensor height could be specified separately. The ABH power was also parameterized in the CAD model, allowing it to be used as a continuous input parameter. However, instead of trying to control amplitude and frequency independently, a broadband objective was used. In this optimization, the average in-plane displacement amplitude across a 10-1000 kHz (averaged across frequency) was used instead. Comparing the broadband objective function to an objective function based on maximum amplitude in the 10-1000 kHz range Figure 10.31), the two objective functions had a strong correlation. This seems to indicate that a single resonance-based amplitude objective function is a good predictor of a broadband resonance design optimization.

The displacement at each frequency step was provided by the average displacement amplitude on one of the ABH tips. A sensitivity analysis was performed and converged

after 53 models. The results of this sensitivity analysis only had a significant Spearman correlation coefficient for the ABH tip width and predicted no sensitivity due to the other parameters.

Figure 10.31: Correlation between average displacement and maximum displacement objective functions

A second DOE was performed so it could be used as an input for the calculation of a response surface. A central composite design was used. A total of 34 models were used to develop and validate a multivariate response surface based on the ANSYS built-in genetic algorithm interpolation across the design space. Just like the analysis procedure for the circular ABH sensor, local sensitivities were calculated. Figure 10.32a shows a local sensitivity chart associated with a 7.5 mm width, 325 µm tip width, 6.3 mm height, 3 mm base height, and ABH power of 3.5. By changing the width to 10 mm, the relative effect of base height and ABH power changed (Figure 10.32b). This indicated that the effects of input parameters were non-monotonic, explaining why the Spearman correlation coefficient predicted no sensitivity from these variables.

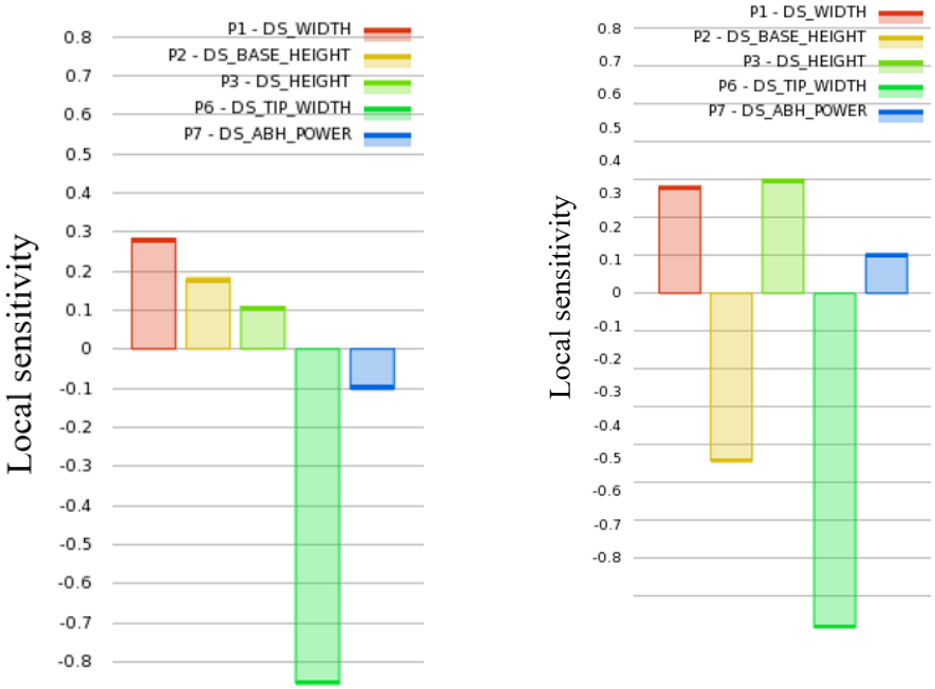

Figure 10.32: Change in local sensitivity curves at different points in the design space indicate that some of the parameter effects are non-monotonic

An adaptive single-objective genetic algorithm was used to identify the ideal design candidate. The tip width was fixed at µm. The ABH power was set to 2 since higher order powers had no benefit on sensor performance from the previous analyses (Figure 10.33). Only the base width, base height, and sensor height were factored into the optimization. The bounds for the input parameters were the same as for the sensitivity analysis above. A total of 80 models were performed in the design optimization.

The optimized design is shown in Figure 10.34 (the depth was set to 14 mm in the final prototype). All three variables were pushed to or near the limits of the design space. The width was maximized, whereas the height and base height were minimized. Conceptually, this makes sense based on the analytical models of the ABH waveguide. The sensor width is maximized to increase the ratio between sensor width and tip width. This is because the energy across the span of the sensor width is being channeled to the smaller

tip width. The minimization of sensor height provides a more gradual ABH curve, helping to maintain non-reflective conditions. The miniaturization of base height helps to minimize the size of the region where the senor geometry is not prescribed by an ABH power law. This is important, as the zero-reflection condition only occurs for a wave that is already within the ABH, not for a wave that is entering an ABH waveguide.

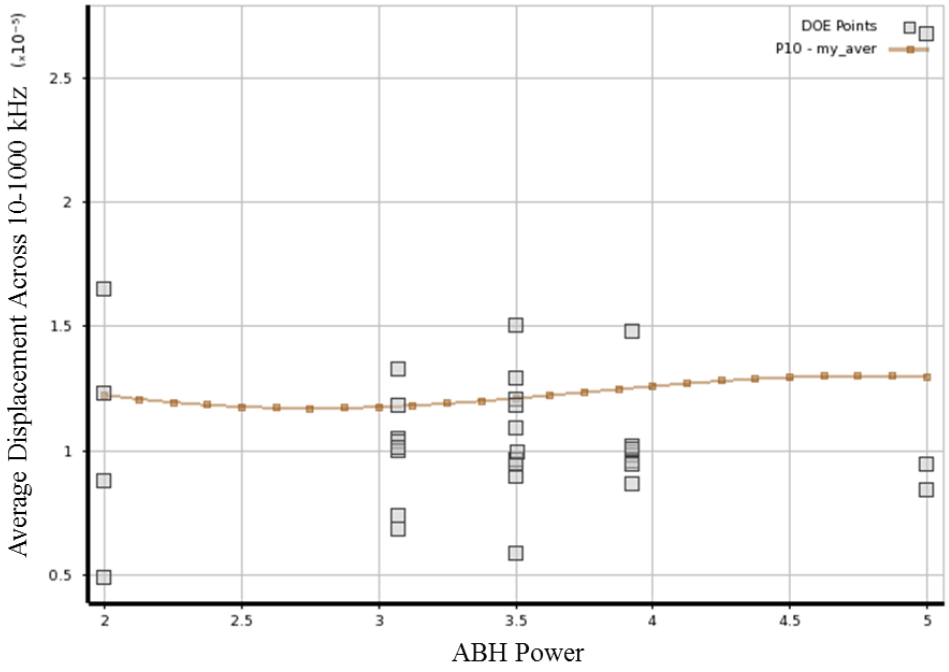

Figure 10.33: No significant effect of power law exponent on ABH sensor amplitude

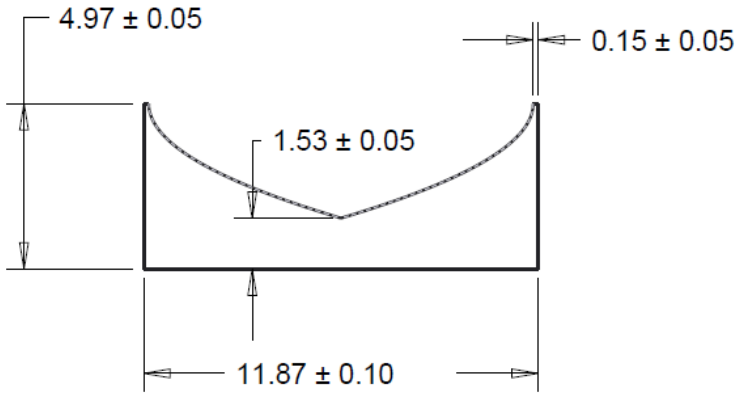

Figure 10.34: Quadratic ABH sensor design

The quadratic ABH sensor design was prototyped in the University of South Carolina machine shop. A long rectangular piece of aluminum 7075 was used as a base, and a power law was created using a 3-axis CNC mill, with a G-code written using Creo Parametric 3.0. During the fabrication process, 2 mm was initially left overhanging on each side for tip thickness. Four individual sensors were cut from the piece of aluminum using a band saw and the sides milled flat with a vertical mill. The ABH tips were then created by milling them in 0.005 inch increments until the first pass where the flat of the tip was completely removed.

10.10 Initial Lamb Wave Evaluation of the Power Law ABH Sensor

The Lamb wave response of the power law ABH sensor was tested on a 1 mm aluminum 2024-T3 plate. This experiment was performed to evaluate two effects:

1. The influence of incident wave directionality on the ABH sensor response
2. The capability of the ABH sensor to detect both in-plane and out-of-plane motion

PWAS were arranged in 15° increments at a distance 400 mm away. The distance

(a) 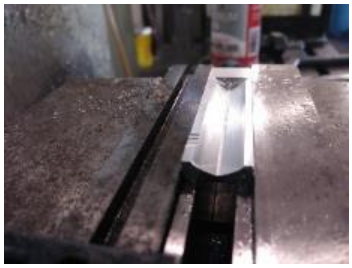 (b) 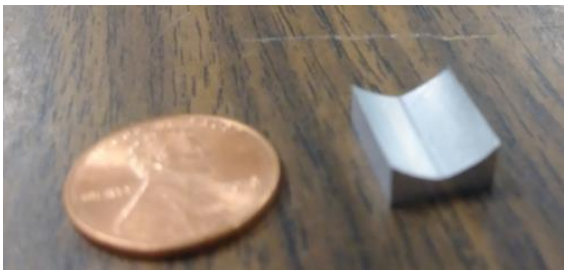

Figure 10.35: (a) ABH power law cut using 3-axis CNC mill, and (b) final ABH sensor prototype

was increased from 150 mm in the last Lamb wave experiments to 400 mm since ringing from the S0 Lamb wave mode response would spill over the A0 mode if there was not sufficient separation time. A photograph of the plate is shown in Figure 10.36.

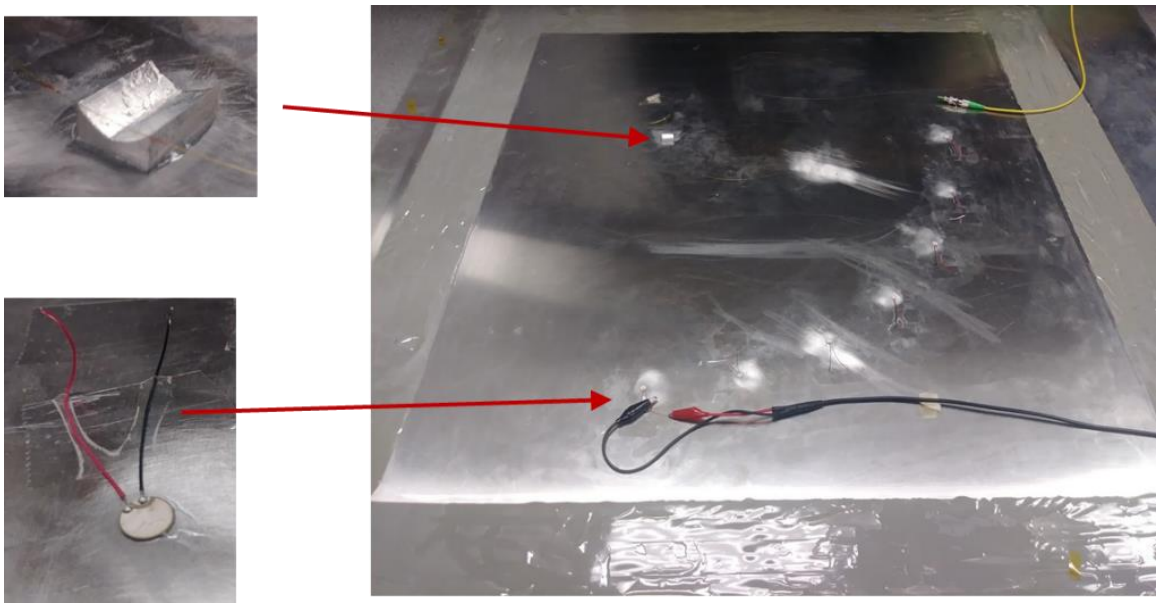

Figure 10.36: 1 mm plate for Lamb wave directional experiments

A pitch-catch was performed using each PWAS in turn, transmitting a 300 kHz 50 V_{pp} 3-count Hanning windowed tone burst. Figure 10.37 shows the response from the 0° PWAS (oriented along the longitudinal axis of the ABH FBG). A clear S0 and A0 mode are distinguishable. This validates the hypothesis that the single-point bonded ABH FBG sensor possesses both dual in-plane and out-of-plane sensitivity. Although the A0 wave mode has a higher amplitude, no conclusions on their relative sensitivity can be made until the calibration curve of the PWAS or measurements of sensor base input motion (e.g. via LDV) are taken into account.

Averaging was used to reduce the noise of the waveform. A quantitative assessment of the sensor signal-to-noise ratio was not performed, as this sensor was developed in the late stages of this dissertation. If this work is to be extended, one of the major suggestions for future work is the quantitative assessment of the quadratic ABH sensor's performance.

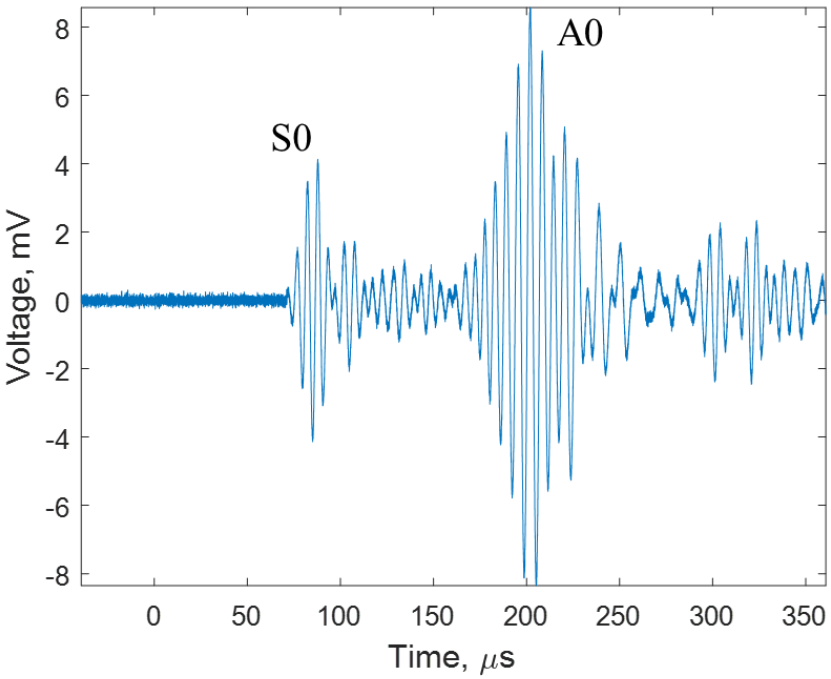

Figure 10.37: ABH sensor response to 300 kHz tone burst

The peak amplitude associated with each S0 and A0 wave mode was calculated and plotted in Figure 10.38. Surprisingly, the S0 wave mode is a maximum at 30 degrees. The A0 wave mode is also not flat or nearly flat, as would be expected. This can be explained in the context of the aperture effect. At this frequency in this specimen, the S0 wave mode has a wavelength of approximately 15 mm. This is very close to the width and depth of the ABH sensor, such that the wave would be largely tuned out. Therefore, the directional effect is highly affected by the projection of the sensor length along the direction of wave propagation. As the angle gets closer to 90° off the ABH FBG axis, there is the added effect that the ABH sensor is only predicted to be sensitivie to in-plane waves from this direction due to Poisson effects. The sharp drop in amplitude for A0 waves transverse to the FBG axis indicates that this may be the case. Similarly, the A0 wave mode has a wavelength of

approximately 5 mm, smaller than the sensor length. This explains the seemingly chaotic behavior in the ABH sensor direction response to the A0 wave mode.

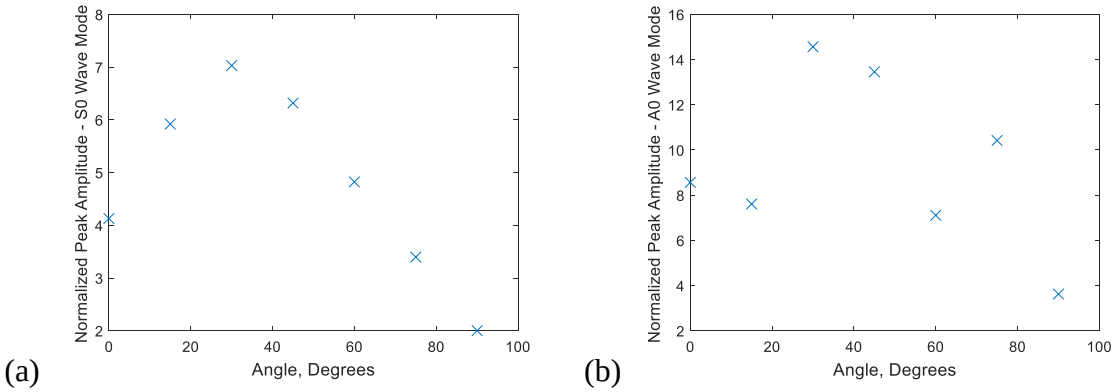

(a) (b)

Figure 10.38: Angular response of ABH sensor to (a) S0 wave mode, and (b) A0 wave mode

10.11 Summary and Conclusions

The theory of an ABH was presented including background, modeling of key wave parameters, and state of the art. A sensor concept was developed, based on the exploitation of an ABH wave trapping and displacement amplification feature. This sensor was developed and prototyped, and preliminary verification has been done. Previous uses of the ABH geometry focused on vibration and noise isolation. From a thorough search of relevant literature, this is believed to be the first use of the ABH geometry for sensing applications. Because of this, we have applied for a US patent with the title “Acoustic Black Holes for Sensing Applications” (Giurgiutiu and Frankforter 2017).

An FEM harmonic analysis was performed for a tapered thickness sensor. When an FBG sensor was bonded at two points to a sensor configuration with two ABH waveguides, the dynamic stiffness of the optical fiber highly diminished the motion of the ABH itself. This was expressed in the context of a sensor/fiber stiffness matching scheme. In FEM, the maximal displacement was obtained only when the dynamic stiffness of sensor and fiber

were matched. Based on this, conceptual sketches of point-contact bonded FBG and FPI sensing elements were developed, as they are expected to have no impact or less impact on the ABH sensor response.

A 100 kHz ABH sensor prototype was designed. Relevant features were identified using a sensitivity analysis and response surface. A goal-driven optimization was performed to seek a maximum amplitude while maintaining a 100 kHz target frequency. There were no combinations of design features that could increase amplitude and maintain a target fundamental resonance frequency, so design optimization for amplification hit a practical limit.

Mode shape validation was performed using a scaled-up sensor prototype. Visualizations of mode shapes were matched to FEM predictions, and the mode shape motion matched extremely well. There were discrepancies in the mode shape natural frequencies, although these can be attributed to the change in boundary conditions by mounting the ABH resonator to the shaker table.

The 100 kHz circular ABH sensor was prototyped and evaluated under free conditions. Preliminary results indicate that the sensor may be broadband over a 100-400 kHz range with a very high sensor sensitivity. A noise quantification could not be determined, as the signal level was large enough that optical equipment noise could not be observed using the equipment given. This is a positive indicator that the sensor may have a very high sensitivity.

FEM harmonic analyses showed potential performance benefits of a power law ABH over the use of a circular taper. A design exploration and broadband objective function was used to optimize for out-of-plane displacement across a 10 – 1000 kHz

frequency range; this resulted in a 12 mm wide quadratic ABH sensor, although the optimization algorithm pushed many of the parameters to their bounds. A prototype of this sensor was sensitive to both in-plane and out-of-plane motion in Lamb wave experiments. Its directional response was assessed. The directional response was heavily affected by the sensor's aperture effect, particularly for the A0 wave mode as its wavelength was smaller than the sensor base length along any direction.

The ABH sensor has promise for use as a highly sensitive in-plane and out-of-plane ultrasonic fiber-optic sensor. However, the biggest limitation so far is that its response has not been placed on a quantitative footing. This is the emphasis of Chapter 11, where calibration curves referring sensor motion to surface motion are calculated for the sensors developed in this work. This calibration was performed for the circular ABH sensor. Since the power law ABH sensor was developed in the very late stages of this work, its calibration was not performed and is left as an avenue for future work.

CHAPTER 11

CALIBRATION OF SENSOR PROTOTYPES

11.1 INTRODUCTION

In Chapters 8-10, there were indications that both the ring sensor and ABH sensor were broadband. Finite element harmonic analyses predicted a broadband response. Chirp excitations of the ABH and ring sensors showed numerous closely spaced resonance peaks. The tuning curve experiments in Chapter 9 indicated that both the original 100 kHz ring sensor and the miniature ring sensor possess broadband responses. However, in terms of sensor characterization, these results were still largely qualitative for three reasons:

- The Lamb wave experiments did not refer sensor strain or voltage back to absolute motion of the plate base
- The frequency spectrum of transmitter PWAS were not deconvoluted from the frequency response of the sensors under evaluation
- In Lamb wave experiments, the frequency content of the excitation signals was wider than the resonance peak spacing observed in chirp experiments.

In this chapter, these limitations are addressed by performing sensor calibration experiments. Although these sensors have wider potential applications than AE sensors the calibration framework is presented in the context of AE sensor calibration. This is because there is a large body of scientific work on AE sensor calibration methods.

This work was not performed to extend the science of calibration as applicable to piezoelectric AE sensors. Current facilities used in state of the art AE sensor calibration are very sophisticated, creating a barrier for entry into this field that is outside the scope of this work. Instead, the aim of this work was to use the principles of AE sensor calibration as a tool for sensor characterization. This allowed for granular measurements of FBG, PWAS, ring sensor, and ABH sensor frequency response functions referenced to absolute surface motion of the host structure. The combination of AE sensor calibration approaches with a strain-calibrated FBG optical system also provided for some theoretical advancements, as described later in this chapter.

11.2 Background on Acoustic Emission Sensor Calibration

An AE calibration curve is prescribed by its voltage output (in dB) per unit surface motion of the host structure. Either displacement or velocity are used as input motion, and the curve is expressed as a function of frequency, often from 10 kHz – 1 MHz.

To experimentally calculate an AE sensor calibration curve, the input motion must be known via theoretical calculation or direct measurement. Direct measurement approaches are typically non-contact such as a capacitive sensor, interferometric sensor, or LDV. Then, the output voltage of the AE sensor is divided by the input motion in the frequency domain, yielding the calibration curve.

Several approaches are amenable to calculation of an AE sensor calibration curve. Each of them essentially serve to prescribe an input motion to an AE sensor base. Using a face-to-face sensor arrangement, a transducer with a known transmission spectrum can be bonded directly to an AE sensor and excited with a pulse. A reciprocity calculation approach uses three AE sensor/transmitters in a round robin fashion to obtain the

calibration curves for each; an inherent assumption that their transmission and receiving spectrums are the same has raised concerns for this method in recent years (Ono 2016). The use of a bulk wave excited through a transfer block can be used, again via measurements of surface motion and bonded sensor response on the other side (Theobald 2009; Ono 2016).

Rayleigh wave calibration methods are some of the most accurate and reproducible, at the expenses of additional facility development time and costs. They are useful as the mechanical effect of the sensor on the host structure is minimized, and they also sidestep questions of in-plane and out-of-plane sensitivity (Rayleigh wave motion rotates elliptically between in-plane and out-of-plane as it propagates). A Rayleigh wave calibration is performed in this chapter's experimental work. Two ASTM standards outline approaches for Rayleigh wave calibration: ASTM E1106 and ASTM E1781. ASTM E1106 uses a pulse applied to a very thick cylinder to generate a Rayleigh wave for calibration. It is one of the most accurate calibration approaches, allowing sensors calibrated by this method to serve as transfer standards. ASTM E1781 provides a means of using a previously calibrated AE sensor to obtain a calibration curve for a second AE sensor. This standard relaxes some of the requirements of ASTM E1106 such as the immense size of the test block geometry. It still provides calibration curves that are generally within 1 dB of a primary calibration, and usually off at the point of maximum error at no more than 3 dB.

A Rayleigh wave calibration is performed in this chapter's experimental work; following are additional assumptions that factor into the calibration. Input motion is assumed to be the motion of the free surface, before the sensor is bonded. The mechanical influence of the sensor on the structure is assumed to be incorporated into the sensor's

transfer function. When the calibration curve is calculated on a given material (typically steel), it is not transferrable to other materials due to factors such as acoustic impedance changes and changes in wavelength at a given frequency. The calibration is also performed under Rayleigh wave conditions and is non-transferrable to other types of waves.

In terms of recent research pertinent to the sensor development work herein, Theobald (2009) developed a calibration approach to separate in-plane and out-of-plane calibration curves. It uses noncontact interferometric displacement measurements of pressure and shear waves transmitted through a transfer block. Using this method, the in-plane motion and out-of-plane motion are decoupled and the sensitivities can be calculated for each separately by dividing the output velocity by the input motion in the frequency domain. He found, that for two nominally out-of-plane sensitive piezoelectric AE sensors, the out-of-plane sensitivity was around ten times higher than the in-plane sensitivity.

For guided wave approaches, the separation of calibration between in-plane and out-of-plane sensitivity may not be necessary. This is because for a guided wave in each specimen geometry and material, there are theoretical ratios between in-plane and out-of-plane surface motion for each wave mode. Instead, it may be better to obtain calibration data with respect to an arbitrarily chosen component of motion for each wave mode for a given specimen geometry and material. In practice, this could be incredibly cumbersome, and approaches at theoretically calculating guided wave calibration curves may be a more fruitful approach.

Ono (Ono, Cho, and Matsu 2010) used laser interferometer surface motion calculations to experimentally obtain calibration curves in bars and plates. He compared bar surface calibration curves with manufacturer face-to-face calibration curves in a 6.4

mm x 25.4 mm cross section, 3.66 m long aluminum 6061 bar. When the bar calibration curves were compared with manufacturer face-to-face calibration curves, they matched in general shape and order of magnitude. However, they presented up to approximately 20 dB discrepancies at some frequencies and did not clearly match the shape of individual resonance peaks.

Ono (2016) clarified an often-used calibration unit given as V/μbar. The use of this unit as the calibration curve amplitude of many commercially available AE sensors precludes their use for quantitative assessment of wave propagation. The use of this unit implies that there is a voltage generated in response to stress applied to the sensor face; however, this is physically inadmissible since the surface where the sensor would be attached is stress free (and the calibration assumes the of use free surface motion for its baseline). Often, the unit is presented as the output of ASTM E976; however, this standard specifically states that it does not provide a sensor calibration curve. This indicates that currently there may be some systematic errors in calibration standards present in the AE industry. Ono (Ono 2016) interpreted that the use of this unit most likely came from practices for hydrophone calibration, where an acoustic pressure in the water would be present on the sensor face. In this context, 1 μbar has an equivalent velocity in water corresponding to 67.6 nm/s as the particle velocity is related to acoustic pressure through the acoustic impedance. Equivalently, adding 143.4 dB to a calibration curve defined in V/μbar converts it to V/(m/s). Ono (Ono 2016) tested this experimentally, finding that this correction factor matched well with experimental calibration curves in a face-to-face calibration setup. Anecdotally, a search of AE sensor manufacturer websites where sensors are calibrated with respect to both velocity and stress finds maximum sensitivities are also

separated approximately by this correction factor of 143.4 dB. This correction factor can be used in the interim to convert from a stress calibration to a velocity calibration.

One final limitation of calibration curves is present. In principle, if both the amplitude and phase of the calibration curve are provided, it can be used to reconstruct the underlying waveform in the time-domain. Frequently, only the amplitude component of the calibration curves is expressed. This restricts analysis to that of amplitude in the frequency domain.

11.3 Sensor Calibration – Experimental Setup

11.3.1 Experimental Configuration and Analysis Method

In this section, a transfer structure was used where the waves propagate as a Rayleigh wave, and the principle of ASTM E1781 was used: transferring a calibration from a previously calibrated sensor to a new sensor. The discrepancies between this study and ASTM E1781 were related to (a) the test block and (b) the choice of excitation.

As it was impractical to purchase a test block sufficient for an ASTM E1781 Rayleigh wave calibration, an alternate specimen was used. In a previous study described in Giurgiutiu (2014), Chapter 12, it was found that waves excited by PWAS bonded to a steel rail travelled as Rayleigh waves. The exact specimen from that study was still available and used in this experiment. The rail was 16 mm thick and approximately 1.4 m long. The rail and experimental setup is shown in Figure 11.1.

Supporting the applicability of the steel rail specimen, Hamstad (2009) found that for relatively thin plates in a Rayleigh wave context (i.e. 24.4 mm steel), waveforms dominated by Rayleigh waves are predominantly sensed if a PLB is excited on the same surface as the sensor. The work of Ono (Ono, Cho, and Matsuo 2010) has also indicated

that calibrations performed in bars can provide a workable calibration curve as compared to a face-to-face calibration.

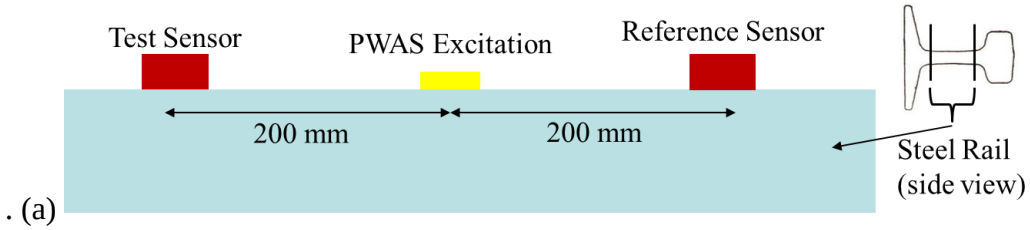

. (a)

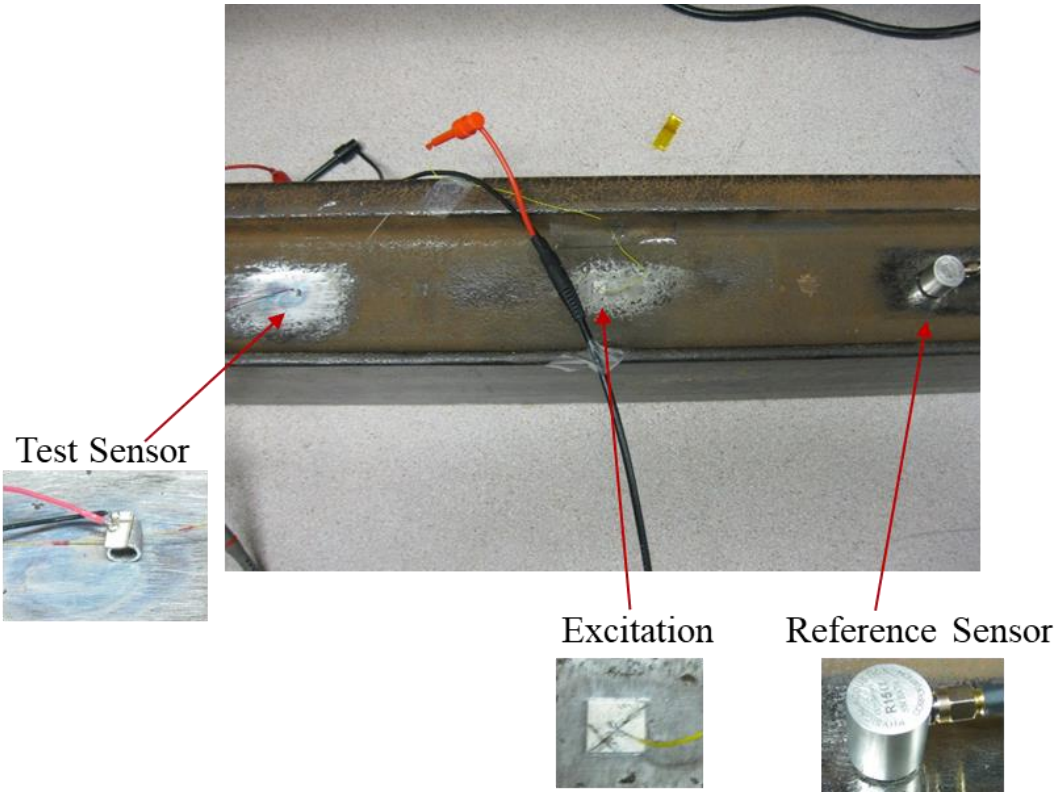

(b)

Figure 11.1: Steel rail calibration (a) Conceptual sketch of excitation and sensors, and (b) photograph of steel rail during experimental setup

To determine if Rayleigh waves were the dominant mode of propagation in this specimen, a series of pitch-catch experiments were performed, transmitting from one PWAS to another PWAS 394.5 mm away. A series of 20 V_{pp} 3-count Hanning windowed tone bursts were excited, with a center frequency ranging from 100 kHz to 1200 kHz. The

time of flight was calculated via the envelope amplitude of the first arriving waveform and used to calculate the group velocity (Figure 11.2).

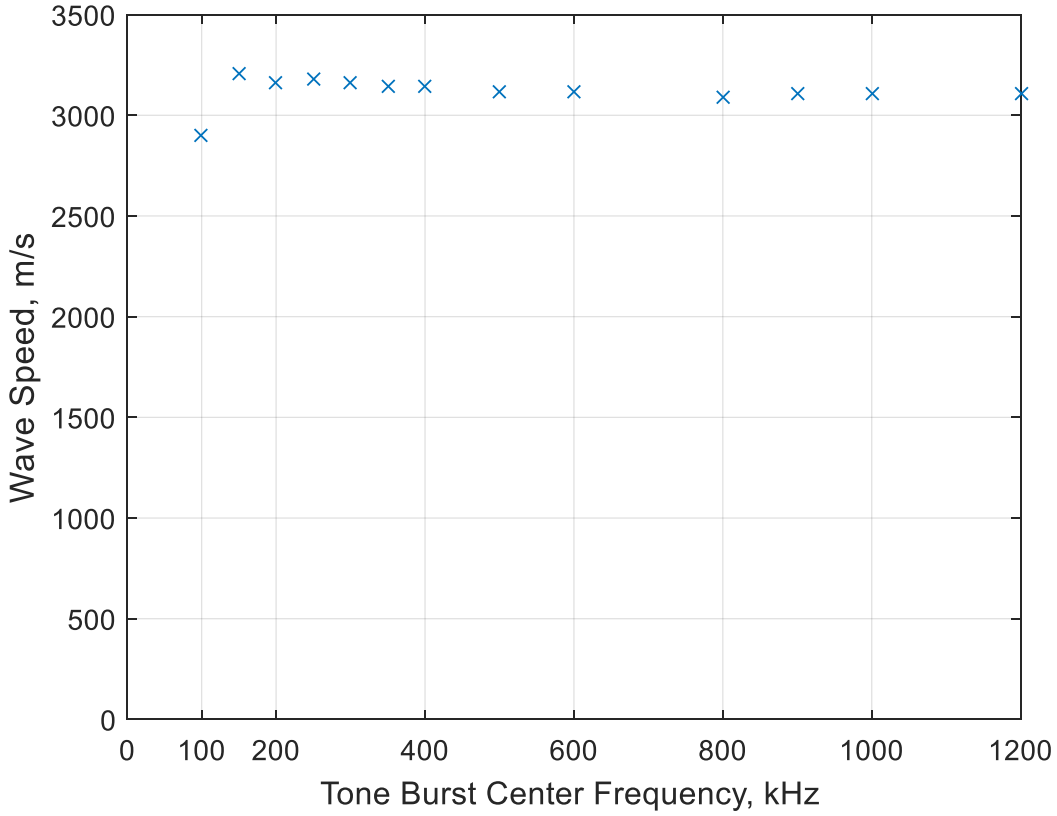

Figure 11.2: Group velocity calculations via time of flight measurements indicating Rayleigh wave propagation in the steel rail

It was found that the group velocity was largely nondispersive, approaching approximately 3100 m/s, significantly close to the Rayleigh wave speed of steel (there was a 7% drop in group velocity at the low frequency at 100 kHz). This confirms the previous work (Giurgiutiu 2014) that the waves propagate as Rayleigh waves.

Three excitation sources were assessed: pencil lead break, glass capillary rod fracture, and PWAS excitation. The glass capillary rod (0.5 mm OD, 0.3 mm ID) was slightly larger than indicated in ASTM E1781; however, no suitable smaller rods were commercially available without a custom order through a manufacturing facility. A

comparison between the sizes of the pencil lead and glass capillary is shown in Figure 11.3. It was found that the waveforms created by capillary rod fracture (Figure 11.4) and pencil-lead break (Figure 11.5) were easily detectable by a PWAS bonded 20 mm away. However, there were limitations that the frequency spectra which significantly decayed significantly by 100 kHz, precluding their use for a broadband calibration.

(a)  (b) 

Figure 11.3 (a) Side-by-side comparison of 0.5 mm pencil lead and 0.5 mm OD glass capillary rod, and (b) pencil lead break fixture recommended in ASTM E976 to improve reproducibility of pencil-lead-break excitations

(a) 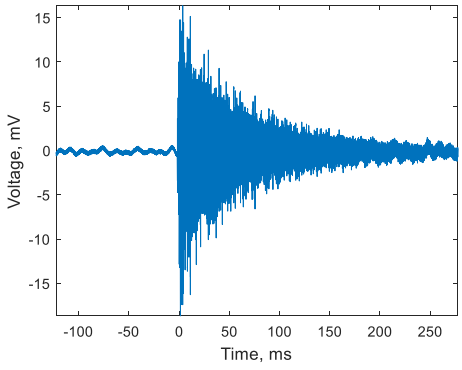

(b) 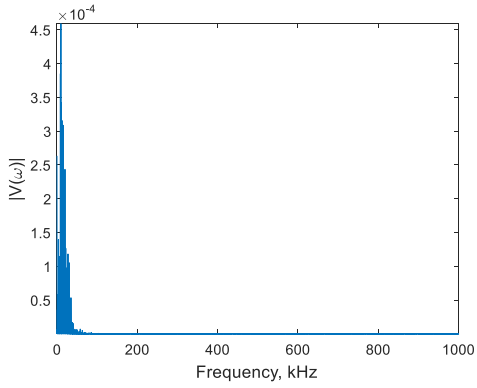

Figure 11.4: Capillary rod excitation detected by a PWAS 20 mm away (a) time-domain response, and (b) frequency-domain response

To provide input motion calibration data, the original intent was to use noncontact LDV velocity measurements. However, it was found neither PLB, capillary rod fracture,

or PWAS waveforms provided a high enough out-of-plane surface velocity to be detected by the LDV.

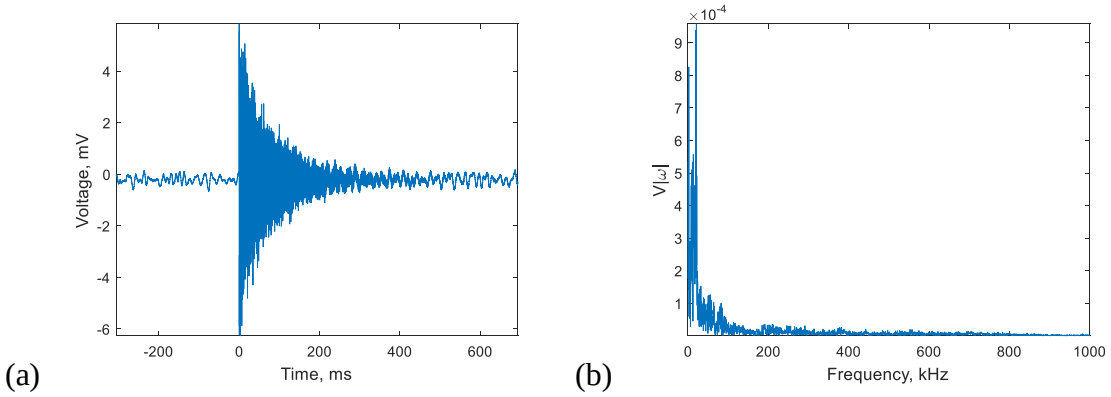

Figure 11.5: PLB excitation, detected by a PWAS 20 mm away (a) time-domain response, and (b) frequency-domain response

Because of this, the experimental approach settled on the use of a PWAS excitation and a transfer of calibration from a reference sensor as specified in ASTM E1781. In fact, the use of PWAS rather than PLB or capillary rod fracture may have provided better calibration curves due to the ability to increase the number of signal averages until the noise levels were negligibly low. Typically, a piezoelectric transducer is not ideal for calibration methods that use analytical or numerical calculations of input motion because the state of the art in bonding layer modeling is not yet accurate enough for calibration. However, it was admissible for the ASTM E1781 principle of transfer of calibration from a pre-calibrated reference sensor; this only require a principle of equivalent excitation at the base of the test sensor and reference sensor. The small size of the PWAS (approximately 7 mm) also helped to meet the approximation that it was a point source.

Rust was removed from the rail using an angle grinder, and the test sensor and reference sensor were bonded 200 mm away from the PWAS. After going through the calibration curves of sensor available in the laboratory, surprisingly, the MISTRAS R15α

provided one of the best candidates. Although it is considered a resonant sensor centered around 150 kHz, it provided significant energy for a calibration up to 600 kHz. It is not typically used for broadband sensing because its frequency response is not flat. However, since a deconvolution from its calibration curve was already part of the post processing, this did not influence the results.

A pulse was chosen for PWAS excitation to meet the dual criteria that the excitation should be both short in time-duration and broadband. The short time-duration was considered a factor to reduce the potential for edge reflections influencing the calibration. A 500 ns pulse was found to be sufficient. Since the excitation time was short, the use of the HSA4014 power amplifier was necessary to preserve the general shape. For detecting this signal, a sampling rate of 25 MHz was used across all calibration experiments to ensure the amplitude did not drop off at higher frequencies.

The time-domain signal of the pulse can be seen to be somewhat rounded (Figure 11.6a), but the overall shape of the frequency-domain was largely preserved (Figure 11.6b). For a calibration region up to 600 kHz, the pulse provided sufficient energy. The pitch-catch response of the 45 V pulse excitation, received by a PWAS 200 mm away is shown in Figure 11.6c (time-domain) Figure 11.66d (frequency-domain). In the frequency-domain, significant energy is present up to 600 kHz for calibration. It was found that the SNR from the pulse was very poor without the use of averaging. To improve the signal strength, 1024 averages were used; however, the SNR was still poor due to the signal amplitude nearing the thermal noise of the oscilloscope. This was corrected with the use of a 40 dB preamplifier. This preamplifier had a 30 kHz high pass filter. Because of this, the calibration curves provided in this chapter are valid in the range from 30 – 600 kHz.

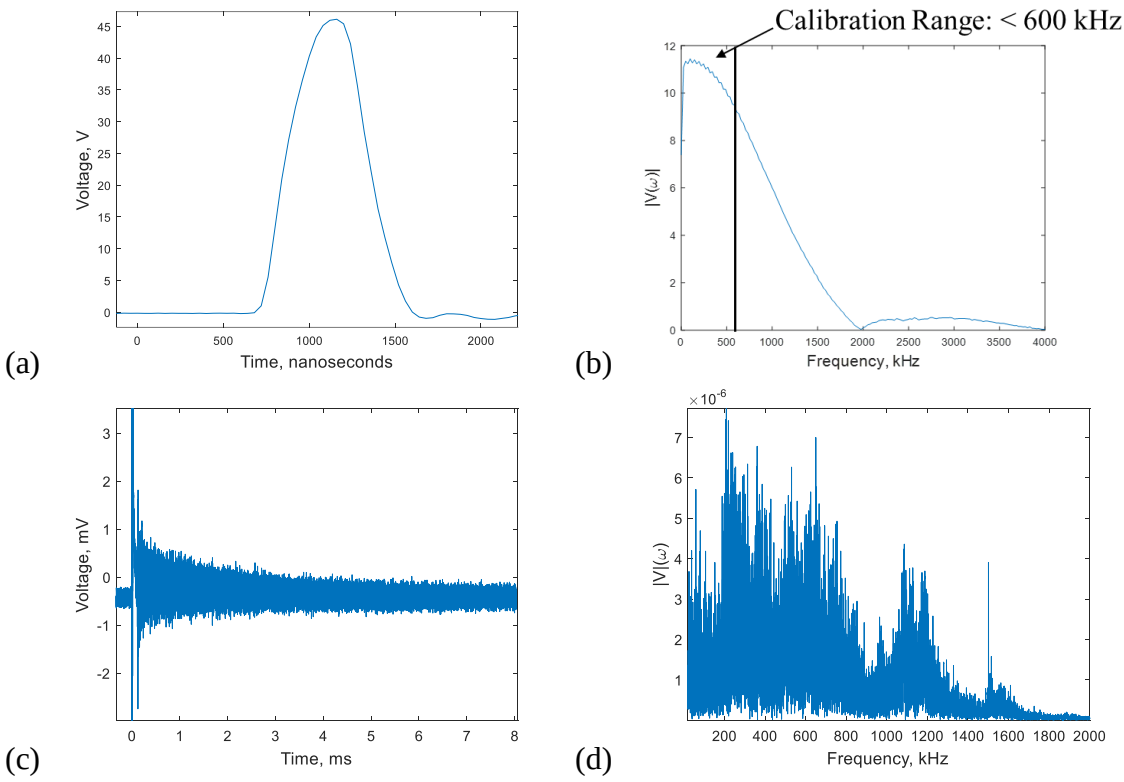

Figure 11.6: (a, b) PWAS 500 ns pulse excitation smoothed due to data acquisition equipment, and (c, d) pitch-catch response detected by a PWAS 394.5 mm away from the transmitter PWAS

11.3.2 Calibration Curve Calculation Method and Methodology Verification

The calculation of the calibration curves in this section relies on a principle of equivalent input motion between the test and reference sensor. In the frequency domain, the voltage $V(f)$ is related to the velocity at the sensor base $v(f)$ through the sensor calibration curve $C(f)$:

$$V_T(f) = C_T(f) \cdot v(f) \tag{11.1}$$

$$V_R(f) = C_R(f) \cdot v(f) \tag{11.2}$$

The subscripts T and R refer to the test sensor with unknown calibration curve and the reference sensor with the known calibration curve, respectively. If the base velocities are equal, dividing (11.1) by (11.2) and rearranging yields:

$$C_T(f) = \frac{V_T(f)}{V_R(f)} C_R(f) \tag{11.3}$$

The calibration curve from the reference sensor is transferred to the test sensor through the voltage ratio of the two sensors. Additional steps were necessary for proper data processing. An FFT is used to convert voltage signals in the time-domain to the frequency domain. Since the FFT algorithm treats the signal as if it is repeating, if the amplitudes at the start and end of the time window are not the same, the presence of a step causes spectral leakage. There are several ways to address this. In this work, a ramp function is added to each waveform as recommended in ASTM E1781. This modifies only the DC portion of the frequency response. Second, a Savitzky–Golay filter is used to smooth the final calibration curves. It effectively interpolated every group of 75 points in the calibration curve with a 3rd order polynomial.

Our approach to transfer calibration from a reference sensor was validated with two MISTRAS R15α sensors for validation. The calibration curves of both sensors were converted from a stress calibration to a velocity calibration using the 143.4 dB conversion factor from Ono (2016). Although both calibration curves were provided by the manufacturer, one R15α sensor was treated as if the calibration curve was unknown and calibrated using the prescribed method. The comparison between the experimentally-derived calibration curve and the manufacturer-provided calibration curve (after conversion to velocity calibration) is shown in Figure 11.7. The calibration curves agreed for most of the frequency spectrum within 3 dB, with a 5 dB discrepancy in approximately the 300-360 kHz range. Comparing this with aluminum beam calibration of Ono (Ono, Cho, and Matsuo 2010) which differed by up to 20 dB, our result can be deemed quite

accurate. These two R15α sensors were calibrated using a face-to-face calibration method, and it is surprising to see that in our result, the two was so close.

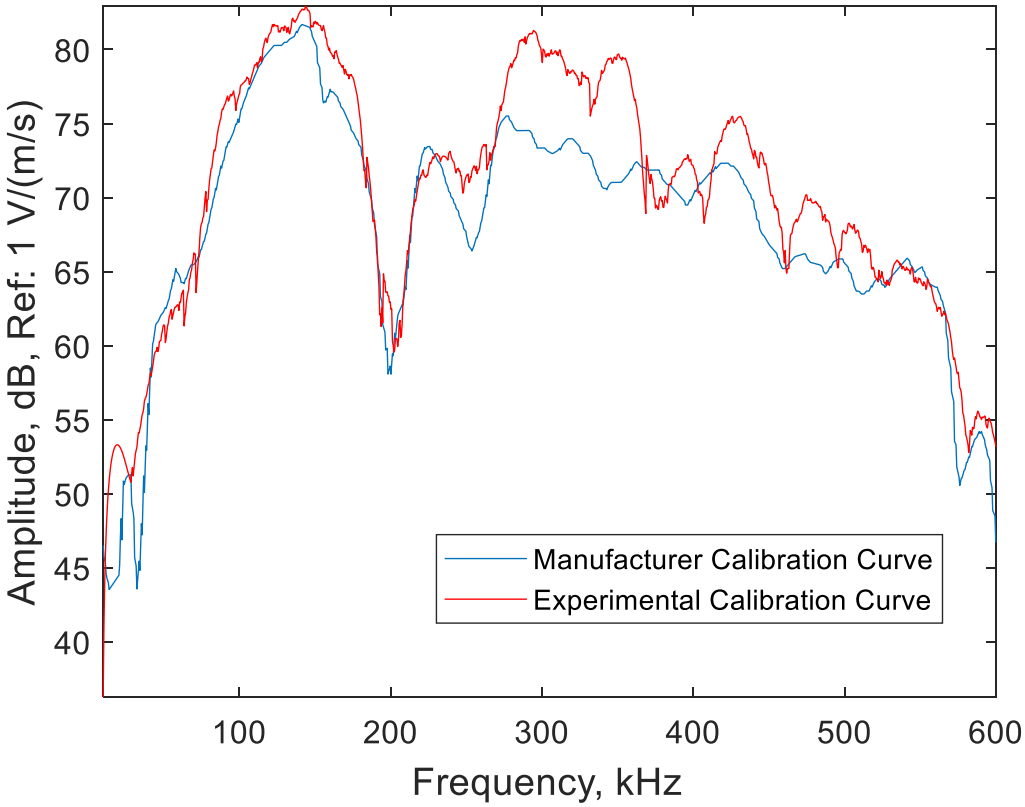

Figure 11.7: Verification of calibration method by comparing experimentally-derived calibration curve with manufacturer-provided calibration curve for two R15α sensors

One concern with this experiment was the presence of edge reflection from the ends of the rail. For example, the waveform received by an R15α sensor, and its frequency-domain response are shown in Figure 11.8a,b. It can be observed that the dime duration of the signal has still not fully decayed even at 32 ms. Since the calculated wave speed on this rail was 3.1 m/ms, this indicates the long decay in the time-domain signals was most likely due to dozens of reflections off the ends of the rail. This was not for the R15α sensor

response, but was seen in the other sensors such as the miniature ring sensor FBG (Figure 11.8bc,d.

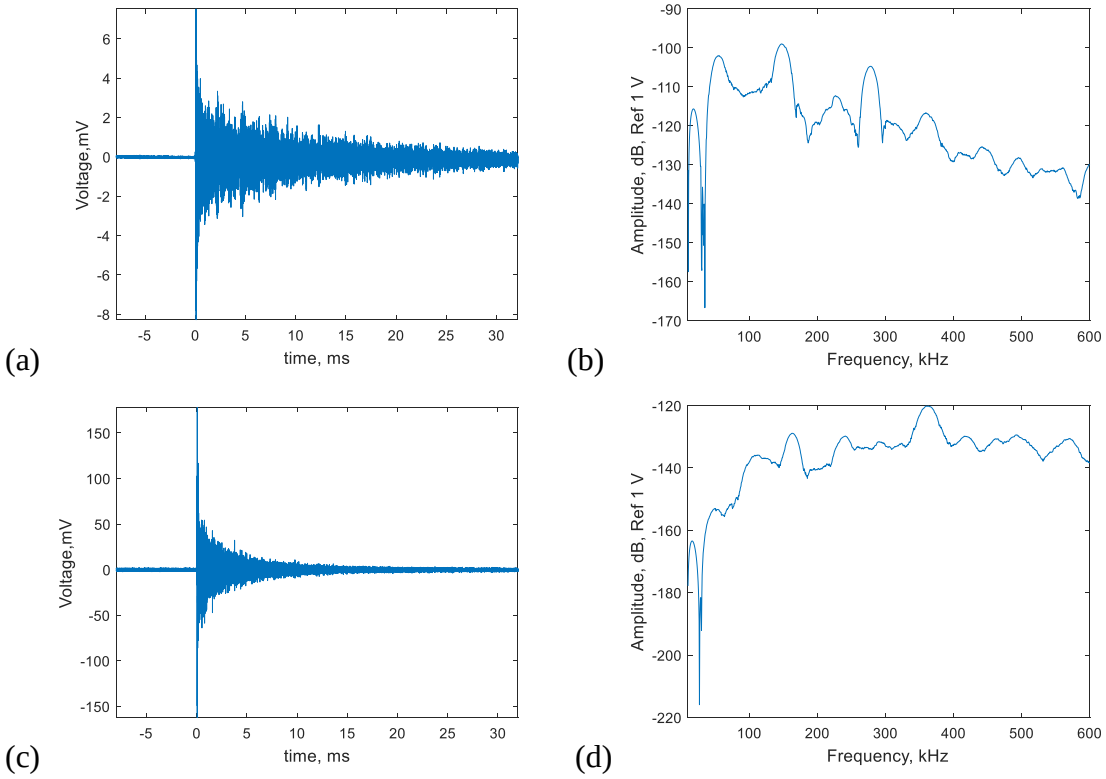

Figure 11.8: PWAS pulse response, received by (a,b) R15α sensor and (c,d) miniature ring sensor FBG

Because of the presence of reflections, at first it was considered that only the very beginning of the waveform should be used for this calibration procedure to eliminate the presence of edge reflections. An assessment of this effect was performed by calculating the calibration curve using several different time windows, ranging from the first few hundred microseconds of the signal, all the way out to the end of the signal capture at approximately 32 ms. It was found that when using only the first few hundred microseconds, the R15α calibration curve had larger discrepancies in amplitude (closer to the frequency spectrum matching within approximately 6 dB) when compared to the manufacturer-provided calibration curve. However, the use of longer-duration time windows (which included the

edge reflections) seemed to produce more accurate calibration curves, as observed by the R15α sensor better matching the manufacturer-provided response. This effect of the "stabilizing" of the shape and amplitude of the calibration curve with longer time windows was seen for all the sensors calibrated in this chapter.

This effect would require more study for explanation. One hypothesis is that a standing wave phenomenon is providing an equivalent excitation to both sensors. However, further study is outside the scope of this chapter, as the emphasis is on the extent of calibration necessary for sensor characterization. From a purely practical perspective, since calibrating with a longer signal was empirically shown to produce better results, the full time-duration of the signal was used for calibration of the rest of the sensors. Any theoretical problems with this are backed with the knowledge that the portion of the wave present before the arrival of any reflections still provided similar, if less accurate, results.

11.4 Sensor Calibration and Strain Amplification Results

11.4.1 Approach for Calibration of Piezoelectric and FBG Sensors

One R15α sensor was removed from the surface, and test sensors were bonded at the same location, calibrated, and removed for the next sensor. The following test sensors were calibrated:

- Surface-bonded FBG and PWAS
- Original 100 kHz ring sensor FBG
- Miniature ring sensor FBG and PWAS
- Circular ABH sensor FBG

The details of the calibration process are the same as those discussed in Section 11.3. For demonstration purposes, time and frequency domain responses of test sensor

(PWAS) and reference sensor (R15α) are shown in Figure 11.8. It can be noted that in the time domain, the SNR is high and both waveforms take a long time to decay. In the frequency responses, regularly spaced peaks and valleys can be seen. For the PWAS, this is indicative of the tuning phenomenon discussed in Chapter 4.

11.4.2 Redefining Calibration Metric to Reflect FBG Strain

When calibrating FBG sensors, it was apparent from the work done in previous chapters that a voltage per unit velocity calibration was not appropriate. This is because the resolution of the FBG system was ultimately in terms of strain and not voltage. For example, an FBG with a different slope could be used to provide a much more sensitive response when compared to other sensors. But, this comparison would not be valid because the noise from the optical system would increase proportionally with the sensitivity increases.

To address this, the strain calibration from Chapter 7 was employed to obtain absolute FBG strain calculations prior to the calculation of the calibration process. In terms of the calibration calculation, this can be expressed as:

$$C_{FBG}^{\varepsilon}(f) = \frac{\varepsilon_{FBG}(f)}{V_R(f)} C_R(f) \tag{11.4}$$

where $\varepsilon_{FBG}(f)$ is the strain measured by the FBG. The FBG calibration curve $C_T^{\varepsilon}(f)$ is the calibration in units of FBG strain detected per unit out-of-plane free surface velocity.

The calibration curve in units of $\varepsilon/(m/s)$ for a surface-bonded FBG is shown in Figure 11.9. Significant peaks and valleys are seen in the FBG response starting at approximately 150 kHz. This is likely due to the wavelength of the Rayleigh wave approaching the 10 mm FBG length at higher frequencies. At 156 kHz, the Rayleigh

wavelength in this specimen is 20 mm, twice the length of the FBG. At 312 kHz, the wavelength is equal to the FBG length.

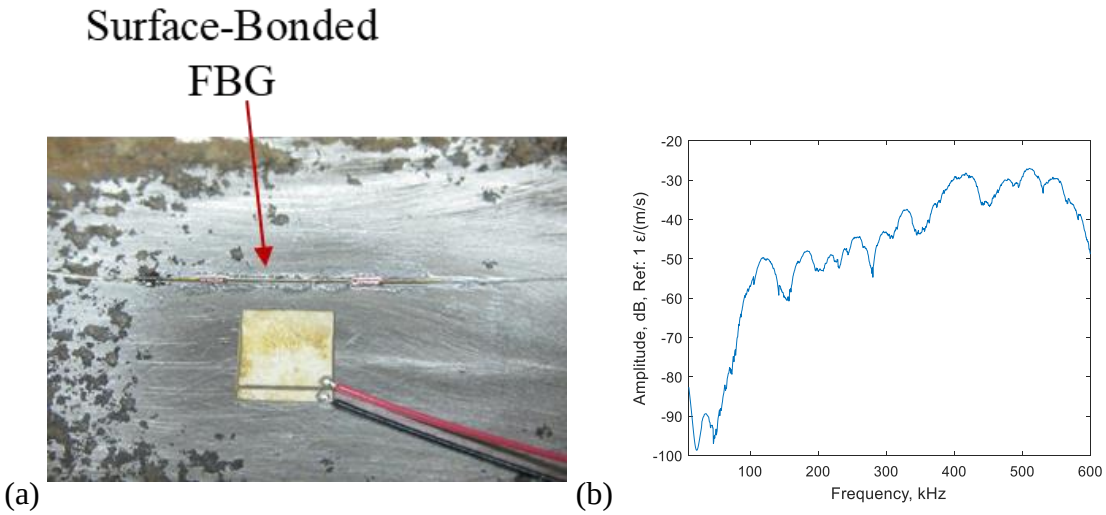

Figure 11.9: (a) Photo of surface-bonded FBG, and (b) Surface-bonded FBG calibration curve expressed in FBG strain per unit input velocity

The calibration of a surface-bonded FBG with respect to out-of-plane velocity was intuitively strange. To address this, the ratio between in-plane and out-of-plane Rayleigh wave motion was calculated using the Rayleigh wave equations from Chapter 2. It was found that on the surface, this ratio is a material-dependent constant. For example, using the elastic properties of 1080 steel, it was found that the in-plane motion is 2.2 times larger in magnitude than the out-of-plane motion. This allows the perspective to be broadened from that of only out-of-plane velocity. Instead, we can make the distinction that it is calibration with respect a *Rayleigh wave amplitude* which produces a given out-of-plane velocity. Thus, the presence and even the amplitude of the in-plane motion is implied.

This knowledge of the fixed ratio between in-plane and out-of-plane motion allows for direct calculation of a strain amplification ratio, i.e.

$$\frac{\varepsilon_{FBG}^{Sensor}(f)}{\varepsilon_{FBG}^{Surface}(f)} = \frac{C_{FBG}^{Sensor}(f)}{C_{FBG}^{Surface}(f)} = R_{Amp}(f) \tag{11.5}$$

The superscript "Sensor" refers to the mechanical sensor (e.g. ring sensor or ABH sensor) and the superscript "Surface" refers to the surface-bonded FBG. $R_{Amp}(f)$ is the strain amplification ratio: the ratio between a mechanical sensor's FBG response (e.g. ring sensor or ABH sensor) and the surface strain detected by an FBG. We have chosen to not factor in the Rayleigh wave 2.2 times displacement ratio in the steel since the ABH sensor detects out-of-plane motion as well. This means that in some cases the amplification ratio is expressed in terms "Sensor FBG strain generated by out-of-plane motion" divided by "in-plane strain". Conceptually, in a fair comparison for an out-of-plane sensitive sensor, this ratio may be conservative by up to a factor of 2.2, or approximately 6.8 dB.

After a thorough review of the literature, we believe this is the first combination of AE sensor calibration principles with a fiber-optic sensing system calibrated for absolute strain measurements. The calibration in terms of strain per unit motion allow separation of the optoelectronic sensor system from the sensor mechanical response. This can allow for sensor modeling, characterization, and interpretation in purely mechanical terms. The use of the strain amplification ratio also provides a readily accessible metric for performance increases over that of a surface-bonded FBG. This provides a quantitative metric to calculate the strain amplification, one of the major design criteria of the mechanical FBG sensors. It should be noted that the strain amplification ratio is calculated based on a 10 mm length FBG. Thus, the response may suffer from aperture effects, particularly over 312 kHz when the wavelength becomes lower than the FBG length. A shorter (e.g. 1 mm or 3 mm) FBG should be used in the future if this approach is to be used again.

Both the strain-output calibration and strain amplification ratios are presented for the ring sensor and ABH sensor FBGs. The strain-output calibration is more useful in application, where the strain amplification ratio is more useful in sensor characterization.

11.4.3 Ring Sensor FBG Calibration and Strain Amplification Results

The calibration curves and strain amplification curves for the original 100 kHz ring sensor FBG and the miniature ring sensor FBG are shown in Figure 11.10.

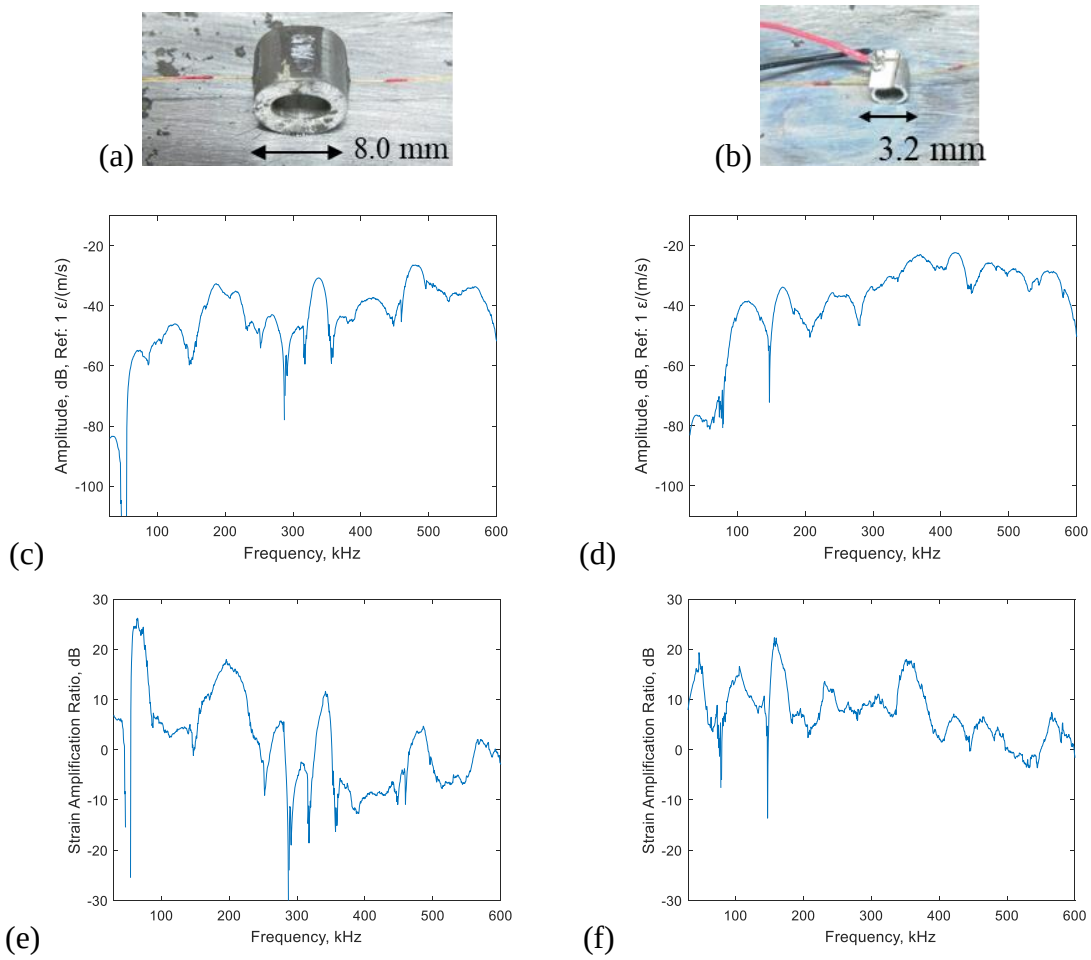

Figure 11.10: (a,c,e) Original 100 kHz ring sensor bonded to steel rail, its calibration curve, and its strain amplification curve, and (b,d,f) Miniature ring sensor bonded to steel rail, its calibration curve, and its strain amplification curve

Both ring sensors have broadband frequency characteristics (although in an AE sensor context, they would not be called “wideband AE sensors” because their curves are

not sufficiently flat). Antiresonances are present in the frequency responses. For the original 100 kHz ring sensor, these are at 47-55 kHz and 287 kHz. For the miniature ring sensor, one is present at 147 kHz. These correspond to the gap between the fundamental resonance and the 2nd harmonic previously discussed. The miniature ring sensor has only a slightly higher peak amplitude (-22 dB, compared to -26 dB). However, it has performance advantages in terms of a higher average sensitivity and improved low frequency and high frequency response.

The original ring sensor had a higher maximum strain amplification (26.2 dB versus 22.2 dB). However, the miniature ring sensor had a higher average sensitivity, staying above the 0 dB line with no attenuation over most of its frequency spectrum (0 dB corresponds to an amplification factor of 1). The original ring sensor prototype drops below -10 dB over a significant portion of its amplification ratio.

Due to the success of the single-point bonding FBG configuration used in the ABH sensor, this method was also tested in the miniature ring sensor (Figure 11.11). It was found to diminish the sensitivity by 20-25 dB across the frequency spectrum, making it a poor candidate as a sensor configuration. Hence, it was not used in subsequent tests.

The 500 ns pulse excitation was compared to a "tone burst stitch" method, where a parametric frequency sweep of 3-count Hanning windowed tone bursts was excited such that the tone bursts had significant overlap in their frequency response. A window of the calibration curve was calculated for each tone burst and the individual windows were "stitched" together to obtain the calibration curve over a wide range. There were some discrepancies in amplitude, approximately 4.5 dB, at 170 kHz and 350 kHz (Figure 11.12). Overall, however, the two methods matched well in amplitude and shape. This approach

has the benefit that it could be used to garner a higher degree of granularity from tuning curve experiments when sensor resonances are more closely spaced than the tone burst frequency band.

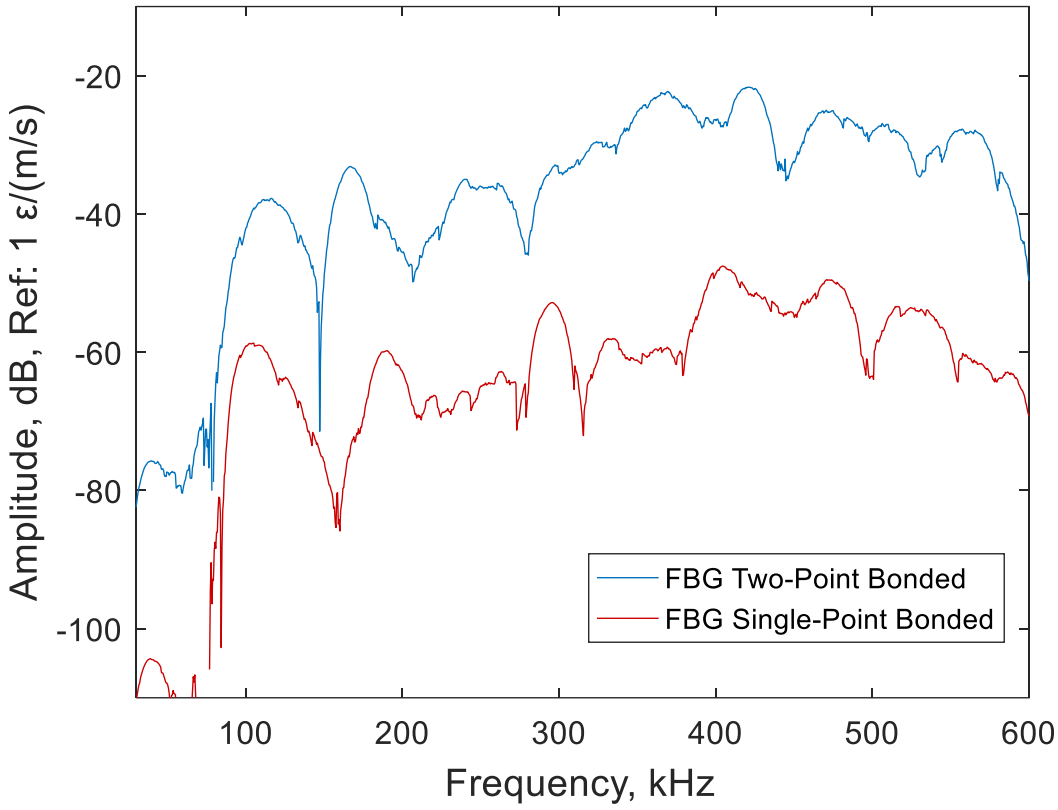

Figure 11.11: Comparison between single-point bonded and two-point bonded configurations on miniature ring sensor

11.4.4 PWAS Calibration Curves

Calibration curves for a surface-bonded PWAS and miniature ring sensor PWAS were calculated (Figure 11.13). Just as in its waveform and FFT from Figure 11.8, the surface-bonded PWAS had regularly spaced peaks and dips in its response, corresponding to its tuning phenomenon. The surface-bonded PWAS had a lower sensitivity than the R15α sensor below 200 kHz and a higher sensitivity above 200 kHz. It is of particular note

that the miniature ring sensor PWAS had a higher sensitivity than the R15α sensor. This was not expected, as the ring sensor was not optimized for use with the PWAS.

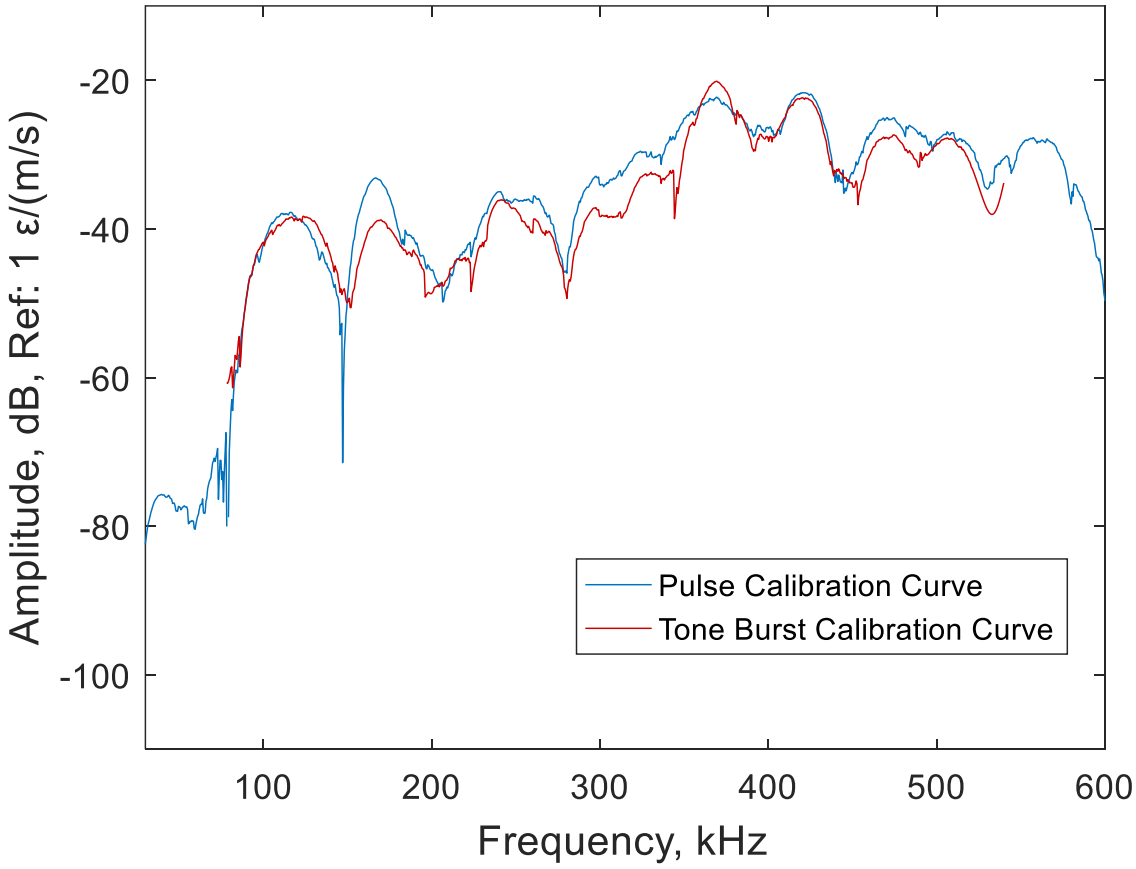

Figure 11.12: Comparison between miniature ring sensor FBG calibration curves generated by tone bursts and pulse excitation

The PZT and aluminum acoustic impedances are also poorly matched. A brass ring sensor with an impedance matching layer at its base would be expected to perform even better for piezoelectric sensing. A compliant PVDF sensing element stretched across the longitudinal axis of the ring sensor may perform better based on its mechanism of motion. However, these validations are outside the scope of this chapter and hence were not pursued at this stage.

At this stage, a large amount of design work would be necessary to enhance the ring sensor piezoelectric sensing capabilities, including the incorporation of a Faraday shield, testing its electrical response, and further calibration work.

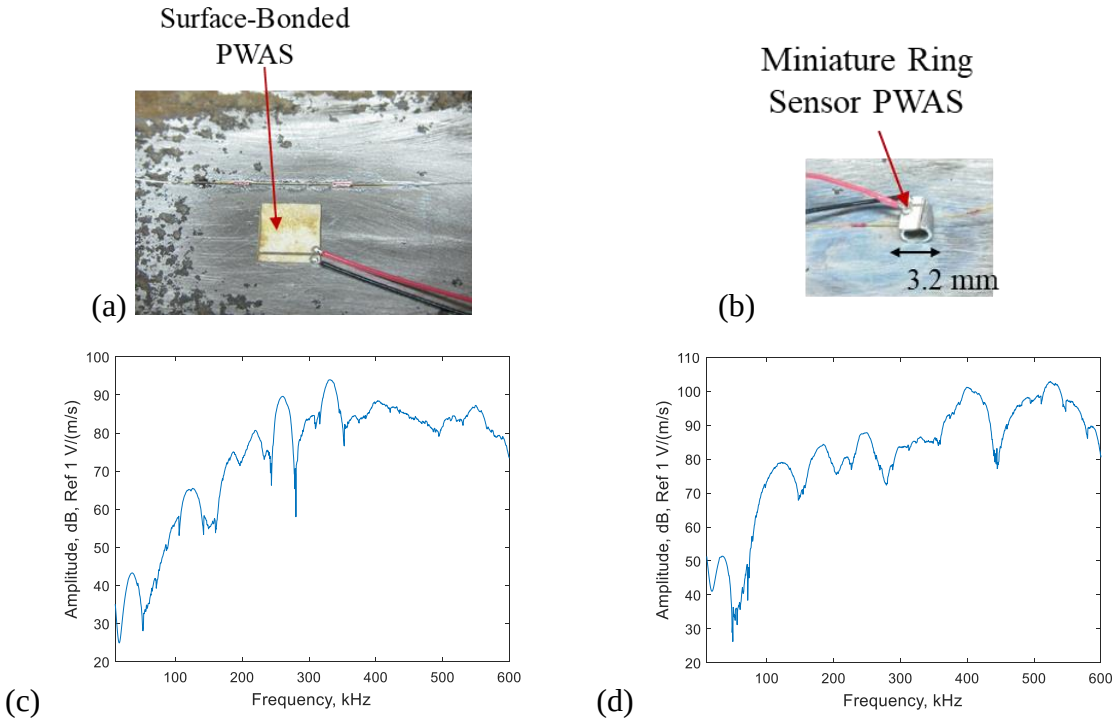

Figure 11.13: (a, c) Surface bonded PWAS and its calibration curve, and (b, d) miniature ring sensor PWAS and its calibration curve

This may be a potential avenue of future work, as a highly sensitive miniature piezoelectric AE sensor has a good prospect for commercialization. If this were to be pursued, the next step would be to test its response in a more robust calibration experiment.

11.4.5 Acoustic Black Hole Sensor Calibration Curves

When calculating calibration curves for the acoustic black hole sensors, two new types of bonding configurations were considered (Figure 11.14). This was done because the single-point bonding when applied to the ring sensor showed such a large diminishment in its response. The original bonding configuration tested in Chapter 10 was an optical fiber bonded only at one point of the ABH face. Special care was taken such that the optical

fiber was not secured at another point on the specimen. A single-point bonding configuration was also assessed at the tip of the specimen using a 5 mm FBG. The FBG was placed deliberately so it was close to the bonding point, but no portion of the FBG would overlap it. A buckled two-point bonding configuration was also assessed. The fiber was buckled by impeding the path between the two bonding points with a small cylinder during the bonding process. The bonding process was very difficult in practice, and some cyanoacrylate adhesive spilled over to the sides of the ABH sensor and the circular inner profile.

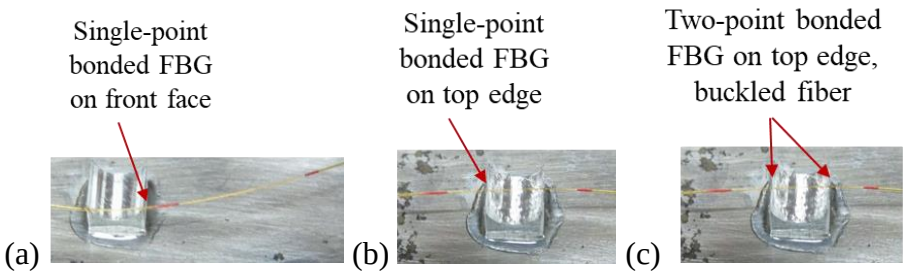

Figure 11.14: (a) Optical fiber bonded at one point on ABH face close to the very tip of the sensor, (b) Optical fiber bonded at one point on the ABH tip, and (c) Optical fiber bonded to both ABH tips in a buckled configuration

Comparing the calibration curves for the single-point bonding configurations (Figure 11.15), it appeared that the FBG on the ABH tip was more sensitive, particularly at higher frequencies, on the order of 20-25 dB.

The strain amplification ratio for this configuration is shown in Figure 11.16. The peak strain amplification is 26 dB, and is most sensitive in the 100 – 220 kHz region. The strain amplification ratio is above the 0 dB line for most of the frequency spectrum. There were no indications observed in the FEM analysis of the ABH sensor that the top of the ABH tip would have such a higher response when compared to the very top of the front face. The FBG on the ABH sensor face was bonded very close to the tip of the ABH, so

the amplitude drops moving away from the tip does not fully explain this. This effect may have something to do with optical fiber mechanical interaction with the front face vs. the tip of the ABH sensor. If this is the case,

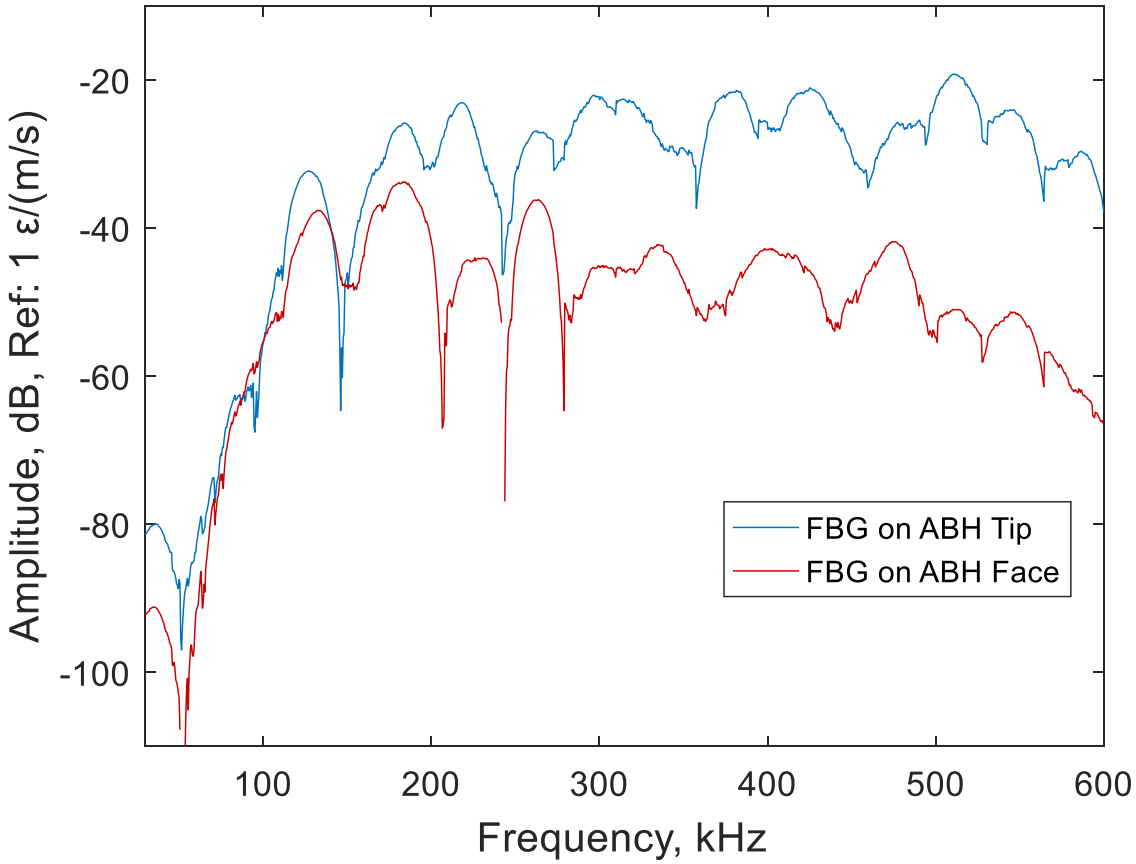

Figure 11.15: Increase in sensor sensitivity by bonding the FBG to the ABH sensor tip

the mechanics of the FBG itself warrant more attention in the modeling and design process, as it may play a large role in the overall response.

The calibration and strain amplification ratio of the two-point bonded configuration are shown in Figure 11.17. Just as for the single-point bonding configuration, the strain amplification ratio is above the 0 dB line for most of the frequency spectrum.

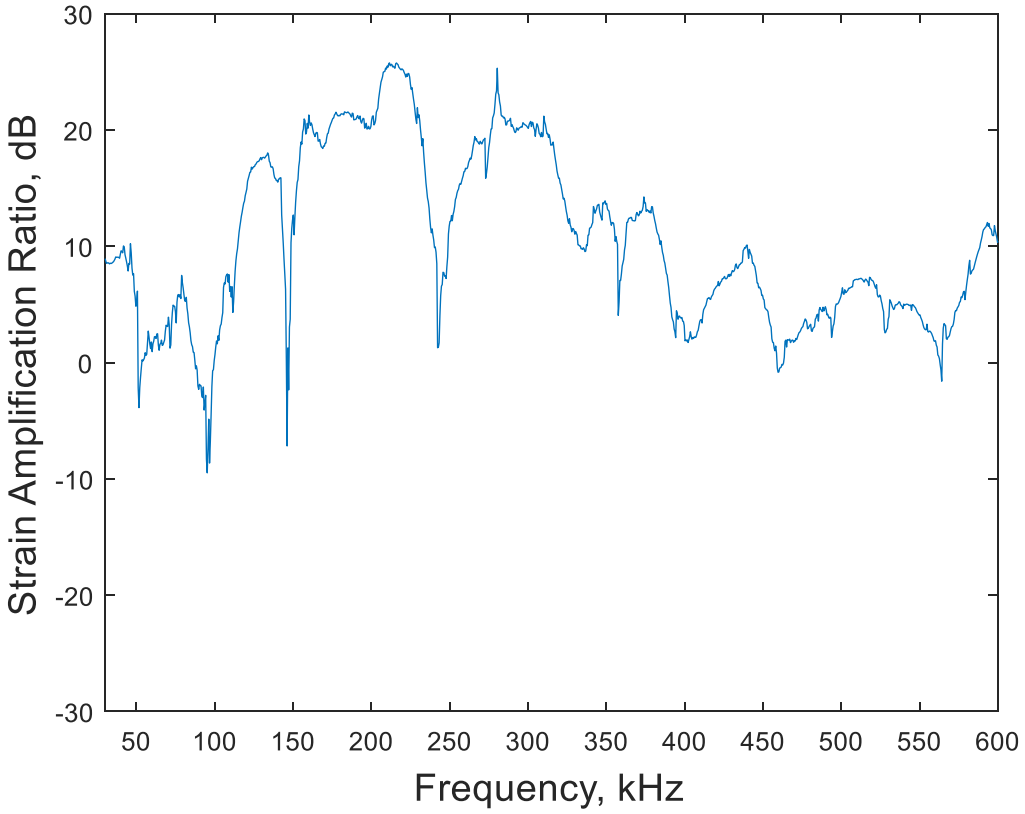

Figure 11.16: Strain amplification ratio of a single-point bonded ABH sensor FBG

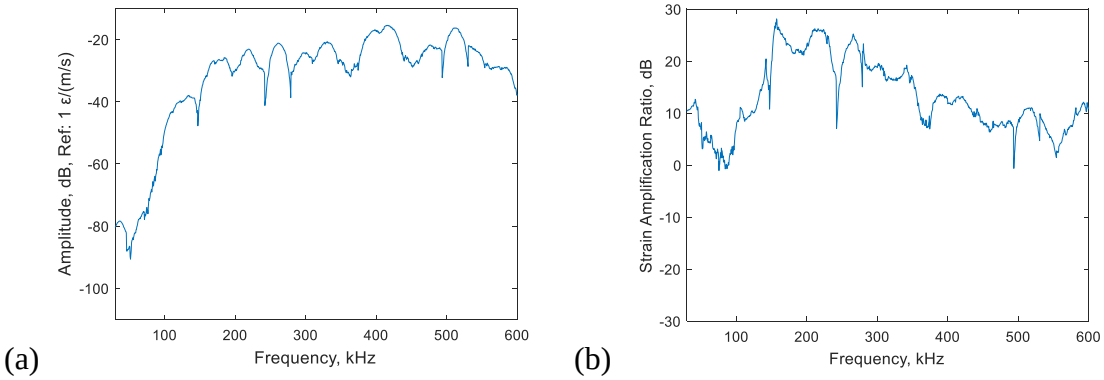

(a) (b)

Figure 11.17: (a) Calibration curve of the two-point bonded ABH sensor is wideband and relatively flat, and (b) strain amplification ratio of the two-point bonded ABH sensor is higher than any of the other sensor configurations investigated

The peak amplification is 28 dB, slightly higher than for the single point bonding configuration. The increase in strain amplification is small enough to be entirely caused by

the constructive interference between longitudinal waves in the optical fiber originating from each ABH tip.

The high sensitivity of both ABH sensor configurations indicates that both are acceptable alternatives. The single-point bonded configuration should be chosen when the detection of both in-plane and out-of-plane motion is desired. The two-point bonded configuration should be chosen when the detection of out-of-plane motion alone is desired. The calibration curve of the miniature ring sensor is compared to the two-point bonded ABH sensor in Figure 11.18. The ABH sensor has a clear advantage in terms of sensitivity across the frequency spectrum.

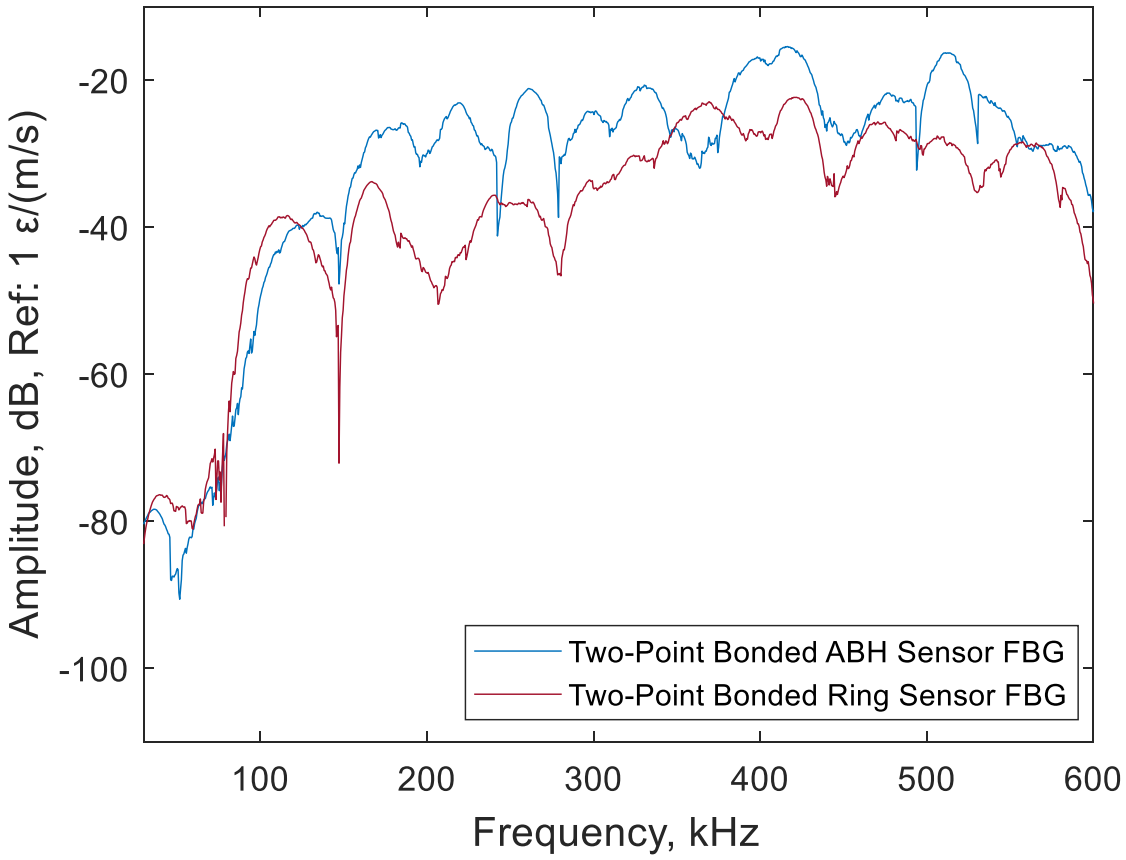

Figure 11.18: Calibration curve comparison between most sensitive ring sensor and most sensitive ABH sensor configurations

11.5 Summary and Conclusions

This chapter discussed the principles and techniques of AE sensor calibration. AE sensor calibration was implemented based on the principles of ASTM E1781, where a calibration curve is transferred from a previously calibrated AE sensor to a test sensor. A unit conversion between acoustic pressure and particle velocity in water allowed for the conversion of the physically inadmissible V/μbar units to standard V/(m/s) units. The calibration curve calculation process was then verified by calculating the calibration curve of a commercially available MISTRAS R15α sensor and comparing it to the manufacturer-provided curve. Theoretical challenges are present in terms of edge reflections. However, calibration based on the initial portion of the wave prior to reflections was sufficiently accurate. Surprisingly, calibration in the presence of many edge reflections seems to have provided a more accurate response, possibly because there was enough time for dozens of edge reflections with small levels of attenuation to provide a roughly equivalent response to both sensing locations.

After a thorough review of the literature, we believe this is the first combination of AE sensor calibration principles with a fiber-optic sensing system calibrated for absolute strain measurements. In addition to the sensor characterization itself, this allowed for two developments in calibration technique.

First, by using an FBG as a reference sensor to obtain surface strain measurements, the strain amplification ratio of a fiber-optic sensor was calculated across a frequency spectrum. This is a powerful metric for both sensor development and characterization. This approach was relatively simple, and was feasible because the ratio between in-plane and out-of-plane surface motion for a Rayleigh wave is constant. In practice, in other specimens

where this ratio is a function of frequency, theoretical calculations of this ratio could be included.

Second, by converting FBG output from voltage to strain, calibration curves were calculated in terms of strain per unit surface motion. This allowed the sensor performance to be interpreted entirely in mechanical terms, decoupling the mechanical calibration curve from sensor's electrical components. This may allow separate development of mechanical sensor and optoelectronic components which could be combined at a later stage. It also allows for immediately accessible calculations of minimum detectable FBG sensor surface motion; this is because FBG optical system resolutions are prescribed in terms of strain per unit bandwidth.

Calibration curves were obtained for a surface-bonded PWAS and a miniature ring sensor PWAS. The miniature ring sensor PWAS calibration curve was calculated to be higher than the R15α calibration curve for all frequencies above 100 kHz. This was a pleasant surprise, as the miniature ring sensor was not optimized for its PWAS response. This may warrant more attention in development of the ring sensor as a piezoelectric AE sensor, but first this result would need to be replicated in a more sophisticated calibration setup.

For the ring sensor FBG calibration curves, the original 100 kHz ring sensor prototype had a higher maximum strain amplification when compared to the miniature ring sensor (26.2 dB versus 22.2 dB). However, the miniature ring sensor had a higher average sensitivity, staying above the 0 dB line (i.e. 0 dB corresponds to an amplification ratio of 1) over most of its frequency spectrum. The original ring sensor prototype drops below -10 dB over a significant portion of its amplification ratio. The effect was surprising, as the

miniature ring sensor performed much better in the Lamb wave experiments. One possibility is that because of the small size of the miniature ring sensor, it does not diminish the response in a 1.2 mm plate the way that the larger 8 mm ring sensor might. This would explain why the performance evened out for Rayleigh wave excitations, as the thick steel would not be influenced much by either ring sensor.

It was found that a single-point FBG bonding configuration did not function well for the ring sensor, but functioned well for the ABH sensor. This may be due to the wavelength sweep characteristic of the ABH sensor discussed in Chapter 10. At the ABH tip, the wavelength approaches the same length scale as the FBG diameter.

The single-point bonding of an FBG to the top surface of the ABH sensor greatly improved its response compared to single-point bonding to the front face of the ABH sensor. The improvement was roughly of the order of 20-25 dB for frequencies above 200 kHz. This result indicates that more care needs to be taken to incorporating the FBG into the design and modeling process. A buckled FBG two-point bonding configuration further improved peak strain amplification ratio, from 26 dB for the single-point bonded ABH FBG to 28 dB for the two-point bonded ABH FBG. This increase is small enough to be accounted for by constructive interference between longitudinal waves in the optical fiber originating from each ABH tip. These two ABH FBG configurations provide two potential alternatives for ABH FBG sensing; one of which possesses in-plane sensitivity and another of which possesses both in-plane and out-of-plane sensitivity.

This chapter provided measurements of calibration curves in terms of output strain or voltage per unit motion across a frequency spectrum. This placed the characterization of the ring sensors and ABH sensor on a reliable foundation by relating them to absolute

surface measurements. The results of this work indicate the potential for several further advancements. A more sophisticated calibration process may be warranted to confirm these results. It could be backed up with a modeling framework to assist in calibration validation and sensor characterization. A Lamb wave calibration could be performed with noncontact LDV measurements used to detect input motion. The directional response could be measured for the ABH sensor, particularly the in-plane configuration which may have more directional sensitivity.

One possible avenue of further work is in the mechanical aspects of the sensor design. The FBG bonding process can be improved for the ABH sensor by providing only the necessary amount of adhesive to bond the FBG to the ABH tip. A sensor housing should be placed around the ring sensor and ABH sensor for protection and for electrical isolation of the ring sensor PWAS. A small wear plate could be added to the ring sensor to make bonding easier, and allow for use with non-permanent couplants to open up its use to NDE applications.

CHAPTER 12

SUMMARY, CONCLUSIONS, AND FUTURE WORK

12.1 RESEARCH CONCLUSIONS

This dissertation has presented the development of two sensor architectures suitable to enhance fiber-optic sensing of guided waves. The work began mid-development by verifying the fiber-optic and piezoelectric sensing capabilities of an 8-mm 100 kHz ring sensor. The optical system was calibrated for obtaining absolute FBG strain measurements. Next, a measure of the strain resolution of the system was determined, and the noise sources were characterized in the tunable laser source.

Lamb wave models were used to assess the 100 kHz ring sensor response. It was found that because the ring sensor responded predominantly to out-of-plane motion, the PWAS and FBG bonded to it responded to out-of-plane motion. Additionally, since the ring responded omnidirectionally to out-of-plane excitation, the FBG also became omnidirectional.

Ring sensor performance was modeled in FEM to help understand its mechanics and improve the placement of PWAS and FBG. It was found through an FEM harmonic analysis that the ring sensor possessed multiband characteristics. This was verified experimentally in free sensor experiments and Lamb wave tuning curves.

Transient analyses were used to relate the ring sensor motion back to vibrational modes observed in the harmonic analysis. It was found that vibrational models helped the

understanding of the ring sensor response. Through exploitation of mode shape nodes and lines of symmetric, it was found that placement of FBG and PWAS along nodes and certain lines of symmetry could be used to control the sensor frequency response, producing a single-mode response near 100 kHz.

Since no mechanical amplification had been obtained for the original 100 kHz ring sensor, a design exploration and optimization were performed. It was found that a circular hole could be used without loss in performance, saving in manufacturing costs. A direct optimization algorithm was performed in ANSYS. However, it matched very closely with a design rule of reducing ring diameter and wall thickness simultaneously; this maintained the 100 kHz resonance while miniaturizing the size and optimizing for amplitude. The final design was approximately 3.2 mm in diameter.

SNR calculations for pitch-catch and PLB-AE experiments showed that the FBG on the 3.2 mm miniature ring sensor provided mechanical strain amplification of the waveforms. This was reflected by SNR_{dB} increases of the 3.2 mm ring sensor over that of the plate-FBG. Quantitatively, these were 14.1 dB (pitch-catch), 11.9 dB (PLB-AE), and 19.3 dB (filtered PLB-AE). The miniature ring sensor was also found to have broadband sensing characteristics and was omnidirectional.

Attempts were made at capturing fatigue-AE events on a 1 mm aluminum plate in which a crack was growing under cyclic fatigue loading. There were indications that the AE waveforms had predominantly in-plane motion (i.e. propagated as S0 wave modes), which could not be detected by the miniature ring sensor which was sensitive to out-of-plane motion only. However, in this same experiment, we could determine that the miniature ring sensor reduced the quasi-static strain sensed by a factor of 9.5. This would

be enough for calibration at zero load and operation of dynamic strain sensing up through the strain associated with yielding in the aluminum. The miniature ring sensor was able to detect PLB-AE events under static tension, and pitch-catch waves during fatigue.

A second sensing architecture based on a wave-trapping acoustic black hole (ABH) principle was developed. There were indications that an FBG bonded at two points may diminish the performance of this sensor, so an optical fiber was used in a point-contact bonding configuration. This also had the benefit of making the ABH sensitive to both in-plane and out-of-plane motion.

A 100 kHz "ABH-like" sensor with a circular taper was designed via a DOE and response curve approach, followed by direct optimization. There were not enough design features to be able to control the amplitude separately from the frequency. However, free sensor tests indicated that this sensor may have been broadband up to 400 kHz and may be highly sensitive.

FEM harmonic analyses showed potential performance benefits for a power law ABH taper over the use of a circular taper. A design exploration and broadband objective function were used to optimize for out-of-plane displacement across a 10-1000 kHz frequency range. The optimization pushed the design variables to their bounds. A 12 mm wide quadratic ABH sensor was prototyped. Its Lamb wave response was tested, indicating that it is sensitive to both in-plane and out-of-plane motion. The directional sensitivity of both the S0 and A0 Lamb wave modes were not straightforward to interpreted, and likely reflected the influence of the aperture effect changing lengths with orientation angle.

A calibration was performed on a steel rail using the principles of ASTM E1781 where a previously calibrated sensor could be used to calibrate another sensor under

equivalent excitation. Verification of this calibration methodology yielded results that were generally within 3 dB of a manufacturer-provided face-to-face calibration curve. There were some questions raised about the effect of edge reflections off the end of the rails. It seemed that when dozens of edge reflections were used for calibration, it gave more accurate results than calibration curves that used shorter time windows which did not measure edge reflections.

By measuring the in-plane strain sensed by an FBG on the surface of the rail, a direct "strain amplification ratio" metric was developed, where the strain sensed by the mechanical sensor was divided by the strain sensed by the plate-bonded FBG in the respective frequency domain. Upon calibration, the original 100 kHz ring sensor prototype had a higher maximum strain amplification when compared to the miniature ring sensor (26.2 dB versus 22.2 dB). However, the miniature ring sensor had a higher average sensitivity, staying above the 0 dB for most of its frequency spectrum. For the ABH sensor, single-point bonding an FBG to the sensor's top surface improved its response on the order of 20-25 dB as compared to an FBG bonded near the tip on the front face. A buckled FBG two-point bonding configuration further improved peak strain amplification ratio, from 26 dB for the single-point bonded ABH FBG to 28 dB for the two-point bonded ABH FBG.

12.2 Major Contributions

This dissertation has contributed to the state of the art in several ways:

1. A proof of concept for an 8 mm 100 kHz FBG ring sensor was demonstrated. The FBG sensor was sensitive to out-of-plane motion and detected waves omnidirectionally in a broad frequency range

2. Using transient FEM analyses, the ring sensor FBG Lamb wave response was related back to vibrational modes of the ring resonator, providing a simple basis for understanding and optimization
3. A simple FEM framework for sensor design was developed, based on standard DOE and design optimization tools available in a commercial FEM software
4. A miniaturized and sensitivity-optimized FBG ring sensor was designed and prototyped. Both its Lamb wave and Rayleigh wave response showed the potential for FBG strain amplification up to 22 dB higher than that of a surface-bonded FBG sensor. In previous studies elsewhere, e.g. Tsuada (2010), a sensor which had the qualitative sensing enhancements of the ring sensor permitted a strain attenuation rather than an amplification
5. The miniature FBG ring sensor reduced quasi-static strain sensed by a factor of 9.5, enough for FBG wavelength calibration at 0 load and sensing at a load that would generate yielding in aluminum
6. A sensor framework was developed based on an ABH feature. Two FBG configurations had the potential for either in plane or dual in-plane/out-of-plane sensing
7. A circular-tapered ABH FBG prototype showed significant strain amplification during calibration, 26 dB for an in-plane/out-of-plane sensitive configuration, and 28 dB for an out-of-plane sensitive configuration

8. A power law ABH FBG sensor was designed and prototyped. It was used to experimentally validate the dual in-plane/out-of-plane sensitivity feature of the ABH sensor when used in conjunction with a point-contact bonded FBG
9. A calibrated FBG optical system was combined with calibrations involving absolute surface measurements. This permitted the expression of calibration curves entirely in mechanical units, which has advantages in modeling and design.

12.3 Recommendations for Future Work

This research has left several clear avenues for future exploration. These can be divided up into several categories: experimentation, sensor improvements, new sensors, sensor modeling, and calibration

Experimentation: It would be beneficial to continue testing the 12 mm wide quadratic ABH sensor, particularly in the Rayleigh wave calibration experiment. With the knowledge that the FBG response will probably be higher with sensor tip bonding rather than the sensor face bonding which was used in its Lamb wave experiment, this may prove to yield a highly sensitive sensor. The ABH sensor with a point bond ABH would be a good candidate to tack back to fatigue AE tests. It would also be a good point to determine whether the ABH sensor isolates its FBG quasi-static strain.

At this stage, it may help to get a better handle on the optical system. An absolute calculation of the strain resolution of the optical system would be helpful for determining minimum detection thresholds of these sensors for guided wave applications. It may even

be worthwhile to look into some collaboration and use these sensors with a more sensitive optical system.

Sensor Improvement: A reduction of the width of the quadratic ABH sensor may be beneficial, as it would reduce the influence of the aperture effect.

The ABH sensor is a good candidate for rapid tests of its response as a damped broadband AE sensor. This is because all that is needed to add significant damping to the ABH tip is a thin viscoelastic damping layer (e.g. vinyl tape).

Since the ABH sensor can support one FBG on each tip, there is a potential for a demodulation approach where 2 FBGs can simultaneously quantify in-plane and out-of-plane motion on the same sensor.

The addition of a sensor housing and a better fiber-optic mechanical protection will help make a stronger case for these sensors. This is so especially since they meet many of the other qualification of an operator "just bonding a sensor to their structure" as described in the introduction.

New Sensors: The ABH sensor has the potential to work very well with a noncontact Fabry-Pérot interferometer which may be an avenue for further sensor development. The ABH sensor may also work well with a capacitive sensing approach, as there is a possibility that the ABH displacement amplification may be sufficient to overcome the drop in electrical performance seen by using a capacitive rather than a piezoelectric sensor. For the ring sensor, since its PWAS performed very well in its calibration curve, it may be a good candidate for development of a high-sensitivity miniature piezoelectric AE sensor.

In pilot FEM studies, an additional taper of the ABH sensor in the thickness direction is predicted to significantly increase its response by adding an additional geometric dimension in which energy is concentrated, i.e. channeling all the energy to a small area. This sensor configuration shows promise for large sensitivity increases, at the cost of difficulty in manufacturing and design of such a precise ABH feature.

Sensor Modeling: There were indications from the ABH experiments that it may be very beneficial to incorporate the FBG into the FEM modeling and optimization. Improved modeling of the aperture effect on sensor performance can also help with the sensor design process.

By combining the calibration curve result with the optical system strain resolution, the minimum detectable base motion for a given sensor could be established. If used judiciously with wave propagation models, this could be used to give a direct comparison with displacement resolutions published for AE sensors.

The nonreflective boundary approach has a potential application in sensor design. A sensor could be optimized based on its response to a harmonic sweep of an S0 or A0 Lamb wave mode in the presence of a nonreflective boundary model. This approach could also be used for FEM calculation of calibration curves.

Calibration: It would be helpful to use an improved calibration setup to determine calibration curves of new sensors. A calibration curve for a Lamb wave could also be performed using Laser Doppler vibrometer data.

Although it is somewhat outside the scope of this work, it may an interesting study to try to determine what happened in the steel rail calibration experiment, specifically, why the results seem to have converged to an accurate solution in the presence of what should be

dozens of edge reflections. One hypothesis is that there is some standing wave phenomenon that is providing an equivalent excitation at both sensing locations.

REFERENCES

Abdelrahman, Marwa, Mohamed ElBatanouny, and Paul Ziehl. 2014. "Acoustic Emission Based Damage Assessment Method for Prestressed Concrete Structures: Modified Index of Damage." *Engineering Structures* 60:258–64. https://doi.org/10.1016/j.engstruct.2013.12.037.

Agrawal, Govind, and Stojan Radic. 1994. "Phase-Shifted Fiber Bragg Gratings and Their Application for Wavelength Demultipexing." *IEEE Photonics Technology Letters* 6 (8):995–97. https://doi.org/10.1109/68.313074.

Anastassopoulos, A., and T. Philippidis. 1995. "Clustering Methodology for the E Valuation of Acoustic Emission from Composites." *Journal of Acoustic Emission* 13:11–22.

Anderson, Brian, Marcel Remillieux, Pierre-Yves Le Bas, T Ulrich, and Lukasz Pieczonka. 2015. "Ultrasonic Radiation from Wedges of Cubic Profile: Experimental Results." *Ultrasonics* 63:141–46. https://doi.org/10.1016/j.ultras.2015.07.002.

Andreykiv, Olexander, Mykola Lysak, Oleh Serhiyenko, and Valentyn Skalsky. 2001. "Analysis of Acoustic Emission Caused by Internal Cracks." *Engineering Fracture Mechanics* 68 (11):1317–33. https://doi.org/10.1007/978-3-319-49350-3_3.

ASTM Standard E976-15, "Standard Guide for Determining the Reproducibility of Acoustic Emission Sensor Response." ASTM International, West Conshohocken, PA, 2015, www.astm.org

ASTM Standard E1106-12(2017), "Standard Test Method for Primary Calibration of Acoustic Emission Sensors." ASTM International, West Conshohocken, PA, 2017, www.astm.org

ASTM Standard E1211 / E1211M-17, Standard Practice for Leak Detection and Location Using Surface-Mounted Acoustic Emission Sensors." ASTM International, West Conshohocken, PA, 2017, www.astm.org

ASTM Standard E1419 / E1419M-15a, Standard Practice for Examination of Seamless, Gas-Filled, Pressure Vessels Using Acoustic Emission." ASTM International, West Conshohocken, PA, 2015, www.astm.org

ASTM Standard E1781 / E1781M-13, "Standard Practice for Secondary Calibration of Acoustic Emission Sensors." ASTM International, West Conshohocken, PA, 2013, www.astm.org

ASTM Standard F914 / F914M-15, "Standard Test Method for Acoustic Emission for Aerial Personnel Devices Without Supplemental Load Handling Attachments." ASTM International, West Conshohocken, PA, 2015, www.astm.org

Bayod, Javier. 2011. "Experimental Study of Vibration Damping in a Modified Elastic Wedge of Power-Law Profile." *Journal of Vibration and Acoustics* 133 (6):61003. https://doi.org/10.1115/1.4003591.

Betz, Daniel, Graham Thursby, Brian Culshaw, and Wieslaw Staszewski. 2003. "Acousto-Ultrasonic Sensing Using Fiber Bragg Gratings." *Smart Materials and Structures* 12 (1):122–28. https://doi.org/10.1088/0964-1726/12/1/314.

———. 2007. "Structural Damage Location with Fiber Bragg Grating Rosettes and Lamb Waves." *Structural Health Monitoring* 6 (4):299–308. https://doi.org/10.1177/1475921707081974.

Bhuiyan, Md., and Victor Giurgiutiu. 2017. "Experimental and Computational Analysis of Acoustic Emission Waveforms for SHM Applications." In *11th International Workshop on Structural Health Monitoring*, 1185–1191. Stanford, CA.

Bhuiyan, Md, Yanfeng Shen, and Victor Giurgiutiu. 2017. "Interaction of Lamb Waves with Revet Hole Cracks from Multiple Directions." *Proceedings of the Institution of Mechanical Engineers, Part C: Journal of Mechanical Engineering Science*. Vol. 231.

Blevins, R., and R. Plunkett. 1980. "Formulas for Natural Frequency and Mode Shape." *Journal of Applied Mechanics* 47:461. https://doi.org/10.1121/1.384246.

Blodgett, M., E. Lindgren, S. Sathish, and K. Jata. 2009. "Nondestructive Evaluation/Nondestructive Testing/Nondestructive Inspection (NDE/NDT/NDI) Sensors—Eddy Current, Ultrasonic, and Acoustic Emission Sensors." *Encyclopedia of Structural Health Monitoring*. Chichester, West Sussex: John Wiley & Sons, Inc.

Bøving, Knud 1987. NDE Handbook: Non-Destructive Examination Methods for Condition Monitoring. Bodmin, Cornwall: Hartnolls Ltd.

Bowyer, E., and V. Krylov. 2014a. "Damping of Flexural Vibrations in Turbofan Blades Using the Acoustic Black Hole Effect." *Applied Acoustics* 76:359–65. https://doi.org/ 10.1016/j.apacoust.2013.09.009.

Bowyer, E, and V Krylov. 2014b. “Experimental Investigation of Damping Flexural Vibrations in Glass Fibre Composite Plates Containing One- and Two-Dimensional Acoustic Black Holes.” *Composite Structures* 107. Elsevier Ltd:406–15. https://doi.org/10.1016/j.compstruct.2013.08.011.

Breckenridge, F., C. Tschiegg, and M. Greenspan. 1975. “Acoustic Emission: Some Applications of Lamb’s Problem.” *The Journal of the Acoustical Society of America* 57 (3):626–31. https://doi.org/10.1121/1.380478.

Breckenridge, F., and M. Greenspan. 1981. “Surface-Wave Displacement: Absolute Measurements Using a Capacitive Transducer.” *The Journal of the Acoustical Society of America* 69 (4):1177–85. https://doi.org/10.1121/1.385698.

Chan, T., L. Yu, H. Tam, Y. Ni, S. Liu, W. Chung, and L. Cheng. 2006. “Fiber Bragg Grating Sensors for Structural Health Monitoring of Tsing Ma Bridge: Background and Experimental Observation.” *Engineering Structures* 28 (5):648–59. https://doi.org/10.1016/j.engstruct.2005.09.018.

Chen, R, G Fernando, T Butler, and R Badcock. 2004. “A Novel Ultrasound Fibre Optic Sensor Based on a Fused-Tapered Optical Fibre Coupler.” *Measurement Science and Technology* 15 (8):1490–95. https://doi.org/10.1088/0957-0233/15/8/010.

Chow, Jong, David McClelland, Malcolm Gray, and Ian Littler. 2005. “Demonstration of a Passive Subpicostrain Fiber Strain Sensor.” *Optics Letters* 30 (15):1923–25. https://doi.org/10.1364/OL.30.001923.

Cranch, G., G. Flockhart, and C. Kirkendall. 2006. “Efficient Large-Scale Multiplexing of Fiber Bragg Grating and Fiber Fabry-Perot Sensors for Structural Health Monitoring Applications.” In *Proceedings of SPIE*, 6179:61790P, March 16, 2006.. https://doi.org/ 10.1117/12.657416.

———. 2008. “Distributed Feedback Fiber Laser Strain Sensors.” *IEEE Sensors Journal* 8 (7):1161–72. https://doi.org/10.1109/JSEN.2008.926876.

Crivelli, Davide, Mario Guagliano, and Alberto Monici. 2014. “Development of an Artificial Neural Network Processing Technique for the Analysis of Damage Evolution in Pultruded Composites with Acoustic Emission.” *Composites Part B: Engineering* 56:948–59. https://doi.org/10.1016/j.compositesb.2013.09.005.

Cuadra, J., P. Vanniamparambil, D. Servansky, I. Bartoli, and a. Kontsos. 2015. “Acoustic Emission Source Modeling Using a Data-Driven Approach.” *Journal of Sound and Vibration* 341. Elsevier:222–36. https://doi.org/10.1016/j.jsv.2014.12.021.

Davis, Claire, David Robertson, Chris Brooks, Patrick Norman, Cedric Rosalie, and Nik Rajic. 2014. “Reduced Length Fibre Bragg Gratings for High Frequency Acoustic Sensing.” *Measurement Science and Technology* 25 (12):125105. https://doi.org/ 10.1088/0957-0233/25/12/125105.

de Groot, Peter, Peter Wijnen, and Roger Janssen. 1995. “Real-Time Frequency Determination of Acoustic Emission for Different Fracture Mechanisms in Carbon/epoxy Composites.” *Composites Science and Technology* 55 (4):405–12. https://doi.org/ 10.1016/0266-3538(95)00121-2.

de Oliveira, R., C. Ramos, and A. Marques. 2008. “Health Monitoring of Composite Structures by Embedded FBG and Interferometric Fabry-Pérot Sensors.” *Computers and Structures* 86 (3):340–46. https://doi.org/10.1016/j.compstruc. 2007.01.040.

Denis, V., F. Gautier, a. Pelat, and J. Poittevin. 2015. “Measurement and Modelling of the Reflection Coefficient of an Acoustic Black Hole Termination.” *Journal of Sound and Vibration* 349. Elsevier:67–79. https://doi.org/10.1016/j.jsv.2015.03. 043.

Diamanti, K., and C. Soutis. 2010. “Structural Health Monitoring Techniques for Aircraft Composite Structures.” *Progress in Aerospace Sciences* 46 (8). Elsevier:342–52. https://doi.org/10.1016/j.paerosci.2010.05.001.

Drouillard, Thomas. 1996. “A History of Acoustic Emission.” *Journal of Acoustic Emission* 14 (1):1–34.

Elbatanouny, Mohamed, Paul Ziehl, Aaron Larosche, Jesé Mangual, Fabio Matta, and Antonio Nanni. 2014. “Acoustic Emission Monitoring for Assessment of Prestressed Concrete Beams.” *Construction and Building Materials* 58:46–53. https://doi.org/10.1016/j.conbuildmat.2014.01.100.

Ernst, R., F. Zwimpfer, and J. Dual. 2016. “One Sensor Acoustic Emission Localization in Plates.” *Ultrasonics* 64:139–50. https://doi.org/10.1016/j.ultras.2015.08.010.

Fabry-Perot Interferometer. (n.d.). In *Wikipedia*. Retrieved April 4, 2017 https://en.wikipedia.org/wiki/Fabry-Pérot_interferometer

Fiber Bragg Grating. (n.d.). In *Wikipedia*. Retrieved April 4, 2017 http://en.wikipedia.org/wiki/Fiber_Bragg_grating

Frankforter, Erik, Jingjing Bao, Bin Lin, and Victor Giurgiutiu. 2015. “Modeling, Optimization, and Experimental Validation of a Resonant Piezo-Optical Ring Sensor for Enhanced Active and Passive Structural Health Monitoring.” In *Proc. of SPIE*, 9436:94360B, March 27, 2015. https://doi.org/10.1117/12.2084457.

Frankforter, Erik, Bin Lin, and Victor Giurgiutiu. 2016. “Characterization and Optimization of an Ultrasonic Piezo-Optical Ring Sensor.” *Smart Materials and Structures* 25 (4):45006. https://doi.org/10.1088/0964-1726/25/4/045006.

Fu, Tao, Yanju Liu, Quanlong Li, and Jinsong Leng. 2009. “Fiber Optic Acoustic Emission Sensor and Its Applications in the Structural Health Monitoring of CFRP Materials.” *Optics and Lasers in Engineering* 47 (10):1056–62. https://doi.org/10.1016/j.optlaseng.2009.03.011.

Gary, J., and M. Hamstad. 1994. “On the Far-Field Structure of Waves Generated by a Pencil Lead Break on a Thin Plate.” *J. Acoustic Emission* 12 (3–4):157–70.

Gawronski, M., M. Miszczynski, P. Kijanka, T. Stepinski, T. Uhl, J. Lis, and P. Packo. 2017. “A Semi-Analytical Approach to Design of a Transducer for Selective Wave Generation.” *Structural Health Monitoring* 16 (5). https://doi.org/10.1177/1475921717698636.

Gerges, A, T Newson, J Jones, and D Jackson. 1989. “High-Sensitivity Fiber-Optic Accelerometer.” *Optics Letters* 14 (4):251–53. https://doi.org/10.1364/OL.14.000251.

Giordano, M., A. Calabro, C. Esposito, A. D’Amore, and L. Nicolais. 1998. “An Acoustic-Emission Characterization of the Failure Modes in Polymer-Composite Materials.” *Composites Science and Technology* 58 (12):1923–28. https://doi.org/10.1016/S0266-3538(98) 00013-X.

Giurgiutiu, Victor. 2010. “Structural Health Monitoring with Piezoelectric Wafer Active Sensors – Predictive Modeling and Simulation.” *Incas Bulletin* 2 (3):31–44. https://doi.org/10.13111/2066-8201.2010.2.3.4.

———. *Structural Health Monitoring with Piezoelectric Wafer Active Sensors*. 2nd ed. Academic Press.

———. 2015. Structural Health Monitoring of Aerospace Composites. Academic Press.

Giurgiutiu, Victor, and Erik Frankforter. 2017. US Patent Application No. 62/506,705.

Giurgiutiu, Victor, Gresil, Matthieu.; Roman, Catalin. “Acousto-ultrasonic sensor” Patent No. US9158054 B2. October 2015

Giurgiutiu, Victor, Catalin Roman, Bin Lin, and Erik Frankforter. 2015. “Omnidirectional Piezo-Optical Ring Sensor for Enhanced Guided Wave Structural Health Monitoring.” *Smart Materials and Structures* 24 (1):15008. https://doi.org/10.1088/0964-1726/24/1/015008.

Glaessgen, Edward, and David Stargel. 2012. “The Digital Twin Paradigm for Future NASA and U.S. Air Force Vehicles.” In *53rd AIAA/ASME/ASCE/AHS/ASC Structures, Structural Dynamics and Materials Conference*, 1–14. https://doi.org/10.2514/6.2012-1818.

Graff, Karl. 1975. *Wave Motion in Elastic Solids*. Dover Publications, Inc.

Greenspan, Martin. 1987. “The NBS Conical Transducer: Analaysis.” *The Journal of the Acoustical Society of America* 81 (1):173–83. https://doi.org/10.1121/1.395027.

Gresil, Matthieu, Lingyu Yu, Victor Giurgiutiu, and Michael Sutton. 2012. “Predictive Modeling of Electromechanical Impedance Spectroscopy for Composite Materials.” *Structural Health Monitoring: An International Journal* 11 (6):671–83. https://doi.org/10.1177/1475921712451954.

Grosse, Christian, and Florian Finck. 2006. “Quantitative Evaluation of Fracture Processes in Concrete Using Signal-Based Acoustic Emission Techniques.” *Cement & Concrete Composites, 28(4)* 28 (4):330–36. https://doi.org/10.1016/j.cemconcomp.2006.02.006.

Hamilton, L., B. Scowcroft, M. Ayers, V, Bailey, and A. Carnesale. 2012. "*Blue Ribbon Commission on America’s Nuclear Future: Report to the Secretary of Energy."Blue Ribbon Commission on America's Nuclear Future (BRC).* Washington, DC: US Department of Energy.

Hamstad, M. 2009. “Some Observations on Rayleigh Waves and Acoustic Emission in Thick Steel Plates.” *Journal of Acoustic Emission Acoustic Emission* 27:114–36.

———. 2010. “On Lamb Modes As a Function of Acoustic Emission Source Rise Time.” *Journal of Acoustic Emission* 28:41–58.

Hamstad, M., and C. Furtunko. 1995. “Development of Practical Wideband High-Fidelity Acoustic Emission Sensors.” In *SPIE Nondestructive Evaluation of Aging Bridges and Highways*, 2456:281–89.

Hamstad, M., J. Gary, and A. O’Gallagher. 1996. “Far-Field Acoustic Emission Waves by Three-Dimensional Finite Element Modeling of Pencil-Lead Breaks on a Thick Plate.” *J. Acoustic Emission* 14 (2):103–14.

Hamstad, M., and J. McColskey. 1997. “Wideband and Narrowband Acoustic Emission Waveforms from Extraneous Sources during Fatigue of Steel Samples.” *Journal of Acoustic Emission* 15 (1–4):1–18.

Hamstad, M., A. O'Gallagher, and J. Gary. 1999. Modeling of buried monopole and dipole sources of acoustic emission with a finite element technique. *Journal of acoustic emission* 17 (3-4): 97–110.

Hardy, Reginald. 2005. Acoustic Emission/Microseismic Activity: Principles, Techniques and Geotechnical Applications. Vol. 1. CRC Press.

Hill, K., Y. Fujii, D. Johnson, and B. Kawasaki. 1978. “Photosensitivity in Optical Fiber Waveguides: Application to Reflection Filter Fabrication.” *Applied Physics Letters* 32 (10):647–49. https://doi.org/10.1063/1.89881.

Holford, K, R Pullin, S Evans, M Eaton, J Hensman, and K Worden. 2009. “Acoustic Emission for Monitoring Aircraft Structures.” *Proceedings of the Institution of Mechanical Engineers, Part G: Journal of Aerospace Engineering* 223 (5):525–32. https://doi.org/10.1243/09544100JAERO404.

Huang, M., L. Jiang, P. Liaw, C. Brooks, R. Seeley, and D. Klarstrom. 1998. Using Acoustic Emission in Fatigue and Fracture Materials Research. *Journal of the Minerals, Metals & Materials Society 50*(11): 1–14.

Inasaki, Ichiro. 1998. “Application of Acoustic Emission Sensor Machining Processes.” *Ultrasonics* 36:273–81. https://doi.org/10.1016/S0041-624X(97)00052-8.

Kalafat, S., and M. Sause. 2015. “Acoustic Emission Source Localization by Artificial Neural Networks.” *Structural Health Monitoring* 14 (6):633–47. https://doi.org/10.1177/1475921715607408.

Kageyama, Kazuro, Hideaki Murayama, Isamu Ohsawa, Makoto Kanai, Keiichi Nagata, Yuichi Machijima, and Fumio Matsumura. 2005. “Acoustic Emission Monitoring of a Reinforced Concrete Structure by Applying New Fiber-Optic Sensors.” *Smart Materials and Structures* 14 (3):S52–59. https://doi.org/10.1088/0964-1726/14/3/007.

Kaiser, J. 1950. An investigation into the occurrence of noises in tensile tests, or a study of acoustic phenomena in tensile tests. PhD thesis, Technical University of Munich.

Koberna, Miroslav. 1993. “Broadband Acoustic Emission Sensor with a Conical Active Element in Practice.” *Journal of Acoustic Emission* 11 (2):61–63.

Kuang, K., R. Kenny, M. Whelan, W. Cantwell, and P. Chalker. 2001. “Embedded Fibre Bragg Grating Sensors in Advanced Composite Materials.” *Composites Science and Technology* 61 (10):1379–87. https://doi.org/10.1016/S0266-3538(01)00037-9.

Krylov, V. 1990. “Localized Acoustic Modes of a Quadratic Solid Wedge.” *Moscow University Physics Bulletin* 45 (6):65–69.

———. 2002. “Acoustic ‘Black Holes’ for Flexural Waves and Their Potential Applications.” In *Proceedings of the Institute of Acoustics Spring Conference*, March 25-27, 2002.

———. 2012. “Geometric Acoustics Approximation for Rayleigh and Lamb Waves.” In *The Ninth International Conference on Condition Monitoring and Machinery Failure Prevention Technologies*, June 12-14, 2012.

Krylov, V, and F Tilman. 2004. “Acoustic ‘Black Holes’ for Flexural Waves as Effective Vibration Dampers.” *Journal of Sound and Vibration* 274 (3):605–19. https://doi.org/10.1016/j.jsv.2003.05.010.

Krylov, V., and R. Winward. 2007. “Experimental Investigation of the Acoustic Black Hole Effect for Flexural Waves in Tapered Plates.” *Journal of Sound and Vibration* 300 (1):43–49. https://doi.org/10.1016/j.jsv.2006.07.035.

Lamb Waves. (n.d.). In *Wikipedia*. Retrieved October 10, 2017, from https://en.wikipedia.org/wiki/Lamb_waves

Lee, Jung-Ryul, Seung-Seok Lee, and Dong-Jin Yoon. 2008. “Simultaneous Multipoint Acoustic Emission Sensing Using Fibre Acoustic Wave Grating Sensors with Identical Spectrum.” *Journal of Optics A: Pure and Applied Optics* 10 (8):85307. https://doi.org/10.1088/1464-4258/10/8/085307.

Lee, Jung-Ryul, Seung-Seok Lee, and Dong-Jin Yoon. 2008. “Simultaneous Multipoint Acoustic Emission Sensing Using Fibre Acoustic Wave Grating Sensors with Identical Spectrum.” *Journal of Optics A: Pure and Applied Optics* 10 (8):85307. https://doi.org/10.1088/1464-4258/10/8/085307.

Lin, Bin., and Victor Giurgiutiu. 2014a. Development of optical equipment for ultrasonic guided wave structural health monitoring. In *Proc. SPIE* vol. 9062, April 10, 2014. http://dx.doi.org/10.1117/12.2045070

———. (2014b). Piezo-Optical Active Sensing With PWAS And FBG Sensors For Structural Health Monitoring. In *ASME 2014 Conference on Smart Materials, Adaptive Structures and Intelligent Systems, September 8-10, 2014*. American Society of Mechanical Engineers. https://doi.org/ 10.1115/SMASIS2014-7581

Lissak, B, a Arie, and M Tur. 1998. “Highly Sensitive Dynamic Strain Measurements by Locking Lasers to Fiber Bragg Gratings.” *Optics Letters* 23 (24):1930–32. https://doi.org/10.1364/OL.23.001930.

Lysak, Mykola. 1996. “Development of The Theory of Acoustic Emission by Propagating Cracks in Terms of Fracture Mechanics.” *Engineering Fracture Mechanics* 55 (3):443–52. https://doi.org/10.1016/0013-7944(96)00026-4.

Maalej, M, S Ahmed, K Kuang, and P Paramasivam. 2004. “Fiber Optic Sensing for Monitoring Corrosion-Induced Damage.” *Structural Health Monitoring* 3 (2):165–76. https://doi.org/10.1177/1475921704042679.

Maji, A., D. Satpathi, and T. Kratochvil. 1997. “Acoustic Emission Source Location Using Lamb Wave Modes” 123 (2):154–61. https://doi.org/10.1061/(ASCE)0733-9399(1997)123:2(154).

Marin-franch, P, T Martin, D L Tunnicliffe, and D K Das-gupta. 2002. “PTCa / PEKK Piezo-Composites for Acoustic Emission Detection.” *Sensors and Actuators, A* 99:236–43. https://doi.org/10.1016/0013-7944(96)00026-4.

Meltz, G., W. Morey, and W. Glenn. 1989. “Formation of Bragg Gratings in Optical Fibers by a Transverse Holographic Method.” *Optics Letters* 14 (15):823–25. https://doi.org/10.1364/OL.14.000823.

Michaels, J., T. Michaels, and W. Sachse. 1981. “Application of Deconvolution to Acoustic Emission Signal Analysis.” *Materials Evaluation* 39 (11):1032–36.

Mita, A.; Yokoi, I. 2000. "Fiber Bragg grating accelerometer for structural health monitoring." *Conference on Motion and vibration control*, December 4-8, 2000.

Murphy, Kent, Michael Gunther, Ashish Vengsarkar, and Richard Claus. 1991. “Quadrature Phase-Shifted, Extrinsic Fabry-Perot Optical Fiber Sensors.” *Optics Letters* 16 (4):273–75. https://doi.org/10.1364/OL.16.000273.

Nair, Archana, and C. S. Cai. 2010. “Acoustic Emission Monitoring of Bridges: Review and Case Studies.” *Engineering Structures* 32 (6). Elsevier Ltd:1704–14. https://doi.org/10.1016/j.engstruct.2010.02.020.

Nakamura, Kentaro. 2012. Ultrasonic transducers: Materials and design for sensors, actuators and medical applications. Elsevier.

Norman P., and C. Davis. 2010. “An intensity-based demodulation approach for the measurement of strains induced by structural vibrations using Bragg gratings.” Technical Report, Report No DSTO-TR-2370, Defense Science and Technology Organisation (DSTO), Australia.

Ono, K. 2005. “Current understanding of mechanisms of acoustic emission.” *The Journal of Strain Analysis for Engineering Design 40*(1): 1–15. https://doi.org/10.1243/030932405X7674

———. (2011). “Acoustic Emission in Material Research - A Review.” *Journal of acoustic emission* 29: 284–308.

———. 2016. “Calibration Methods of Acoustic Emission Sensors.” *Materials* 9 (7):508. https://doi.org/10.3390/ma9070508.

Ono, K., and M. Ohtsu. 1984. “A generalized theory of acoustic emission and Green's functions in a half space.” *Journal of Acoustic Emission*, 3: 27–40.

Ohtsu, M. 1995. Acoustic emission theory for moment tensor analysis. *Journal of Research in Nondestructive Evaluation 6*(3) 169–184.

Or, S, H Chan, and C Choy. 2000. “P (VDF-TrFE) Copolymer Acoustic Emission Sensors.” *Sensors and Actuators* 80:237–41. https://doi.org/https://doi.org/10.1016/S0924-4247(99)00305-2.

Ouyang, C., E. Landis, and S. Shah. 1991. “Damage assessment in concrete using quantitative acoustic emission.” *Journal of Engineering Mechanics* 117(11), 2681–2698.

Park, C.; K. Peters, and M. Zikry. 2010 "The effects of embedded optical fiber density on the impact response and lifetime of laminated composites."*Journal of Intelligent Material Systems and Structures* 21(18):1819–1829.

Pavlakovic, B, and M. Lowe. 2003. "Disperse Software Manual Version 2.0. 1 6B." Imperial College, London, UK.

Perez, I, H. Cui, and E. Udd. 2001. "Acoustic emission detection using fiber Bragg gratings." *SPIE's 8th Annual International Symposium on Smart Structures and Materials, March 4-8, 2011*. International Society for Optics and Photonics.

Peters, K. 2009a. “Fiber Bragg Grating Sensors.” Encyclopedia of Structural Health Monitoring. Chichester, West Sussex: John Wiley & Sons.

Peters, K. (2009b). “Fiber Optic Sensor Principles.” Encyclopedia of Structural Health Monitoring. Chichester, West Sussex: John Wiley & Sons.

Peters, K. 2010. "Polymer optical fiber sensors—a review." *Smart materials and structures* 20(1) 013002. https://doi.org/10.1088/0964-1726/20/1/013002.

Poddar, Banibrata., and Victor Giurgiutiu. (2015). Experimental validation of analytical model for Lamb wave interaction with geometric discontinuity. In *Structural Health Monitoring and Inspection of Advanced Materials, Aerospace, and Civil Infrastructure, April 1, 2015*. International Society for Optics and Photonics.

Poddar, Banibrata, and Victor Giurgiutiu. 2016. "Scattering of Lamb waves from a discontinuity: An improved analytical approach." *Wave Motion* 65: 79–91. https://doi.org/10.1016/j.wavemoti.2016.03.009

Proctor, Thomas. 1982. “An improved piezoelectric acoustic emission transducer.” *The Journal of the Acoustical Society of America 71*(5): 1163–1168. https://doi.org/10.1121/1.387763

———. 1986. “More recent improvements on the NBS conical transducer.” *Journal of Acoustic Emission* 5:134–142.

———. 1988. “A high fidelity piezoelectric tangential displacement transducer for acoustic emission.” *Journal of acoustic emission* 7(1):41–47.

Ranganayakulu, S., M. Kiran, J. Raju, and B. Kumar. 2016. “Studies of Acoustic Emission Signatures for Quality Assurance of SS316L Welded Samples Under Dynamic Load Conditions.” *Journal of Engineering Science and Technology* 11(10):1499–1517.

Read, I., P. Foote, and S. Murray. 2001. "Optical fibre acoustic emission sensor for damage detection in carbon fibre composite structures." *Measurement Science and Technology* 13(1): N5.

Rice, J. R. (1980). Elastic wave emission from damage processes. *Journal of Nondestructive Evaluation* 1(4):215–224.

Roberts, T., and M. Talebzadeh. 2003. “Acoustic emission monitoring of fatigue crack propagation.” *Journal of Constructional Steel Research 59*(6):695-712. https://doi.org/10.1016/S0143-974X(02)00064-0.

Roman, Catalin. 2013 *Structural Health Monitoring of Composite Laminates Using Piezoelectric and Fiber Optics Sensors*. PhD dissertation, University of South Carolina

Rosenthal, A., D. Razansky, and V. Ntziachristos. 2011. "High-sensitivity compact ultrasonic detector based on a pi-phase-shifted fiber Bragg grating." *Optics letters* 36(10):1833–1835. https://doi.org/10.1364/OL.36.001833.

Sagar, Vidya, and Raghu Prasad. 2012. “A review of recent developments in parametric based acoustic emission techniques applied to concrete structures.” *Nondestructive Testing and Evaluation*, *27*(1):47–68. http://dx.doi.org/10.1080/10589759.2011.589029.

Sause, M, and S. Horn. 2010. “Simulation of acoustic emission in planar carbon fiber reinforced plastic specimens.” *Journal of Nondestructive Evaluation*, *29*(2):123–142. https://doi.org/10.1007/s10921-010-0071-7.

Sause, Markus, M. Hamstad, and S. Horn. 2012. “Finite element modeling of conical acoustic emission sensors and corresponding experiments.” *Sensors and Actuators A: Physical*, *184:*64–71. https://doi.org/10.1016/j.sna.2012.06.034.

Sause, M, T. Müller, A. Horoschenkoff, and S. Horn. (2012). “Quantification of failure mechanisms in mode-I loading of fiber reinforced plastics utilizing acoustic emission analysis.” *Composites science and technology* 72(2):167–174. https://doi.org/10.1016/j.compscitech.2011.10.013.

Sause, Markus, and Stefan Richler. 2015. “Finite element modelling of cracks as acoustic emission sources.” *Journal of nondestructive evaluation* 34(1) 4. https://doi.org/ 10.1007/s10921-015-0278-8.

Scala, C. 1983. “Acoustic emission sensors.” *Journal of Acoustic Emission* 2:275-279.

Schmidt, Markus, and Norbert Fürstenau. 1999. "Fiber-optic extrinsic Fabry–Perot interferometer sensors with three-wavelength digital phase demodulation." *Optics letters* 24(9): 599–601. https://doi.org/10.1364/OL.24.000599.

Scruby, C. 1984. “Acoustic emission measurements using point-contact transducers.” Cern Report No. AERE-R-11328-MF.

Scruby, C., G. Baldwin, and K. Stacey. 1985. “Characterisation of fatigue crack extension by quantitative acoustic emission.” *International Journal of Fracture* 28(4):201–222.

Scruby, C., and H. Wadley. 1978. “A calibrated capacitance transducer for the detection of acoustic emission.” *Journal of Physics D: Applied Physics* 11(11):1487–1494.

Shen, Yanfeng, and Victor Giurgiutiu. 2014. “WaveFormRevealer: an analytical framework and predictive tool for the simulation of multi-modal guided wave propagation and interaction with damage.” *Structural Health Monitoring* 13(5):491–511. https://doi.org/10.1177/1475921714532986.

———. 2015. "Effective non-reflective boundary for Lamb waves: Theory, finite element implementation, and applications." *Wave Motion* 58: 22-41. https://doi.org/ 10.1016/j.wavemoti.2015.05.009.

Stefani, Alessio, Søren Andresen, Wu Yuan, Nicolai Herholdt-Rasmussen, and Ole Bang. 2012. "High sensitivity polymer optical fiber-Bragg-grating-based accelerometer." *IEEE Photonics Technology Letters* 24.9: 763-765.https://doi.org/ 10.1109/LPT.2012.2188024.

Svečko, Rajko, Dragan Kusić, Tomaž Kek, Andrej Sarjaš, Aleš Hančič, and Janez Grum. 2013. Acoustic emission detection of macro-cracks on engraving tool steel inserts during the injection molding cycle using PZT sensors. *Sensors* 13(5): 6365–6379. https://doi.org /10.3390/s130506365.

Sun, Xiaoyi, Bin Lin, Jingjing Bao, Victor Giurgiutiu, Travis Knight, Poh-Sang Lam, and Lingyu Yu "Developing a structural health monitoring system for nuclear dry cask storage canister." In *SPIE Smart Structures and Materials+ Nondestructive Evaluation and Health Monitoring*, March 27, 2015. International Society for Optics and Photonics.

Tabatabai, Habib, David Oliver, John Rohrbaugh, and Christopher Papadopoulos. 2013. "Novel applications of laser Doppler vibration measurements to medical imaging." *Sensing and Imaging: An International Journal 14*(1-2):13–28. https://doi.org/10.1007/s11220-013-0077-1.

Takeda, Nobuo, Yoji Okabe, Junichiro Kuwahara, Seiji Kojima, and Toshimichi Ogisu. 2005. "Development of smart composite structures with small-diameter fiber Bragg grating sensors for damage detection: Quantitative evaluation of delamination length in CFRP laminates using Lamb wave sensing." *Composites science and technology* 65(15): 2575-2587. https://doi.org/10.1016/j.compscitech.2005.07.014.

Takeda, S., Y. Okabe, and N. Takeda. 2002. "Delamination detection in CFRP laminates with embedded small-diameter fiber Bragg grating sensors." *Composites Part A: applied science and manufacturing* 33(7): 971–980. https://doi.org/10.1016/S1359-835X(02)00036-2.

Takuma, Masanori, Shigeyoshi Hisada, Kenichi Saitoh, Yoshimasa Takahashi, Yuuki Kobayashi, Akira Kadono, Atushi Murata, Satoshi Iwata, and Toshinori Sasaki. 2014. "Acoustic emission measurement by fiber Bragg grating glued to cylindrical sensor holder." Advances in Materials Science and Engineering 2014. http://dx.doi.org/10.1155/2014/274071.

Temkin, S. 1981. *Elements of acoustics*. New York: Wiley.

Theobald, P. D. 2009. "Optical calibration for both out-of-plane and in-plane displacement sensitivity of acoustic emission sensors." *Ultrasonics 49*(8):623–627. https://doi.org/ 10.1016/j.ultras.2009.03.004.

Todd, M., G. Johnson, B. Althouse, and S. Vohra. 1998. "Flexural beam-based fiber Bragg grating accelerometers." *IEEE Photonics Technology Letters*10(11):1605–1607.

Tsuda, H.; K. Kumakura, and S.Ogihara. 2010 "Ultrasonic sensitivity of strain-insensitive fiber Bragg grating sensors and evaluation of ultrasound-induced strain." *Sensors* 10(12): 11248-11258. https://doi.org/10.3390/s101211248.

Tsuda, H. "Ultrasound and damage detection in CFRP using fiber Bragg grating sensors." *Composites science and technology* 66.5 (2006): 676-683.

Tsuda, Hiroshi, Eiichi Sato, Tomio Nakajima, Hideyuki Nakamura, Takahiro Arakawa, Hideyuki Shiono, Masashi Minato, Hideyuki Kurabayashi, and Akiyoshi Sato. 2009. "Acoustic emission measurement using a strain-insensitive fiber Bragg grating sensor under varying load conditions." *Optics letters* 34(19):2942–2944. https://doi.org/10.1364/ OL.34.002942.

Udd, E. *Fiber optic smart structures*. Vol. 12. Wiley-Interscience, 1995.

Unnþórsson, R. 2013. Hit detection and determination in AE bursts. In *Acoustic Emission-Research and Applications, March 6, 2013*. InTech.

U.S. Department of Transportation Federal Highway Administration. 2014. *Deficient Bridges by State and Highway System*. Washington, DC.

U.S. Department of Transportation Federal Highway Administration. (2014). *Estimated 2013 Costs to Replace or Rehabilitate Structurally Deficient Bridges*. Washington, DC.

Vella, T., S. Chadderdon, R. Selfridge, S. Schultz, S. Webb, C. Park, K. Peters, and M. Zikry. 2010. "Full-spectrum interrogation of fiber Bragg gratings at 100 kHz for detection of impact loading." *Measurement Science and Technology* 21(9): 094009. https://doi.org/10.1088/0957-0233/21/9/094009.

Wang, G., K. Pran, G. Sagvolden, G. Havsgård, A. Jensen, G. Johnson, and S. Vohra. 2001."Ship hull structure monitoring using fibre optic sensors." *Smart materials and structures* 10(3): 472–478.

Webb, D., J. Surowiec, M. Sweeney, D. Jackson, L. Gavrilov, J. Hand, L. Zhang, and I. Bennion. 1996. "Miniature fiber optic ultrasonic probe." *SPIE's 1996 International Symposium on Optical Science, Engineering, and Instrumentation,* October 25, 1996. International Society for Optics and Photonics.

Wee, J., D. Hackney P. Bradford, and K. Peters. 2017. “Simulating increased Lamb wave detection sensitivity of surface bonded fiber Bragg grating.” *Smart Materials and Structures 26*(4): 045034. https://doi.org/10.1088/1361-665X/aa646b.

Wee, J., D. Hackney, K. Peters, B. Wells, and P. Bradbord. "Sensitivity of contact-free fiber Bragg grating sensor to ultrasonic Lamb wave." *SPIE Smart Structures and Materials+ Nondestructive Evaluation and Health Monitoring,* April 20, 2016. International Society for Optics and Photonics.

Wu, Qi, and Yoji Okabe. 2012. "High-sensitivity ultrasonic phase-shifted fiber Bragg grating balanced sensing system." *Optics express* 20(27): 28353–28362. https://doi.org/ 10.1364/OE.20.028353.

Xiong, Z., G. Peng, B. Wu, and P. Chu. 1999. "Highly tunable Bragg gratings in single-mode polymer optical fibers." *IEEE Photonics technology letters* 11(3):352–354. https://doi.org/10.1109/68.748232.

Yalcinkaya, Hazim, and Didem Ozevin. 2013. “The design and calibration of particular geometry piezoelectric acoustic emission transducer for leak detection and localization.” *Measurement Science and Technology*, *24*(9):095103. https://10.1088/0957-0233/24/9/095103

Yan, T., P. Theobald, and B. Jones. 2004. “A conical piezoelectric transducer with integral sensor as a self-calibrating acoustic emission energy source.” *Ultrasonics 42*(1):431–438. https://doi.org/10.1016/j.ultras.2003.12.039

Yu, Lingyu, Sepandarmaz Momeni, Valery Godinez, and Victor Giurgiutiu. 2011. “Adaptation of PWAS transducers to acoustic emission sensors.” In *SPIE smart structures and materials nondestructive evaluation and health monitoring*, April 20, 2011. *International Society for Optics and Photonics*. https://doi.org/10.1117/12.880157

Yu, Fengming, Qi Wu, Yoji Okabe, Satoshi Kobayashi, and Kazuya Saito 2016. "The identification of damage types in carbon fiber–reinforced plastic cross-ply laminates using a novel fiber-optic acoustic emission sensor." *Structural Health Monitoring* 15(1): 93-103. https://doi.org.10.1177/1475921715624503

Zhao, L., Conlon S., and Semperlotti, F. 2014. “Broadband energy harvesting using acoustic black hole structural tailoring.” *Smart Materials and Structures* 23(6):065021. https://doi.org/10.1088/0964-1726/23/6/065021